Numerical Simulation of Laminar and Turbulent Hybrid Forced-Buoyancy Convection in Channels with a Step

PhD Thesis

Saad Inam

James Weir Fluid Laboratory

Department of Mechanical and Aerospace Engineering

University of Strathclyde, Glasgow

February 19, 2022

This thesis is the result of the author's original research. It has been composed by the author and has not been previously submitted for examination which has led to the award of a degree.

The copyright of this thesis belongs to the author under the terms of the United Kingdom Copyright Acts as qualified by University of Strathclyde Regulation 3.50. Due acknowledgement must always be made of the use of any material contained in, or derived from, this thesis.

Saad Inam
University of Strathclyde, February 19, 2022

Research Output

The outcomes of this work explained in Part II of this thesis have also been utilised to produce four research articles which have been submitted to different peer-reviewed International Scientific Journals. Two of these research works have been published, while other two papers are currently under review.

Journal Papers

1. Lappa, M. and Inam, S., 2020. "Thermogravitational and hybrid convection in an obstructed compact cavity. *International Journal of Thermal Sciences*", 156, p.106478.

2. Inam, S. and Lappa, M., 2021. "Flow topology and bifurcations of buoyancy and mixed convection in an elongated channel with an abrupt section variation", *International Journal of Heat and Mass Transfer*, 173, p.121267.

3. Inam, S. and Lappa, M., "Hybrid Forced-buoyancy convection in a channel with a backward facing step" (under review)

4. Inam, S. and Lappa, M., "Large eddy simulation of three-dimensional hybrid forced-buoyancy convection in channels with a step" (ready for submission).

Abstract

The flow over a topography or a step is a fundamental problem in fluid dynamics with relevance to many fields and circumstances. In the present analysis direct numerical simulation (DNS) is initially used to examine the properties of the thermofluid-dynamic field in two-dimensional channels with a *heated obstruction* located on the bottom. The involved dynamics include forced flow driven by injection of cold fluid and the buoyancy convection of thermal origin, which naturally emerges in these channels as a result of the prevailing temperature gradients. The sensitivity of these systems to thermal buoyancy for each considered rate of fluid injection (measured through the related Richardson number, Ri) is explored by varying parametrically the corresponding Rayleigh number (Ra) over a large interval of orders of magnitude (up to the onset of chaos). Different orientations of the step with respect to the forced flow are assumed (Forward-Facing and Backward-Facing Steps) and two alternate paradigms are considered for the bottom of the considered channel, namely an adiabatic or kept-at-constant temperature (hot) boundary. Through this conceptual framework and using a peculiar analysis hierarchy where selected effects are intentionally switched on or off depending on the targeted regime, a kaleidoscope of situations is revealed in the (Ri, Ra) space, which differ in terms of flow patterning behaviour, thermal plume generation phenomena, intensity of heat exchange at the walls and bifurcation scenario. Comparison of forward facing and backward facing step configurations indicates that, besides the differences, these two systems display interesting analogies. These are further explored by removing the constraint of two-dimensionality and allowing the flow to develop along the spanwise direction. To reduce the scale of the three-dimensional problem to a level where it is affordable, however, this study is developed in the framework of a large eddy simulation (LES) approach. The results of the three-dimensional simulations are used to clarify some still poorly known aspects, i.e., the dynamics in proximity to the point where the abrupt change in the channel cross-sectional area occurs and the effect of problem dimensionality on the flow behaviour at different length scales .

Acknowledgements

First, I would like to thank Allah Almighty for giving me the strength and ability to successfully overcome this challenge, which has been one of the greatest experience of my life. I would like to thank and express my gratitude to my supervisor Dr. Marcello Lappa, who has inarguably been a thoughtful supervisor, providing me with continuous advice and guidance throughout this research journey. I consider myself lucky and honoured to have worked with an experienced supervisor like him. I am extremely grateful to him for his untiring support in every aspect of this PhD journey, helping me to understand complex concepts and providing consistent feedbacks on my draft chapters. I'm also grateful to Dr Hermes Ferialdi for helping me to become familiar with the computational platform OpenFOAM as well as Dr Paolo Capobianchi, Dr Thomas Burel and Alessio Boaro for their precious support in overcoming some troubles related to this software.

I would also like to thank my beloved family, particularly my parents, who have done so much for me. Without their support I would have never been able to achieve any goal in my life. I hope this work will make them proud of me. A heartfelt thanks to my uncle Sarwat Naeem for looking after me during my stay in Glasgow and my elder brother Dr Danial Inam, who supported me financially throughout my PhD. A special appreciation for Irfan Bhai who gave me a part time job which helped me to fund my PhD.

Finally, a special thanks to another person behind the scenes for providing me with emotional support during this challenging journey (I hope you know who you are and how much you mean to me).

Nomenclature

Latin Symbols

A	Domain aspect ratio
d	Transverse channel size
d_s	Vertical step size
g	Gravity acceleration
q	Wavenumber
$\underline{i}_g$	Unit vector along gravity
l	Horizontal step extension
L	Overall horizontal extension
M	Mach number
p	Pressure
Pr	Prandtl number
Pr_T	Turbulent Prandtl number
Nu	Nusselt number
Gr	Grashof number
Ra	Rayleigh number
Ra_{cr}	Critical Rayleigh number
Re	Reynolds number
Ri	Richardson number
t	Time
T	Temperature
u	Velocity component along x
v	Velocity component along y
w	Velocity component along z
c_p	Heat capacity at constant pressure
c_v	Heat capacity at constant volume
U	Inflow (horizontal) velocity
V	Fluid velocity (vector)
x	Horizontal coordinate
x_1	Reattachment length
x_2	Secondary roll leading edge
x_3	Secondary trailing edge
y	Vertical coordinate
z	Spanwise coordinate
k_{sgs}	Subgrid-scale kinetic energy
$\overline{D}$	Strain rate tensor
L_z	Domain length along spanwise direction
f	Non-dimensional frequency
Δ	Mesh size
δ_{ij}	Hydrostatic stress tensor

Greek Symbols

α	Thermal diffusivity
α_T	Turbulent thermal diffusivity
β	Thermal expansion coefficient
ν	Kinematic viscosity
ω	Angular frequency of oscillation
ν_T	Turbulent kinematic viscosity
λ	thermal conductivity
ζ	Kolmogorov length
ρ	density
μ	dynamic viscosity
$\underline{\underline{\tau}}$	Stress tensor
τ_{ij}	Subgrid-scale stress tensor
ΔT	Temperature difference

Acronyms

A	**Aspect ratio**
ER	Expansion ratio (d/d_s)
LR	Length ratio (L/l)
2D	Two-dimensional
3D	Three-dimensional
RB	Rayleigh-Bénard
BCs	Boundary conditions
OBC	Open boundary condition
PBC	Periodic boundary conditions
CFD	Computational Fluid Dynamics
FFS	Forward Facing Step
BFS	Backward Facing Step
PTV	Particle Tracking Velocimetry
LSA	Linear Stability Analysis
OLR	Oscillatory Longitudinal Rolls
SLR	Stationary Longitudinal Rolls
DNS	Direct Numerical Simulation
LES	Large Eddy Simulation
RANS	Reynolds Average Navier Stokes
FFT	Fast Fourier Transform
PISO	Pressure Implicit Split Operator
AMG	Algebraic Multigrid scheme
PBiCG	Preconditioned Bi-Conjugate Gradient
DILU	Diagnol Incomplete Lower Upper
GAMG	Generalized Geometric-Algebraic Multi-Grid

Contents

Part I

Physical and mathematical framework

Chapter 1

Introduction

In a variety of practical and industrial processes, fluids evolve under the effect of an imposed pressure difference in channels or ducts with variable geometry. These channels often exhibit abrupt changes in their cross-sectional area or undergo sudden expansions or compressions. In such a context, ducts with a forward facing step (FFS) or a backward facing step (BFS) have therefore enjoyed widespread attention as archetypal systems for the analysis of many problems with practical or technological relevance.

Inherently multidisciplinary, these fundamental fluid-dynamic subjects really stand at the interface between different technological fields, which include (but are not limited to) mechanical, civil and aeronautical engineering (e.g., the interaction of gas currents with vehicles, buildings and airfoils at a large angle of attack, Skinner and Behtash, 2017), thermal engineering (combustors, condensers, industrial heat exchangers, Papazian et al. 2020; Brottier and Bennacer 2020; Souissi et al. 2020), and many other strictly related applications (e.g., the cooling of nuclear reactors, power plants and various types of electronic equipment, Sun and Jaluria, 2011).

Other relevant examples can be found in chemical plants or food-processing industries. Related hydraulic circuits are often featured by sudden changes in the cross-sectional area and/or other kinds of obstructions mounted in a direction perpendicular to the prevailing current (e.g., ribs and baffles, which prevent the flow from developing a regular path). These concepts also apply to the very general area of fluid machinery where flow separation typically leads to an increase in the frictional shear stress (thereby causing significant energy losses, Hattori and Nagano, 2010). This subject also displays notable kinships with other important engineering challenges such as the determination of the pressure and shear stress distribution over ground vehicles (Dai et al. 2020; Redchyts et al., 2020) or the production of wind energy (Sherry et al. 2010).

For all these reasons, the general problem relating to the topology and nature (steady, oscillatory or turbulent) of flows over and around wall-mounted obstacles (or in the presence of geometrical contractions or orifices) has long attracted the interest of researchers.

Although problems involving fluids flowing over steps can support a multifaceted spectrum of different research initiatives and are omnipresent in technical and engineering applications, however, as implicitly made evident by the focused review of literature reported in the following sections of this chapter, a significant lack of information seems to still exist with regard to conditions for which *forced flow and thermal (buoyancy) convection compete in determining the patterning behaviour and the evolutionary progress of these systems towards chaos*.

For these reasons, this thesis mostly revolves around “hybrid convection”, i.e., the flow induced by the combination of forced flow and gravitational convection induced by the presence of temperature gradients. In line with past efforts, the domains considered in this study are essentially the canonical FFS and BFS configurations. Unlike earlier analyses, however, here

much emphasis is put on the conditions in which the thermal flow component is dominant and/or forced flow and buoyancy convection have a comparable magnitude.
The thesis is articulated as follows. While Chapter 1 is essentially used to introduce the problem and provide the reader with a rich review of the existing literature on these subjects, Chapter 2 is concerned with the definition of a relevant physical-mathematical models and presents the related governing equations and non-dimensional numbers. Chapter 3 is devoted to a presentation of the considered geometrical configurations and the associated boundary conditions, whereas numerical methods, mesh selection and validation are the main subject of Chapter 4.
Geometrical systems with an increasing degree of complexity are examined as the discussion progresses, i.e., a two-dimensional (2D) compact cavity with aligned and misaligned inlet and outlet (Chapter 5), a 2D extended channel with a FFS (Chapter 6), a (yet 2D) elongated channel with a BFS (Chapter 7). All the numerical simulations presented in these chapters have been produced in the frame of a Direct Numerical Simulation (DNS) approach. Chapter 8 is finally dedicated to fully three-dimensional (3D) simulations, which are conducted using a turbulence model to overcome the otherwise prohibitive grid densities required by DNS .
As explained above, the present chapter further provides a comprehensive overview of the existing literature highlighting the work of those researchers who studied fluid flow inside systems with FFS and BFS. Furthermore, a through overview of thermo-gravitational convection, its types and different modes of instability is also provided.

1.1 Literature Review:

As explained in the introduction, piping systems often possess varied geometrical features such as a sudden expansion or contraction of the area or small ribs and turbulators might be present (perpendicular to the direction of flow). These complex geometrical features prevent the fluid from travelling along a straight path and play a significant role in making it unsteady or turbulent through the formation of recirculation regions and various vortices (Molochnikov et al., 2019). The same behaviour can also be noticed across different fluid machinery where the presence of these ribs causes flow separation and reattachment which promotes frictional shear stress resulting in considerable amount of energy losses (Hattori and Nagano, 2010). The fluid separation which occurs as a result of such complex geometrical features has also enjoyed a significant degree of attention from engineers and researchers. For instance, Zhang et al. (2017) studied the impact of putting pantograph (component of a high-speed train) at different locations on the performance of trains and Largeau and Moriniere (2007) examined different undesired environmental effects produced by separated flow around aerodynamic bodies such as sound generation and structure vibrations.
A configuration that has attracted much attention is the *forward-facing step* (FFS). The simplified geometry makes it an attractive choice for the analysis of different kind of flow patterns which emerge when the flow comes in contact with blunt obstacle. Investigations along these lines are, for instance, those by Hillier and Cherry (1981), Han et al. (1994), Stüer et al.,

(1999), Abdalla et al. (2009), Sherry et al., (2010), Zh and Fu (2017) and Graziani et al., (2017). Additionally, the mirror image configuration, i.e., the BFS has also been investigated by different researchers. Existing studies suggest that the flow over a forward-facing step produces more involved dynamics owing to the presence of obstacle in the downstream direction (Kiya and Sasaki, 1983; Cherry et al., 1984). These two simple geometries can also be differentiated on the basis of disconnected vortex regions which are formed before or after the step. In the case of BFS, only one separated flow region is observed just after the step in the expanded portion of the channel. However, for the forward-facing step, the flow has the tendency to become more chaotic owing to the presence of two disconnected regions located in upstream and downstream portions of the channel. The separating region downstream is usually formed due to fluid coming in contact with perpendicularly mounted obstacle. This region is characterized by its ability to generate an increased amount of vorticity leading to instability through the formation of a bubble (Wilhelm et al., 2003). As a result, the recirculating region formed in the downstream direction is responsible for rendering the flow unsteady and produce complex situations (Abu-Mulaweh et al., 1993; Smith and Walton, 1998; Abu-Mulaweh, 2003; Moosavi and Nasaab, 2008).

Some studies performed by the researchers also suggest that the transition of flow from a steady state to oscillatory and turbulent regimes can play an important role especially in scenarios where significant number of chemical species or heat transport is present (Seban, 1966; Nassab et al., 2009; Oztop et al., 2012; Kherbeet et al. 2016 ; Xie and Xi, 2017).

Additional details for the FFS and the BFS are reported in Sects. 1.1.1 and 1.1.2 respectively. The literature described therein essentially concerns cases where only forced flow was considered and even if temperature differences were present, they were unable to create significant buoyancy convection or the contribution brought in by this form of convection was neglected (numerical studies).

1.1.1 Forward Facing Step:

Forward-facing step has long attracted the interest of researchers serving as a workhorse to support the investigation of patterning behaviour which emerges due to interaction of fluid with an obstacle (see, e.g., Antonia and Luxton, 1971; Counihan et al., 1974; Moss et al., 1980). Kumar and Naidu (1993) proposed a stream function-vorticity formulation for the solution of two dimensional Navier-Stokes equations for laminar flow in a cavity with forward-facing step. The same method was then employed by Han et al. (1994) using a second order finite difference scheme to examine the behaviour of the flow past a forward-facing step. The results indicated the formation of a recirculation zone near the corner of the step causing flow separation.

Stüer et al. (1999) examined the separation after the encounter of fluid with FFS under a laminar flow regime with the help of hydrogen bubble technique to achieve visualisation. Furthermore, PTV method was utilised to assess the 3-D flow field in Eulerian form closer to the step. The analysis illustrated that the laminar separation assumes the shape of a 3-D bubble which shows a quasi-periodic behaviour. The fluid is entrained inside the bubble and then it is released in the

form of longitudinal vortices. Most of the vorticity was observed to be largely aligned with the span-wise direction.

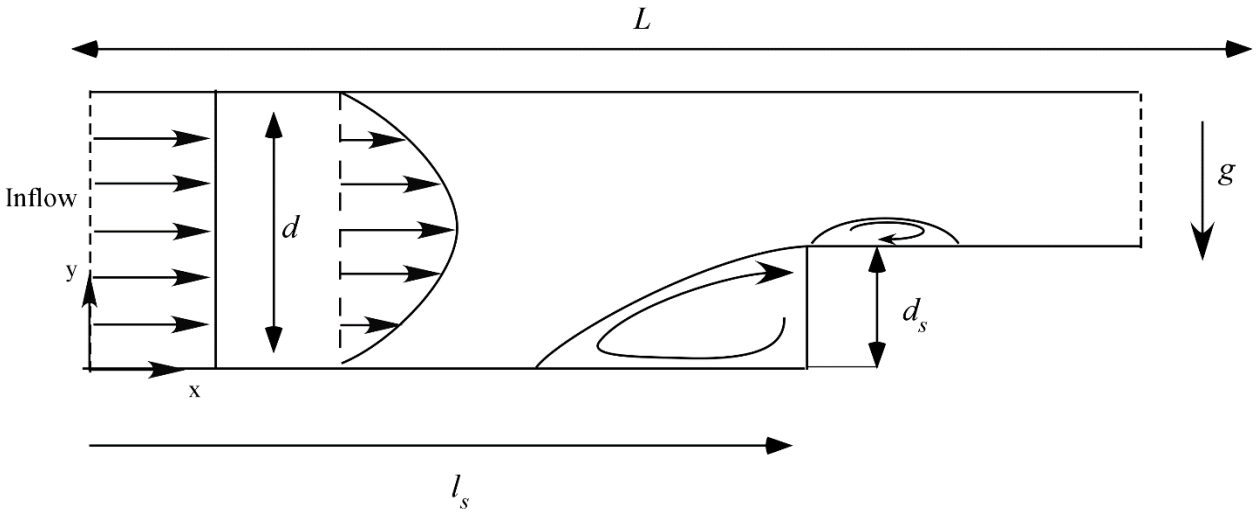

Figure 1.1: Sketch of the Forward Facing Step (FFS) configuration.

Some other related problems, for instance the behaviour of a turbulent flow over a double and triple FFS have also been investigated by some researchers. For the research related to double FFS, the reader may consider Oztop (2006) who analysed numerically the turbulent forced convection over double FFS. He studied the impact of different parameters such as step heights and lengths as well as Reynolds number on heat transfer and fluid flow and illustrated that the second step play a crucial role in controlling both. In another research by Oztop et al., (2012), it was observed that varying the obstacle/step height leads to the formation of an increased number of eddies in the downstream direction which consequently enhances the flow circulation and heat transfer. Furthermore, it also increases the value of the *Nusselt number* which means a substantial amount of *heat* exchange takes place between the incoming fluid and solid walls of the cavity. Taher and Adam et al. (2010) considered a triple FFS geometry and found flow separation to be more significant for high values of Reynolds number and step height. In addition, turbulent kinetic energy and dissipation rate was also found to increase for higher values of step height ratios and Reynolds number. Vorticity was also found to be affected by the presence of consecutive steps and increase in Reynolds number.

Another important research which focussed on the investigation of the recirculation zone appearing in the downstream direction of a FFS submerged in a turbulent boundary layer was conducted by Sherry et al. (2010). The author analysed the dimensions of recirculation region and reattachment length for different values of Reynolds number (dependant on step height and fluid velocity) in the range $1400<Re_h<19000$. The results indicated that an increase in the length of reattachment region occurs with an increase in Reynolds number for a given channel vertical

extension ratio. Interestingly, two regimes were identified in this analysis depending on the value of Reynolds number. The reattachment length was highly influenced by Reynolds number in the first regime which occurred for approximately Re<8500. On the contrary, the reattachment length was slightly affected in the second regime which appeared for Re>8500. A possible explanation for the existence of these two regimes was assumed to be a shift in behaviour of the recirculation regions formed in upstream and downstream direction of the step as well as transition in shear layer straight after separation.

1.1.2 Backward Facing Step:

This configuration has attracted the attention of researchers due to the complex hydrodynamic effects that it generates. These are enabled as the so-called expansion ratio (ratio of the hydraulic diameter of the duct *d* and the thickness of the step) and the Reynolds number are varied in the space of parameters. The study conducted by Armaly et al., (1983) could be considered as a milestone as it set up the basis for many later studies. The author performed a thorough analysis of these aspects considering isothermal air and different values of Reynolds number in the range $70 < Re < 8000$, where Reynolds number was based on the total transversal extension or hydraulic diameter of the duct).

The research performed in recent years has led to several two-dimensional (2D) and three-dimensional (3D) numerical simulations. The results gathered have played a major role in placing the problem in a precise theoretical context by highlighting (both qualitatively and quantitatively) the relationship between the aforementioned controlling parameters and the emergence of *spatially localized features*. These commonly appear as stretched recirculations at fixed position, simply known as "bubbles"; most researchers have conveniently specified these through the definition of 'characteristic' points in the flow (generally indicated as x_i where the subscript "i" takes a different value depending on the considered topological flow feature and its position in the domain). These points represent the boundary among 'regions' which exhibits a distinct fluid-dynamic behaviour: a separated shear layer (originating from the corner of the step), a portion of recirculating fluid under the shear layer, a sub-domain where flow reattachment occurs, and an attached/recovery area (the interested reader being referred to Chen et al., 2018 and all references therein for additional details). As shown in Fig. 1.2, the point where the flow reattachment occurs is generally specified by x_1 (reattachment length). Additionally, a secondary bubble (situated on the top wall between x_2 and x_3) and a tertiary recirculation (located on the bottom wall between x_4 and x_5) are formed owing to an increase in Reynolds number for a fixed expansion ratio ER (see, e.g., Erturk, 2008).

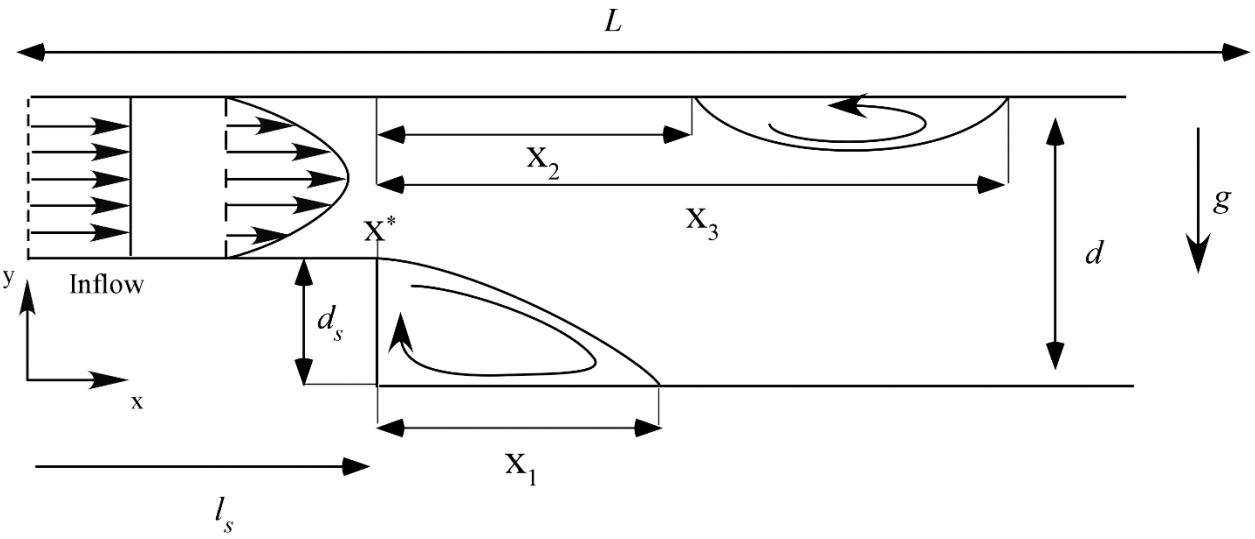

Figure 1.2: Sketch of the Backward Facing Step (BFS) configuration.

Analysis of the literature reveals general agreement about the finding that the reattachment length can be decreased with an increase in ER (expansion ratio i.e., the ratio of the duct diameter and step thickness) for small or moderate values of Re, whereas having a higher value of Reynolds number in principle would result in displacement of x_1 in the downstream direction. Such aspects have been the focus of research because of the undesirable presence of flow separation in several engineering application as it produces a pressure drop (and generates energy loses which must be overcome through extra pumping power).

The other area of interest i.e., the emergence of unsteadiness has been examined thoroughly essentially in the frame of linear stability analyses (LSA) or numerical solution of the original unsteady non-linear governing equations. For the research with LSA-based efforts, the reader is directed towards Fortin et al. (1997), who analysed the stability of the 2D steady incompressible flow over the BFS with ER=2 until a Reynolds number of 1600. No Hopf bifurcations (i.e., pair of eigenvalues crossing the imaginary axes) was found in such a range. Along the same line (for ER=2), Barkley et al. (2002) found that the flow remains linearly stable to two-dimensional perturbations up to Re=1500. More recently, the study of Xie and Xi (2017) based on the solution of the governing equations in their complete (yet 2D, but unsteady and non-linear) form has revealed the formation of localized oscillation downstream of the reattachment point for ER=2 and Re=1400 which can be further seen in the shear layer for a higher value of Reynolds number i.e., Re=2000.

The references mentioned above are just a few examples of the relevant work on this subject which is now enormous. It was not possible to mention all the related work in this section. For a more exhaustive review, the reader may refer to the studies of Biswas et al. (2004), Kherbeet et al. (2016) and Chen et al. (2018), which provide a synthetic account of all such attempts.

As mentioned before, Armaly et al. (1983) was the first to perform a comprehensive experimental analysis (complemented by a numerical study) for ER≅2, which was instrumental

in revealing that, for Reynolds numbers not exceeding 400, the flow retains a strong two-dimensional behaviour on the plane of symmetry. Interestingly, for a value of Reynolds number greater than 400, an inconsistency was observed in the primary recirculation length between the results obtained experimentally and the numerical predictions. These findings were later validated by Kim and Moin (1985) who found that the value of Re required to cause a departure of 2D numerical simulations from experiments was approximately 600. It can be seen from the above-mentioned reviews, however, even beyond this limit there is still some value associated with numerical studies conducted under the constraint of two-dimensionality as they serve as useful benchmarks and test-beds for the later assessment of fully three-dimensional effects. Furthermore, they can provide meaningful information about the typical sequence of bifurcations which characterize systems of such a kind. Although, beyond a given value of the Reynolds number, 2D investigations must obviously be regarded as an oversimplification of reality, 2D and 3D scenarios still share notable similarities as witnessed by relevant arguments provided by several researchers (see, e.g., Biswas et al., 2004; Erturk, 2008).

Other studies have focused on oscillatory flow and the effects produced by them such as the fluctuations which ultimately results in the enhancement of the Nusselt number. Although, the majority of them have considered the one-way coupled configuration, that is, the situation in which the velocity field is not influenced directly by the temperature (valid in the limit as the Richardson number, defined as the ratio of the Rayleigh and the square of the Reynolds number is very small or tends to zero; for the case of air and ER=2, the interested reader may consider Iwai et al., 2000 for Re=125; Kanna, and Das, 2006 for Re=800; Rouizi et al., 2010 for Re up to 800; Xu et al., 2017 for Re up to 1200 and Xie and Xi, 2017 for Re up to 2000).

In such a context, it is also worth recalling that Vogel and Eaton (1985) had shown experimentally that if the flow becomes turbulent, the classical Reynolds analogy (stating that the heat transfer at the wall is proportional to wall shear) does not hold for the mean flow but more for the fluctuating values, especially in the recirculation zone (i.e., $x<x_1$). A description of related numerical studies can be found in Keating et al. (2004) and in the masterful review by Avancha and Pletcher (2002). Such research efforts can be considered crucial as they increased awareness in the scientific community regarding the use of specific turbulence models in comparison to others which are not considered suitable to deal adequately with turbulent separating and reattaching flows in the presence of heat transfer.

1.1.3 Hybrid convection in ducts with a step

As a critical analysis of the literature described above would immediately indicate, despite many valuable efforts, *a significant lack of information still seems to exist for what concerns the interplay of thermal buoyancy effects and forced convection in these systems*. Most of existing investigations have addressed situations in which fluid motion was isothermal or, although heat transfer was considered (between the fluid and walls delimiting the channel), perturbations of buoyant nature were not taken into account. The only exceptions seem to be Abu-Mulaweh et al. (1993) and Abu-Mulaweh (2003) for the FFS and Barbosa-Saldaña et al. (2005) and Khanafer et

al. (2008) for the BFS, where some emphasis was put on buoyancy effects and the related ability to generate thermal plumes and affect accordingly the overall flow. These are briefly reviewed here.

Abu-Mulaweh et al., (1993) specifically investigated experimentally the configuration of horizontal FFS which was further complemented by another meaningful research by Abu-Mulaweh (2003). These investigations were performed for different ranges of the relevant control parameters i.e., the so-called Reynolds number and Grashof number. The authors varied the Reynolds number and Grashof numbers (based on the step height) in the intervals, $O(10^2) \leq Re \leq O(10^3)$ and $O(10^3) \leq Gr \leq O(10^4)$. It was found that an increase in thickness of the step causes the spatial extension of the recirculation region to grow whereas it leads to a decrease in the rate of heat transfer from the heated downstream wall. Interestingly, both quantities were found to increase with an increase in inlet velocity. Further observations revealed that in certain situation, no upper circulation area is detected, however in other scenarios disturbances responsible for shift from laminar state to turbulent flow emerges in this particular region.

To the best of our understanding, the studies mentioned before are the only ones which have examined the interplay of buoyancy and forced convection inside a FFS configuration. Some additional partially related information can possibly be collected from the already existing numerical studies highlighting common instabilities of gravity-driven and hybrid thermocapillary-thermogravitational convection in crucibles having various shapes primarily used for the production of semiconductor or opto-electronic materials (see , for instance, Lappa, 2017; Lappa, 2019; Khatra et al., 2019) or other researches which focused on building heating and ventilation or electronic devices cooling (Yarin, 2009; Sun and Jaluria, 2011; Venkatasubbaiah and Jaluria, 2012; Morsli et al., 2018; Kachi et al., 2019).

Following the observations by Guo et al. (1996) on the ability of thermal effects to cause non-trivial modifications in the patterning behaviour of the velocity field, some numerical investigations have also become available where the general problem represented by mixed forced-buoyancy convection in the BFS configuration was treated for *finite values of the Richardson number*. Exemplars pertaining to this line of inquiry are the works by Barbosa-Saldana et al. (2005) and Khanafer et al. (2008), who investigated the BFS with ER=2 through numerical solution of the 3D and 2D governing equations, respectively. Although obtained in restricted sub-regions of the space of parameters (Reynolds number Re fixed to 200 and $Ri \leq O(1)$ in the 3D study by Saldana et al., 2005, and $O(10^{-1}) \leq Ri \leq O(10)$ with Rayleigh number *Ra* fixed to 5680 in the 2D analysis by Khanafer et al., 2008), these numerical results definitely confirmed that the features of the mixed convective flow are significantly different from that of forced convective flow.

As yet indicated by available studies, another drawback concerns the dimensionality of such systems, which in most cases was limited to two dimensions only to avoid the otherwise prohibitive computational times required for the numerical investigation of three-dimensional (3D) flows (especially when relatively high values of the related non-dimensional governing parameters, i.e., the Reynolds and Rayleigh numbers, are considered).

Efforts based on 3D DNS (direct numerical simulation) are relatively rare and sparse. Relevant examples for the case of isothermal flow are Wilhelm et al., (2003) and Le et al. (1997) for the FFS and the BFS, respectively; similarly, for 3D DNS with heat transfer but no buoyancy the reader may consider Barbosa-Saldaña and Anand (2007) and Xu et al (2017), respectively. In these analyses, not to increase excessively the density of the required mesh (known to grow with the values of the characteristic non-dimensional parameters), circumstances for which the flow is laminar were examined.

Attempts based on turbulence models, where the characteristic parameters can take much higher values are just the beginning. Initial efforts along these lines have essentially shown that conventional turbulence modelling methods, such as the Reynolds Averaged Navier–Stokes (RANS) approach are generally inadequate in predicting the effects of turbulent separating and reattaching flows with heat transfer, whereas large eddy simulation (LES) seems to capture properly such dynamics. However, only a limited number of LES works have appeared where the BFS with heat transfer was considered (see, e.g., Avancha and Pletcher, 2002; Labbe et al., 2002; Keating et al., 2004) and even fewer articles have been devoted to the equivalent FFS (Rao and Lynch, 2021).

To the best of our knowledge, no work exists where 3D LES simulations of mixed flow on the FFS or BFS have been performed (the computations by Schumm et al., 2016 for the BFS were limited to a 2D configuration). Therefore, in the present thesis, an attempt has also been made to bridge this gap through the implementation and application of a relevant LES strategy to the general 3D case in which the flow is non-isothermal and with a significant level of buoyancy which would be discussed in Chapter 8.

Given the lack of results about buoyancy convection in systems with a step, the remainder of this chapter is used to recall the main properties of purely gravitational (buoyancy) flow for some simple (canonical) geometries and fundamental situations. Part of this information will prove useful later for the interpretation of some of the results obtained in the following chapters.

1.1.4 Thermo-gravitational convection:

Thermal or buoyancy convection is an important process occurring in a variety of natural and industrial processes. Thermal convection can be further divided into two types depending upon the relative direction of the gravitational field and the prevailing temperature gradient. If the system is being heated from below, then the direction of temperature gradient is parallel to the gravitational force, giving rise to Rayleigh-Bénard convection. However, if the gradient of temperature is perpendicular to gravity, then a different type of convection takes place, known as Hadley convection. Although both these convection processes are similar in nature, they display different behaviours when the Rayleigh number is increased, which provides an explanation for the above-mentioned distinction.

The study of Rayleigh-Bénard convection was founded by two scientists, Lord Rayleigh (1916) who conducted theoretical studies and Henri Bénard (1900, 1901), who focussed on experimental observations, thus giving their names to this phenomenon. Rayleigh-Bénard

convection has been the focal point of many studies in the past century due to its conceptual and practical applications. The variety of complex patterns, bifurcations and chaotic behaviour (Gollub and Benson, 1980) this type of convection showcases provides a possible justification for the attention it has received. Busse and co-workers (Busse, 1978; Clever and Busse, 1974; Busse and Clever, 1979) defined the so-called Busse Balloon, i.e., the region of stability delimited by all the expected secondary instabilities occurring in Rayleigh-Bénard convection.
The other type of thermal convection which is Hadley convection was named after George Hadley (1735) who put forward it as an atmospheric circulation mechanism. This type of convection is relevant to several industrial manufacturing processes and is relevant to the cooling of nuclear reactors (Hurle, 1972; Carruthers, 1977; Thevenard et al. 1991). Hadley flow can also undergo different types of perturbing mechanisms (e.g., Lappa, 2007).

1.1.4.1 Rayleigh-Bénard Convection

Rayleigh-Benard convection is a classical problem in the field of fluid dynamics. This phenomenon contributed to the foundation of the stability theory in hydrodynamics (Drazin and Reid, 1981) and enjoyed a significant level of interest from the researchers due to its practical implications and complex spatio-temporal patterns (Getling, 1998). From the research perspective, the geometry which is widely used to study the effects of this type of convection is the infinite two-dimensional layer. This idealised geometry is considered suitable to study all the complex patterns and bifurcations that are induced in the system from a theoretical angle. From a real-world perspective, an infinite layer can be experimentally mimicked by keeping the horizontal extension of the fluid layer large enough in comparison with the vertical depth. The configuration is shown in Figure 1.3.

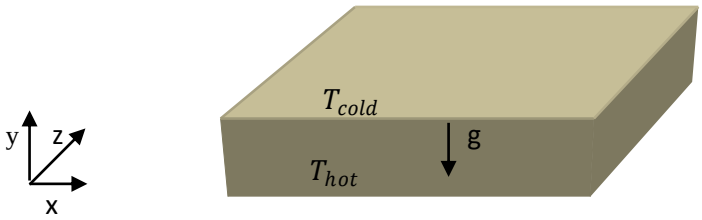

Figure 1.3: Rayleigh-Bénard geometry with infinite horizontal layer

The system undergoing this convection usually shows a steady behaviour for relatively small values of Rayleigh numbers. However, at higher values of *Ra*, instability occurs and bifurcations take place that make the flow behaviour much more complex. The aim of the following section is to provide some additional fundamental information about these behaviours.

Initial instability-Pitchfork bifurcation

A quiescent or steady state is an inevitable solution for very small values of Rayleigh numbers. However, the situation completely changes if an increase is introduced in this parameter, initiating an instability mechanism which leads to the formation of steady and parallel convective rolls. Rayleigh (1916) proposed an analytical solution with regards to critical Rayleigh number considering stress-free boundaries. The solution was based on a quantity known as wavenumber:

$$Ra_{cr} = \frac{\left(q^2 + (n\pi)^2\right)^3}{q^2} \tag{1.1}$$

In terms of no-slip boundary condition, a value of Ra_{cr}= 1707 was first put forward by Jeffreys (1926, 1928). The results acquired for both stress-free and no-slip walls are visually represented in Figure 1.4.

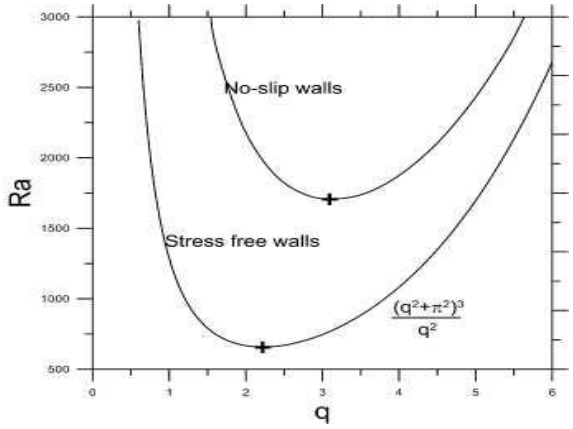

Figure 1.4: Marginal stability curves formed for Rayleigh-Bénard convection in the configuration with infinite horizontal layer for stress free and zero velocity (no slip) on solid walls.

The solution demonstrates that the linearised problem considered above yields eigenvalues which are real (Pellew and Southwell, 1940) which also indicates the fact that the initial mode of instability is always stationary, i.e., leading to a steady state.

Secondary modes of instability: the Busse balloon

As already discussed before, in the case of RB convection, convective disturbances usually emerge in the form of parallel convective rolls formed in the horizontal direction. These rolls are formed for relatively lower value of Rayleigh number; however, a further increase in *Ra* renders the flow more unstable giving rise to a plethora of complex patterns. Such secondary instabilities were first addressed by Busse and his co-workers (Schluter et al., 1965; Clever and Busse, 1974; Busse, 1978; Busse and Clever, 1979). Their research initially focussed on two dimensional ideal straight rolls which were described by means of a Galerkin expansion. Furthermore, they used a method known as Toroidal-Poloidal Decomposition to represent the solution in slightly supercritical conditions (see Lappa, 2009). They identified three parameters which have the tendency to affect the initial stable state of RB convection namely wavenumber q, Prandtl number (Pr) and Rayleigh number (*Ra*).

Thus, a region of stability was defined by them which was given the name Busse balloon (Busse, 1978) as shown in Figure. 1.5. The flow is initially stable inside the boundaries of the so-called Busse balloon, however as soon as the boundary is crossed; a variety of secondary modes of instability disturbs the initially parallel rolls. An overview of different kinds of possible secondary modes is provided in Fig. 1.5 which clearly shows that the evolution from an initial stable state to a secondary one depends on the Rayleigh, Prandtl and wavenumber. It is important to highlight that certain secondary modes are universal, regardless of the role played by RB convection in generating a pattern. Such modes in practice depend on the symmetries of formed rolls, for instance, the eckhaus instability and zig-zag instability which remains invariant through translation and rotation respectively or cross-roll instability which emerge owing to the reduced strength of convection in the vicinity of marginal curve. However, RB convection has a marked influence on the generation of other kind of secondary modes such as bimodal instability. There are variety of secondary modes which occur; however, a comprehensive explanation is not possible as it is beyond the scope of present work (see Lappa, 2009 for a more clear and detailed description).

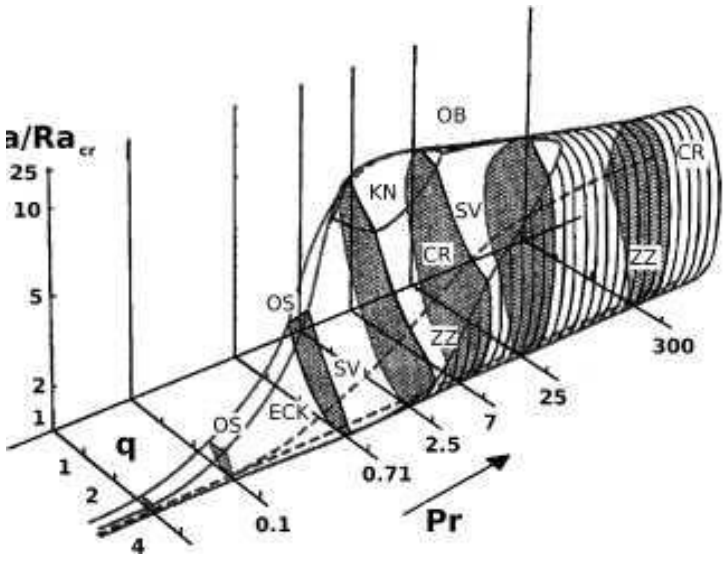

Figure 1.5: Three-dimensional diagram of Busse Balloon from Busse (1978) representing Prandtl number, Rayleigh number and wavenumber along x, y and z directions respectively. The two-dimensional secondary modes remain stable inside the boundaries represented by solid curves. The abbreviations mentioned outside the Busse Balloon highlight the following secondary instabilities: ECK for Eckhaus instability, SV for skewed varicose instability, CR for cross roll instability, OS for oscillatory instability with travelling waves, ZZ for zig-zag instability, KN for knot instability and OB for oscillatory blob instability.

Impact of sideward walls

The effects of lateral or side walls on the behaviour of the flow can be significant. The condition of infinite layer adopted for the configuration used in RB convection can be satisfied in the laboratory only if the depth of cavity is much smaller that its length. It is observed that the walls have a remarkable impact on the pattern originating in the system if this condition is not satisfied (Pellew and Southwell, 1940 and Zierep, 1963) . Davis (1967) further studied the effect of lateral walls on the convective mechanism occurring in a rectangular box by utilising the technique of linear stability calculation. Another important study pointing out the effect of lateral wall was conducted by Cross et al. (1980) which showed that the presence of finite sidewalls disrupts the amount of wave vectors entering the system.

1.1.4.2 The Hadley Flow

Hadley flow has also been investigated significantly in the past just as Rayleigh-Bénard convection. The difference between these mechanisms simply lies in the respective directions of gravity and temperature gradient. However, rotating the direction of temperature by 90 (Hadley flow) is enough to introduce substantial changes in the behaviour of the flow. Even though these processes share a common physical origin, however difference in terms of dynamics of the flow

makes it essential to consider Hadley flow as a separate branch of thermo-gravitational convection.

Following the same approach used for the RB problem, here an infinite layer is considered (having adiabatic horizontal boundaries). The ability of this model to provide an exact solution makes it a desirable choice. However, it is worth mentioning that the quiescent state no longer provides a solution of the dimensionless equations (mass, momentum and energy). No Critical Rayleigh number must be exceeded to produce flow as it always occurs regardless of the magnitude of *Ra*. Unlike Rayleigh-Bénard convection that is typically produced as a set of parallel rolls in an infinite layer, the Hadley flow gives rise to a single roll stretched in the horizontal direction. The geometry of the system is shown in Fig. 1.6.

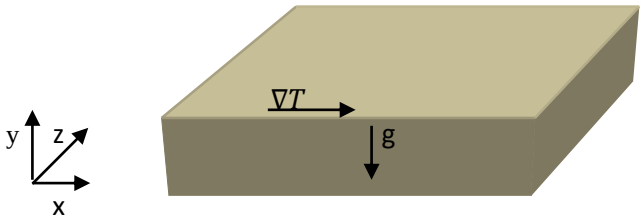

Figure 1.6: Hadley Flow geometry with infinite layer

The Hadley flow (in the form of to a single roll stretched in the horizontal direction) can be subjected to a variety of perturbing mechanisms which highly depend on the value of Prandtl number. The general mode of perturbations which exist at low Pr (<1) corresponds to transverse rolls (2D hydrodynamic mode) and longitudinal rolls (steady or oscillatory). For a situation where the Prandtl number of the fluids is high i.e.,Pr>1, another form of instability occurs known as Rayleigh mode. A rich spectrum of patterns is produced due to different kinds of instabilities dependant on the value of the Prandtl number. Hence, these instabilities are discussed here in two different section according to the value of the Prandtl number

Instability modes in Low Prandtl fluids (Pr<1)

The transverse and longitudinal disturbances which emerge in the low Prandtl fluids were described by Hart (1972, 1983). He investigated the influence of such disturbances on the behaviour and nature of flow. Furthermore, Gill (1974) concentrated on the sensitivity of the Hadley flow to longitudinal disturbances. Both these disturbances are represented in Fig. 1.7. The roll axis in 2D hydrodynamic mode (transverse mode) is at an angle of 90 (perpendicular) to the temperature gradient. However, in the case of longitudinal rolls, both the rolls axis and temperature gradient are parallel.

Both Hart (1972, 1983) and Gill (1974) verified that the perturbations occurring in the transverse mode are a direct consequence of a shear instability i.e., they are hydrodynamic in nature. On the contrary, the instability induced by longitudinal rolls occurs due to marked increase in the thermal effects as a result of dynamic coupling among gravitational and inertial forces.

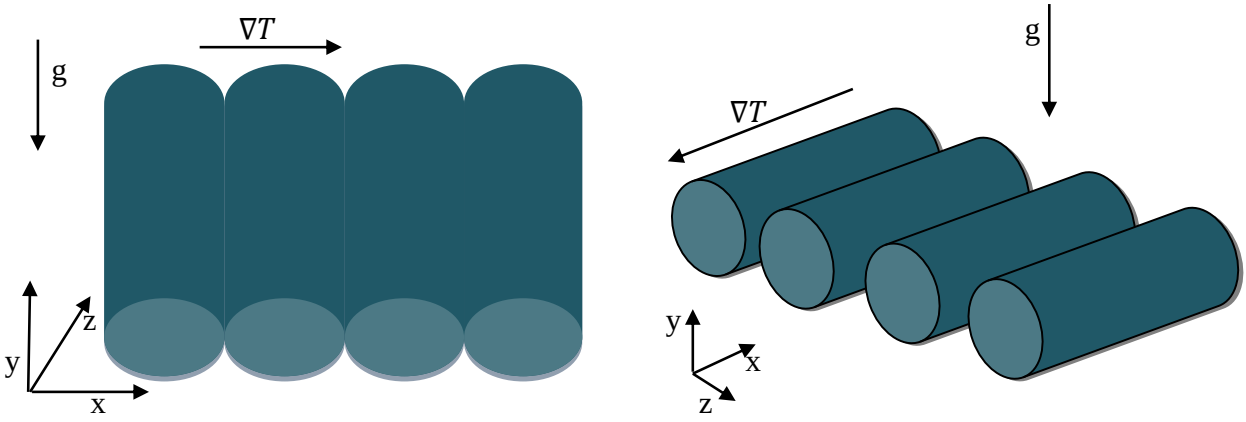

(a) 2D hydrodynamic (or transverse) mode (b) Longitudinal rolls

Figure 1.7: Fundamental shapes of modes in Hadley Flow

The longitudinal rolls are also known as helical wave mode or oscillatory longitudinal rolls (OLR) due to the formation of a helical trajectory when they merge with the basic Hadley flow.

Kuo and Korpela (1988) identified that mean shear stress or hydrodynamic instability contributes to the formation of transverse rolls for $Pr \leq 0.03$. Moreover, Prandtl number in the range $0.033 < Pr < 0.2$ gives rise to oscillating longitudinal rolls (OLR) whereas stationary longitudinal rolls (SLR) are formed at $Pr \geq 0.2$. The plots reported in Figure 1.8a and 1.8b represents the critical Grashof number and wave number for these different disturbances.

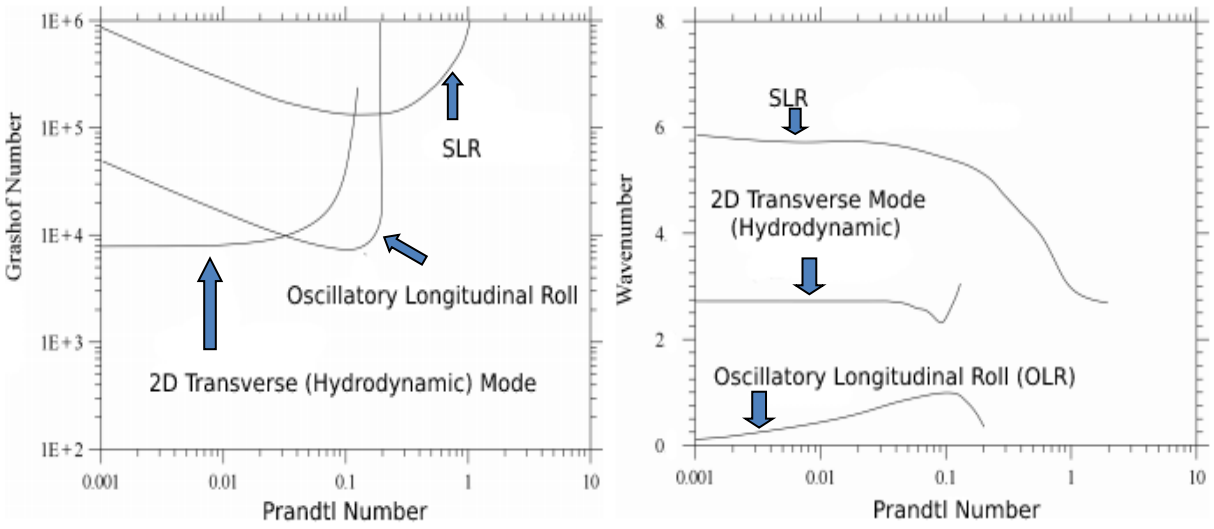

(a) (b)

Figure 1.8: Plots of results produced by Kuo and Korpela (1988) after performing linear stability analysis for the Hadley flow: a) Critical Grashof number as a function of Pr b) Critical wavenumber as a function of Pr. The formula for Grashof number is $Gr = g\beta_T \gamma d^4/\nu^2$, where γ represents the imposed temperature gradient along horizontal direction and d specifies the depth.

Instability modes in High Prandtl liquids (Pr>1)

The previous subsection highlighted various instability modes that exist in the case of $Pr<O(1)$. They are the 2D transverse mode and 3D longitudinal rolls (stationary or oscillatory). These perturbations exist in a certain range of the Prandtl number. However, as mentioned before, these disturbances are possible only for low values of Prandtl number.

For this purpose, Gershuni et al. (1992) performed linear stability analysis and introduced a third mode of instability known as the 'Rayleigh mode' for $Pr>O(1)$. This mode is due to the presence of unstable density variations (stratification) in the vicinity of upper and lower horizontal walls when these behave as conducting boundaries. Such stratified regions were found to favour the growth and occurrence of the Rayleigh-Bénard instability giving rise to longitudinal rolls of steady nature (whose axis are parallel with the temperature gradient). However, a further increase in Rayleigh number results in the formation of transverse rolls of 2D oscillatory nature(whose axis is at 90 with the temperature gradient). All the possible modes of instabilities which emerge for different values of Prandtl number are summarised in Fig. 1.9.

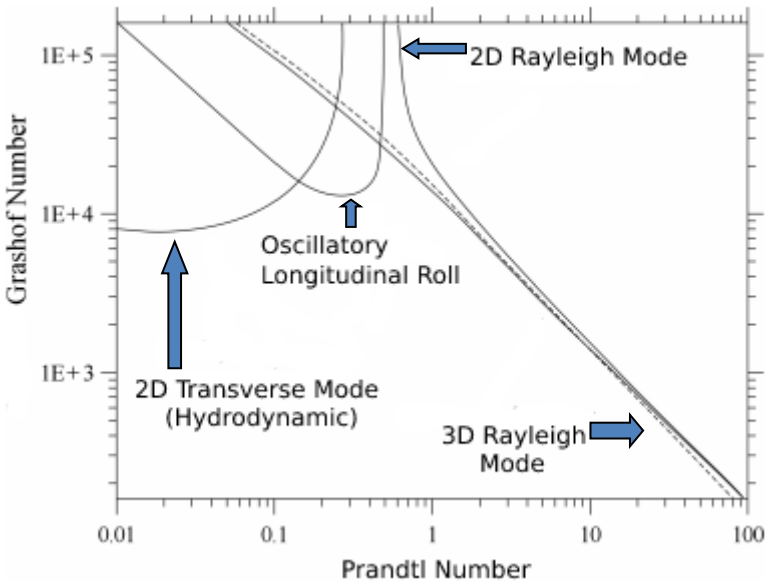

Figure 1.9: Minimal Grashof number as a function of Prandtl number by Gershuni et al. (1992). The 3D Rayleigh mode represented by solid line highlights the instability mode with even pattern whereas the dashed line represents the 2D Rayleigh mode which illustrates the instability modes with odd pattern. The formula for Grashof number is $Gr = g\beta_T \gamma d^4/\nu^2$, where γ represents the imposed temperature gradient along horizontal direction and d specifies the depth.

It is clearly evident from Fig. 1.9 that for value of Pr> 0.44, Rayleigh mode is the major source of instability even for larger values of Pr. This perturbation mechanism is not possible without the presence of unstable stratification zones, for instance, the case considered by Kuo and Korpela (1988) having horizontal insulated boundaries. It is worth mentioning that Rayleigh mode is a steady mode as the flow becomes stable when the Prandtl number approaches to unity or higher value. The 3D Rayleigh mode has the ability to exist in both odd and even arrangement as illustrated in Fig.1.10.

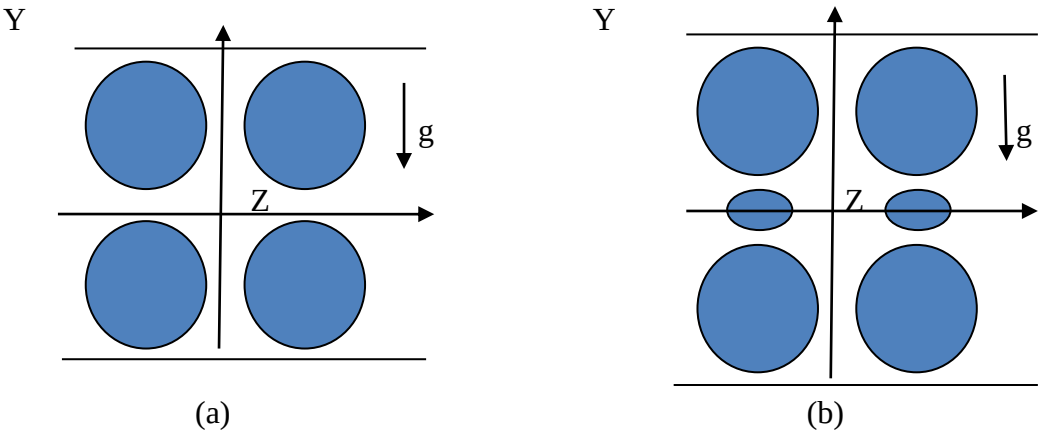

Figure 1.10: 3D Rayleigh mode showing even and odd pattern (Note that the direction of temperature gradient is along x-axis)

Instability modes for Pr≅1 in the presence of vertical sidewalls

This subsection is finally used to describe a specific instability mode that is very relevant to the problem considered in the present thesis, i.e., the travelling waves that can be produced in differentially heated cavities supporting the Hadley flow in the presence of solid lateral boundaries (i.e., wall parallel to the direction of gravity; the information reported in the previous subsection was about the Hadley flow in infinite layers).

It is an established fact that for Hadley flow prevalent in compact cavities with Pr≅1, an increase in *Ra* results in a shift in behaviour from steady state to *permanent* 2D oscillatory states. Over the years, numerous researchers have performed numerical analysis on this subject. For instance, Le Quéré and Penot (1987) and Henkes and Hoogendoorn (1990) conducted numerical studies on cavities having horizontal walls that were kept adiabatic and filled with air. Bucchignani (2009) considered a square cavity, Yahata (1999) performed numerical simulation for the case of cavities with different aspect ratio A ranging from 1/10 to 1 whereas Auteri and Parolini (2002) considered an aspect ratio A=1/8. In some situations, the flow even demonstrated a turbulent behaviour (for instance, Paolucci and Chenoweth, 1989; Paolucci, 1990; Janssen and Henkes, 1995; Xin and Le Quéré, 1995; Farhangnia et al., 1996; Yahata, 1997; Le Quéréand Behnia, 1998; Mayne et al., 2000). It was clarified that such flow instabilities have no relationship with the archetypal instability mechanisms described in the previous section for infinite layers. Rather, different interpretations were provided for this type of instability (described in the remainder of this section).

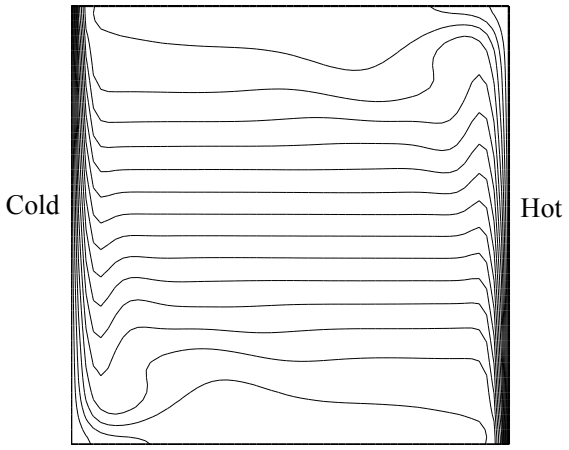

a)

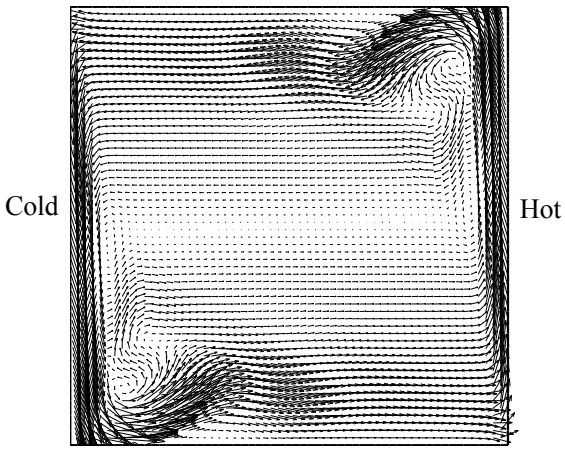

b)

Figs. 1.11: Regions with stable thermal stratification, horizontal intrusion thermal layers and vertical thermal boundary layers in a cavity with A=1 (Pr=0.71 and Ra=1x10^7; adiabatic horizontal walls): (a) Temperature distribution; (b) Velocity field (numerical simulation, M. Lappa, 2009).

An increase in Rayleigh leads to a shift in the behaviour of the flow i.e. a transition occurs from a diffusive regime to a boundary layer regime. Consequently, the temperature drop and vorticity production are observed to be concentrated in thin boundary layers alongside the sidewalls, while a stagnant region is formed in the central portion of the cavity, as show in Fig. 1.11. In such situation, the flow at the centre takes place only by means of entrainment of mass from the vertical boundary layers. This process generally results in a stable core region with a cross-stream thermal stratification.

Delgado-Buscalioni (2001a) demonstrated that while the core flow is stable, flow instabilities can develop *inside the boundary layers adjacent to the lateral walls*. Based on these arguments, there is consensus in the literature that the oscillatory instabilities (observed by many researchers in the past) in cavities of finite extent for Pr≥O(1) (such as air, water and silicone oils) should be attributed to the existence of such boundary layers.

Some important information along these lines related to the boundary layer instabilities of thermal convection is available in the theoretical study performed by Gill and Davey (1969) and Daniels and Patterson (1997 and 2001). A plethora of numerical analysis are also available for the studies involving finite cavities (as mentioned above), whose main outcomes are reported comprehensively in the following:

Ravi et al. (1994) originally performed numerical analysis to study the characteristics of high-Ra convection and considered a simple geometry (square cavity) and Pr=0.71 (air). Initially, the investigations were performed for steady conditions , however further studies for high values of *Ra* indicated the presence of a *recirculating pocket* near the corners, downstream of the vertical walls with a flow separation and reattachment occurring near the horizontal walls in proximity of this recirculation. Furthermore, a substantial thickening of the boundary layer was also observed

in proximity to these pockets, as shown in Fig. 1.11b. Later studies (Paolucci and Chenoweth (1989), Le Quéré and Behnia (1998), Tian and Karayiannis (2000)) could show that fluid instabilities originate in the vicinity of the abovementioned pocket. A slight increase in Rayleigh results in a second (shear-driven) instability making the boundary layer itself unstable. These instabilities appear in the form of waves growing along the vertical boundary layers (Xin and Le Quéré (1995)). These authors conduced numerical simulations on a tall geometry (vertical cavity) with A=1/4 and Pr=0.71 (air) considering three different values of the Rayleigh number (Ra=6.4x10^8, 2x10^9 and 10^{10}). The results demonstrated the influence of travelling waves (propagating downstream in the boundary layers) on the solution rendering it time-dependent.

Chapter 2

Physical and Mathematical Model

2.1 Introduction

A review of the existing literature on forced convection in forward-facing step (FFS) and backward facing step (BFS) geometries has been provided in the previous chapter together with a description of the limited results existing for hybrid flows in these systems. Some fundamental information has also been provided for purely buoyancy convection produced by vertical or horizontal temperature gradients.
The objective of the present chapter is to introduce the various partial differential equations which govern all these convection phenomena. These include the continuity, momentum and energy equations.

2.1.1 Continuity Equation

The continuity equation can be regarded as mathematical formulation of the mass conservation principle. It reads:

$$\frac{\partial \rho}{\partial t} + \underline{\nabla} \cdot \left(\rho \underline{V} \right) = 0 \tag{2.1}$$

As in the present study, situations are considered where the concerned fluid satisfies the incompressibility constraint (corresponding to values of the Mach number M≤0.3, Cengel et al., 2008) hence, the equation can be simplified as:

$$\underline{\nabla} \cdot \underline{V} = 0 \tag{2.2}$$

It clearly illustrates that the divergence of vector (velocity) should be zero in any part of the domain. From another viewpoint it means that velocity field must be solenoidal, i.e., no sources or sinks of mass can exist.

2.1.2 Energy equation

Energy equation is another crucial equation governing the considered dynamics. Mathematically, it can be expressed as follows:

$$\frac{\partial \rho c_v T}{\partial t} + \underline{\nabla} \cdot \left(\rho \underline{V} c_p T \right) = \underline{\nabla} \cdot \left(\lambda \nabla T \right) \tag{2.3}$$

As the investigation performed in the present thesis involves fluids which hold incompressibility constraint and possess non-variable thermophysical properties, this equation can also be simplified (see Sect. 2.4.3 where the corresponding non-dimensional form is provided).

2.1.3 Momentum equation (the Navier-Stokes equations)

Just like continuity and energy equation, the momentum equation is a balance equation. For the general case of a compressible fluid, it can be cast in its final form as follows:

$$\frac{\partial \rho \underline{V}}{\partial t} + \nabla \cdot \left(\rho \underline{V}^T \underline{V} \right) = -\nabla p + \nabla \cdot \underline{\underline{\tau}} + \rho \underline{g} \tag{2.4}$$

As incompressible fluids are considered, it can be simplified as follows:

$$\rho \frac{\partial \underline{V}}{\partial t} + \rho \underline{V} \cdot \left(\nabla \underline{V} \right) = -\nabla p + \nabla \cdot \underline{\underline{\tau}} + \rho \underline{g} \tag{2.5}$$

Equation 2.5 contains a stress tensor which has to be further expanded in order to obtain the final form of the momentum equation. According to Stokes law in the framework of Newtonian fluid model:

$$\tau = \mu \left(\nabla \underline{V} + (\nabla \underline{V})^T \right) \tag{2.6}$$

After inserting the equation for stress tensor 2.6 in 2.4, the final form for compressible fluid becomes:

$$\frac{\partial \rho \underline{V}}{\partial t} + \nabla \cdot \left(\rho \underline{V}^T \underline{V} \right) = -\nabla p + \nabla \cdot \left(\mu (\nabla \underline{V} + (\nabla \underline{V})^T \right) + \rho \underline{g} \tag{2.7}$$

For a fluid with constant density and viscosity realising that $\nabla \cdot \nabla \underline{V}^T = 0$,equation 2.7 becomes:

$$\rho \frac{\partial \underline{V}}{\partial t} + \rho \underline{V} \left(\nabla \underline{V} \right) = -\nabla p + \mu \nabla^2 \underline{V} + \rho \underline{g} \tag{2.8}$$

Thus equations 2.7 and 2.8 are Navier-Stokes equation in compressible and incompressible form respectively which alongside with continuity equations (2.1 or 2.2) and the energy equations (2.3) must be regarded as the set of equations governing the considered dynamics.

2.2 The Boussinesq approximation

The main focus of the present thesis is hybrid convection which involves both thermal convection and forced convection. The former depends on the term ρg present at the right-hand side of the momentum equation, which therefore requires further attention in terms of mathematical modelling.

Buoyancy is the main driving force behind natural convection. In simple words this means that as a rise in temperature results in a decrease in density, heated fluid becomes less dense and rises whereas colder fluid tends to fall due to its relatively higher density. This implies that variations in density are the root cause of thermal or natural convection and that some attention must be paid to this aspect from a mathematical point of view if one is using the assumption of incompressible fluid. This poses a question here: how to consider the buoyancy forces if the equations governing the process of convection satisfy the incompressibility constraint? This is possible and can be done by adopting the so-called Boussinesq approximation which is commonly used in thermal convection (buoyancy driven flows). This implies that density is neglected in all terms unless it appears in the last term (RHS of equation 2.8) where it is multiplied with acceleration due to gravity ($\rho \underline{g}$). According to the Boussinesq model, in the last term of 2.8 the density is assumed to undergo a linear variation with temperature:

$$\rho \cong \rho_0 \left(1 - \beta \left(T - T_0\right)\right) \tag{2.9}$$

Here ρ_0 represents the density which exists at the reference temperature T_0 .The parameter β_T appearing in this expression is the well-known fluid thermal expansion coefficient; it accounts for the variations of fluid density induced by thermal effects in the framework of the linear relationship represented by eq. 2.9. The Boussinesq approximation is known to be valid when the product of $\beta\Delta$T is less than one.

The next step involves considering equation 2.9 as well as the pressure deprived of the hydrostatic component $\left(p = p + \rho_0 g H\right)$ .Inserting 2.9 and pressure into 2.8, the momentum equation yields the following equation:

$$\rho \frac{\partial \underline{V}}{\partial t} + \rho \underline{V} \left(\nabla \underline{V}\right) = -\nabla p' + \mu \nabla^2 \underline{V} - g * \left(\rho_0 (\beta (T - T_0))\right) \tag{2.10}$$

In the remaining section of this chapter, every time the pressure term comes up it would exclude the hydrostatic term; hence for simplicity the superscript is omitted. All the simulations performed in this thesis rely on the Boussinesq approximation.

2.3 Non-dimensional numbers and equations

The present section presents the non-dimensional characteristic numbers associated with the different kinds of convection mechanisms investigated thoroughly in this study, namely, buoyancy convection and forced convection (their combination giving rise to hybrid convection) Afterwards, the mass, momentum, and energy (Navier Stokes) equations are presented in their non-dimensional form.

2.3.1 Buoyancy convection non-dimensional numbers

The first dimensionless number is **Prandtl number**. It only depends on the nature of the fluid under consideration and can be expressed as follows:

$$Pr = \frac{\nu}{\alpha} \tag{2.11}$$

Where ν is the kinematic viscosity also known as momentum diffusivity and α is the thermal diffusivity respectively. Among other things, from a physical point of view, the Prandtl number accounts for the relative thickness between the velocity and thermal boundary layers. A small value of Pr indicates that heat diffuses at a faster rate in comparison with the velocity which leads to the formation of much thicker thermal boundary layer than its counterpart. The values of Pr number exist in various ranges for instance it can be as low as O (10^{-2}) for different substances such as liquid metals and semi-conductor melts or take values in the range between 100 and 40,000 for engine oil. In the case of gases, the Prandtl number is close to 1 which indicates that the rates of dissipation of momentum and heat are similar.
After this, another dimensionless parameter can be introduced known as **Rayleigh number** which can be defined as:

$$Ra = \frac{\beta g \Delta T d^3}{\nu \alpha} \tag{2.12}$$

In the above-mentioned equation, β is the thermal expansion coefficient, ΔT is the temperature difference that exists in the system and d represents the reference length. The Rayleigh number accounts for the strength of buoyancy convection. It can also be written as the product of Grashof number and Prandtl number as follows:

$$Ra = Gr * Pr \tag{2.13}$$

Where $Gr = \frac{\beta g \Delta T d^3}{\nu^2}$. The flow is usually laminar for relatively small values of the Rayleigh number whereas a high Ra can make the flow turbulent.

2.3.2 Forced convection non-dimensional numbers:

The typical non-dimensional number related to forced convection is the **Reynolds number** which in this thesis relates directly to the velocity with which the fluid is injected inside the channel. On the basis of its classical definition, it simply reads:

$$Re = \frac{U_{forced} d}{\nu} \tag{2.14}$$

The Reynolds number can be seen as the ratio between forces of inertial and viscous nature. It also provides an indication regarding the nature of flow and flow patterns for instance a low value of Reynolds number implies that the flow is laminar (high strength of viscous forces). However, a higher value of Reynolds number may imply that the flow is turbulent and chaotic (higher strength of inertial forces).
It is important to highlight that both Reynolds and Rayleigh numbers can be merged together to form another important parameter commonly known as **Richardson number**. The final form is as follows:

$$Ri = \frac{g\beta_T \Delta T d}{U_{forced}^2} = \frac{Ra}{\mathrm{Pr}\,\mathrm{Re}^2} \tag{2.15}$$

This additional parameter has been extensively used in the past to classify the dynamics of hybrid (thermal & forced) convection into different flow regimes, for instance the commonly known 'near and far field' models (Dunn et al., 1975; Lee and Chu. 2003). It can also be used to characterize the instabilities related to thermal plume formation and evolution (Vincent and Yuen, 1999; Hier Majumder et al., 2004). As a result of the intrinsic ability of this parameter to determine the relative significance of thermal (buoyancy) and forced convection it can be regarded as an influential and vital parameter for both convective mechanisms. It is worth mentioning that a higher value of *Ri* indicates that buoyancy is dominant whereas a value less than unity may indicate a situation with dominant forced convection (these two limit cases i.e., pure buoyancy convection and forced convection are restored in the limit when the value of *Ri* reaches infinity and zero, respectively).

2.3.3 Non-dimensional set of equations

The continuity (equation 2.2), energy (equation 2.3) and momentum (equation 2.4) can be converted into their non-dimensional form by referring velocity and pressure to proper scales. For this purpose, α/d is used as a velocity scale, $\rho\alpha^2/d^2$ is used as pressure scale (where ρ is the fluid density) and d^2/α is used as a reference quantity for time scale, where d is a reference length (the vertical extension or diameter of the channel in the present thesis)). This leads to the following non-dimensional form of these equations:

$$\underline{\nabla} \cdot \underline{V} = 0 \tag{2.16}$$

$$\frac{\partial \underline{V}}{\partial t} = -\underline{\nabla} p - \underline{\nabla} \cdot \left[\underline{V}\underline{V} \right] + \nabla^2 \underline{V} - \mathrm{Pr}\, Ra T \ \underline{i}_g \tag{2.17}$$

The term $\underline{i}_g$ appearing in equation 2.17 is a unit vector whose direction is towards the direction of gravity. In terms of energy equation, defining the non-dimensional temperature as the ratio among the local temperature subtracted from a reference temperature and the imposed ΔT, leads to a non-dimensional form of energy equation which can be cast in compact form as follows:

$$\frac{\partial T}{\partial t} + \underline{\nabla} \cdot \left[\underline{V} T \right] = \nabla^2 T \tag{2.18}$$

Chapter 3

Geometrical configurations and boundary conditions

In the previous chapter, an overview has been given regarding different partial differential equations which represent the backbone of any numerical strategy for the investigation of the different convection mechanisms being considered in this thesis. It was evident from the discussion that such equations are of great importance as they can consistently describe the motion of the fluid. Furthermore, important non-dimensional parameters associated with buoyancy and forced convection were defined.

This section presents the different geometrical configurations used in the present study and their boundary conditions. The physical domains considered are a compact cavity with an obstruction located in its bottom-right corner, a 2D elongated cavity or channel with forward-facing step, a 2D channel with backward-facing step and analogous 3D configurations. Each physical domain has its own set of boundary conditions with tuneable geometrical effects such as the domain aspect ratio and the position of the inlet and outlet sections.

3.1 Obstructed Compact cavity

3.1.1 The geometry

The abovementioned obstructed cavity is shown in Fig. 3.1. It consists of a square two-dimensional cavity (aspect ratio A=width/height=1) having a square shaped (hot) obstruction embedded at the bottom. The cavity is also equipped with two small orifices on either side which serve as inflow and outflow sections. The sketch provides more precise information in terms of the location of the orifices: while the outflow section is located at mid-height between the horizontal hot surface of the obstacle and the top wall of the cavity, the position of the inflow section can change as shown in Fig. 3.1 (the fluid is introduced through the section close to the bottom ‘or’ that close to the top so that it can follow different trajectories).

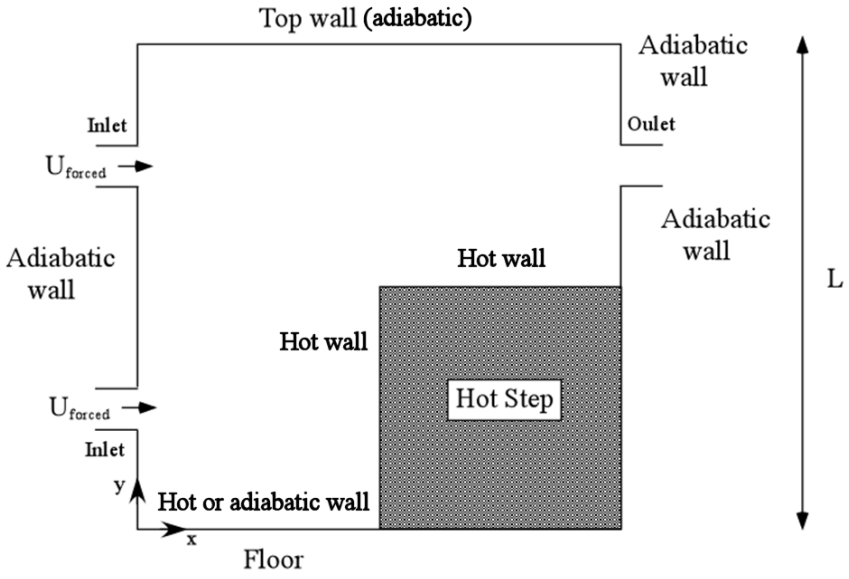

Figure 3.1: Sketch of the considered geometry and related kinematic and thermal boundary conditions.

For this case, in addition to hybrid flow, purely buoyant flow is also considered (i.e., no inflow and outflow). In this case, the fluid injection velocity U_{forced} is set to zero.
From a thermal point of view, the sidewalls are kept adiabatic for all the cases being investigated whereas the floor (y=0) takes a dual role as it is assumed either adiabatic or at constant temperature (namely, set at the same temperature T_{hot} of the obstruction). On the contrary, a separate concept is applied on the top wall, which is kept cold (T_{cold}) and isothermal for pure buoyancy convection (U_{forced} =0) or adiabatic in the case of hybrid convection ($U_{forced}\neq0$). In the case of hybrid convection, the cooling role of the top wall (ceiling) is performed by the fluid forced inside the cavity (the velocity and temperature in this scenario are set to U_{forced} and T_{cold}, respectively).

3.1.2 Boundary conditions

The non-dimensional thermal boundary conditions (BCs) for the considered problems can be summarized as follows:

Side walls (x=0 or x =1): $\partial T/\partial x=0$ (3.1)

Step walls (x=1/2, $0\leq y\leq 1/2$ and y=1/2, $1/2\leq x\leq 1$) $T=1$ (3.2)

Floor (y=0, $0\leq x\leq 1/2$), $\partial T/\partial y=0$ (adiabatic) (3.3a)
or $T=1$ (isothermal) (3.3b)

Top wall (y=1, $0\leq x\leq 1$) $T=0$ (isothermal, Re=0) or $\partial T/\partial y=0$ (adiabatic, $Re\neq0$) (3.4)

The Nusselt number associated with the vertical and horizontal walls of the step can be defined accordingly as follows:

$$Nu_{step}^{vert} = -2\int_{0}^{1/2} \frac{\partial T}{\partial x} dy \text{ and } Nu_{step}^{horiz} = 2\int_{1/2}^{1} \frac{\partial T}{\partial y} dx \quad (3.5)$$

From a kinematic point of view, all the walls in the geometry are regarded as no-slip surfaces, which indicates that the two velocity components along x and y (u,v) directions are formally set to zero. For the cases with Re≠0, additional conditions are required at the inflow and outflow section (assumed to have a non-dimensional vertical extension l=0.1). For the inflow section the boundary condition can be simply set as:

Inflow (x=0, 0.2≤y≤0.3 or 0.7≤y≤0.8): $u = U_{\text{forced}}$, v=0, T=0 (3.6)

The BCs for the outflow section are more complex and require additional reasoning or explanations. In order to impose proper conditions on open boundaries, increased care and attention is required to make certain that *no spurious oscillations are produced*, which would disturb the physical consistency of the entire velocity (and temperature) field and generate numerical instabilities. As a result of already existing research on the subject, a relevant approach can be adopted known as the "open boundary condition" (OBC) framework (Hattori et al. 2013; Dong et al. 2014). Such involved spatio-temporal conditions are represented in mathematical form through the so-called "prognostic equation":

Outflow (x=1, 0.7≤y≤0.8): $\frac{\partial u}{\partial t} + D\frac{\partial u}{\partial x} = 0$, $\frac{\partial v}{\partial t} + D\frac{\partial v}{\partial x} = 0$, $\frac{\partial T}{\partial t} + D\frac{\partial T}{\partial x} = 0$ (3.7)

namely, a transport equation where D is a constant assumed to be equal to the averaged velocity perpendicular to the boundary $D = \underline{V} \cdot \underline{\hat{n}}$. This modus operandi has been proven to provide reasonable algorithm stability and guarantee the physical consistency of the solution by preventing the propagation of non-physical fluctuations of pressure and/or temperature in the upstream direction. According to literature it is always valid regardless of the value of Reynolds number but in the limit as the Reynolds number tends to zero this should be replaced with a condition where the derivative of the quantity along the direction perpendicular to the boundary is set to zero. Related numerical results are presented in Chapter 5.

3.2 Elongated Cavity with forward-facing step

3.2.1 The geometry

This second geometry is represented in its physical form in Fig. 3.2. The configuration comprises of a rectangular two-dimensional channel having a transverse size d and total length L=10d. The

entire channel is equally divided into two parts having same extension in horizontal direction. This is done by an abrupt change in the available cross-section area which is achieved by inserting a forward-facing step having thickness equal to half of the channel height, i.e., *d/2*

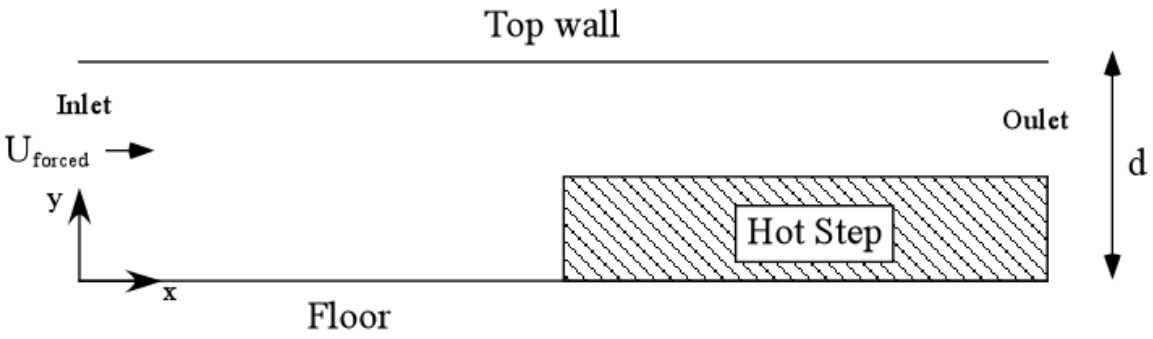

Figure 3.2: Sketch of the considered FFS geometry and related kinematic and thermal boundary conditions.

The floor (bottom wall) and ceiling (top wall) are solid. For all the cases where the value of Reynolds number is non-zero, the temperature is set as zero gradient for top wall i.e., adiabatic behaviour. However, for the case of pure buoyancy convection, the top wall is considered isothermal (at temperature T_{cold}) with the parameters such as Reynolds number set to Re=0 (U_{forced} =0). Additionally, for pure buoyancy convection the inflow and outflow sections located on left and right are substituted by solid adiabatic walls. This situation of pure thermal convection is considered for the sake of completeness and to understand better the role potentially played by buoyancy convection in the hybrid flow case.. For Re≠0, the fluid introduced inside the extended cavity is assumed to have initial temperature T_{cold}.
A separate discussion is required to explain the boundary conditions applied on the floor and the step boundary (which consist of a small vertical segment and the horizontal wall which extends from its corner in the downstream direction). The floor (y=0) is either heated at constant temperature (set at the temperature T_{hot}) or kept adiabatic (zero gradient). On the other hand, the entire boundary of the step is always kept at temperature T_{hot} irrespective of all the different thermal boundary conditions assumed for the ceiling and floor (top and bottom wall.

3.2.2 Boundary conditions

By specifying with A, the ratio *L*/d, the non-dimensional thermal boundary conditions for the FFS domain can be outlined as follows:

$\underline{V}$=0 on all solid walls (3.8)

Step walls (x=A/2, 0≤y≤1/2 and y=1/2, A/2≤x≤A) T=1 (3.9)

Floor (y=0, 0≤x≤A/2), $\partial T/\partial$y=0 (adiabatic) (3.10a)

or T=1 (isothermal) (3.10b)

Top wall (y=1, 0≤x≤A) T=0 (isothermal, Re=0) or $\partial T/\partial$y=0 (adiabatic, Re≠0) (3.11)

A separate discussion is needed for the lateral boundaries located at x=0 and x=A. These boundaries are considered solid and adiabatic if no forced flow is considered, whereas, for Re≠0 the left and right boundaries are assumed to be inflow and outflow sections, respectively. Therefore:

For Re=0, $\partial T/\partial$x=0 at x=0 and x=A (3.12)

For Re≠0, x=0 (inflow, 0≤y≤1), T=0 and u= U_{forced} (3.13)

x=A (outflow, 0.5≤y≤1): $\frac{\partial u}{\partial t}+D\frac{\partial u}{\partial x}=0$, $\frac{\partial v}{\partial t}+D\frac{\partial v}{\partial x}=0$, $\frac{\partial T}{\partial t}+D\frac{\partial T}{\partial x}=0$ (3.14)

Moreover, the Nusselt for the vertical and horizontal walls of the step is defined here as:

$$Nu_{step}^{vert}=-2\int_{0}^{1/2}\frac{\partial T}{\partial x}dy \text{ and } Nu_{step}^{horiz}=\frac{2}{A}\int_{A/2}^{1}\frac{\partial T}{\partial y}dx \quad (3.15)$$

Related numerical results are presented in Chapter 6.

3.3 Elongated Cavity with backward-facing step

3.3.1 The geometry

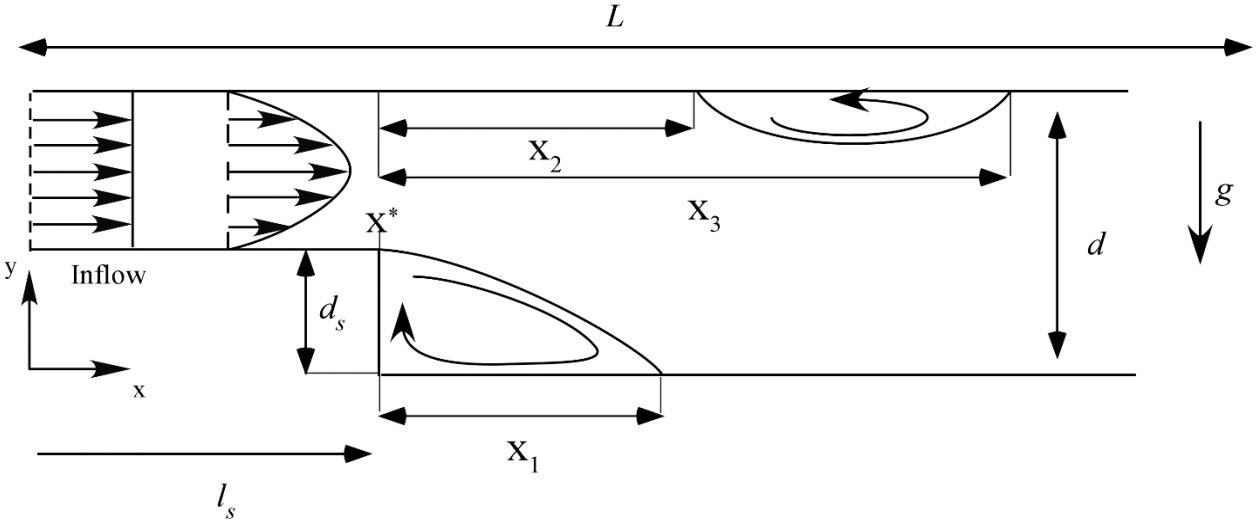

Figure 3.3: Sketch of the Backward Facing Step (BFS) configuration.

As anticipated in the introduction, the geometry with the BFS can be seen as the mirror image of that with the FFS (see Fig. 3.3). It simply consists of a two-dimensional duct with a sudden expansion in the cross-sectional area in the direction perpendicular to the (horizontal) flow. The (vertical) step size and the transverse channel size after the expansion are denoted by d_s and d, respectively (accordingly, the aforementioned expansion ratio can be defined as ER= d / d_s). Similarly, a length ratio can be introduced as LR = L/l_s (where L is the overall horizontal extension of the considered duct while l_s indicates the horizontal position of the section where the variation in size occurs). Another relevant geometrical parameter is represented by the physical domain aspect ratio, namely A=L/d.

3.3.2 Boundary conditions

The non-dimensional boundary conditions for the BFS configuration considered in the present work can be summarized as follows:

$\underline{V}$=0 on all solid walls (3.16)

x=0 (inflow, $ER^{-1} \le y \le 1$), T=0 (cold fluid) and $u = U_{forced}$ (3.17)

x=A (outflow, $0 \le y \le 1$): $\frac{\partial u}{\partial t} + D\frac{\partial u}{\partial x} = 0$, $\frac{\partial v}{\partial t} + D\frac{\partial v}{\partial x} = 0$, $\frac{\partial T}{\partial t} + D\frac{\partial T}{\partial x} = 0$ (3.18)

The following additional thermal boundary conditions apply to the boundary delimiting the fluid from below.

Step walls $y=ER^{-1}$, $0 \le x \le A/LR$, $\partial T/\partial y=0$ (adiabatic)
and $x=A/LR$, $0 \le y \le ER^{-1}$, $\partial T/\partial x=0$ (adiabatic) (3.19a)
or T=1 for both walls (isothermal case) (3.19b)

Floor (y=0, $A/2 \le x \le A$), $\partial T/\partial y=0$ (adiabatic) (3.20a)
or T=1 (isothermal) (3.20b)

Top wall (y=1, $0 \le x \le A$) $\partial T/\partial y=0$ (adiabatic) (3.21)

Related numerical results are presented in Chapter 7.

3.4 Three-dimensional channels with a step

3.4.1 The geometry

The 3D geometries considered in this thesis are shown in Fig. 3.4.

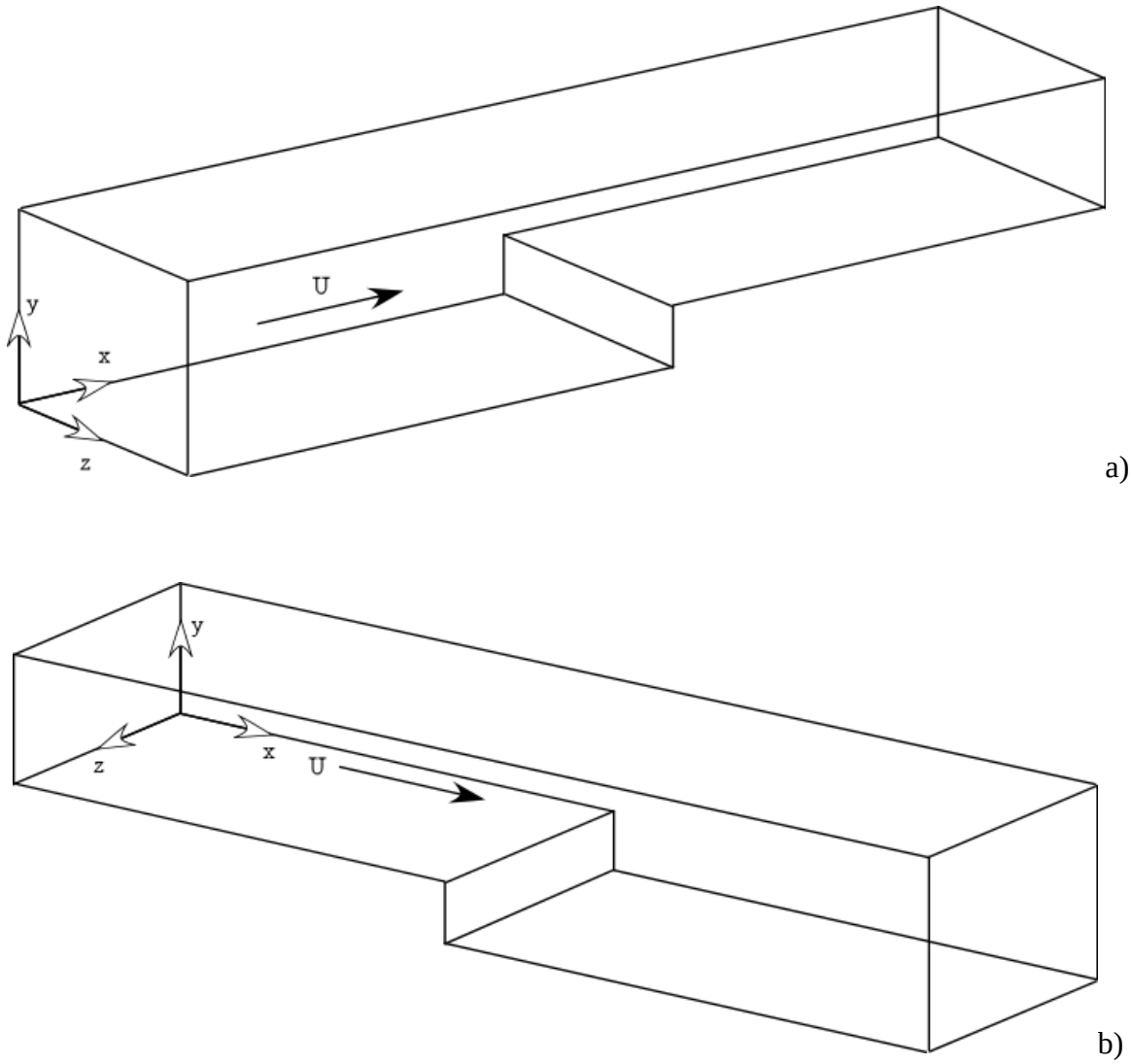

Figure 3.4: Considered channels with a sudden variation in the cross-sectional area: a) Forward-facing step (FFS), b) Backward-facing step (BFS).

Both are characterized by an inflow section and an outflow section located at x=0 and x=A_x, respectively, where A_x is the ratio of the overall length L_x of the domain in the horizontal direction to its total vertical extension *d*. The other boundaries are solid walls. Other characteristic geometrical parameters are $A_z = L_z/d$ and the ratio of d and the step height *s* (ER=d/*s* fixed to 2 in the present work, while in line with the corresponding 2D configurations, the value considered for the domain aspect ratio is A_x =10 with the step being located halfway between the inflow and outflow sections). The fluid (Pr=1) is injected into the domain at a temperature T_{cold}, while the entire bottom boundary or the horizontal and vertical sides of the step only are kept at a larger temperature T_{hot} and the entire top boundary is considered thermally insulated. Periodic boundary conditions are assumed to hold along the boundaries delimiting the system in the spanwise direction, i.e., at z=0 and z= L_z, with A_z =1.

3.4.2 Boundary conditions

x=0 (inflow), T=0 (cold fluid) and u= PrRe (3.22)

The other required conditions read

$u=v=w=0$ on all solid walls (3.23)

(having indicated with u, v and w, the velocity components along x, y and z, respectively) and

x=A_x (outflow): $\frac{\partial \underline{V}}{\partial t} + D\frac{\partial \underline{V}}{\partial x} = 0$, $\frac{\partial T}{\partial t} + D\frac{\partial T}{\partial x} = 0$ (3.24)

As mentioned before equation (3.38) is the so-called "prognostic' equation, by which the occurrence of unphysical oscillations of the thermofluid-dynamic variables at the outlet can be prevented.
The following additional thermal boundary conditions are considered for the boundary delimiting the fluid from below and from above.

Top wall (y=1) $\partial T/\partial$y=0 (adiabatic) (3.25)

Step vertical side (x=A_x/2), T=1 (isothermal) (3.26)

Step horizontal side (y=ER^{-1}):
FFS ($A_x/2 \le x \le A_x$), T=1 (isothermal) (3.27)
BFS ($0 \le x \le A_x/2$), T=1 (isothermal) (3.28)

Channel floor (y=0)

FFS ($0 \le x \le A_x/2$) , $\partial T/\partial y = 0$ (adiabatic) (3.29)
or $T=1$ (isothermal (3.30)

BFS ($A_x/2 \le x \le A_x$), $\partial T/\partial y = 0$ (adiabatic) (3.31)
or $T=1$ (isothermal) (3.32)

Moreover, periodic boundary conditions (PBC) have been set at z=0 and $z=A_z$ for both temperature and velocity. This means that the "wavelength" along the z direction (assumed to be virtually infinite through the use of PBC) is fixed to 1. Although fixing this periodic wavelength might have an impact on the fluid-dynamic disturbances, a periodic extension in the spanwise direction comparable to the vertical extension of the system should be considered a physically relevant one (future work might be dedicated to assess the influence of the extension set for the z direction). Related numerical results are presented in Chapter 8.

Chapter 4: Numerical methods, Mesh Selection and Validation Study:

This chapter is dedicated to the numerical methods that have been used to solve the governing equations. For all the systems described in Chapter 3, the PISO (Pressure Implicit Split Operator) method originally elaborated by Issa (1986) has been utilized to solve the non-dimensional equations reported in Chapter 2 and the associated set of boundary conditions (summarized in Chapter 3). Towards the end, OpenFoam has been used as it contains the PISO techniques in the form of a native solver. Further details about the underlying approach are illustrated in the following.

4.1 The Projection Method

From a purely theoretical point of view, it is worth recalling briefly that the PISO technique is based on the well-known Hodge decomposition theorem (Ladyzhenskaya, 1969) according to which any type of vector field can be expressed in the form of a divergence free contribution and curl free part i.e., the gradient of a scalar potential. This theorem is of great significance in the context of CFD algorithms for incompressible flows as it constitutes the required pre-requisite to split the computation of the velocity field into different parts (corresponding to distinct algorithm steps) while rendering it 'fixed' (i.e., making sure that the final field satisfies the original balance equations for mass and momentum). More specifically, this approach stands at the root of many methods (for instance, Harlow and Welch, 1965; Chorin, 1968; Temam, 1969; Lappa, 1997; Armfield and Street, 1999, 2002; Lee et al. 2001) commonly known as projection or fractional-step techniques. As an element common to all these variants, in the first stage of evaluation, the velocity is determined from a simplified version of the momentum equation from which the pressure gradient ∇p has been excluded. Although unphysical, this 'intermediate' velocity has the same vorticity the effective velocity would have (the curl of the gradient of pressure being zero). By denoting the intermediate velocity with V^*, the related equation simply reduces to

$$\frac{\partial \underline{V}^*}{\partial t} = \left[-\underline{\nabla} \cdot \left[\underline{V}\underline{V} \right] + \mathrm{Pr} \nabla^2 \underline{V} + \mathrm{Pr}\, RaT \underline{i}_g \right] \tag{4.1}$$

The asterisk used as superscript is representative of the fact that although intermediate velocity is physically accurate with regard to vorticity, nevertheless it fails to fulfil the requirement relating to the incompressible nature of the flow (i.e., divergence of the flow velocity must be zero). From a practical standpoint, the solenoidal behaviour of the flow is recovered in a second step, where the velocity is 'corrected' using the previously disregarded gradient of pressure. This is formally implemented through a linear relationship as indicated below:

$$\underline{V} = \underline{V}^* - \xi \underline{\nabla} p \tag{4.2}$$

where ξ is a constant. Inserting this equation into the continuity equation, formally yields the last computational stage needed to close the problem from a numerical point of view, i.e., a separate equations for the pressure:

$$\nabla^2 p = \frac{1}{\Delta t} \underline{\nabla} \cdot \underline{V}^* \tag{4.3}$$

The use of OpenFoam provides the opportunity to solve these equations by employing a collocated grid method where the centre of the cells serves as a place for defining the primitive variables (V and p), while a specific interpolation scheme is used to reconstruct the velocity on the cell faces in order to guarantee accurate coupling of these quantities.

It is important to highlight the following. A second order central difference scheme has been used to discretize the convective and diffusive terms which appear in both momentum and energy equations. A Preconditioned Bi-Conjugate Gradient (PBiCG) having an incomplete Lower Upper(DILU) preconditioner in the predictor step has been availed for the purpose of treating the resulting system of algebraic equations. Finally, the solution of the Poisson (elliptic) equation (4.3) has been obtained in the framework of a Generalized Geometric-Algebraic Multi-Grid (GAMG) strategy.

4.2 Validation Study:

In order to demonstrate the reliability of the algorithm described in Sect. 4.1 and its ability to address the problem set in the previous three chapters, a comparison has been made with available benchmarks and test cases. In particular, such a process has been articulated into four distinct stages of verification. Initially, two different archetypal settings have been considered, namely steady RB and Hadley convection in a square cavity (related validation results being summarized in Tables 4.1 and 4.2, respectively).

Table 4.1: A=1, Rayleigh-Bénard convection in a square cavity with adiabatic sidewalls, $Ra=10^5$, Pr=0.71. Comparison with Table 2 of Ouertatani et al. (2008), uniform mesh 128x128. Velocity scaled with $u_0=\mathrm{sqrt}(g\beta_T H \Delta T)$. The authors used an in-house code based on projection method.

Quantity	Present	Ouertatani et al. (2008)
U_{max}	0.3443	0.3442
V_{max}	0.3754	0.3756
Nu_h	3.9204	3.9097

Table 4.2: Hadley flow, $Ra=10^6$, Pr=0.71, square cavity with adiabatic top and bottom wall, uniform mesh 100x100 (Legend: $|\psi|_{max}$ - Maximum absolute value of the stream function, v_{max} - Max vertical velocity component on a horizontal mid-plane, x_{max} - Position of v_{max}, u_{max} - Max horizontal component on a vertical mid-plane, y_{max} - Position of u_{max}. Nu_{hot} - Average Nusselt number on the hot boundary. $Nu_{max,hot}$ - Maximum Nusselt number on the hot boundary, $y_{Nu,max}$ - Position of $Nu_{max,hot}$, $Nu_{min,hot}$ - Minimum Nusselt number on the hot boundary, $y_{Nu,min}$ - Position of $Nu_{min,hot}$). The author used an in-house code based on finite difference method to solve the stream function vorticity formulation of the equations.

Parameter	Present	De Vahl Davis and Jones (1983)
$\|\psi\|_{max}$	16.919	16.750
v_{max}	216.09	219.36
x_{max}	0.0368	0.0379
u_{max}	64.97	64.63
y_{max}	0.848	0.850
Nu_{hot}	8.913	8.817
$Nu_{max,hot}$	18.193	17.925
$y_{Nu,max}$	0.0368	0.0378
$Nu_{min,hot}$	0.970	0.989
$y_{Nu,min}$	1	1

As a second stage of validation, the ability of the present numerical approach *to capture properly the transition from steady to oscillatory flow* has been assessed (the outcomes of this dedicated study being summarized in Figs. 4.1 and Table 4.3). This type of instability corresponds to the so-called "Hopf bifurcation" for which, using the typical terminology of the linear stability analysis (LSA), an eigenvalue of the Jacobian matrix (in general a complex conjugate pair of eigenvalues) of the governing equations crosses the imaginary axis (i.e., the real part of the eigenvalue becomes positive with a corresponding value of imaginary part that is not zero(Mizushima and Adachi, 1997). For such a comparison, a case of classical buoyancy convection in a cavity heated from below and cooled from above with conducting solid sidewall has been considered. As shown by Mizushima and Adachi (1997)for Pr=7, this apparently innocuous system can take many and complicated routes to attain equilibrium or chaotic states, which involve (but are not limited to) textural transitions and 'multistability'. The latter concerns the ability of the flow to evolve along distinct branches of solutions, which exist in parallel in the space of parameters and stem from different initial conditions (coexisting 'attractors'). In particular, the specific dynamics occurring in the interval $47000<Ra<50000$, have been

considered, where, according to Mizushima and Adachi (1997)(see Figs. 6 and 8 in their paper), the flow undergoes a subcritical Hopf bifurcations along a branch of evolution that originates from the point $Ra \cong 49600$. Such a bifurcation is properly captured by the present solver as witnessed by the temperature and velocity fields in Figs. 4.1 (showing the 'diagonal mode' of convection emerging as a result of the bifurcation) and the data (frequency of oscillation) in Table 4.3.

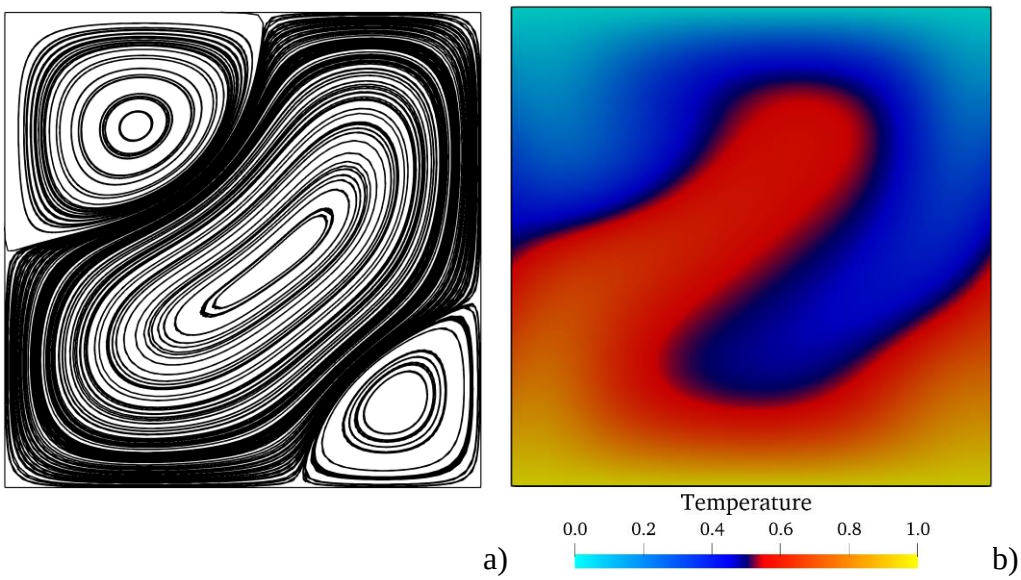

Figure 4.1: Snapshots of streamlines(a) and temperature distribution (b) for Rayleigh-Bénard convection in a square cavity with conducting sidewalls (Pr=7, *Ra*=48000, time-periodic state, see Table 4.3 for the related frequency).

Table 4.3: Non-dimensional frequency f defined as $f^{Dim} L^2/\alpha$ where f^{Dim} is the dimensional frequency of the oscillation (Newtonian fluid, Pr=7, Rayleigh-Bénard convection in a square cavity with conducting sidewalls, uniform mesh: 10000 nodes, Hopf bifurcation, comparison with the results produced using linear stability analysis (LSA) by Mizushima and Adachi (1997).

Data source	*F*
Mizushima and Adachi (1997)	16.31
Present solver	16.19

As a third level of validation, some of the cases specifically considered in the present work (the FFS problem) have been also simulated (for different representative values of *Ra* and *Ri*) using different computational platforms, i.e., a commercial software (ANSYS Fluent) and the same code that Lappa (2019) used to analyse the dynamics of thermal plumes in cross flow. Both rely on 2nd order upwind schemes (standard central differences being employed for the diffusive terms only). However, the software developed by Lappa (2019) is completely explicit in time,

whereas ANSYS Fluent is based on an implicit approach. Moreover, in order to accelerate convergence, it takes advantage of a classical Algebraic Multigrid scheme (AMG) with standard parameters, i.e., the so-called Gauss-Seidel smoother (Hutchinson and Raithby, 1986). Although OpenFoam (Sect. 4.1) and these alternate computational platforms rely on quite different numerical implementations, as witnessed by Table 4.4, the values obtained for the Nusselt number and the (non-dimensional) angular frequency of oscillation (ω) are in good agreement (the maximum percentage difference in the worst case being ≅5%).

Table 4.4: Properties of Hybrid Forced-buoyancy flow in the FFS configuration for various representative conditions. Comparisons of results obtained with different computational platforms (ω is the non-dimensional angular frequency; for unsteady regimes the time-averaged value of the Nusselt number is considered)

Ri	*Ra*	Floor	Regime	Parameter	Parameter
∞	10^6	Adiabatic	Quasi-periodic	Present Nu_{step}^{horiz} : 9.86	Nu_{step}^{vert} 17.52
				Code by (Lappa, 2019) Nu_{step}^{horiz} : 9.98	Nu_{step}^{vert} 17.94
∞	10^6	Hot	Periodic	Present Nu_{step}^{horiz} : 10.83	Nu_{step}^{vert} 3.01
				Code by (Lappa, 2019) Nu_{step}^{horiz} : 10.80	Nu_{step}^{vert} 3.1
100	10^5	Adiabatic	Steady	Present Nu_{step}^{horiz} : 3.23	Nu_{step}^{vert} 10.64
				ANSYS Fluent Nu_{step}^{horiz} : 3.19	Nu_{step}^{vert} 10.52
				Code by (Lappa, 2019) Nu_{step}^{horiz} : 3.30	Nu_{step}^{vert} 10.66
1	10^7	Adiabatic	Unsteady with dominant frequency	Present Nu_{step}^{horiz} : 39.07	Nu_{step}^{vert} 45.41
				Code by (Lappa, 2019) Nu_{step}^{horiz} : 40.12	Nu_{step}^{vert} 45.11
1	10^7	Hot	Unsteady with dominant frequency	Present Nu_{step}^{horiz} : 38.10	Nu_{step}^{vert} 16.58
				Code by (Lappa, 2019) Nu_{step}^{horiz} : 39.50	Nu_{step}^{vert} 16.25
30	10^7	Adiabatic	Periodic	Present ω: 6280	
				Code by (Lappa, 2019) ω: 6543	
1	10^7	Adiabatic	Unsteady with dominant frequency	Present ω: 3.58 10^4	
				Code by (Lappa, 2019) ω: 3.77 10^4	
1	10^7	Hot	Unsteady with dominant frequency	Present ω: 3.38 10^4	
				Code by (Lappa, 2019) ω: 3.2 10^4	

As a natural extension of the specific approach illustrated above, a final level of validation has been implemented through consideration of BFS specific (representative) cases. Following Khanafer et al. (2008), for such a task the horizontal and vertical side of the step have been assumed adiabatic, i.e., eq. (3.19a) and the floor at a fixed temperature, i.e., eq. (3.20b). The geometrical parameters have been fixed to A=20, ER=2, LR=4 (i.e., the step being located at x=A/4).

Again, two different software (the OpenFOAM method described in Sect. 4.1 and the independent solver developed by Lappa, 2019) have been used to get the required extra layer of validation. The outcomes of such focused assessment are summarized in Tables 4.5 and 4.6 where it can be seen that the differences between the results obtained with two completely independent computational platforms lie below 3%.

Table 4.5: Nondimensional position of characteristic points for Pr=0.71, A=20, ER=2, LR=4, *Ra*=5680 and different values of the Reynolds number (Mesh 1000x100, the coordinate in brackets indicates the corresponding value obtained with the independent solver developed by Lappa, 2019; refer to Figure 3.3 for the meaning of x_1, x_2 and x_3).

Reynolds Number	**x_1 (reattachment length)**	**x_2 (secondary roll leading edge)**	**x_3 (secondary roll trailing edge)**
200	2.53 (2.53)	-	-
350	3.76 (3.78)	-	-
500	4.64 (4.68)	4.04 (4.08)	6.42 (6.46)
700	5.38 (5.36)	4.53 (4.55)	8.74 (8.80)

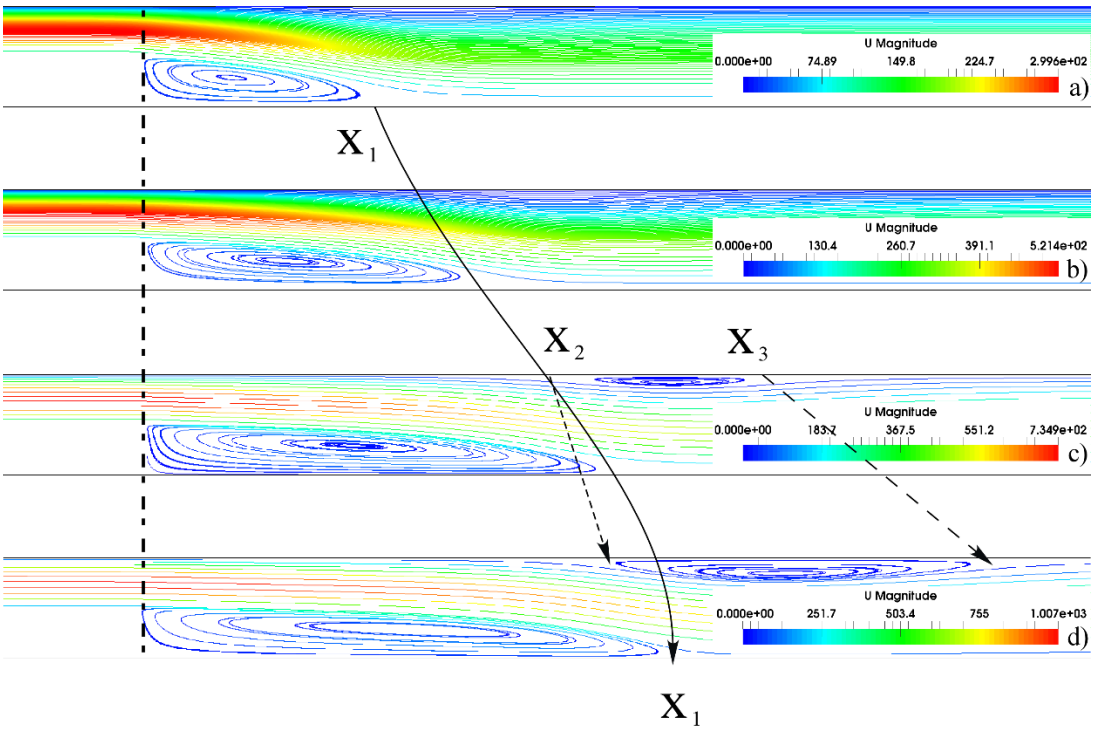

Figure 4.2: Streamlines for Pr=0.71, A=20, ER=2, LR=4 and *Ra*=5680 as a function of Re for adiabatic step and hot floor: a) Re=200, b) Re=350, c) Re=500, d) Re=700.

Table 4.6: Nondimensional position of characteristic points for Pr=0.71, A=20, ER=2, LR=4, Re=200 and different values of Rayleigh number (Mesh 1000x100, the value in brackets indicates the corresponding roll length obtained with the independent solver developed by Lappa, 2019).

Rayleigh Number	**x_1 (reattachment length)**
5680	2.53 (2.53)
22720	2.74 (2.82)
45440	3.02 (3.06)
68160	3.31 (3.39)
90880	3.59 (3.64)

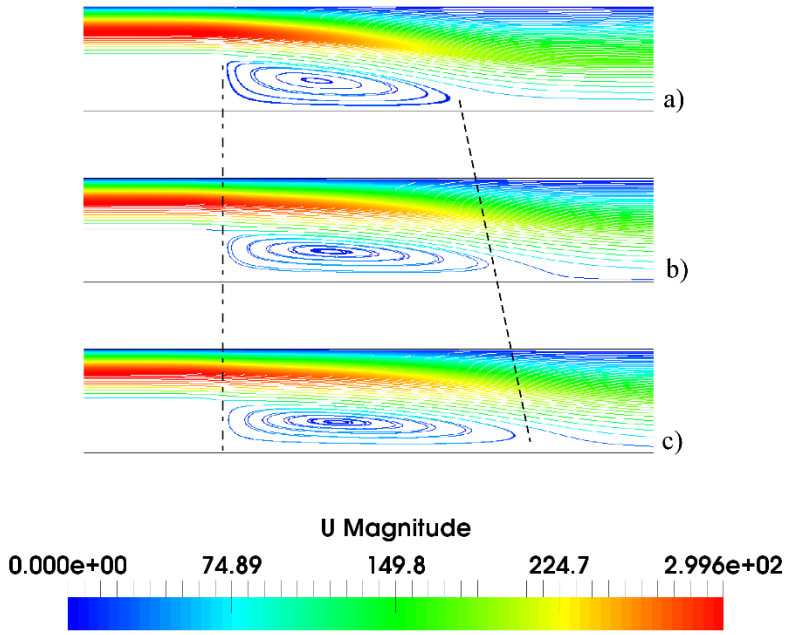

Figure 4.3: Streamlines for Pr=0.71, A=20, ER=2, LR=4 and Re=200 as a function of *Ra* for adiabatic step and hot floor: a) *Ra*=5680, b) *Ra*=45440, c) *Ra*=90880.

Apart from lending additional reliability to the present approach, however, these tables also serve as an analysis of the combined influence of *Ra* and Re on the position of x_1 in steady conditions. Along these lines, Fig. 4.2 shows that, in agreement with the trends reported by Khanafer et al. (2008), an increase in Re at fixed *Ra* obviously makes the recirculation zone along the heated surface larger (the current leaving the step being more energetic). Notably, an increase in *Ra* (at fixed Re) has the same effect, i.e., the reattachment point moves in the downstream direction (see Fig. 4.3). In this case, the root cause must be sought in the buoyancy force, which tends to strengthen the primary roll, thereby increasing its horizontal extension. Interestingly, while x_1 shows a quadratic dependence on the Reynolds number (Fig. 4.4a), its relationship with *Ra* is essentially linear (Fig. 4.4b).

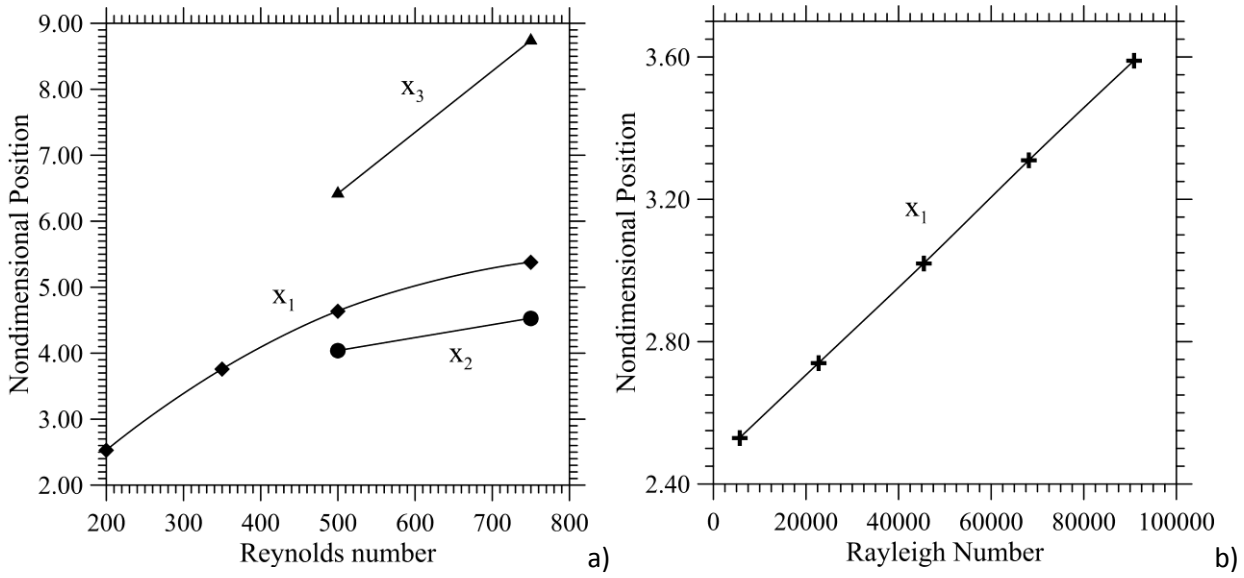

Figure 4.4: Position of characteristic points (refer to Figure 3.3) as a function of Re and *Ra* for adiabatic step and hot floor: a) *Ra*=5680; b) Re=200.

4.3 Mesh resolution and Kolmogorov length scale

In the present thesis, the following ranges have been considered for the Rayleigh number, the Reynolds number (based on the injection velocity U_{forced}) and the corresponding Richardson number:

$$O(10^3) \leq Ra \leq O(10^8),\ O(10) \leq Re \leq O(10^4)$$
$$Pr=1,\ O(10^{-1}) \leq Ri \leq O(10^2)$$

with the only exception of the 3D geometries for which the analysis has been limited to the turbulent state obtained for $Ra=10^7$ and $Ri=O(10^2)$ (this specific point will be discussed in Sect. 4.6.1).

Given these ranges, the choice of an adequate mesh when the problem is approached in the framework of DNS (Direct Numerical Simulation) is not as straightforward as one would imagine. In general, two requirements must be satisfied in order to make the simulations reliable. First of all, a parametric investigation must be carried out to make sure that the solution does not depend on the considered grid. This implies testing the percentage variation experienced by some representative fluid-dynamic quantities when the density of the mesh is increased. If simulations are carried out for values of the characteristic numbers (e.g., *Ra*) spanning several orders of magnitude, this refinement study must be conducted for each order of magnitude considered or, as an alternative, the mesh which makes the solution grid-independent obtained for the highest considered value of *Ra* must be used for all the cases (this modus operandi being the most expensive in terms of computational cost or efficiency).

As a second requirement, if the considered flow is in turbulent conditions, the size of the mesh must be comparable (or equal) to the so-called *Kolmogorov length scale* (ζ), i.e., the smallest flow scale present in the considered problem.
Estimates about this quantity can be found in the literature for different circumstances. For forced flow, it can conveniently be evaluated (Pope, 2000) as:

$$\zeta_{\mathrm{Re}} \cong \mathrm{Re}^{-3/4} \tag{4.4}$$

This correlation should obviously be used when Ri<O(1) (Coceal et al. 2006), whereas, in the opposite limiting condition in which thermal convection is the most important convective mechanism (namely, Ri>O(1)) alternate estimates should be used. These, in turn, can change depending on the relative direction of the prevailing temperature gradient and gravity. Indeed, the progression of thermal convection towards turbulence and its spatial and temporal features can be markedly different according to whether convection originates from a heated horizontal or vertical wall.
In the former case, following Kerr (1996) and De et al. (2017):

$$\zeta_{Ra\|} = 1.3Ra^{-0.32} \tag{4.5}$$

while for what concerns the other situation with prevailing horizontal gradients of temperature, a quantitative measure of such a length scale can be found in the works by Paolucci (1990) and Farhangnia et al. (1996):

$$\zeta_{Ra\perp} = \pi\left(\frac{16\,\mathrm{Pr}}{Ra}\right)^{3/8} \tag{4.6}$$

When circumstances where multiple mechanisms of convection coexist are the main subject of the analysis as in the present case, the smallest possible value of ζ should be considered (see, e.g., Lappa and Gradinscak (2018) i.e.

$$\zeta = \min\left\{\zeta_{\mathrm{Re}}, \zeta_{Ra\perp}, \zeta_{Ra\|}\right\} \tag{4.7}$$

For the aforementioned conditions examined in the present thesis ($O(10^3) \leq Ra \leq O(10^8)$, $O(10) \leq Re \leq O(10^4)$), it is easy to verify that the smallest possible scale always corresponds to eq. (4.5). This equation has therefore been used to determine the size of the mesh in the most demanding conditions (i.e., $Ra \geq 10^7$ for which turbulent states have been found). For smaller values of Ra, the grid density has been decided on the basis of a case-by-case preliminary mesh refinement assessment, as further discussed in the following sections.

4.4 Elongated Channel with FFS:

The data about the grids used for the compact cavity are directly provided in Chapter 5. Some results representatives of the grid refinement study for the channel with the FFS considered in this thesis are summarized in Tables 4.7 and 4.8 (these are just selective examples, as mentioned before, a mesh refinement study has been conducted for each considered value of Ra).

Table 4.7: Non-dimensional frequency f for different mesh sizes for the case of hybrid forced/buoyancy convection (Ri=100) with adiabatic bottom wall and Ra=4.7x10^5**.**

Mesh Size	f
1500x150	1.200 x10^3
1600x160	1.214 x10^3
1700x170	1.218 x10^3

Table 4.8: Non-dimensional frequency for different mesh sizes for the case of hybrid forced/buoyancy convection (Ri=30), with hot bottom wall and Ra=3x10^5**.**

Mesh Size	f
1600x160	6.983 x10^2
1700x170	6.912 x10^2
1800x180	6.924 x10^2

In these examples, it can be seen that for the case with Ri=100, adiabatic bottom wall and Ra=4.7x10^5, for an increase of 200 points along the horizontal direction, the corresponding percentage variation in the frequency of oscillation lies below 2% (which explains why a mesh 1500x150 has been selected). The same concept applies to the case with Ri=30, hot bottom wall and Ra=3x10^5 for which the percentage variation is even smaller (1%).

As explained before, a more sophisticated strategy, however, has been implemented for larger values of Ra to ensure that the turbulent properties of the flow (eventually emerging in this range of the control parameter) are properly captured.

For such cases, the needed resolution has been estimated on the basis of the concept of Kolmogorov length scale (ζ) already explained in Sect. 4.3. It can also be seen as the length scale that bounds from below the process of energy transfer from large scales to smaller scales which is typical of turbulent flow (Kolmogorov, 1941ab; Kraichnan, 1974).

For turbulent states, mesh convergence has been judged on the basis of the frequency spectrum (by verifying that the (-5/3) scaling trend predicted by the Kolmogorov law is independent from the mesh in terms of velocity amplitude and related frequency distribution, see Sect. 6.4 for the related plots). Using the set of criteria described in the present section, the required numerical

resolution has been determined for each considered case (the needed number of points ranging from a minimum of 400x40 to a maximum of 2000x200 depending on the considered value of the Rayleigh number).

4.5 Elongated Cavity with BFS:

Following the same approach implemented for the FFS, the mesh density has been increased parametrically up to make the percentage variation experienced by the aforementioned representative quantities smaller than a given threshold (2%, see, e.g., Tables 4.9 and 4.10).

Table 4.9: Non-dimensional frequency for different mesh sizes for the case of hybrid forced/buoyancy convection (Pr=1, Ri=7.5, Ra=3x10^6, A=10, ER=LR=2) with adiabatic floor**.**

Mesh Size	f
1500x150	1.305 x10^3
1600x160	1.308 x10^3
1700x170	1.310 x10^3

Table 4.10: Non-dimensional frequency for different mesh sizes for the case of hybrid forced/buoyancy convection (Pr=1, Ri=7.5, Ra=3x10^6, A=10, ER=LR=2), with hot floor**.**

Mesh Size	f
1800x180	1.085 x10^3
1900x190	1.078 x10^3
2000x200	1.066 x10^3

A different approach has been implemented for conditions where the flow is no longer laminar (Ra≥10^7) and therefore focusing on a well-defined quantity is no longer possible. For these cases, the assessment has been conducted referring again to well-known properties of turbulence, which can be considered general and somehow 'universal', i.e., the scaling trend of the frequency spectrum (Kraichnan, 1974). Assuming the so-called Kolmogorov length scale (ζ, known to be dependent on the Rayleigh and Reynolds number as indicated, e.g., in Sect. 4.3 as the typical

mesh size, it has been verified that the (-5/3) scaling trend predicted by Kolmogorov (1941ab) is independent from the mesh in terms of velocity amplitude and related frequency distribution. Using this set of criteria, the required number of points has been found to range between a minimum of 400 and a maximum of 2800 in the horizontal direction (and a minimum of 40 and a maximum of 300 in the vertical direction) depending on the considered conditions.

4.6 Three-dimensional cases and the Large-Eddy-Simulation approach

The arguments and related details provided in the earlier sections represent the basis of the so-called Direct Numerical Simulation (DNS) approach, that is, the case where these equations are directly discretized and solved to determine the velocity and temperature fields.
However, this method is not always a viable approach. When the flow becomes turbulent, fulfilling the requirement about a mesh having the same size of the Kolmogorov length can lead to an overall number of grid points that is not compatible with available computational resources in the general 3D case. For this reason, in the present thesis, the 3D configurations have been treated using a Large-Eddy-Simulation (LES) approach, that is a turbulence model by which the requirement in terms of grid points can be relaxed.
The physical foundation of the entire class of existing LES methods are linked to the theory that Kolmogorov (1941abc, 1942) elaborated approximately 80 years go. Stripped to its basics, this theory relies on the two-fold idea that 1) turbulence typically develops a hierarchy of scales through which the energy flows from larger scales towards smaller scales, and 2) since it can be expected that the motion of fluid on the small scales has small time scales, these motions *are statistically independent of the relatively slow dynamics occurring on the large scale*. The most remarkable implication of the latter realization is that the behaviours on small scales should depend only on the rate at which the fluid is supplied with energy by the large-scale flow and on the kinematic viscosity; in turn, this allows the postulation of the existence of an ‘‘inertial” wavenumber region, i.e. an interval of length scales where *local equilibrium* is attained, i.e. the energy injected in the flow per unit time is balanced precisely by the amount of energy dissipated per unit time and the flux of the cascading quantity across any scale is a function only of dynamic variables on that scale, until kinetic energy is finally completely dissipated by friction on the smallest possible length scale developed by the considered flow (the so-called Kolmogorov length). This behaviour is reflected mathematically by the well-known $\omega^{-5/3}$ scaling law that many real flows have proven to display in their FFT spectrum in the range of high frequencies (equivalent to a $k^{-5/3}$ scaling law in terms of related wavenumbers). Most remarkably, from a physical point of view, this indicates that, under a certain length scale, turbulence takes a universal (repetitive) behaviour in space, i.e. it becomes *homogeneous*, *isotropic* (direction independent) and self-similar (if a portion of the pattern is enlarged, the pattern displays the same properties).
These physical and mathematical considerations represent the sought aforementioned foundation of the LES approach. As the behaviour of turbulence on those scales is universal and obeys

precise mathematical laws, it can be "modeled", thereby alleviating the user from the burden of capturing those behaviours through a numerical resolution comparable with the Kolmogorov length scale (i.e., by means of very dense grids).

Put simply, the hallmark of LES is that small-scale motion (smaller than the so-called "filter width") is implicitly removed from the numerical simulation and determined as a function of local flow conditions. Typically, this is achieved through the introduction of the concept of *eddy viscosity* (ν_T), i.e. in order to filter out all the scales under a certain limit (namely the scale of the mesh effectively used for the numerical simulation), the kinematic viscosity ν of the considered fluid must be enriched with an additional term that accounts for the frictional effects occurring on the numerically neglected scales (generally called "unresolved" scales to distinguish them from the flow "resolved", i.e. the velocity determined numerically). As one may expect, this additional term (typically referred to as the *subgrid-scale* viscosity) depends (grows with) the size of the effectively used mesh, which may be regarded as the essence of the so-called Smagorinsky (1963)model.

For turbulence in non-isothermal fluids (with buoyancy), however, besides kinetic energy, turbulent thermal energy, whose density scales with the square of the local temperature fluctuations, must also be regarded as a relevant aspect of the problem. In analogy with the arguments elaborated before for the kinetic energy, this additional form of energy can be thought of (see, e.g., the arguments elaborated by Kraichnan, 1974) as being injected at a large length scale, namely the vertical distance over which a temperature difference is maintained and dissipated at small length scales by the thermal diffusivity.

Although Bolgiano (1959) and Obukhov (1959) could show that in a stably stratified fluid, the kinetic energy spectrum can become $E(k) \propto k^{-11/5}$ if the thermal flux largely exceeds the kinetic energy flux, however, Kumar et al. (2014) and Bhattacharjee (2015) have confirmed that for a convectively unstable configuration like that considered in the present study, Kolmogorov arguments for the scaling of the energy spectrum are still applicable (i.e. $E(k) \propto k^{-5/3}$). This is the required principle allowing to treat the cascading behaviour of thermal energy in a fashion similar to that used for the turbulent kinetic energy, that is, through the introduction of a turbulent thermal diffusivity α_T to be added to that of the fluid (α) (Wong and Lilly, 1994). This parameter can be related to the turbulent viscosity ν_T, through a simple constant scaling factor, i.e., the so-called turbulent Prandtl number Pr_T (defined as ν_T/α_T in analogy with the classical fluid Prandtl number $Pr = \nu/\alpha$).

As a result, the original set of governing equations for mass, momentum and energy can be turned into an equivalent set of *space-averaged* equations and their solution can capture a large interval of scales, which range from the smallest physically relevant scale when the filter width tends to zero (the space-averaged equations tend to original flow equations) to the 'mean' large-scale turbulent flow when a very large filter width is assumed. Different variants of this approach exist and have been used with various degrees of success in the literature. In the original Smagorinsky algebraic model (also known as 0-equation model), the parameter ν_T depends only on the size of the mesh and the local value of the resolved strain rate, i.e.

$$\nu_T = \tilde{\lambda}^2 \sqrt{2\overline{D}_{ij}^{\,2}} \tag{4.8}$$

where $\overline{D}_{ij}$ is the resolved strain rate (in dimensional form)

$$\overline{D}_{ij} = \frac{1}{2}\left(\frac{\partial \overline{u}_i}{\partial x_j} + \frac{\partial \overline{u}_j}{\partial x_i} \right) \tag{4.9}$$

and $\tilde{\lambda} = C_s \Delta$, Δ is the mesh size and is a constant value in the model that must be specified prior to a simulation. Although this approach has led to valuable results (Lappa, 2019), more sophisticated versions have been introduced over the years to fix some drawbacks of the original implementation. Here, the present work relies on the so-called one-equation model that Yoshizawa and Horiuti (1985) introduced to improve the local balance assumption between the subgrid-scale energy production and dissipation adopted in the 0-equation version.
With this model, the subgrid-scale kinetic energy is defined as

$$k_{sgs} = \frac{1}{2}\tau_{kk} = \frac{1}{2}(\overline{u_k u_k} - \overline{u}_k \overline{u}_k) \tag{4.10}$$

and ν_T is computed as

$$\nu_T = C_k \Delta \sqrt{k_{sgs}} \tag{4.11}$$

Accordingly, the subgrid scale stress tensor reads

$$\begin{aligned} \tau_{ij} &= \overline{u_i u_j} - \overline{u}_i \overline{u}_j = \frac{1}{3}\tau_{kk}\delta_{ij} + \left(\tau_{ij} - \frac{1}{3}\tau_{kk}\delta_{ij} \right) \\ &\approx \frac{1}{3}\tau_{kk}\delta_{ij} - 2\nu_T dev(\overline{D})_{ij} = \frac{2}{3}k_{sgs}\delta_{ij} - 2\nu_T dev(\overline{D})_{ij} \end{aligned} \tag{4.12}$$

The subgrid-scale kinetic energy required for the determination of ν_T is computed resorting to the aforementioned hypothesis of local equilibrium, that is, the balance between the subgrid scale energy production and dissipation, which in mathematical form can be casted in compact form as

$$\overline{D} : \tau_{ij} + C_\epsilon \frac{k_{sgs}^{1.5}}{\Delta} = 0 \tag{4.13}$$

where the operator ":" is a double inner product of two second-rank tensors (i.e., the summation of the nine products of the corresponding tensor components of the two tensors) and $C_{\in}$ is a second constant required by the model. Taking into account eq. (4.12), eq. (4.13) can be further rearranged as

$$\overline{D}:\left(\frac{2}{3}k_{sgs}I-2\nu_T dev(\overline{D})\right)+C_{\in}\frac{k_{sgs}^{1.5}}{\Delta}=0\rightarrow$$
$$\overline{D}:\left(\frac{2}{3}k_{sgs}I-2C_k\Delta\sqrt{k_{sgs}}dev(\overline{D})\right)+C_{\in}\frac{k_{sgs}^{1.5}}{\Delta}=0\rightarrow$$
$$\sqrt{k_{sgs}}\left(\frac{C_{\in}}{\Delta}k_{sgs}+\frac{2}{3}tr(\overline{D})\sqrt{k_{sgs}}-2C_k\Delta\left(dev(\overline{D}):\overline{D}\right)\right)=0\rightarrow$$

$$ak_{sgs}+b\sqrt{k_{sgs}}-c=0 \tag{4.14}$$

For which the solutions can be simply obtained as

$$k_{sgs}=\left(\frac{-b\pm\sqrt{b^2-4ac}}{2a}\right)^2 \tag{4.15}$$

Where

$$\begin{cases} a=\dfrac{C_{\in}}{\Delta} \\ b=\dfrac{2}{3}tr(\overline{D}) \\ c=2C_k\Delta\left(dev(\overline{D}):\overline{D}\right) \end{cases} \tag{4.16}$$

In the case of incompressible flow, this reduces to

$$\begin{cases} b=\dfrac{2}{3}tr(\overline{D})=0 \\ c=2C_k\Delta\left(dev(\overline{D}):\overline{D}\right)=C_k\Delta\left|\overline{D}\right|^2 \end{cases} \tag{4.17}$$

where $\left|\overline{D}\right|=\sqrt{2\overline{D}:\overline{D}.}$

Therefore, by substitution of eq. (4.17) into eq. (4.15) one gets

$$k_{sgs} = \frac{c}{a} = \frac{C_k \Delta^2 \left|\overline{D}\right|^2}{C_\epsilon} \tag{4.18}$$

And by further substituting eq. (4.18) into eq. (4.10), the turbulent viscosity finally reads:

$$\nu_T = C_k \sqrt{\frac{C_k}{C_\epsilon}} \Delta^2 \left|\overline{D}\right| \tag{4.19}$$

Notably, by comparing it with eq. (4.8) at the basis of the algebraic Smagorinsky model, it follows that

$$\nu_T = (C_s \Delta)^2 \left|\overline{D}\right| \rightarrow C_s^2 = C_k \sqrt{\frac{C_k}{C_\epsilon}} \rightarrow C_k = \left(C_s^{4/3} C_\epsilon^{1/3}\right) \tag{4.20}$$

This value has finally to be corrected to fix the otherwise un-physical behavior by which the subgrid-scale viscosity would not become zero on solid walls (where standard viscous effects are dominant and tend to damp turbulence effects). The assumption of a constant ν_T in these regions (where $\left|\overline{D}\right|$ is relatively high) would overestimate the subgrid-scale stresses and might prevent flow transition to turbulence (this important concept will be further discussed in Chapter 8). Here the discussion is limited to highlight that the issue can be fixed in a relatively simple way by using the damping function originally proposed by van Driest (1956), namely

$$\nu_T = C_k \sqrt{\frac{C_k}{C_\epsilon}} \Delta^2 \left(1 - e^{-y^+/25}\right)^2 \left|\overline{D}\right| \tag{4.21}$$

where $y^+ = yu/\nu$ is the distance from the wall in wall coordinates (see, e.g., Moghadam et al., 2021), by which the correct asymptotic behavior is recovered.

This approach finally leads to a space-averaged version of the balance equations for mass, momentum and energy, which are formally similar to the original equations, the only difference being represented by the presence of an additional coefficient, namely, the turbulent kinematic viscosity and thermal diffusivity in front of the diffusive term appearing in the momentum and energy equations, respectively. Again, using as reference quantities, d, α/d, $\rho\alpha^2/d^2$, d^2/α and ΔT for the geometrical coordinates, velocity ($\underline{V}$), pressure (p), time (t) and temperature (T), respectively, the non-dimensional form such of equations simply reads

$$\underline{\nabla}\cdot\underline{V}=0 \tag{4.22}$$

$$\frac{\partial \underline{V}}{\partial t}=-\underline{\nabla}p-\underline{\nabla}\cdot\left[\underline{V}\underline{V}\right]+\left(1+\Pr\nu_T^*\right)\nabla^2\underline{V}-\Pr RaT\ \ \underline{i}_g \tag{4.23}$$

$$\frac{\partial T}{\partial t}+\underline{\nabla}\cdot\left[\underline{V}T\right]=\left(1+\alpha_T^*\right)\nabla^2 T \tag{4.24}$$

where $\nu_T^*=\nu_T/\nu$ and $\alpha_T^*=\alpha_T/\alpha$, $\underline{i}_g$ is the unit vector along the direction of gravity

4.6.1 Mesh selection for LES of Three-Dimensional Channel with a step

The selection of a relevant mesh for the application of the LES approach is not as straightforward as one would imagine (Celik et al., 2006). The empirical criteria valid for inertially-driven, i.e. forced, flows (see, e.g., Goergiadis et al.,2010; Choi and Moin, 2012 and references therein) are not directly applicable to circumstances in which thermals (thermal plumes of buoyant origin) contribute significantly to the development of turbulence (Farhangnia et al.,1996). For natural or mixed convection, special care must be provided to satisfy the fundamental (crucial) requirement at the basis of the LES philosophy, that is, the size of the mesh is located within *the inertial range of space scales*.

This apparently innocuous argument implies that a meaningful strategy must be found to evaluate a priori the upper and lower boundaries of the inertial range in the overall interval of space scales relevant to the considered problem. In this regard, it is worth recalling that some useful correlations exist by which the scale delimiting this interval from below (that is, the aforementioned Kolmogorov length scale, ζ, i.e., the length scale at which the cascading energy is finally dissipated) can be estimated. As explained before, this quantity typically depends on the considered values of the characteristic numbers, which measure the relative importance of the forces that induce fluid motion with respect to those which hinder it. In the present case, these are the Reynolds number, which measures the relative importance of inertial and viscous forces, and the Rayleigh number, which measures the relative importance of buoyant effects with respect to the counteracting influence of viscosity and thermal diffusion. In the presence of concurrent driving forces (inertia and buoyancy in the present case), the most restrictive condition should be considered, i.e., the one for which the smallest possible value of the Kolmogorov length is obtained. For what concerns the dominant inertia-driven flows and thermal convection i.e., RB convection and Hadley flow, the equations for the Kolmogorov length scale are already highlighted in Sect. 4.3 (eq. 4.4, 4.5, 4.6 respectively).

As 3D situations have been considered in which Ri>O(1) (see Chapter 8), and values of Pr and Ra for which $\zeta_{Ra\perp}>\zeta_{Ra\parallel}$, eq. (4.5) should therefore be considered as the effective Kolmogorov length controlling law, giving for Ra=10^7, $\zeta\cong 7.5\text{x}10^{-3}$. Any mesh with size δx larger than this

might be located in the inertial range of scales, which sets a first bullet for the proper definition of the mesh size. A mesh with too large size, however, might be located beyond the upper boundary of the inertial range, which indicates that estimates of the Kolmogorov length alone are not enough to close the problem (an upper boundary of the inertial range is also needed).
Still assuming (in line with the considerations above on the Kolmogorov length scale) the heating from below situation as the turbulence controlling condition, the extension $L_{inertial}$ of the inertial range might be estimated using the relevant information provided by De et al. (2017), where the following relationships were provided

$$L_{inertial} = 2.22 Ra^{-0.196} \text{ in the bulk} \quad (4.25a)$$

$$L_{inertial} = 1.01 Ra^{-0.18} \text{ in proximity to the heated wall} \quad (4.25b)$$

which give for $Ra=10^7$, $L_{inertial}=9.4\text{x}10^{-2}$ and $L_{inertial}=5.5\text{x}10^{-2}$, thereby constraining the required (non-dimensional) mesh size in the range $7.5\text{x}10^{-3}\leq\Delta\leq5.5\text{x}10^{-2}$.
In order to verify the consistency of such approach, a comparison has been made between the frequency spectrum obtained through DNS with that produced by the LES approach in equivalent conditions for some representative cases. As illustrated in Sect. 8.1, 8.2 and 8.3 by virtue of this modus operandi, it has been verified that LES can properly reproduce the system dynamics over a wide interval of frequencies, until a "cutoff" frequency is reached that corresponds to the flow wavenumber beyond which the flow is no longer resolved numerically as the effect of turbulence are implicitly taken into account via the model described in Sect. 4.6.

Part II

Results

Chapter 5

Thermogravitational and hybrid convection in an obstructed compact cavity

As anticipated in the introduction, before considering horizontally extended channels the response of the compact system sketched in Fig. 3.1 has been initially explored with respect to different kinematic and thermal degrees of freedom (namely, the injection of cold fluid into the cavity at different heights and different possible thermal behaviours of the top and bottom walls). At this stage, it is worth highlighting that an important aspect of these systems relates to the development of *thermal plumes*. Indeed, over the range of values of the Rayleigh number considered in the present work, plumes pertaining to different regimes can be formed and influence with their properties the overall flow dynamics. Precise information along these lines can be found in the study by Hier Majumder et al. (2004), who categorized thermal plumes on the basis of the related amount of vorticity and the gradient of temperature associated with their stem and cap. These features greatly depend on the considered fluid (Prandtl number) and the Rayleigh number. In particular, for the value of the Prandtl number assumed in the present thesis (Pr=1), plumes evolve from the so-called DV (Diffusive–Viscous) regime into the IVND (Inviscid–Nondiffusive) regime as soon as the Rayleigh number exceeds $Ra \cong 10^6$ (Lappa, 2009). Given these premises, in the following, first those cases are discussed for which the cavity has no inflow and outflow sections (Sect. 5.1) where the dynamics are expected to be entirely driven by the buoyancy effects and thermal plumes; then, those situations are considered where significant forced flow can cause alterations in the flow topology and related evolution towards chaos (Sects. 5.2 and 5.3).

5.1 Closed cavity

As already explained in Sect. 4.2.1 for each fundamental case a mesh refinement study was carried out to identify the minimum grid required to make the solution mesh-independent. As expected, this resulted in the need to increase the number of points with the considered value of the Rayleigh number. Related information is summarized in Tables 5.1 and 5.2, where for each case (in an ordered fashion) the following information has been reported: the value of *Ra*, the corresponding density of the mesh for which the solution was found to be grid-independent, the nondimensional (total) heat flux through the horizontal and vertical walls of the step (the hot obstruction) and, finally, the nature of the observed regime.

Table 5.1: Cases examined for the case of pure buoyancy convection with adiabatic bottom wall

Ra	Mesh Size	Nu_{step}^{horiz}	Nu_{step}^{vert}	Regime
10^3	40x40	1.21997	2.42394	Steady
10^4	40x40	2.24234	2.03534	Steady
10^5	80x80	3.6756	6.0646	Steady
10^6	100x100	≅4.17 (average)	≅11.7 (average)	Single-frequency
10^7	270x270	≅5.74 (average)	≅20.3 (average)	Single-frequency
10^8	500×500	≅11.53 (average)	≅32.2 (average)	Weakly Turbulent

Following the approach described in Sect. 3.1.2, in particular, two aspects are considered, namely, the hierarchy of convective and thermal structures which are produced within the cavity as the *Ra* number increases, and the *differences in terms of patterning behaviour* that are developed when the thermal boundary condition at the bottom floor is changed (floor being assumed to be adiabatic or kept at constant temperature as formalized by eqs. (3.3a) and (3.3b), respectively).

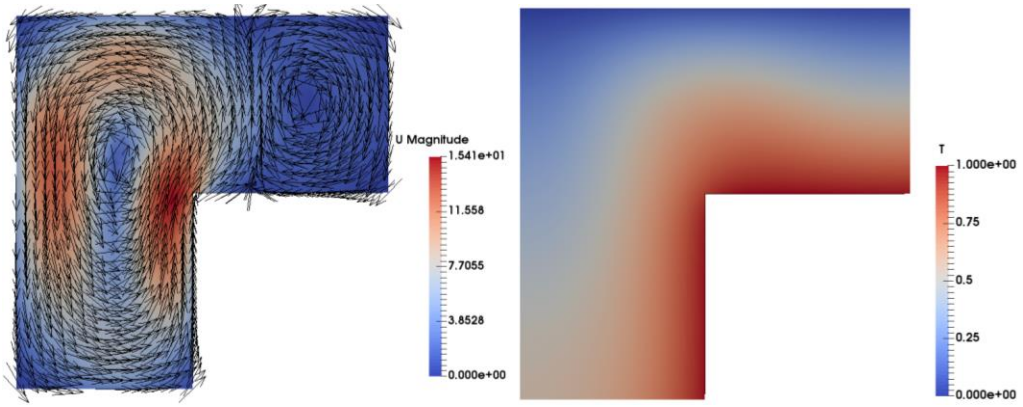

(a)

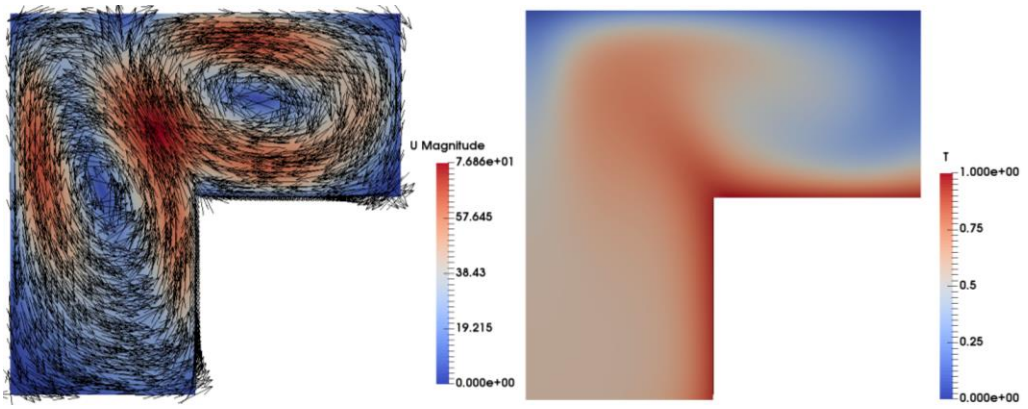

(b)

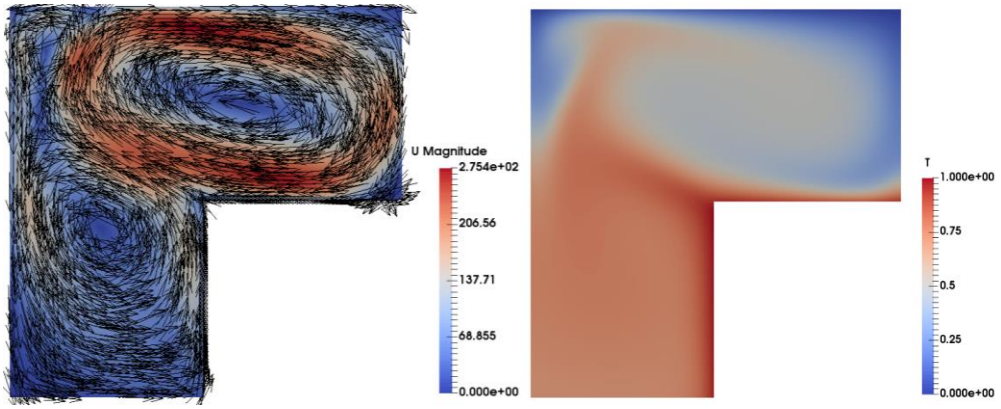

(c)

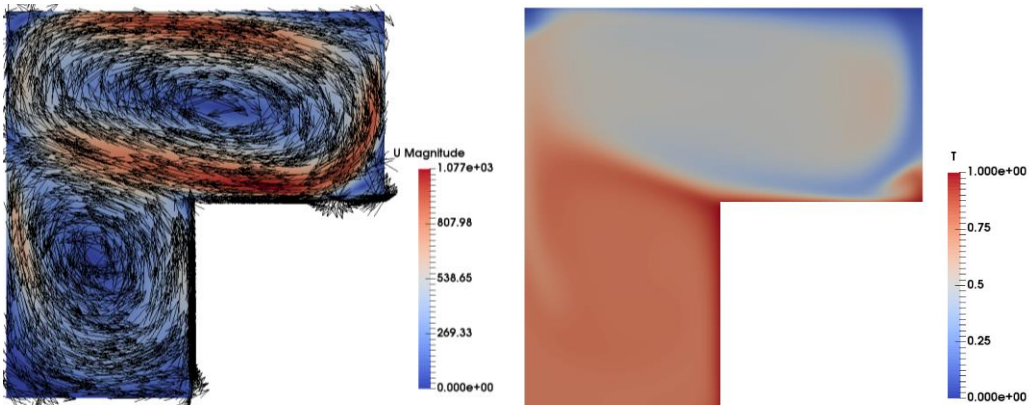

(d)

Figure 5.1: Snapshots of velocity field (left) and temperature distribution (right) for the case of pure buoyancy convection and cavity with adiabatic bottom wall: a) $Ra=10^4$, b) $Ra=10^5$, c) $Ra=10^6$, d) $Ra=10^7$.

5.1.1 Patterning Behaviour for the cavity with adiabatic floor

Most conveniently, first the cases with adiabatic floor are discussed for different values of the Rayleigh number and then examine the differences produced by an increase in the buoyancy effect due to a change in the thermal boundary condition.

As quantitatively substantiated by Figures 5.1-5.3, a growth of the (non-dimensional) velocity can be noticed for all cases as *Ra* becomes higher. Very interesting modifications, however, can also be spotted in terms of *structure of the flow* (i.e., morphology and extension of the rolls or vortices) established inside the cavity and related temporal behaviour (i.e., evolution in time).

Along these lines, it is appropriate to begin from the simple remark that the velocity magnitude pattern within the cavity is very similar for $Ra=1x10^3$ (not shown)and $Ra=1x10^4$ (Fig. 5.1(a)). Indeed, for both values of the Rayleigh number the flow is steady and one main oval-shaped vertical velocity roll is formed. This roll develops in the lower third of the cavity (between the left sidewall and the vertical side of the step) and extends vertically into the upper section of the fluid domain. The highest velocity area is located on the right-hand side of the roll near the top left corner of the obstruction (the step). As evident in Fig. 5.1(a), the highest temperature occurs in the region surrounding the step (where, as expected, a relatively thick thermal boundary layer is established) and the temperature then gradually decreases towards the floor, the left-hand side wall and the ceiling of the cavity.

Interestingly, for $Ra=1x10^5$ (Fig. 5.1(b)) the complexity of the velocity field increases as two oval-shaped convection rolls having a comparable magnitude can be seen at the same time. The flow is still steady and one roll is confined in the upper portion of the domain (it is located above the step), while the other originates from the lower third of the cavity. It can also be noticed that for this value of *Ra*, the temperature changes occurring in proximity to the step become much more pronounced. A thin thermal (hot) boundary layer, clearly recognizable, develops along the horizontal heated wall of the obstruction and along its vertical heated wall (the two sides of the step). A thermal (cold) boundary layer is also formed close to the top (cooled) wall. Moreover, a mushroom like shape plume appears in the cavity originating from the left corner of the step and protruding towards the left top corner (plume oriented along a diagonal direction).

For $Ra=1x10^6$ (Fig. 5.1(c)), the boundary layers become even more pronounced (which is in agreement with known scaling laws, see, e.g., (Napolitano, 1982; Lappa, 2011). Similarly, the stem of the plume is narrower than in the previous situation. Moreover, it can be seen that a secondary plume originates from the main plume cap.

The most striking difference with respect to the previous cases, however, is the nature of the flow, which *becomes time-dependent*. A related frequency spectrum analysis (performed using the signal of a ‘numerical probe’) can be seen in Fig. 5.2. From this it could be infered that this is a time-periodic case in which all the frequencies are multiples of a fundamental one.

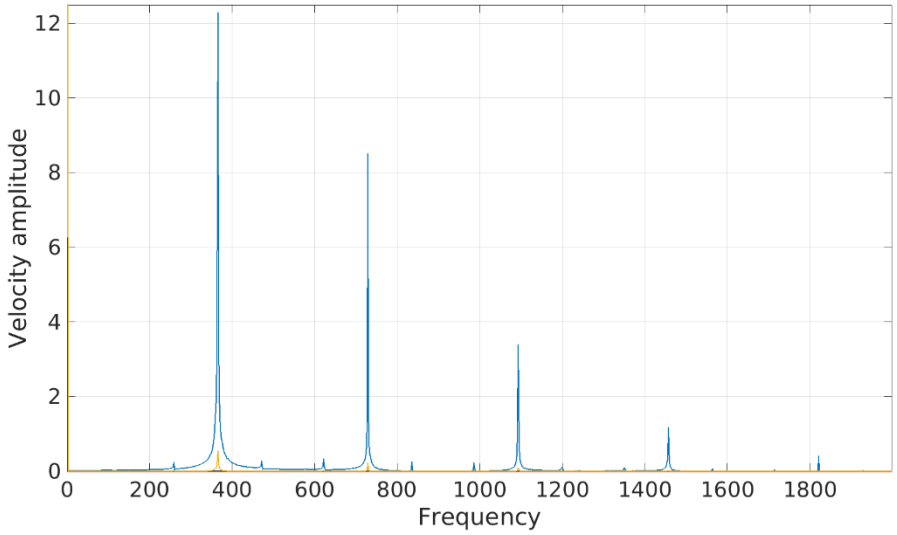

Figure 5.2: Frequency Spectrum (distribution of velocity amplitude for Ra=1x10^6, closed cavity with adiabatic floor, signal probe located at x=0.25 and y=0.75).

If the Rayleigh number is increased to Ra=1x10^7 (Fig. 5.1(d)), the pattern is relatively similar to that already seen for Ra=1x10^6. However, a very narrow stemmed, almost horizontal plume extends from the top left-hand corner of the object to the left-hand wall. Below the stem of the plume the fluid occupying the lower section of the cavity has a relatively high temperature (that decreases gradually towards the left hand while still remaining relatively high). This indicates that the peculiar circulation pattern established inside the fluid domain for this value of the Rayleigh number tends to create a *heat island* in its entire lower half. The heat released in the fluid by the vertical heated wall of the step cannot be transferred to the upper part of the cavity and tends to accumulate in the lower part causing an increase in the local temperature. The situation is clearly different in the upper domain where the heat released in the fluid by the horizontal heated wall can convectively be transferred to the top (cold) wall where it is extracted from the cavity. The frequency spectrum for this case (not shown), however, confirms that the flow is still time-periodic (the reader being referred to Sect. 5.1.4 for a discussion of the case Ra =1x10^8).

The values of the Nusselt number corresponding to all these situations can be found in Table 5.1 (where it is shown that the intensity of heat exchange between the surface of the step and the fluid increases as the Rayleigh number becomes higher). Interestingly, the set of values reported there also indicates that the mechanism of the Hadley type described in Sect. 1.1.4.2 (being operative near the vertical side of the step) is much more efficient in transporting heat than that due to a heating-from-below condition at work along the horizontal side of the step (this finding being in line with other studies where square cavities with a heated plate built in vertically or horizontally or with a finned heated plate were considered, see, e.g., Oztop et al. (2004);

Saravanana et al. (2008); Saravanan and Sivaraj (2015); Nadjib et al. (2018); this concept will be further discussed in Sect. 5.1.3).

5.1.2 Patterning Behaviour for the cavity with isothermal (hot) floor

Having completed a sketch of the different situations which are established inside the cavity with the step for the case with adiabatic bottom wall, the other fundamental situation is now examined where the bottom wall is kept at constant temperature (heated wall, see Table 5.2). Most of these cases are summarized in Fig. 5.3.

For $Ra \leq 1x10^4$, the flow field descriptions already given for the adiabatic cases are more or less applicable to the hot floor cases. Appreciable differences, however, can be identified in the temperature field. In the hot floor case (see the right frames of Fig. 5.3), a relatively high temperature region is established where the floor of the cavity meets the vertical side of the step. In practice, a continuous hot boundary layer develops along all the heated surfaces. It consists of two horizontal branches and one vertical branch. A cold boundary layer can also be seen at the ceiling of the cavity. Increasing the Rayleigh number to $Ra=1x10^5$ (Fig. 5.3(b)) leads to a decrease in the thickness of the temperature boundary layers at the ceiling and the floor of the cavity and at the side and top of the step. Moreover, for this value of *Ra* (Fig. 5.3(b)) a recognizable plume begins to form at the top left-hand corner of the step (protruding towards the top left-hand corner of the cavity).

Table 5.2: Cases examined for the case of pure buoyancy convection with hot bottom wall.

Ra	Mesh Size	Nu_{step}^{horiz}	Nu_{step}^{vert}	Regime
10^3	40x40	≅1	2.41656	Steady
10^4	40x40	1.279432	2.0596	Steady
10^5	80x80	3.12286	5.49028	Steady
10^6	150x150	4.2792	9.72496	Steady
10^7	270x270	6.05596	15.14134	Steady
10^8	500x500	≅12.25 (average)	≅25.53 (average)	Weakly Turbulent

Though these patterns, with the exception of the additional branch of thermal boundary layer formed along the bottom wall, may be considered relatively similar to those already described for the other boundary condition, however, distinguishing features can be highlighted for $Ra=1x10^6$ in terms of structure of the flow field (Fig. 5.3(c)). Two almost symmetrical counter-rotating circular shaped rolls develop in the upper half of the cavity. At the same time, two other

circular shaped velocity rolls develop in the lower half of the cavity. A very complex multi-cellular flow emerges with the maximum velocity magnitude being attained where the rolls meet in the upper half of the cavity.

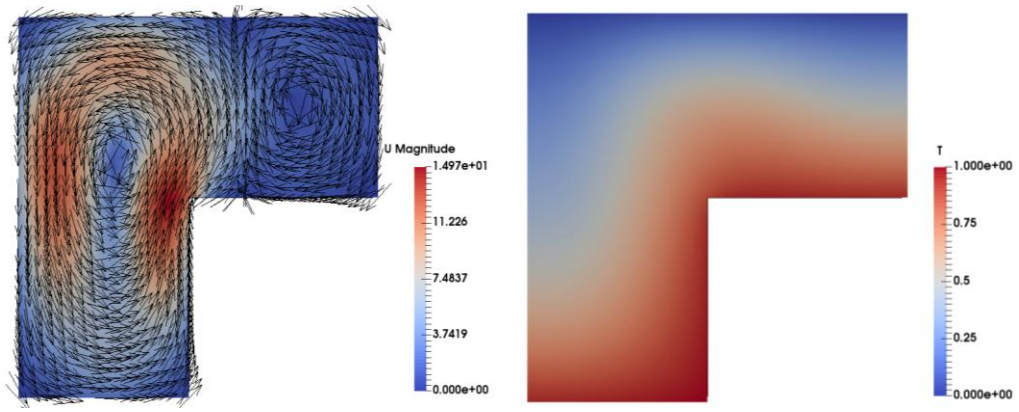

(a)

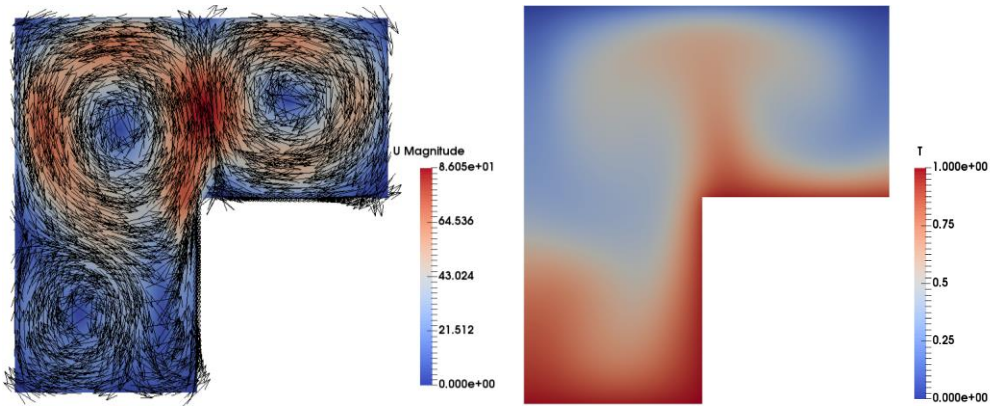

(b)

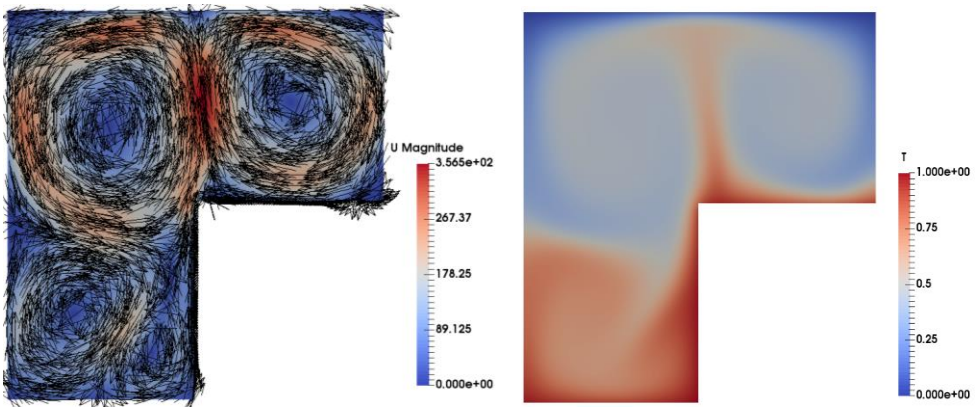

(c)

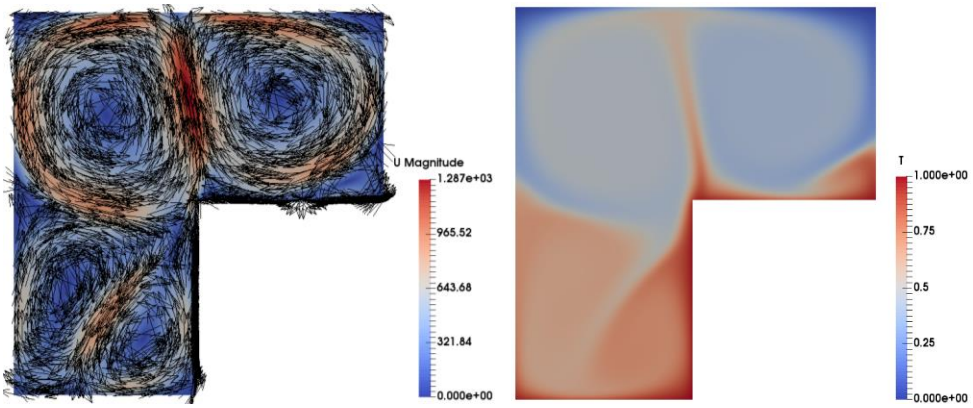

(d)

Figure 5.3: Snapshots of velocity field (left) and temperature distribution (right) for the case of pure buoyancy convection and cavity with hot bottom wall: a) $Ra=10^4$, b) $Ra=10^5$, c) $Ra=10^6$, d) $Ra=10^7$.

Apart from the notable departure from the corresponding situation shown in Fig. 5.1(c) in terms of flow structure, other remarkable modifications concern the temperature field. The thermal plume, which in the case of adiabatic bottom was displaying an essentially *horizontal direction* (Fig. 5.1(c)), appears now with a main *direction rotated by 90 degrees*, i.e., it has an almost *vertical structure* (Fig. 5.3(c)). Moreover, the flow is steady (it was time-dependent for the case with adiabatic bottom).

When the Rayleigh number is increased to $Ra=1\text{x}10^7$ (Fig. 5.3(d)), most surprisingly, the flow is still steady. Four velocity rolls are developed like those seen for $Ra=1\text{x}10^6$.

For all these cases, interestingly, a second rising hot plume is established along the left wall of the cavity (not present when the bottom wall is adiabatic).

5.1.3 Heat Exchange and related trends

Notably, direct comparison of the information reported in Tables 5.1 and 5.2 can be used to get interesting insights into the impact exerted by the different thermal boundary condition assumed for the bottom floor on the emerging dynamics. Indeed, it can be seen that the mechanisms of heat exchange being operative along the sides of the step sensitively depends on the type of bottom floor. The magnitude of heat exchange along the vertical side of the obstruction tends to decrease when the bottom floor is heated, which is a relatively counter-intuitive finding.

In practice, an explanation for this trend can be elaborated in its simplest form on the basis of the argument that the magnitude of heat removal largely depends on the specific structure of the velocity field, and that this structure is more favourable to heat exchange when the bottom floor is adiabatic (as in this case a significant amount of fluid can be transported towards the upper side of the step due to the existence of a single roll occupying the entire lower half of the cavity).

In such a context, it is also worth highlighting that Nu_{step}^{vert} for the cavity with the adiabatic floor (Table 5.1) follows almost exactly the scaling law for the classical Hadley flow in an

unobstructed square cavity, i.e. $Nu \cong 0.13 \times Ra^{0.31}$ (see, e.g., Yu et al. 2007; Corvaro and Paroncini 2007), which is in line with the considerations elaborated above about the presence of a single roll on the left of the vertical hot side of the step (resembling the classical Hadley flow which would be established in a classical square cavity with no step inside). As reported in Table 5.2, Nu_{step}^{vert} takes slightly smaller values when the hot floor is considered (with respect to the adiabatic case) for relatively high values of *Ra*, which can be ascribed to the aforementioned presence of a secondary roll developing in the lower half of the cavity (able to cause a decrease in the amount of fluid being transported upwards along the vertical face of the step).

Another outcome of the focused comparison of Table 5.1 and 5.2 is the realization that regardless of the thermal condition implemented for the bottom floor, Nu_{step}^{horiz} is always smaller than Nu_{step}^{vert}. This trend is relatively counterintuitive if one considers that in the light of existing studies for the pure Rayleigh-Bénard flow (see, e.g., Stevens et al. 2010), the Nusselt number should take values much higher than those reported in these tables and display a $\cong Ra^{\gamma}$ scaling with $2/7<\gamma<1/3$).

The key to understanding these results lies in considering that the region located above the step (though it is heated form below and cooled from above) *does not behave as a pure RB system*. This is clearly witnessed by the lack of small scale thermal plumes, which one would expect for $Ra \geq O(10^6)$. Even for $Ra=10^7$ no small scale plumes can be seen in the present case, see Figs. 5.3. By contrast, for *pure* RB flow and high values of *Ra*, the flow is known to display the pervasive presence of small-scale plumes, continuously produced at the heated or cooled boundaries, which can later detach from such boundaries and have a two-fold remarkable effect: 1) contribute to increase the Nusselt number at the walls (see, e.g., Stevens et al. 2010), 2) support the overall erratic dynamics in the bulk of the fluid (see, e.g., Lappa, 2011). As shown by the present results, such a mechanism is suppressed in the presence of an extended (hot) vertical surface in favour of large scale plumes originating from such surface or related hot corners.

5.1.4 The progression towards Chaos

Another (separated) discussion is needed for the values of the Rayleigh number required to produce a transition from the steady solution to a time-periodic (single frequency) state for the two fundamental situations corresponding adiabatic and isothermal bottom wall.

According to the results for the adiabatic floor case obtained by parametrically varying the Rayleigh number (Table 5.1, Sect. 5.1.1), a *Hopf bifurcation* i.e., transition from stationary to oscillatory conditions should obviously take place somewhere in the range between $Ra= 10^5$ and $Ra= 10^6$.

Dedicated simulations were performed to identify precisely such a value and it was found to be $Ra_{critical} \cong 6.1 \times 10^5$.

For the hot floor case (Sect. 5.1.2, Table 5.2), as the reader might have already realized at this stage, the transition is delayed to higher values of *Ra* (between $Ra= 10^7$ and $Ra= 10^8$, which is

yet a relatively counter-intuitive fact if one considers that the flow should be more energetic in these conditions given the additional source of buoyancy represented by the portion of bottom wall kept at constant (hot) temperature) It was found for this case that $Ra_{critical} \cong 1.1 \times 10^7$.
An interpretation of such counter-intuitive findings is not as straightforward as one would assume. A relevant explanation, however, can yet be rooted in the different nature and behaviour of buoyancy flow according to the direction of the prevailing temperature gradient that generates it and *the nature of the disturbances responsible for the first Hopf bifurcation, i.e., the transition from steady state to oscillatory flow*.
These flows can be very different in terms of structure and undergo a completely different hierarchy of bifurcations. As an example, while the critical Rayleigh number for the transition to oscillatory flow of classical RB convection (Sect. 1.1.4.1) in a square cavity heated from below, cooled from above and with vertical adiabatic walls is $O(10^5)$ in the case of air (Goldhirsch et al. 1989; Bouabdallah et al. 2016), the corresponding value for the case in which the cavity is rotated by 90° (differentially heated vertical walls and adiabatic horizontal boundaries) is $O(10^8)$ (Paolucci and Chenoweth, 1989; Le Quéré and Behnia, 1998). As also shown by other authors for the companion case of inclined systems (see, e.g., Lappa and Gradinscak, 2018, when vertical and horizontal temperature gradients are present at the same time as in the present case), the above-mentioned two types of convection (Hadley & RB) can interact in a relatively complex way and cause flow stabilization or destabilization depending on the prevailing effect.
In the light of all these arguments, further insights into the scenario revealed by the present numerical simulations are yielded in this section on the basis of a *direct analysis of the flow disturbances* (these disturbances have been obtained by subtracting the time-averaged velocity field to the instantaneous velocity).

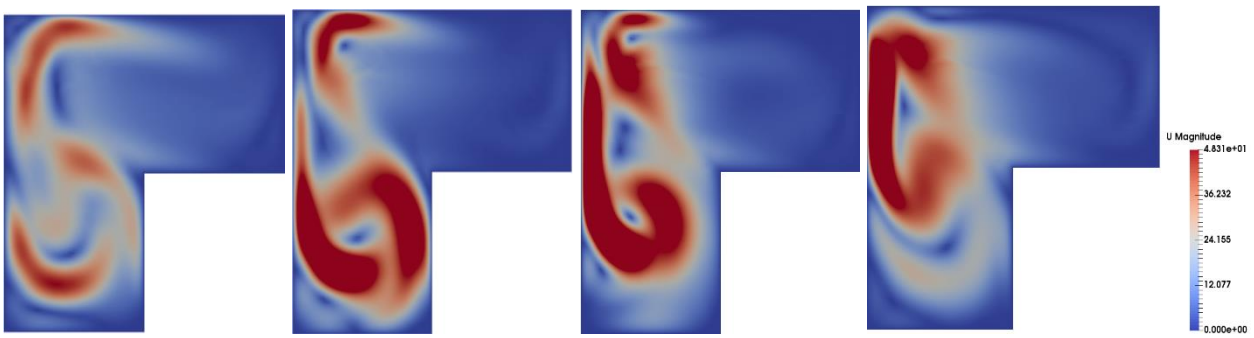

Figure 5.4: Four snapshots of velocity disturbances evenly spaced in time for the cavity with adiabatic floor, $Ra=1 \times 10^6$.

Notably, in Fig. 5.4 it can be seen that for the adiabatic floor case, disturbances behave as a spiralling wave travelling in the clockwise direction along the boundary including the left side of the step, the bottom, floor and the entire left sidewall of the cavity. Following a cyclic process, a velocity peak originates in proximity to the corner of the step, it is then transferred to the lower roll that transports it from the left side of the step to the left side of the cavity. The disturbance

then rises along the left wall until it reaches the left top corner where it is damped (giving rise to a new cycle).

As already reported in Sect 5.1.1, increasing the Rayleigh number to 10^7 does not substantially modify this mechanism. For Ra=1x10^8, however, a notable change in the temporal behaviour occurs. This is shown in Fig. 5.5. For this value of *Ra*, *a heat island* located in the lower half of the cavity is still a characteristic of the temperature pattern (Fig. 5.5(a)). However, as witnessed by Fig. 5.5(b), the frequency spectrum becomes much more complex (e.g., with respect to that seen in Fig. 5.2). It now displays a continuous interval of frequencies.

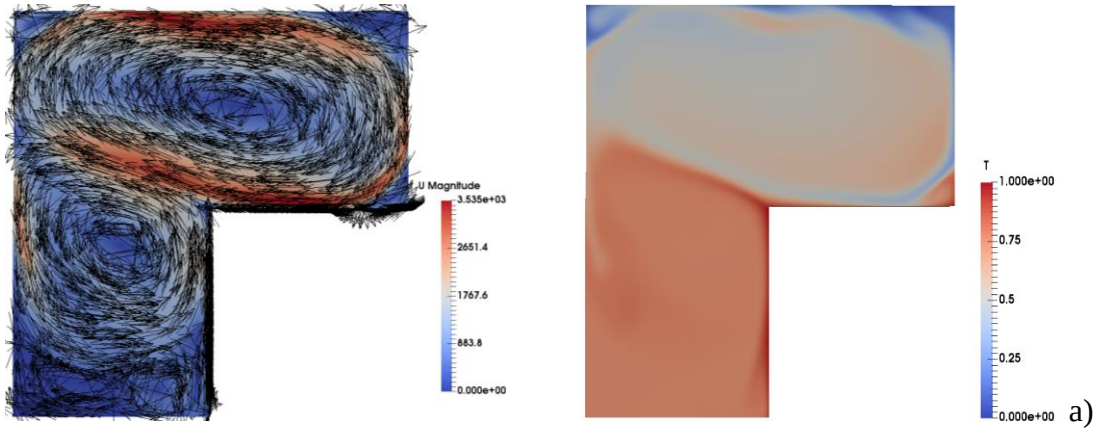

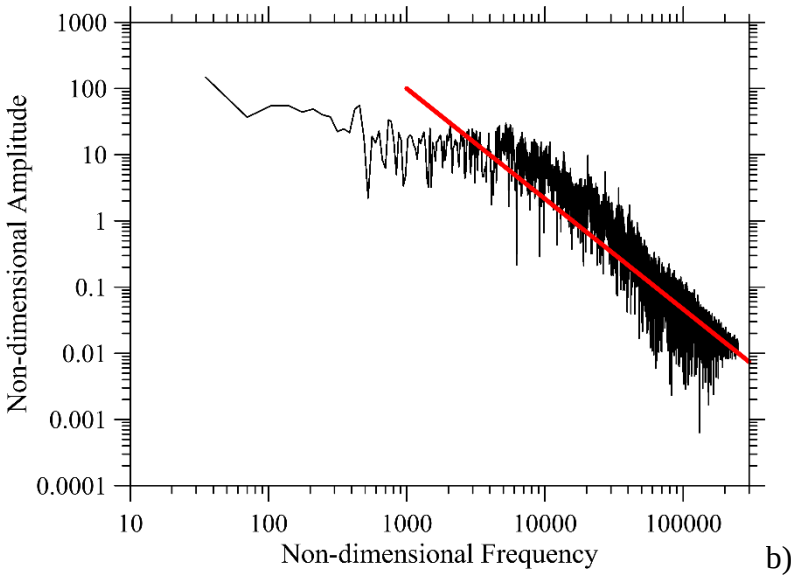

Figure 5.5: Pure buoyancy convection in the cavity with adiabatic bottom wall, Ra=1x10^8: (a) snapshot of velocity field (left) and temperature distribution (right), (b) frequency spectrum related to the velocity signal measured by a numerical probe located at x=0.25 and y=0.75 (the red line indicates the Kolmogorov scaling law).

Interestingly, it can also be seen that the frequency spectrum (frequency and related amplitude plotted using logarithmic scales for the axes) aligns to a good approximation with a $\omega^{-5/3}$ law in a certain range of frequencies (from $O(10^3)$ to $O(10^5)$, the reader being referred to the solid red line in Fig. 5.5(b)).

The key to understand these results lies in considering the well-accepted idea that, under certain length scales, fluid flow starts to behave following a universal (repetitive) behaviour. This physical intuition, originally elaborated by Kolmogorov (1941a,b,c), is nowadays known as the *inertial turbulence theory*; the related interval where the energy spectrum aligns with a -5/3 law is the so-called *inertial range of space scales* (where turbulence is homogeneous and isotropic (De et al. 2017, Kraichnan, 1974).

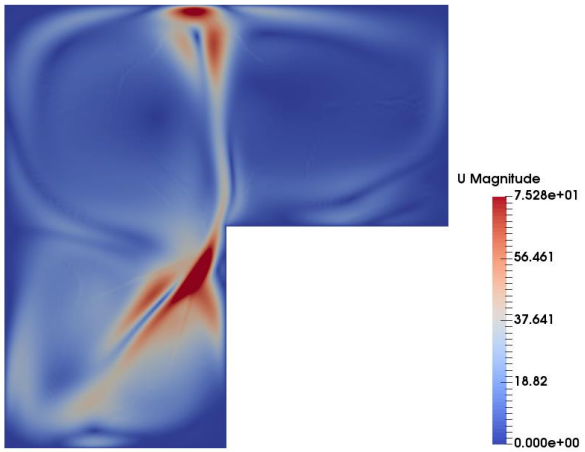

Figure 5.6: Snapshot of the velocity disturbances for the cavity with the hot floor, Ra=1.15x10^7.

The bifurcation scenario dramatically changes when the configuration with the hot bottom is considered. As shown in Fig. 5.6 for slightly supercritical conditions (Ra slightly larger than $Ra_{critical}\cong$1.1x10^7), the disturbances do not behave as a wave; rather they tend to be localized in the stem and cap of the vertical hot plume originating from the corner of the step and in the inclined descending plume of cold fluid (corresponding to the line of contact between the two rolls located in the lower part of the domain). While for the adiabatic-floor case (Fig. 5.4) a kinship may be identified with the typical disturbances known to affect the classical Hadley flow in unobstructed cavities (generally taking the form of waves travelling along the solid boundary, see, e.g., (Le Quéré and Behnia, 1998, see also the arguments provided in Sect. 1.1.4.2), this case should be regarded as a realization of the typical instabilities that can affect plumes in the IVND regime (Pera and Gebhart, 1971; Desrayaud and Lauriat, 1993; Cortese and Balachandar, 1993; Vincent and Yuen, 1999; Majumder et al. 2004). These instabilities are generally induced by the horizontal shear in the bulk of the fluid (which can take relatively high values for the conditions considered in the present work, especially in proximity to the stem of the plumes originating from the corner of the step).

Put simply, Fig. 5.6 reveals that the mechanism for the transition from steady to time-dependent conditions can sensitively depend on the type of thermal conditions considered for the bottom floor. Indeed, the main cause of the bifurcation is transferred from the boundary-layer mechanism seen in Fig. 5.4 for the adiabatic floor to the thermal-plume driven one for the situation with the isothermal hot floor.

As a concluding remark for this section, it is important to highlight that also for this boundary condition, the frequency spectrum can be made more involved on increasing further *Ra* (as illustrated in Fig. 5.7).

As the reader will realize by inspecting this figure, some differences can be noticed with respect to Fig. 5.5 (owing to the different mechanisms responsible for the excitation of oscillatory flow, the spectrum is more energetic). Nevertheless, the amplitudes still align to a good approximation with the aforementioned Kolmogorov law over a limited range of frequencies, representative of the universal behaviour taken by turbulence on the small scales (Lappa and Gradinscak, 2018).

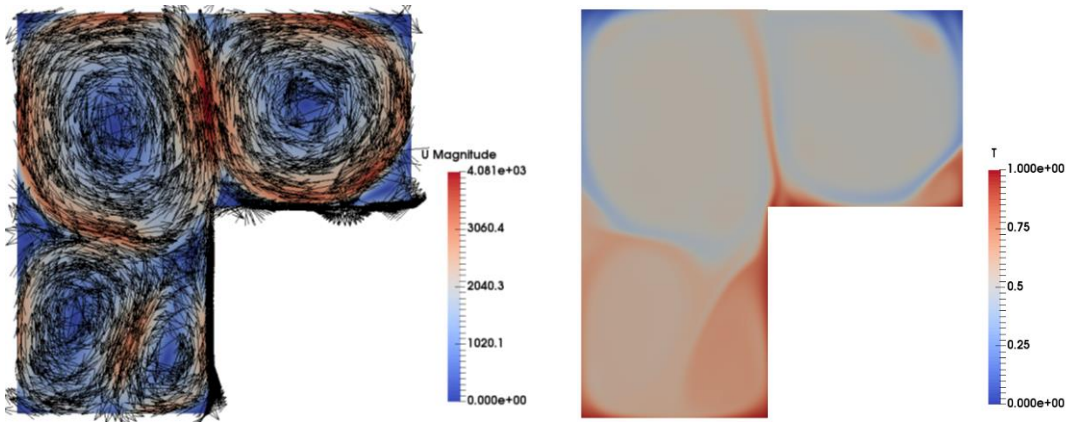

a)

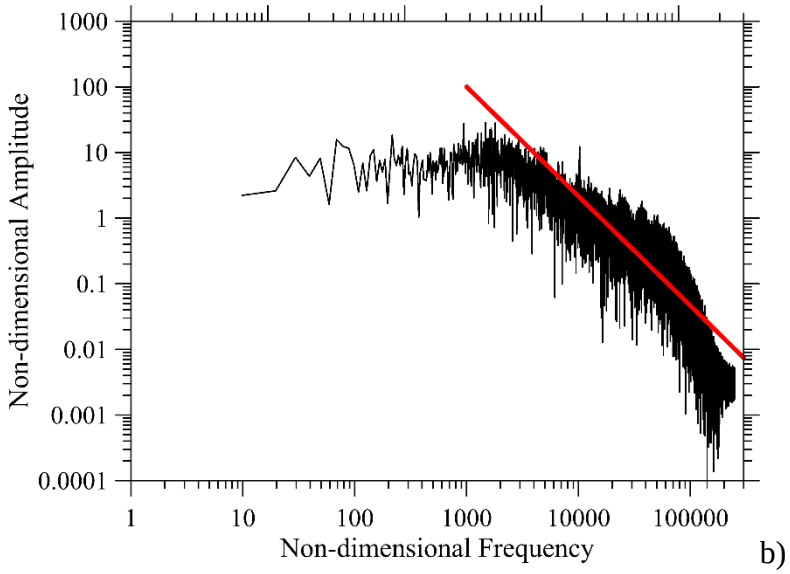

Figure 5.7: Pure buoyancy convection in the cavity with hot bottom wall, Ra=1x10^8: (a) snapshot of velocity field (left) and temperature distribution (right), (b) frequency spectrum related to the velocity signal measured by a numerical probe located at x=0.25 and y=0.75 (the red line indicates the Kolmogorov scaling law).

5.2 Cavity with coaxial inflow and outflow sections

The foregoing discussion has deliberately been limited to illustrating the dynamics for pure buoyancy convection. The present section continues this inquiry by probing the additional role played by forced convection (due to cold fluid being injected through an inflow section located on the left sidewall). Our specific aim in this regard is to assess the changes experienced by convection, its route to chaos and related patterning scenario in the presence of forced flow over the same range of values of the Rayleigh number considered in the preceding section for a fixed value of the Richardson number (*corresponding to buoyant and forced flow having a comparable strength or intensity*), i.e., Ri=1. For the purpose of quantifying these effects, the same two alternate configurations already examined in Sect. 5.1 are considered, i.e., the case in which the bottom wall of the cavity is adiabatic or kept at a fixed temperature. Several interesting effects can be spotted accordingly in term of the behaviour of the flow and temperature distribution. For consistency with the approach already undertaken in Sect. 5.1, first the numerical simulations conducted for the adiabatic floor are described and afterwards the second case is discussed

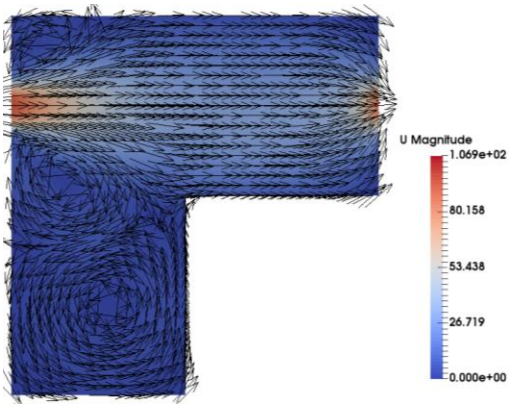
U Magnitude
1.069e+02
80.158
53.438
26.719
0.000e+00

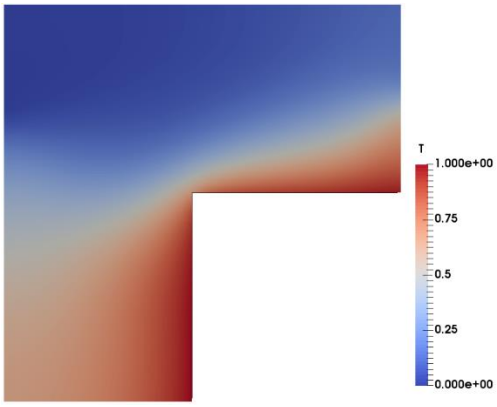
T
1.000e+00
0.75
0.5
0.25
0.000e+00

(a)

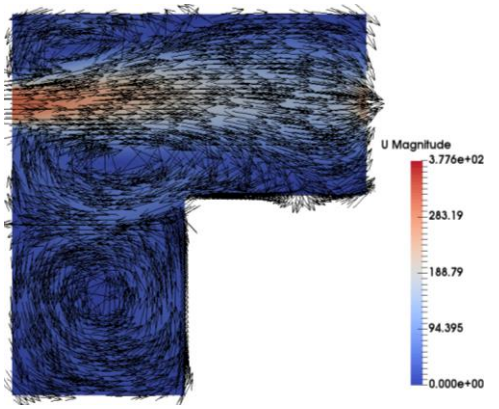
U Magnitude
3.776e+02
283.19
188.79
94.395
0.000e+00

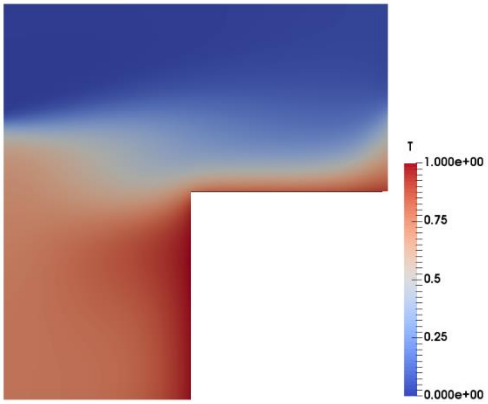
T
1.000e+00
0.75
0.5
0.25
0.000e+00

(b)

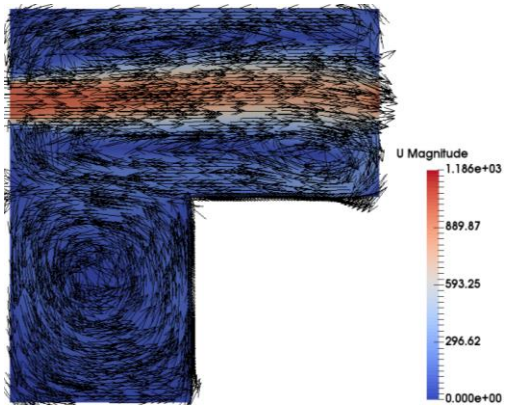
U Magnitude
1.186e+03
889.87
593.25
296.62
0.000e+00

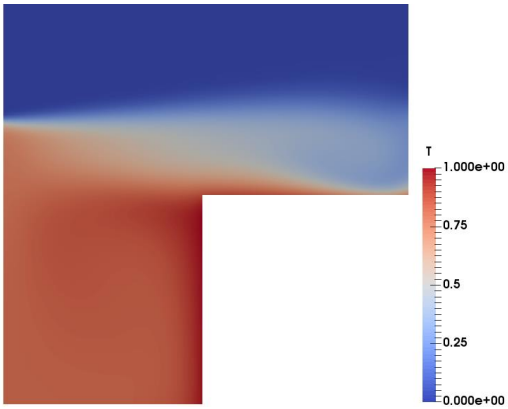
T
1.000e+00
0.75
0.5
0.25
0.000e+00

(c)

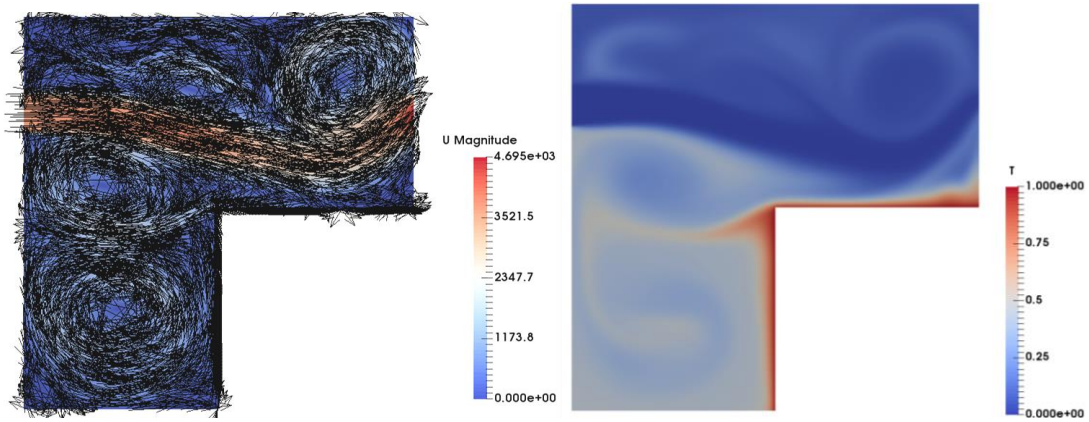

(d)

Figure 5.8: Snapshots of velocity field (left) and temperature distribution (right) for the case of hybrid forced/buoyancy convection (*Ri*=1), coaxial inflow and outflow sections and cavity with adiabatic bottom wall: a) $Ra=10^4$, b) $Ra=10^5$, c) $Ra=10^6$, d) $Ra=10^7$.

Table 5.3: Cases examined for hybrid forced/buoyancy convection (*Ri*=1), coaxial inflow and outflow sections and cavity with adiabatic bottom wall.

Ra	Mesh Size	Nu_{step}^{horiz}	Nu_{step}^{vert}	Regime
10^4	40x40	2.69812	4.88732	Steady
10^5	80x80	2.08836	7.02482	Steady
10^6	120x120	2.1104	13.18764	Steady
10^7	270x270	≅16.7 (average)	≅34.2 (average)	Moderately Turbulent

Following a logical process, with systems of increasing complexity being described as the discussion progresses, the analysis begins from the simplest case, namely, that shown in Fig. 5.8(a) ($Ra=1x10^4$). One velocity roll, mainly of buoyancy nature is formed in the lower portion of the cavity (oriented in the counter-clockwise sense in the figure). It can also be seen that the stream (jet) of cold fluid entering through the inlet spreads itself in the vertical direction and forms a nozzle-like structure in the upper part of the cavity (Fig. 5.8(a)). This structure is maintained up to the outlet. In proximity to the inflow section, a secondary (minor) roll develops between this current and the aforementioned main roll of buoyancy nature. The fluid attains its highest velocity at the inlet and the outlet. Moreover, relatively high temperature regions are located in proximity to the vertical and horizontal wall of the step. The flow is steady.

For $Ra=1x10^5$ (Fig. 5.8(b)), the velocity field is more complex. An increase in *Ra* and Re at fixed *Ri* obviously causes a rise of the magnitude of velocity. Interestingly, two main rolls exist in this situation. The first roll (square shaped) has a larger extension and it is located in the bottom portion of the cavity (yet it could be argued it is essentially of buoyancy nature as the fluid rises

along the heated wall of the step). The second roll, relatively smaller, is located just above the mid-plane of the cavity and it is slightly elongated in the horizontal direction. It can be noticed that the 'nozzle-like' streamline structure that was formed for Ra=1x10^4 is disturbed in this case owing to the formation of this roll (which tends to alter the flow directed form left to right and to prevent it from spreading freely in the vertical direction). The fluid enters from inlet with a high velocity, it continues to travel straight and then starts to spread after it has passed the middle portion of the cavity. In Fig. 5.8(b) it is also evident that the heat is accumulated entirely in the lower portion of the cavity due to the amount of heat laterally released from the hot step and the scarce mixing occurring between the fluid located in the upper and lower portions of the cavity. This develops a *heat island* in the entire lower half of the cavity. This island partially protrudes into the upper portion of the cavity near the inflow section owing to the presence of the aforementioned second roll. Moreover, a relatively thick horizontal thermal boundary layer is formed above the hot step. The flow is steady.

Continuing with the description of the modifications induced by an increase in *Ra*, for Ra=1x10^6 (Fig. 5.8(c)) the temperature distribution is very similar to the previous situation with a *heat island* still present in the entire lower half. In this case the *horizontal return flow* parallel to the main jet (warm fluid moving from left to right along the top surface of the step) also contributes to this effect. The flow is still steady.

On increasing the Rayleigh number to Ra=1x10^7 (Fig. 5.8(d)), however, a marked change is produced, i.e., the emergence of three equally sized velocity rolls. The first one is formed in the lower portion of the cavity as a result of buoyancy (fluid rising along the vertical wall of the step). Another one forms close to the ceiling in the upper portion of the cavity due to the combined effect of buoyancy and fluid flowing from the inflow section towards the outflow section. Remarkably, it causes a disruption in the straight movement of the fluid entering from the inlet. Notable changes can also be spotted in the case of temperature field (Fig. 5.8(d)). *The heat island occupying the lower half in the previous cases disappears* and only a hot thin boundary layer can be spotted along the vertical wall and a thicker one along the horizontal wall of the step. The flow is relatively turbulent in this case as shown by the frequency spectrum in Fig. 5.9. Interestingly, it aligns with the Kolmogorov law over a range more extended (from O(10^3) to O(10^6)) than that seen for the corresponding configuration with no inflow and outflow sections (which explains why it is referred to as 'moderately turbulent' in Table 5.3).

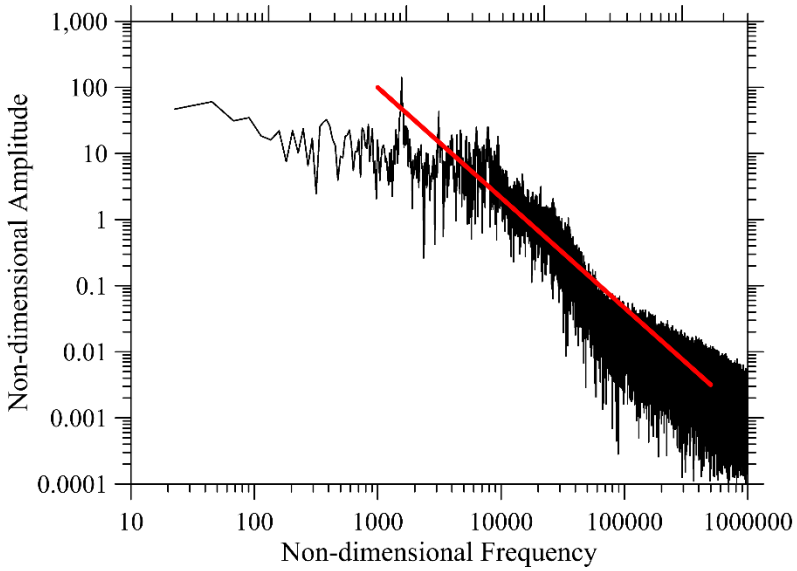

Figure 5.9: Hybrid convection in the cavity with adiabatic bottom wall, Ra=1x10^7: (a) frequency spectrum related to the velocity signal measured by a numerical probe located at x=0.25 and y=0.75 (the red line indicates the Kolmogorov scaling law).

Following up on the previous point about the suppression of the heat island effect, such change can be ascribed to the topological bifurcation displayed by the stream of cold fluid entering the cavity from the left. As shown in Fig. 5.8(d), owing to the presence of a new vortex (located just under the inflow section and driven by the joint effects of forced and buoyancy convection) such a stream breaks into two branches before reaching the step and the lower stream is routed into the lower domain, thereby strongly contributing to mitigate the temperature in that area. Moreover, it can be seen that, since the main horizontal jet originating from the inlet is distorted and impinges on the top surface of the obstruction, the aforementioned 'return flow' transporting heat from the entire top surface of the step directly into the left region is suppressed.

Notably, another way to somehow interpret all these results is to take a look at Table 5.3 and focus on the behaviour of the Nusselt number. The most striking variation indeed occurs for Ra=1x10^7, for which a notable change can be seen in the relative importance of Nu_{step}^{horiz} and Nu_{step}^{vert} (Nu_{step}^{horiz} = 15% and 50% of Nu_{step}^{vert} for Ra=10^6, and Ra=10^7, respectively). In particular, the parameter Nu_{step}^{horiz} jumps from a value ≅2 for Ra=10^6 to ≅17 for Ra=1x10^7.

An interpretation for this fascinating trend can easily be elaborated considering again the flow topological arguments provided above. A close look at Fig. 5.8(d), indeed reveals that what sets this specific value of the Rayleigh number apart from the other cases considered earlier is the fact that, after being split into two main branches (the lower one being funnelled into the lower domain as explained before), the upper branch of cold fluid originating from the inflow section directly hits the top surface of the step thereby strongly contributing to the heat exchange there.

Cross comparison of Table 5.3 with Table 5.1 is also instructive as it shows (as expected) that replacing a top wall steadily maintained at a cold temperature with a limited amount of cold fluid being injected into the cavity per unit time at $Ri \cong 1$, makes the heat removal process from the step horizontal wall less efficient for moderate values of *Ra* (obviously this observation only applies to the specific flow rate considered in the present work, additional studies being required in the future to parametrically investigate the effect of the non-dimensional size of the inflow and outflow sections).

Now the other case is examined in which the floor is kept at a constant temperature (Table 5.4). For $Ra=1\text{x}10^4$ (Fig. 5.10(a)) the flow pattern is almost the same already seen before with a slight difference in the structure of the rolls. It can be noticed in the velocity field that the size of the velocity roll close to the bottom is relatively smaller with respect to the case with adiabatic floor and it is unable to take a square like shape. To justify this behaviour, it is convenient to start from the simple remark that the buoyant effect due to heating from below now directly contributes to the secondary roll located in proximity to the inflow section. As a result, it tends to become larger and expand into the lower region of the cavity.

Table 5.4: Cases examined for hybrid forced/buoyancy convection (*Ri*=1), coaxial inflow and outflow sections and cavity with hot bottom wall.

Ra	Mesh Size	Nu_{step}^{horiz}	Nu_{step}^{vert}	Regime
10^4	40x40	2.13828	4.96214	Steady
10^5	80x80	1.289478	7.0278	Steady
10^6	120x120	1.040622	13.22984	Steady
10^7	270x270	≅13.5 (average)	≅38.9 (average)	Moderately Turbulent

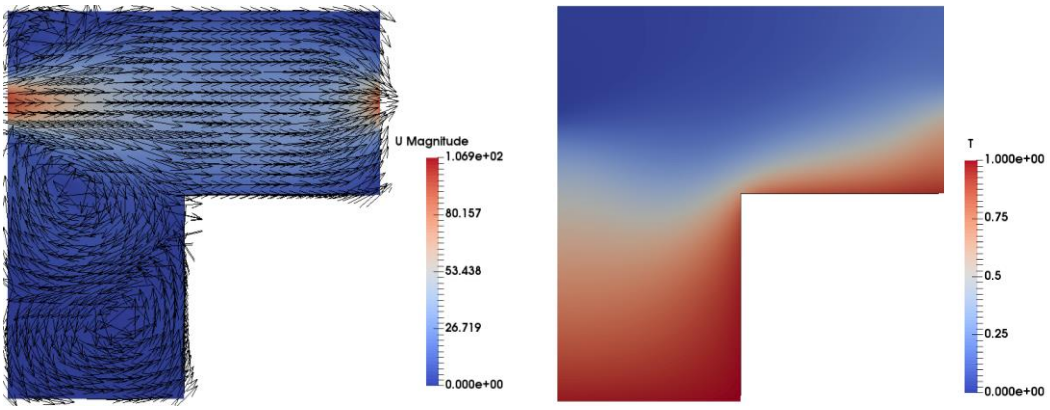

(a)

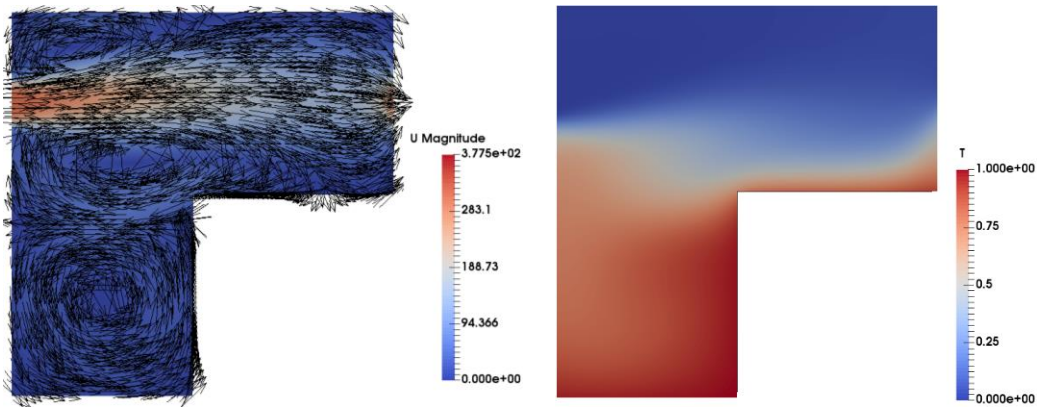

(b)

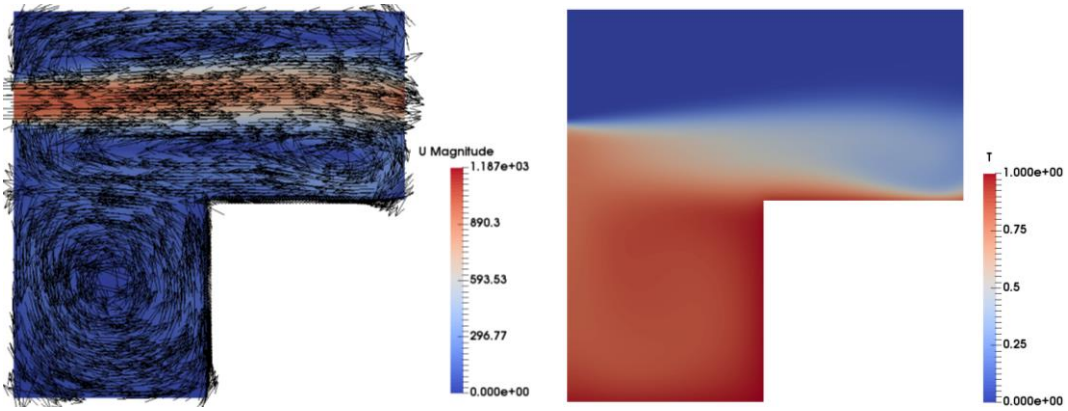

(c)

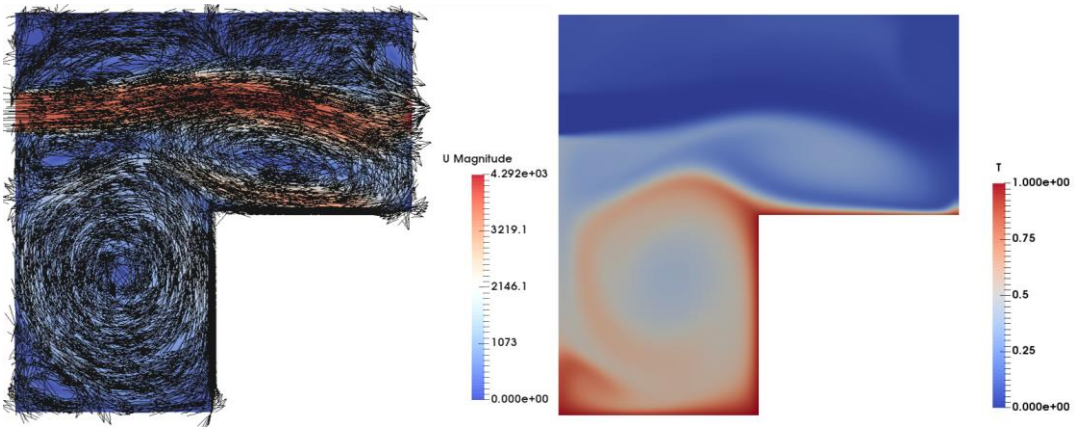

(d)

Figure 5.10: Snapshots of velocity field (left) and temperature distribution (right) for the case of hybrid forced/buoyancy convection (*Ri*=1), coaxial inflow and outflow sections and cavity with hot bottom wall: a) $Ra=10^4$, b) $Ra=10^5$, c) $Ra=10^6$, d) $Ra=10^7$.

For $Ra=1\text{x}10^5$ and $Ra=1\text{x}10^6$ (Fig. 5.10(b) and (c)) no significant differences can be highlighted in terms of the flow and temperature patterns as they are roughly the same as for the adiabatic floor case.

Once again, a significant departure, however, can be seen when $Ra=1\text{x}10^7$ is considered (Fig. 5.10(d)). Though in this case, the heat released by the top surface of the step can reach the left

region, the temperature in the lower portion is mitigated by the cold fluid entering the cavity. Indeed, part of this fluid is directly injected in the lower half due to the presence of a small eddy located in proximity to the inflow section (just under the main jet). Fluid motion is still moderately chaotic as witnessed by the time-velocity plot in Fig. 5.11.

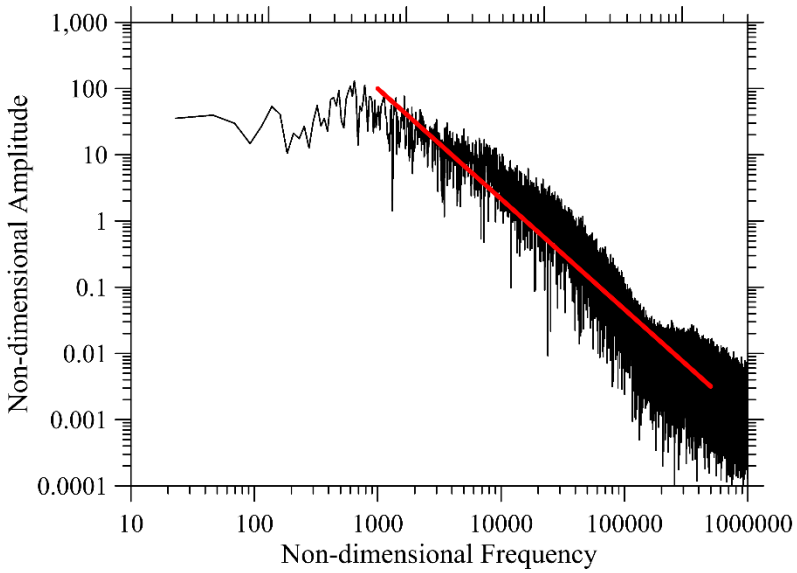

Figure 5.11: Hybrid convection in the cavity with hot bottom wall, Ra=1x10^7: (a) frequency spectrum related to the velocity signal measured by a numerical probe located at x=0.25 and y=0.75 (the red line indicates the Kolmogorov scaling law).

In order to clarify the evolution of these systems when the control parameter is increased, a calculation has been performed to precisely evaluate the critical values of the Rayleigh number for the transition from steady to time-periodic (single-frequency) flow. It was found to be $Ra_{critical}\cong$1.2x10^6 for both cavities with adiabatic and hot bottom wall, respectively.

The related disturbances are reported in Fig. 5.12. This figure is instructive as it shows that thermal boundary layers or plumes are no longer at the root of the instability mechanism. As a comparison of Fig. 5.12a and 5.12b with Figs. 5.4 and 5.6 would immediately reveal, disturbances are now located essentially in the right portion of the cavity and there is strong evidence for their essentially vertical-shear-driven nature (the interested reader being also referred to the similar studies recently carried out by Ali and Dey (2017) and Hemchandra et al. (2018).

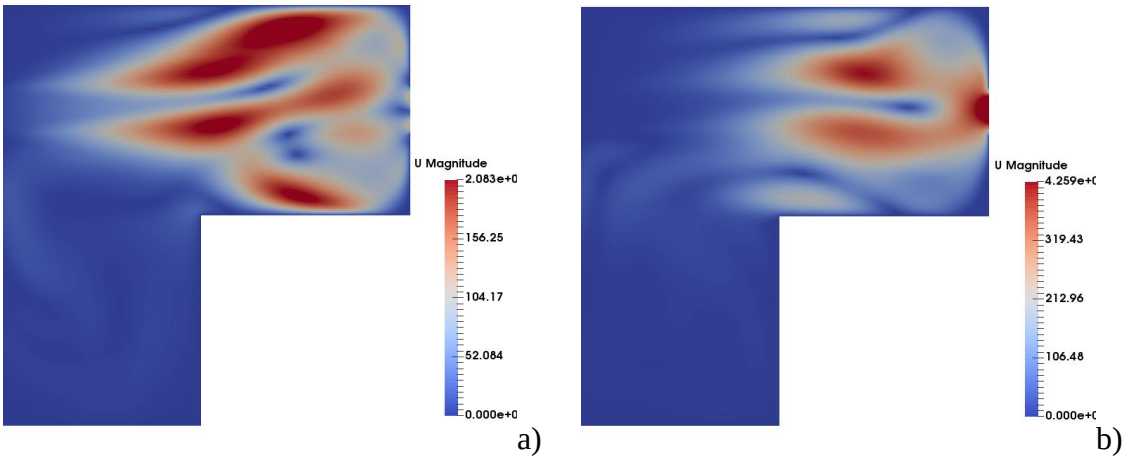

Figure 5.12: Snapshot of velocity disturbances for the case of hybrid forced/buoyancy convection (*Ri*=1), coaxial inflow and outflow sections: a) cavity with adiabatic floor, *Ra*≅1.25x10^6; b) cavity with hot floor, *Ra*=1.25x10^6

5.3 Cavity with misaligned inflow and outflow sections

Table 5.5: Cases examined for hybrid forced/buoyancy convection (*Ri*=1), misaligned inflow and outflow sections and cavity with adiabatic bottom wall.

Ra	Mesh Size	Nu_{step}^{horiz}	Nu_{step}^{vert}	Regime
1x10^4	40x40	6.93572	3.5079	Steady
1x10^5	80x80	12.09462	4.70892	Steady
1x10^6	120x120	21.0776	9.35676	Steady
1x10^7	270x270	≅40.3 (average)	≅31.6 (average)	Weakly Turbulent

After discussing in the previous section, the dynamics of hybrid forced-buoyancy convection as a result of cold fluid injection through an inflow section located on top of the left sidewall, the final case is addressed for which the inflow section is positioned relatively close to the floor. The relative height of the outflow section is not varied with respect to the previous analysis, i.e., it is located along the right wall in the upper part of the cavity (above the step at a certain distance from its horizontal surface).

Though this problem may be regarded as formally equivalent to that treated earlier, and the implemented change may appear as a minor variation, its effects can be dramatic, as further discussed in the remainder of this section (Figs. 5.13-5.16).

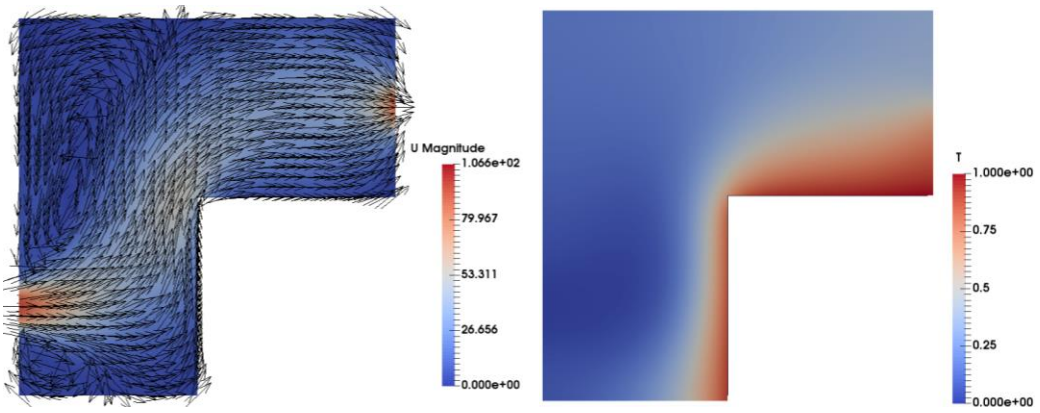
U Magnitude
1.066e+02
79.967
53.311
26.656
0.000e+00
T
1.000e+00
0.75
0.5
0.25
0.000e+00

(a)

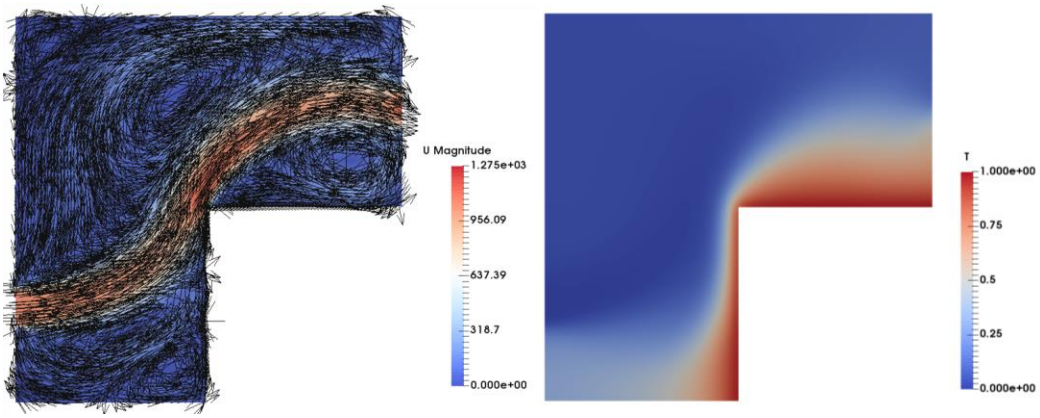
U Magnitude
1.275e+03
956.09
637.39
318.7
0.000e+00
T
1.000e+00
0.75
0.5
0.25
0.000e+00

(b)

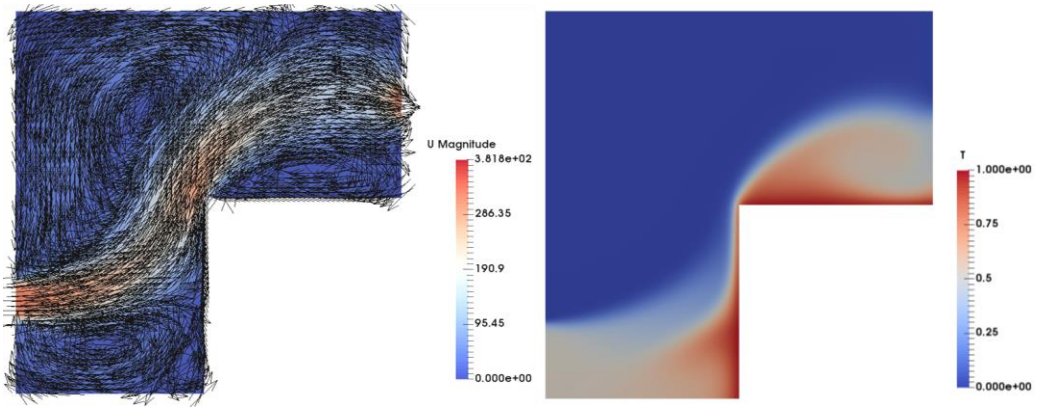
U Magnitude
3.818e+02
286.35
190.9
95.45
0.000e+00
T
1.000e+00
0.75
0.5
0.25
0.000e+00

(c)

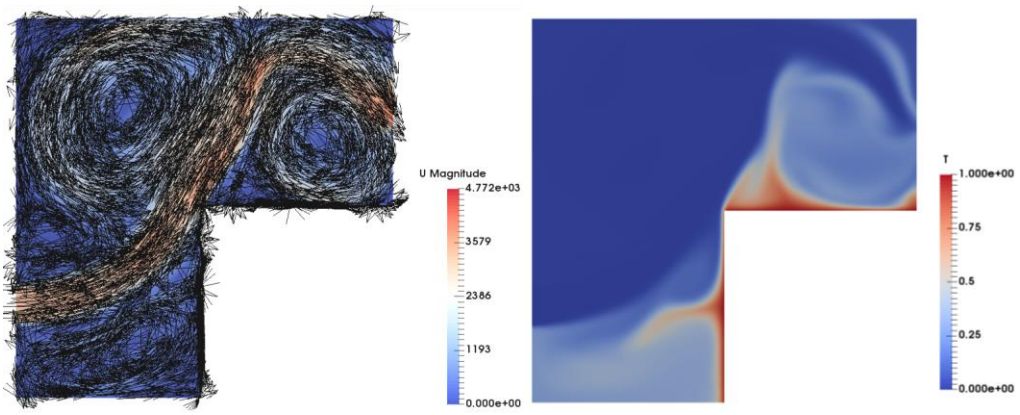

(d)

Figure 5.13: Snapshots of velocity field (left) and temperature distribution (right) for the case of hybrid forced/buoyancy convection (*Ri*=1), misaligned inflow and outflow sections and cavity with adiabatic bottom wall: a) $Ra=10^4$, b) $Ra=10^5$, c) $Ra=10^6$, d) $Ra=10^7$.

Since comparison of the emerging patterns for adiabatic and hot floor also provides important clues regarding the nature of the observed convective structures, the same approach is adopted based on a description of the former case followed by comparison with the latter (the impact of such a change on the patterning behaviour and evolution towards chaos is summarized in Figs. 5.13 and 5.15 for the case with adiabatic and isothermal (hot) floor, respectively).

As evident in Fig. 5.13(a), for $Ra=1x10^4$ and adiabatic bottom wall a small velocity roll (close to the floor) is formed in the lower portion of the cavity. The cold fluid enters the inlet with a relatively high velocity and continues to travel straight. It then deflected upward due to continuity effects (fluid must obviously turn around the step in order to reach the outflow section). In this process it is reinforced by buoyancy effects (which tend to propel the relatively warm fluid located in proximity to the vertical wall of the step upwards). It can be seen that the streamlines are relatively regular and give rise to a balloon like structure stretched in the vertical direction, which occupies most of the upper portion of the cavity. Thermal boundary layers are established close to the vertical and horizontal walls of the step, whereas the rest of the cavity is at a moderate temperature. The flow is steady.

Interestingly, for $Ra=1x10^5$ (Fig. 5.13(b)) the fluid entering the cavity through the inlet does not spread itself completely in the vertical direction. Indeed, the velocity field does no longer display a vertically stretched balloon like structure. Rather, while some of the fluid is forced out through the outflow section, a certain portion of it is reflected inwards and moves close to the adiabatic ceiling towards the left sidewall giving rise to an extended vortex. The fluid attains its highest velocity values at the inlet, close to the corner of the step and at the outlet.

For $Ra=1x10^6$ (Fig. 5.13(c)) no substantial changes can be seen in the structure of the velocity field with respect to $Ra=1x10^5$. Rather, what distinguishes this specific behaviour from the other ones discussed earlier is the increase in the magnitude of flow velocity and strength and vertical size of the roll located just above the step. This increase is indeed responsible for the emergence

of the characteristic curl-like shape taken by the thermal plume, which originates from the corner of the step and extends to the right. The flow is steady.

The roll located above the step is further strengthened when the case with Ra=1x10^7 is considered (Fig. 5.13(d)).

More importantly, as evident in Fig. 5.13(d), in this case the cold fluid entering the cavity from the left follows a slightly different path. While in the earlier situations, it was flowing along a parabolic route bringing it directly from the inflow section to the outflow one, it now rises continuously until it hits the ceiling (this leading to the formation of a vertically extended thermal plume originating from the corner of the step as evident in the figure). Only after it has collided with the ceiling, this jet can then move again downward and be absorbed by the outflow section. Like the cases treated in Sect. 5.2, the flow is relatively turbulent (see Fig. 5.14); some localized small eddies develop frequently along the vertical heated wall of the step as witnessed by the presence of small plumes originating from this wall in a direction perpendicular to it (towards the left). Nevertheless, direct comparison with the equivalent case with aligned inflow and outflow sections reveals that in the present case the inertial range is less extended (shifted to the right of 10^4, this observation will be analysed later).

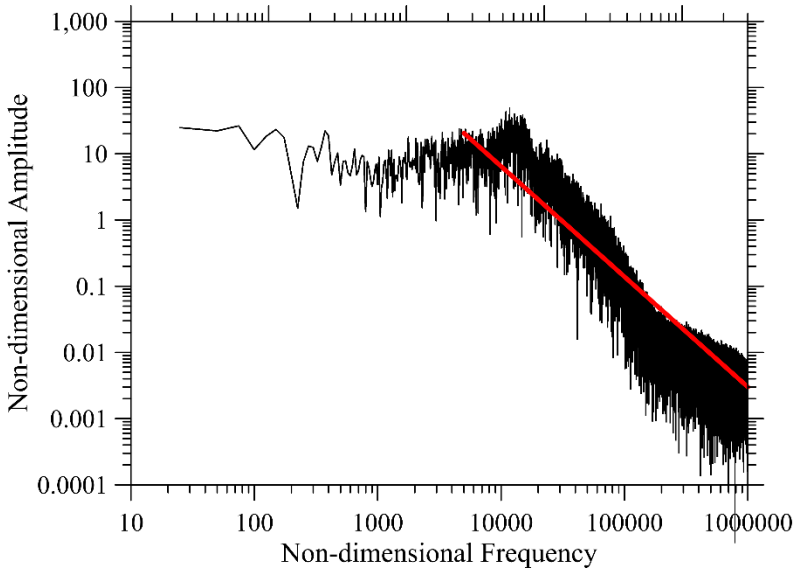

Figure 5.14: Hybrid convection in the cavity with adiabatic bottom wall, Ra=1x10^7: (a) frequency spectrum related to the velocity signal measured by a numerical probe located at x=0.25 and y=0.75 (the red line indicates the Kolmogorov scaling law).

Comparison of Table 5.5 with Table 5.3 also reveals that the relative importance of Nu_{step}^{horiz} and Nu_{step}^{vert} *is reverted for the present case* (Nu_{step}^{horiz} is larger than Nu_{step}^{vert} when the inflow and outflow sections are not horizontally aligned, whereas the vice versa holds for coaxial sections). An analysis of the flow topology is still useful in this regard. Indeed, the notable increase of Nu_{step}^{horiz} can be ascribed to the specific path taken by the streamlines originating from the inflow section, which always force (regardless of the value of *Ra*) relatively colder fluid to lick the corner and the horizontal hot side of the step.

In the remainder of this section, the situation with the hot bottom is finally discussed (Fig. 5.15). For Ra=1x10^4 (Fig. 5.15(a)) the flow pattern is more or less the same as for adiabatic floor case. A very thick hot boundary layer can be seen covering the floor. For Ra=1x10^5 (Fig. 5.15(b)) the flow pattern is roughly the same as for the adiabatic floor case too (Fig. 5.13(b)). The flow is still steady.

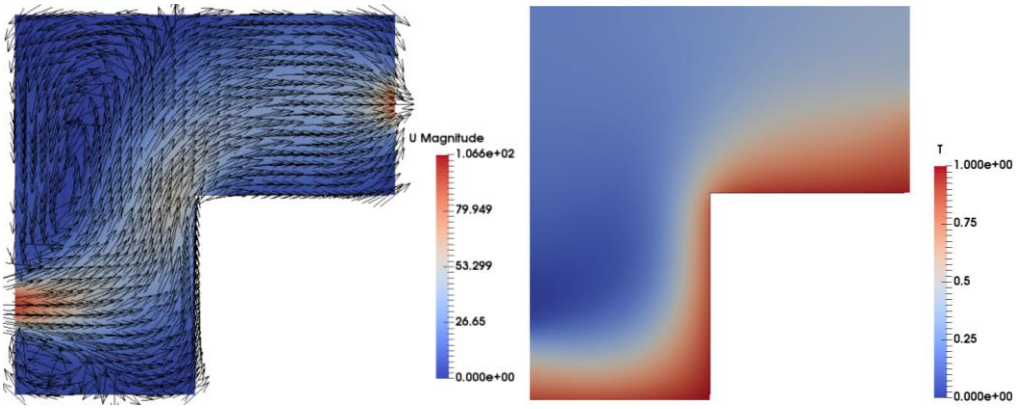

(a)

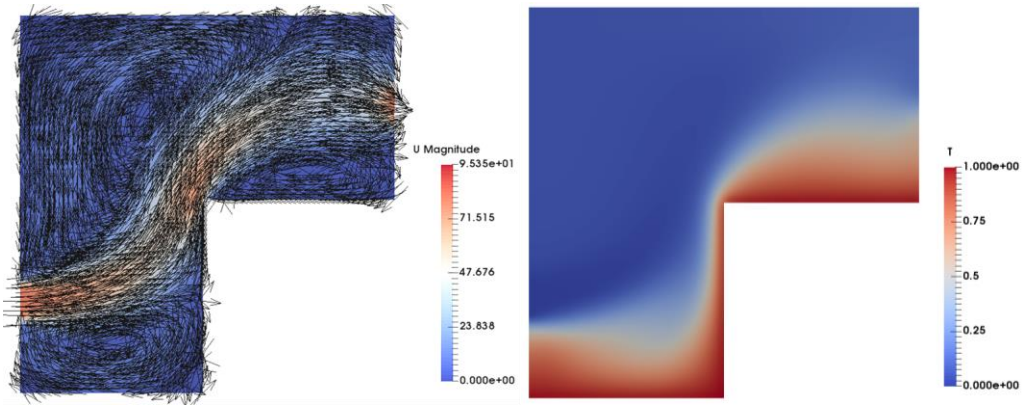

(b)

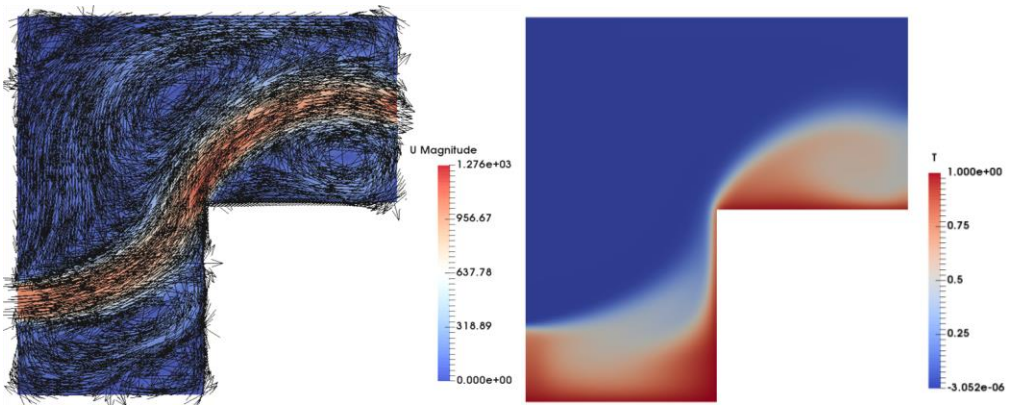

(c)

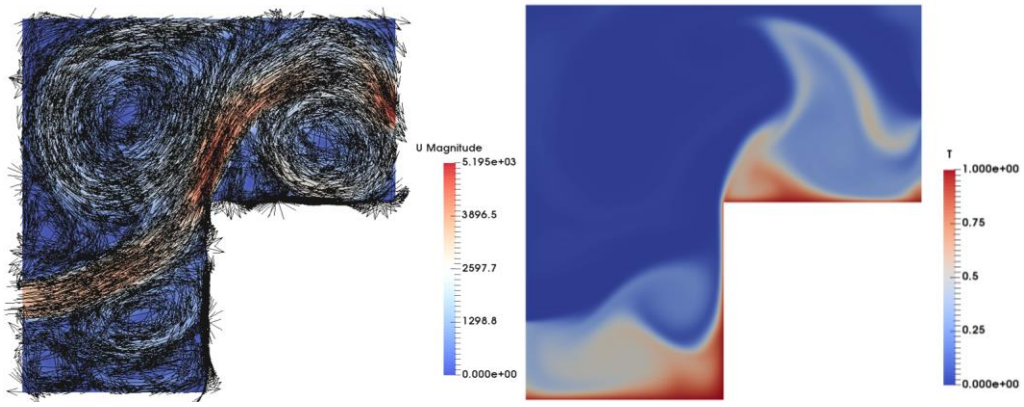

(d)

Figure 5.15: Snapshots of velocity field (left) and temperature distribution (right) for the case of hybrid forced/buoyancy convection (*Ri*=1), misaligned inflow and outflow sections and cavity with hot bottom wall: a) $Ra=10^4$, b) $Ra=10^5$, c) $Ra=10^6$, d) $Ra=10^7$.

Table 5.6: Cases examined for hybrid forced/buoyancy convection (*Ri*=1), misaligned inflow and outflow sections and cavity with hot bottom wall.

Ra	Mesh Size	Nu_{step}^{horiz}	Nu_{step}^{vert}	Regime
$1x10^4$	40x40	4.79508	3.2581	Steady
$1x10^5$	80x80	10.93178	4.53742	Steady
$1x10^6$	120x120	19.7574	9.15618	Steady
$1x10^7$	270x270	≅31.9 (average)	≅33.2 (average)	Weakly Turbulent

For $Ra=1x10^6$ (Fig. 5.15(c)) three velocity rolls can be distinguished. The regular movement of the cold fluid entering the inlet and following a parabolic trajectory until it meets the outflow section is not disturbed in this case (like in the adiabatic floor case). A swirl can yet be seen in

the temperature distribution just above the step (compare Figs. 5.15c and 5.13c) . The flow is steady.

For Ra=1x10^7 (Fig. 5.15(d)) the behaviour is similar to that found for the adiabatic floor case and the same value of Ra. Like the corresponding circumstances with adiabatic floor, the flow is weakly turbulent (Fig. 5.16) and characterized by the presence of small eddies located along the horizontal and vertical walls of the step. However, in this case small eddies are also formed along the bottom heated floor (compare Figs. 5.15d and 5.13d).

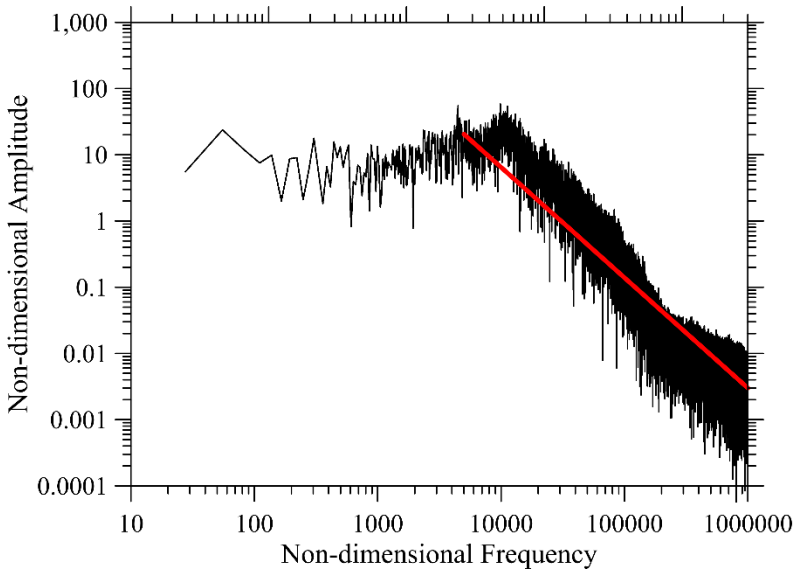

Figure 5.16: Hybrid convection in the cavity with hot bottom wall, Ra=1x10^7: frequency spectrum related to the velocity signal measured by a numerical probe located at x=0.25 and y=0.75 (the red line indicates the Kolmogorov scaling law).

Since a steady behaviour has been found for Ra<10^6 for both types of thermal conditions assumed for the floor, further analysis was carried out to determine the value of $Ra_{critical}$ for which the flow becomes time-periodic. According to our simulations, such values are $Ra_{critical}$≅3.8x10^6 and $Ra_{critical}$≅3.2x10^6, for the cavity with adiabatic and isothermal (hot) floor, respectively, which indicate that in these cases an increase in buoyancy has a slightly destabilizing influence.

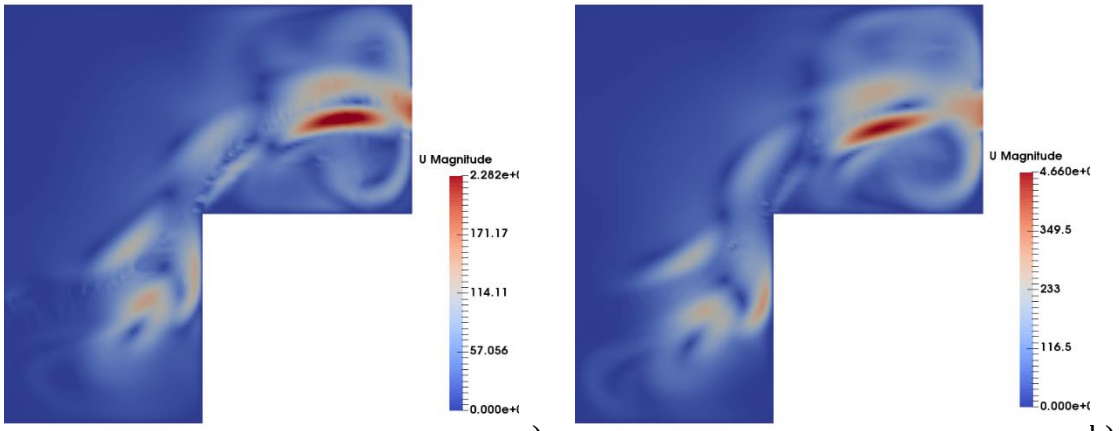

Figure 5.17: Snapshot of velocity disturbances for the case of hybrid forced/buoyancy convection (*Ri*=1), misaligned inflow and outflow sections: a) cavity with adiabatic floor, Ra=3.8x10^6; b) cavity with hot floor, Ra=3.2x10^6.

The small difference in the critical value of the Rayleigh number is in line with the behaviour of the disturbances, which as shown in Fig. 5.17 display a relatively similar configuration for both cases. In particular, they exhibit a similar magnitude and are concentrated along the main path taken by the cold fluid (entering the cavity from the left) to reach the outflow section. Among other things, this figure is also useful as it reveals that the instability is still of a shear-driven nature. Apart from the region located above the step, disturbances are also significant in the left lower portion of the cavity where their presence can directly be ascribed to the strong horizontal shear stress that is attained there as a result of the curvature of the main current. This can be seen as an important distinguishing mark with respect to the perturbation patterns seen in Figs. 5.12 where disturbances were more concentrated in the portion of the domain located just above the step (where vertical shear stresses are high).

Comparison with the configuration with horizontally aligned inflow and outflow sections also leads to the conclusion that a decrease in the height (distance from the floor) of the inflow section can have a stabilizing influence on the flow (the $Ra_{critical}$ for misaligned sections being approximately three times that needed to induce time-dependent flow in the situation with coaxial sections, which also explains why in the present case the inertial range is shifted to the right in both Figs. 5.14 and 5.16).

Further insights into the thermal behaviour can finally be gained by comparing the values of Nu_{step}^{horiz} in Tables 5.5 and 5.6. The non-negligible shrinkage in the values of Nu_{step}^{horiz} for the case with hot floor and moderate values of *Ra*, can be ascribed to the effect that such boundary exerts on the cold fluid entering from the left side (causing a quick rise in the temperature of such fluid thereby mitigating its ability to extract heat from the top surface of the step).

5.4 Conclusions

The main conclusions of the present chapter can be summarized as follows:

- Multicellular configurations are produced with number of rolls changing according to the value of the Rayleigh number.
- For relatively high values of *Ra*, these multicellular systems are driven by the development of spatially extended thermal plumes in the system, which tend to originate from the corner of the obstruction and *assume different inclination according to the considered condition* (switching from an almost horizontal or slightly inclined configuration for the case with adiabatic bottom to an almost vertical state when the bottom is kept at a fixed hot temperature).
- For these cases, *heat islands* can be produced in some circumstances. The tendency of these to be located in the lower part of the domain for pure buoyancy must be ascribed to the insufficient mixing between the upper and lower fluid regions that is established when the flow pattern takes a specific topological configuration (at relatively high values of *Ra*).
- Replacement of the adiabatic bottom with an isothermal wall, leads to a stabilization of the flow field. This is due to the non-trivial coupling established in the pure buoyancy case between the flow of Hadley type (which develops from the vertical side of the obstruction) and that of RB nature, driven by horizontal hot boundaries.
- The other patterns emerging for the unit value of the Richardson number correspond to different possible realizations of the route that cold fluid can take to reach the outlet. A more precise interpretation can be elaborated as follows: These possible multiple paths follow naturally from the relative position of the inlet with respect to the floor and the rich variety of possible interactions that can be established between the cold fluid injected in the cavity and the buoyancy flow of thermal nature originating from the hot surfaces. The latter can support or oppose to the transport of fluid from the inflow to the outflow section depending on the considered circumstances.
- Changing the position of the inflow section can also have remarkable effects on such dynamics. Heat islands that, for the case of inflow section horizontally aligned with the outflow section, are formed in the lower portion of the domain (as in the pure buoyancy case), disappear when the inflow section is close to the bottom wall.
- A change in the position of the inflow section also affects in an appreciable way the route towards time-dependence and chaos and how this, in turn, is influenced by the nature of the bottom wall (being it adiabatic or isothermal). While, in general, for hybrid convection, a switch from the adiabatic to the isothermal boundary condition causes a stabilization of the flow, the effective change experienced by the critical Rayleigh number strongly depends on the location of the inflow section.

Chapter 6

Flow topology and bifurcations of buoyancy and mixed convection in an elongated domain with a forward-facing step

The layout of this section is as follows. Each sub-section represents a self-contained discussion of the patterning behaviour for a fixed value of the Richardson number. In particular, Sect. 6.1 is concerned with the results for pure buoyancy convection (formally corresponding to $Ri \to \infty$); Sect. 6.2 describes the outcomes of the simulations for circumstances where, though forced convection is present (finite values of *Ri*), buoyancy still plays a dominant role (*Ri*=100 and *Ri*=30); Sect. 6.3 examines small-*Ri* behaviour (representing the idealized situation in which forced flow and buoyancy convection have a comparable magnitude). The value of the Prandtl number has been fixed to Pr=1. A critical comparison of the different situations, leading to general conclusions on the overall bifurcation and heat transfer scenarios, is finally elaborated in Section 6.4.

6.1 Pure buoyancy case

Following the same approach implemented in Chapter 5, the first section contains material that provides a foundation for the rest. Being entirely focused on pure buoyancy convection, it immediately supplies the reader with a clear account of the considered interval of values of the Rayleigh number and the typical convective modes that this type of flow can produce in such a range of *Ra* (for the two variants of thermal boundary conditions at the bottom wall defined by eq. (3.10)). Related results are summarized in Figs. 6.1-6.4. As further elaborated in Sect. 6.4, these dynamics can be used as a basis to disentangle the role played by buoyancy effects in more complex situations where the Richardson number takes finite values.

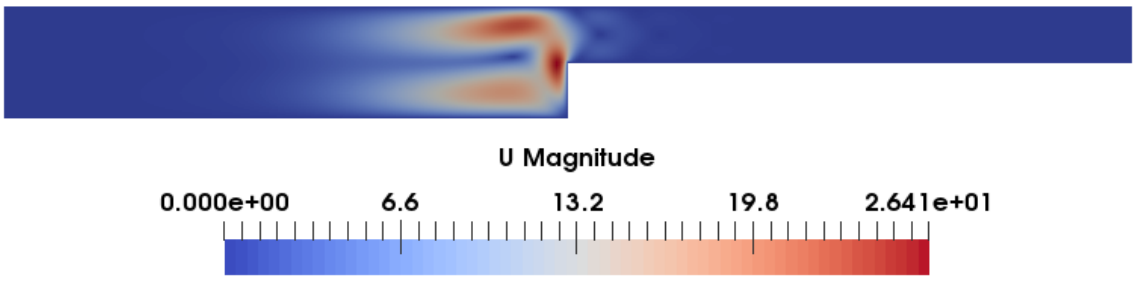

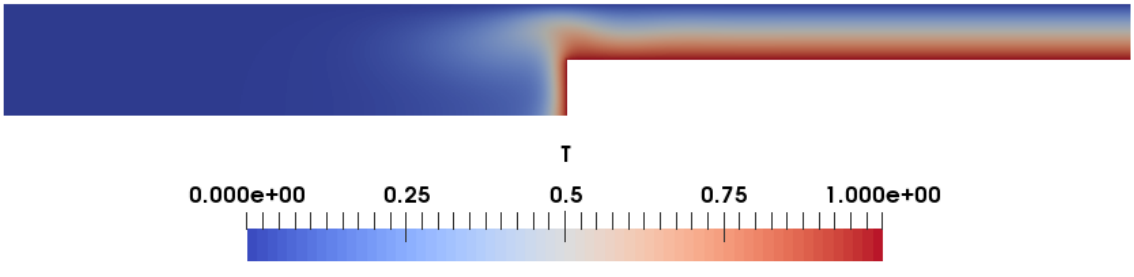
T
0.000e+00
0.25
0.5
0.75
1.000e+00

a)

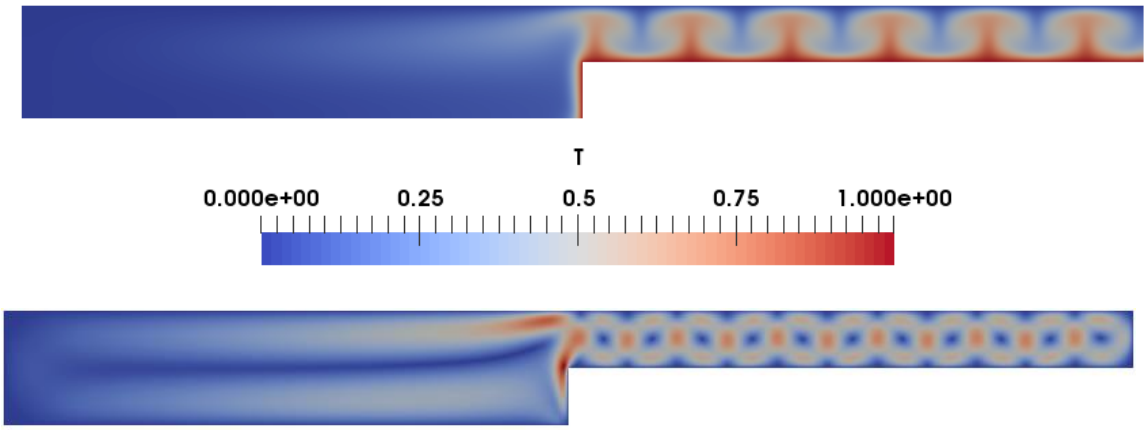
T
0.000e+00
0.25
0.5
0.75
1.000e+00
U Magnitude
0.000e+00
27.4
54.9
82.3
1.098e+02

b)

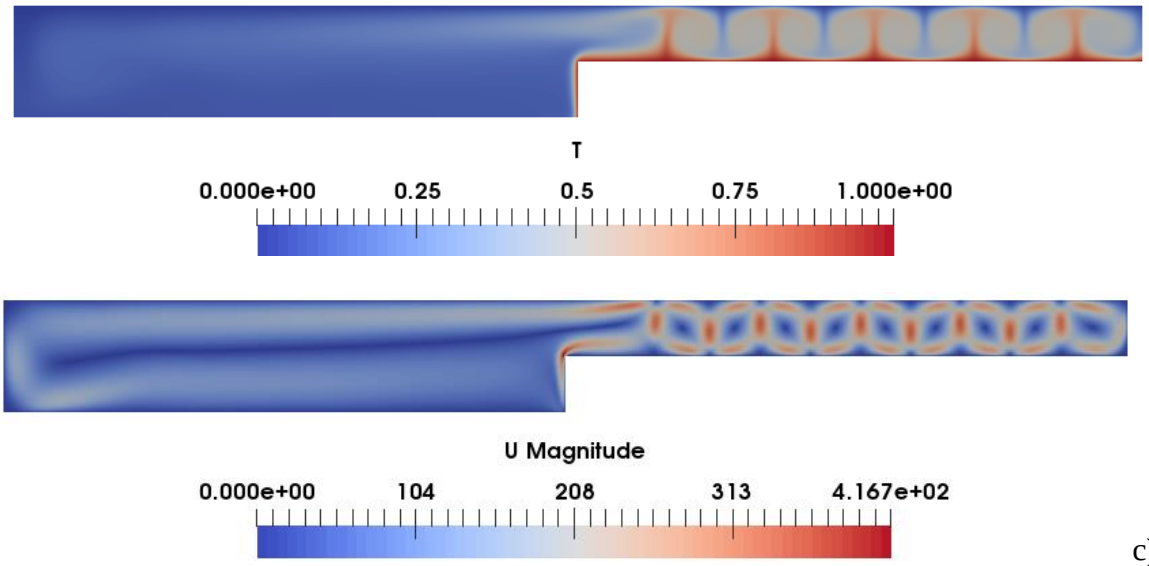
T
0.000e+00
0.25
0.5
0.75
1.000e+00
U Magnitude
0.000e+00
104
208
313
4.167e+02

c)

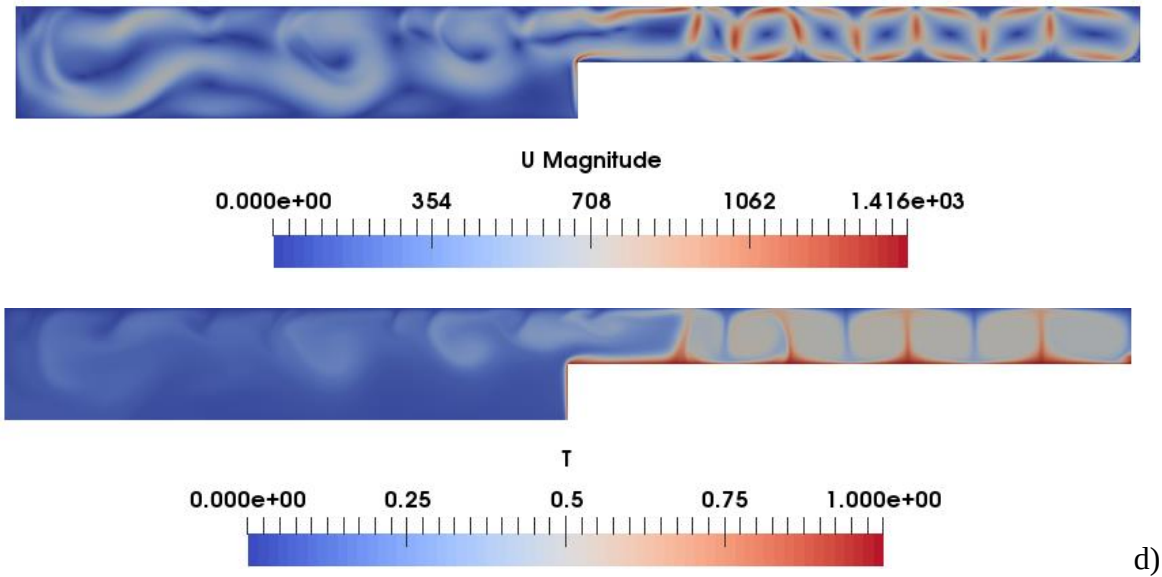

d)

Figure 6.1: Snapshots of velocity field and temperature distribution for the case of pure buoyancy convection and cavity with adiabatic bottom wall: a) $Ra=10^4$, b) $Ra=10^5$, c) $Ra=10^6$, d) $Ra=10^7$.

Following a logical approach, initially the simplest possible case is examined that is the situation with $Ra=10^4$ and bottom wall ($0<x<A/2$) with adiabatic conditions. As evident in the velocity distribution (see the top view reported in Fig. 6.1a), a strong circulation is created in the left part of the domain (the region characterized by larger cross-sectional area). As also revealed by the inclined thermal plume originating from the corner of the step, this circulation of the *Hadley type* (Sect. 1.1.4.2) is essentially driven by the vertical heated sidewall of the step. Less evident in this figure is the presence of small rolls formed in the shallow region constrained between the top rigid boundary and the top surface of the step. Unlike the other larger vortex (occupying the region $x<A/2$), these (nine) rolls may be regarded as the manifestation of the almost pure *Rayleigh-Bénard convection* (Sect. 1.1.4.1), which emerges as a result of the prevailing vertical temperature gradient established for $x>A/2$. These rolls are weak as witnessed by the presence of an almost undisturbed thermal boundary layer, which is relatively thicker in comparison to the one formed on the vertical wall. The Hadley flow being developed in the left part of the domain ($x<A/2$) is dominant in terms of strength. Despite the inherent complexity of the overall convective configuration (which features two coexisting modes of convection), the two convective mechanisms exist in an almost independent way and the overall flow is steady.
For $Ra=1x10^5$ (Fig. 6.1b), the Hadley flow and RB convection have comparable strength. An interesting change can also be spotted in the number of small rolls located above the step, which increases from nine to eleven. A big transverse roll (Hadley flow) is still steadily located in the entire left portion of the cavity. The maximum velocity magnitude is attained just before the section where a discontinuity in the cross-sectional area occurs, i.e., along the vertical heated wall of the step ($x\cong A/2$). In terms of temperature distribution, well-defined thermal plumes are

formed for x>A/2 whereas for x<A/2 the fluid is relatively cold and undisturbed. As time passes the plume lobes remain distinct and are not significant deformed. A hot thin boundary layer is formed on the vertical wall of the step. The flow is still steady.

If the Rayleigh number is further increased (Ra=1x10^6 in Fig. 6.1c), interestingly, there is a decrease in the number of flow features visible in the right portion of the cavity. The number of velocity rolls formed in this case comes back to nine (same as for Ra=1x10^4). As revealed by Fig. 6.1c, this effect is the result of the *coalescence* of the first roll of RB nature with the larger circulation of the Hadley type developing in the left part of the domain. Notably, in such conditions each plume has a thin, sharp stem with a well-defined cap and lobes that are significantly deformed by vortex structures, which means that the plumes established in the cavity for Ra=1x10^6 pertain to the IVND regime (the so-called Inviscid-Non diffusive Regime according to the classification originally elaborated by Hier Majumder et al. 2004). This regime takes place for high Rayleigh number (Ra > O(10^6) and Prandtl number near 1. Most remarkably, for such conditions the flow is unsteady (quasi-periodic) as shown in Fig. 6.2.

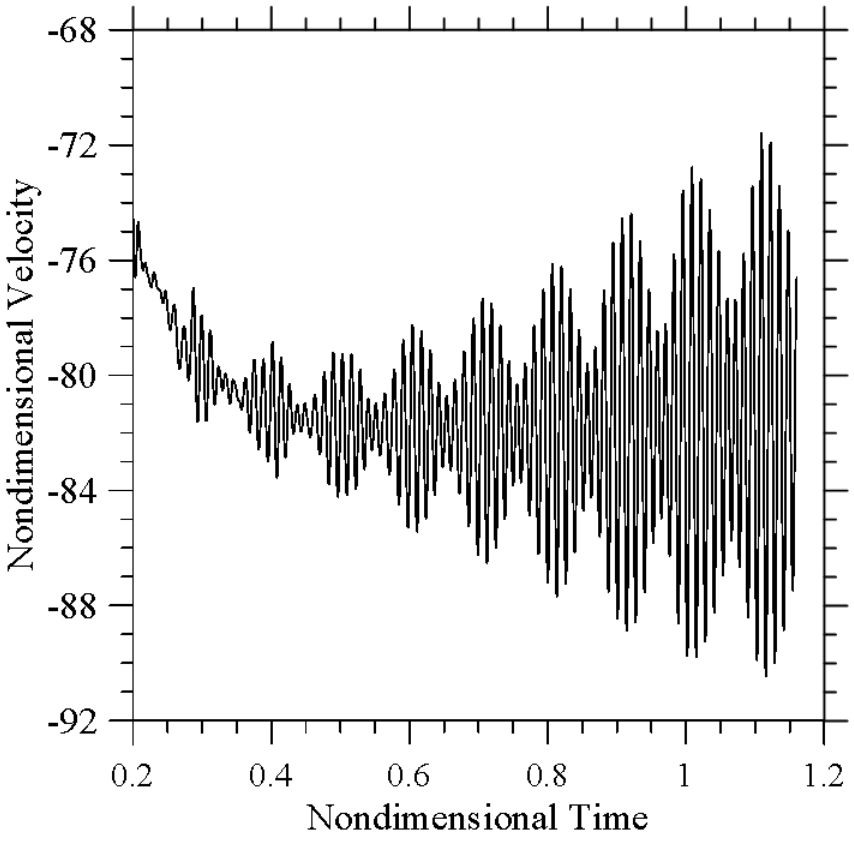

Figure 6.2: Velocity (horizontal component) signal for Ra=10^6 and adiabatic bottom measured by a numerical probe located at (0.25, 0.75).

Finally, for Ra=1x10^7 (Fig. 6.1d), a further decrease in the number of RB rolls occurs due to enhancement of the aforementioned coalescence process (by which the RB rolls are absorbed by the elongated circulation occupying the left region). The most evident change, however, concerns the region with large cross-sectional area. The initially unicellular (Hadley) roll established there is broken into distinct vortices, which travel continuously from left to the right (their average number in time being three). This phenomenon is produced by a *wave travelling towards the left* along the top boundary of the duct (clearly visible in the temperature distribution). More precisely, it manifests itself through the periodic shooting of 'packets' of hot fluid in the cold fluid located in the left region of the cavity. Such disturbances originate from the head of the plume formed close to the corner of the step (x≅A/2) and travel towards the left, i.e. in the downstream direction (in other words, the wave uses the leftward-directed branch of the Hadley cell as a substrate for propagation (This phenomenon, which is typical of the Hadley flow for Pr≅1 in cavities subjected to horizontal temperature gradients will be discussed later, the reader being also referred to the information provided in Sect. 1.1.4.2)

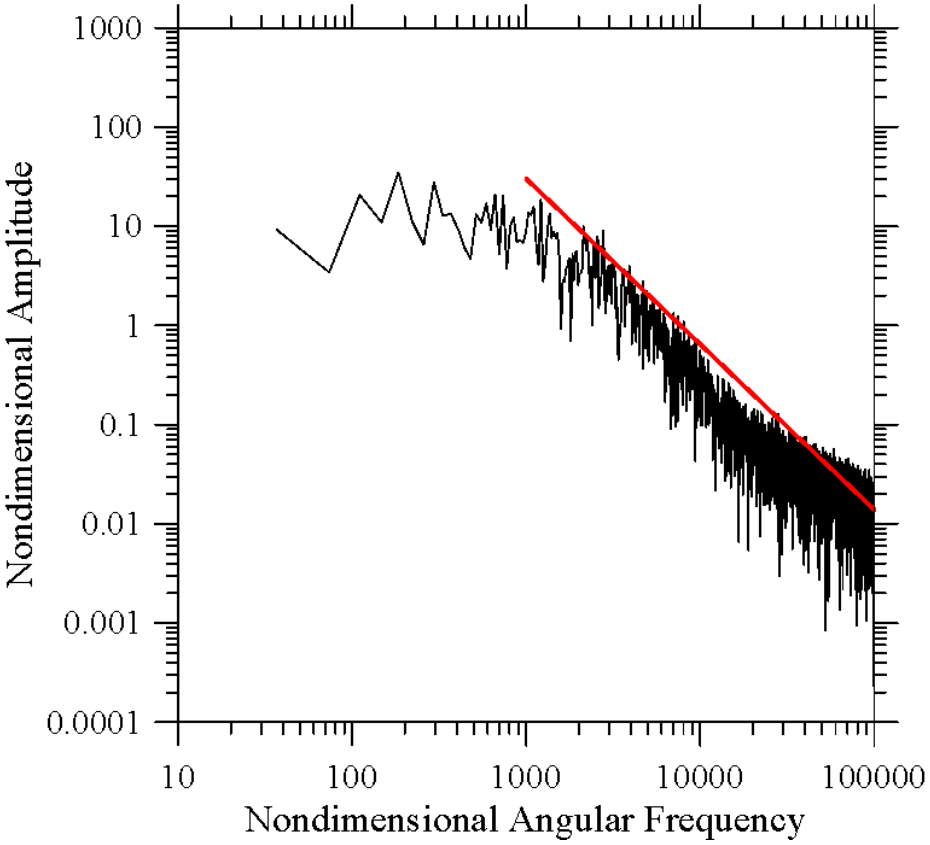

Figure 6.3: Frequency spectrum for Ra=10^7 and adiabatic bottom. The red straight line indicates the (-5/3) scaling trend predicted by the Kolmogorov law.

In such conditions the flow is moderately turbulent as witnessed by the frequency spectrum shown in Fig. 6.3 (see also Table 6.1). In agreement with the expected behaviour of turbulence on small length scales i.e., the so-called self-similarity property of turbulence (Kolmogorov 1941a,b; Kraichnan, 1974; Hutchinson and Raithby, 1986) the spectrum *aligns with a* $\omega^{-5/3}$ *law* in a certain range of (high) frequencies.

After discussing the different situations for the cavity with a hot step and adiabatic bottom wall, it is also worth examining the other configuration (differing in regard to the thermal boundary condition used for the bottom wall, kept at constant temperature, see Fig. 6.4).

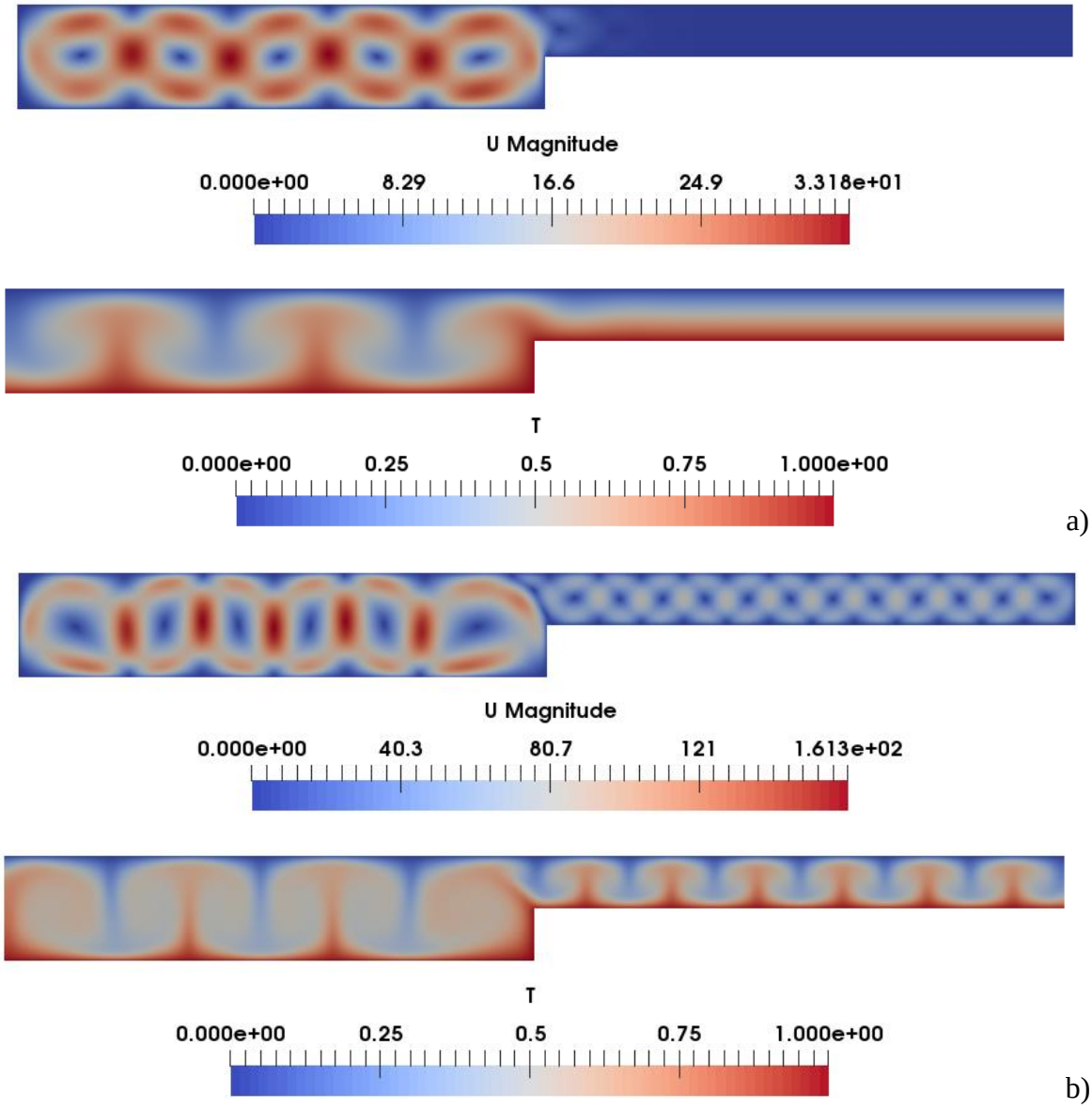

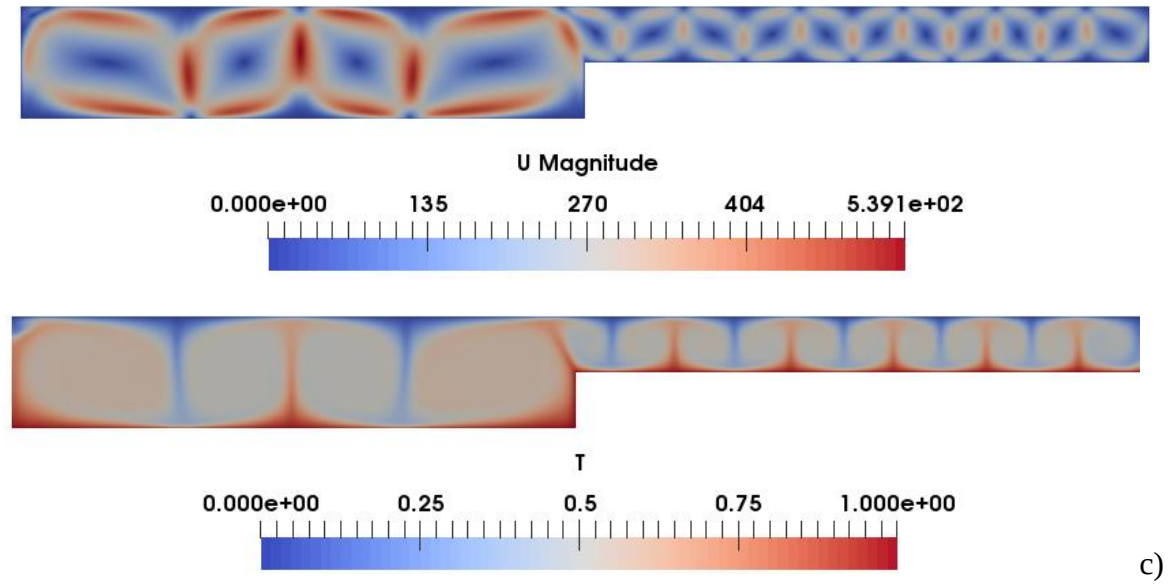

c)

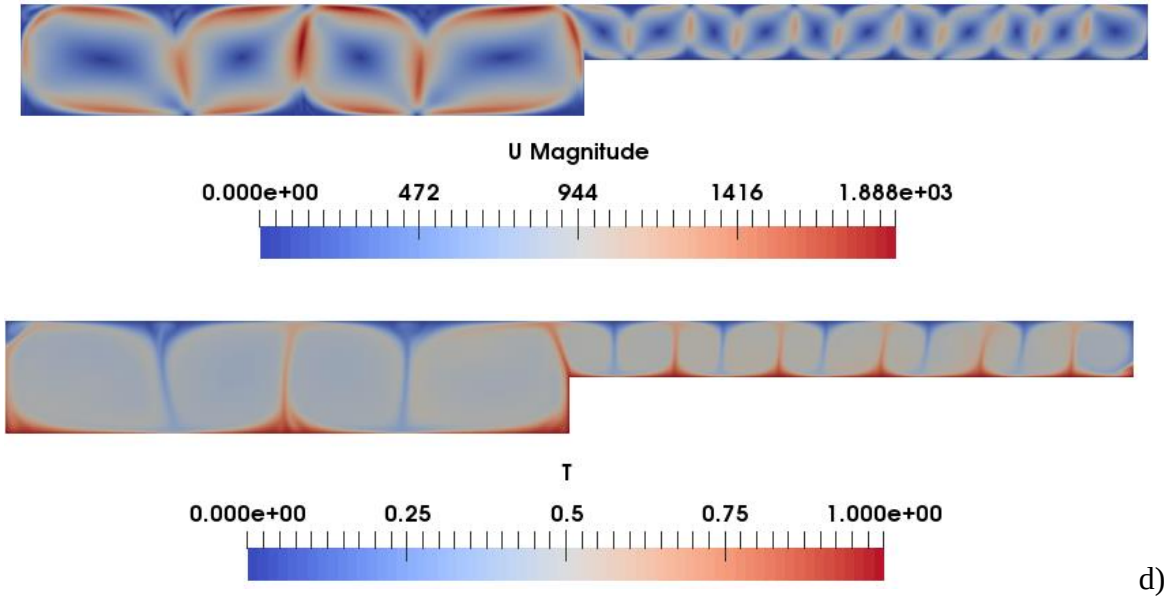

d)

Figure 6.4: Snapshots of velocity field and temperature distribution for the case of pure buoyancy convection and cavity with hot bottom wall: a) $Ra=10^4$, b) $Ra=10^5$, c) $Ra=10^6$, d) $Ra=10^7$.

As qualitatively illustrated by Fig. 6.4a, for $Ra=1x10^4$ again nine weak small velocity rolls can be seen in the shallow region above the step (as for the adiabatic-floor case). However, five medium-sized velocity rolls are now present in the left half portion of the cavity. They are clearly rolls of RB nature (Sect. 1.1.4.1) as indirectly demonstrated by the simultaneous development of evenly spaced thermal plumes. The different distortions undergone by the temperature field in the left and right regions of the cavity qualitatively substantiate the realization that convection produced for x<A/2 is much stronger than that of the same nature emerging for x>A/2. This trend

can be immediately explained simply taking into account the cubic dependence of this form of convection on the vertical extension of the considered layer of fluid ($d/2$ for x>A/2 corresponding to an effective value of the Rayleigh number $Ra_{eff}=Ra/8$). The flow is steady in both sides of the cavity.

On increasing *Ra* to 10^5, thermal plumes become a pervasive feature of the temperature pattern (Fig. 6.4b). All plumes have a vertical stem with the exception of that originating from the step corner, which is inclined to the left. The number of small (right region) and large (left region) rolls increases from nine to twelve and from five to six, respectively, which indicates that (as expected) the Rayleigh number has a significant influence on the wavenumber. The most remarkable change, however, concerns the spatio-temporal behaviour of the flow, which becomes *unsteady*.

This finding indicates that transition to time-dependent flow can be obtained with a smaller value of the Rayleigh number when the configuration with the heated bottom is considered (*Ra* had to be increased to $Ra=10^6$ to observe similar phenomena for the adiabatic wall case; these aspects will be further explored in Sect. 6.4 where detailed information about the hierarchy of bifurcations will be provided).

For $Ra=1x10^6$ (Fig. 6.4c), there is a decrease in the number of rolls (from twelve to eleven) in the right portion of the cavity (the same process was observed for the adiabatic floor case). A similar trend is effective for the rolls located in the left region (their number being reduced from six to four). The shrinkage in the number of rolls essentially results from roll coalescence phenomena.

When the Rayleigh number is finally increased to $Ra=1x10^7$ (Fig. 6.4d), no change occurs in terms of patterning behaviour. However, the flow becomes weakly turbulent (see Table 6.2) and the less chaotic nature of the flow (with respect to the equivalent case with the adiabatic floor) can be ascribed to the lack of a wave-propagation mechanism such as that visible in Fig. 6.1d (requiring the presence of horizontal currents of the Hadley type, Sect. 1.1.4.2).

6.2 Mixed convection for Ri=100 and Ri=30

Now the case where the buoyancy flow, naturally produced by the heated surfaces embedded in the physical domain, *interacts with cold fluid being injected from the left* is considered (which leads to a typical problem of mixed forced-buoyancy convection, Figs. 6.5-6.7).

On the basis of the same approach undertaken in Sect. 6.1, snapshots of the thermo-fluid-dynamic fields for increasing values of the Rayleigh number and $Ri=100$ are orderly collected in Figs. 6.5 and 6.6 for the two aforementioned archetypal situations with adiabatic and hot bottom wall, respectively.

The simplest situation is that presented in Fig. 6.5a for $Ra=1x10^4$. It is shown that the cold fluid entering through the inlet continues to travel straight with a moderate velocity until it comes in contact with the hot obstruction (the step). The hot step causes the velocity to increase due to the contraction of the cross-sectional area and the incompressibility constraint. Moreover, a thick hot

boundary layer develops along the entire length of the horizontal and vertical walls of the step. The increasing thickness of the thermal boundary layer in the downstream direction is obviously a consequence of the heat being released by the hot surface of the step in the region x>A/2.
The next figure of the sequence (Fig. 6.5b) simply illustrates that if the Rayleigh number is increased by one order of magnitude (Ra=1x10^5 and Re grows accordingly due to the Ri=const=100 condition, i.e., Re≅31.6), the thickness of the boundary layer becomes smaller. This can obviously be ascribed to the larger amount of cold fluid being injected in the system per unit time as a consequence of the increase in the Reynolds number. The flow remains steady as it was for Ra=10^4.

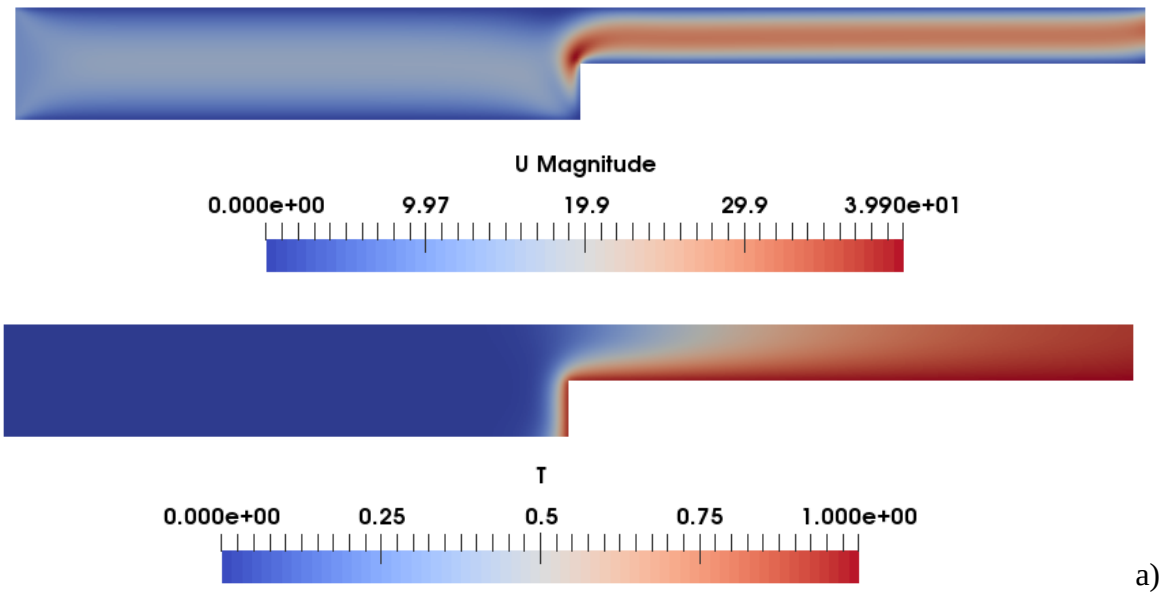

a)

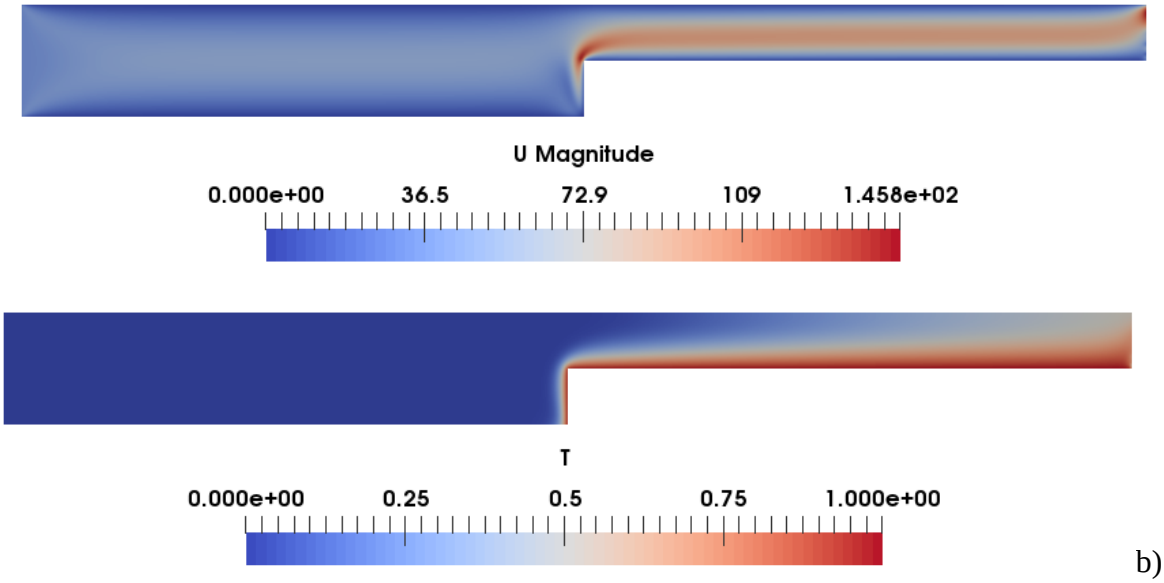

b)

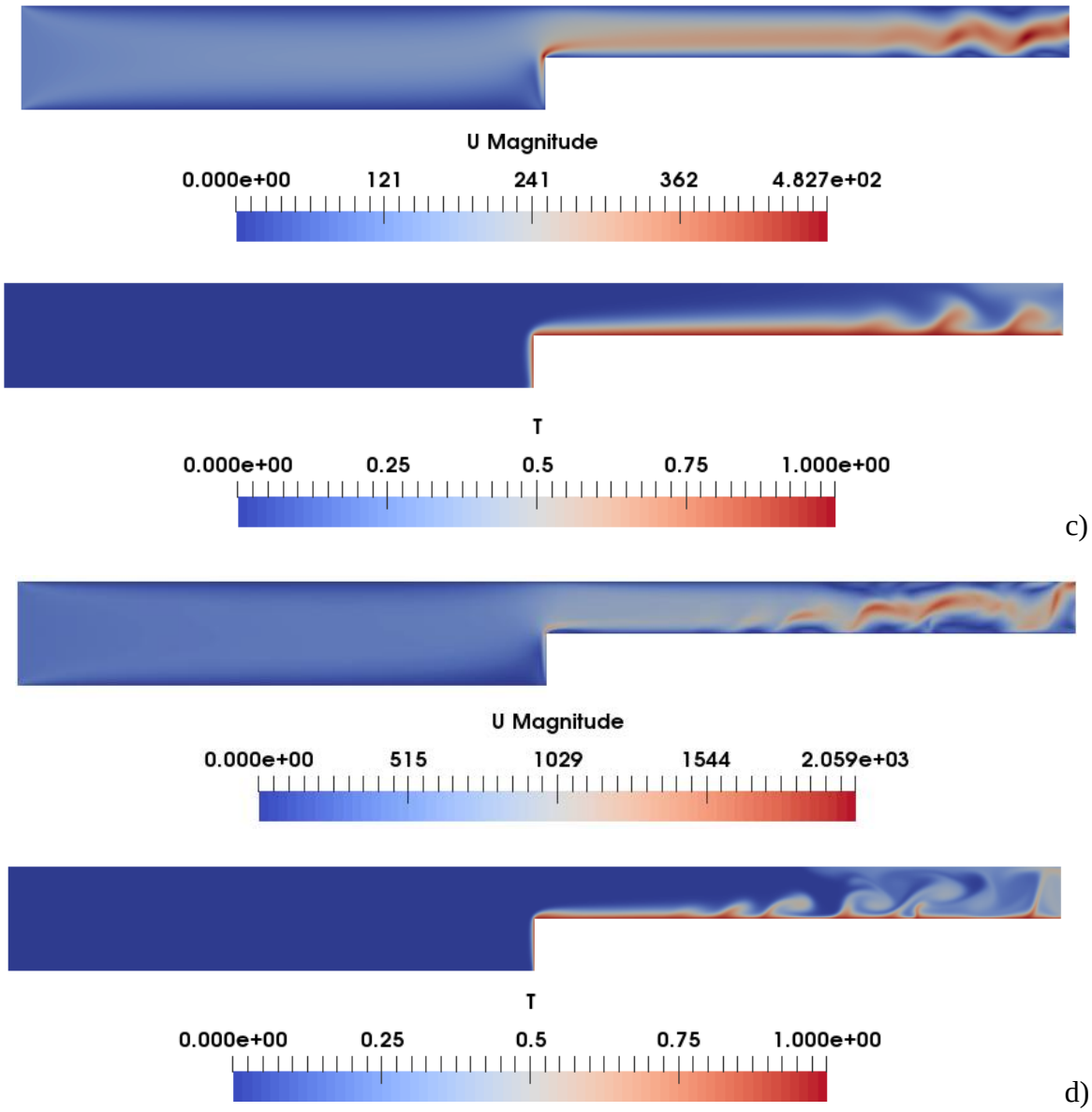

Figure 6.5: Snapshots of velocity field and temperature distribution for the case of hybrid forced/buoyancy convection (*Ri*=100) and cavity with adiabatic bottom wall: a) *Ra*=10^4, b) *Ra*=10^5, c) *Ra*=10^6, d) *Ra*=10^7.

A notable change, however, starts to affect the dynamics for *Ra*=1x10^6 (Fig. 6.5c). A Hopf bifurcation takes place and the flow evolves accordingly from a steady regime to a time dependent one. Some sinusoidal distortions can be seen in the topological development of the main current located above the step. These disturbances seem to be directly correlated to the thermal features appearing in the temperature distribution. Where the concavity of the stream centreline is towards the bottom (velocity field), a thermal plume is visible in the temperature field and, vice versa (concavity towards the top corresponds to plume absence). These convective

and thermal localized phenomena appear at a certain distance from the leading edge, i.e. the corner of step (approximately a non-dimensional distance 5 times the height of the fluid located above the step, i.e. $l \cong 5/2$). The number N of visible convective distortions is on average equal to 3. These plumes do not hold a fixed position, rather they continuously travel in the downstream direction. However, it is important to remark that the fluid has not yet entered the turbulent phase (the flow being still in a quasi-periodic condition, not shown).

A further increase in the order of magnitude of the Rayleigh number (Ra=1x10^7, Re≅316, Fig. 6.5d) causes (as expected) transition to a more chaotic state. The thermal boundary layer becomes very thin. The distortions affecting the main stream above the step are no longer regular and evenly distributed in space (this being reflected by an equivalent behaviour of the thermal plumes). The increase in *Ra* at fixed *Ri* has also another notable consequence. Plumes are produced *at a much smaller distance from the leading edge* ($l \cong 2$). Moreover, their *extension in the vertical direction is generally smaller* than that seen for Ra=1x10^6, which can be interpreted taking into account the dual influence of a simultaneous increase of *Ra* and Re. In such a context, indeed, it is worth recalling that in standard RB convection, plume caps are known to become progressively smaller as the Rayleigh number becomes higher (Lappa, 2011, see also Sect. 1.1.4.1). Superimposed on this is the effect of the Reynolds number. As this parameter (the inflow velocity) grows, plumes have less time to develop in the vertical direction before they are transported towards the outflow section and leave the domain through it (the reader being also referred to Lappa (2019) for some equivalent considerations elaborated in the case of thermal plumes interacting with a free cross flow).

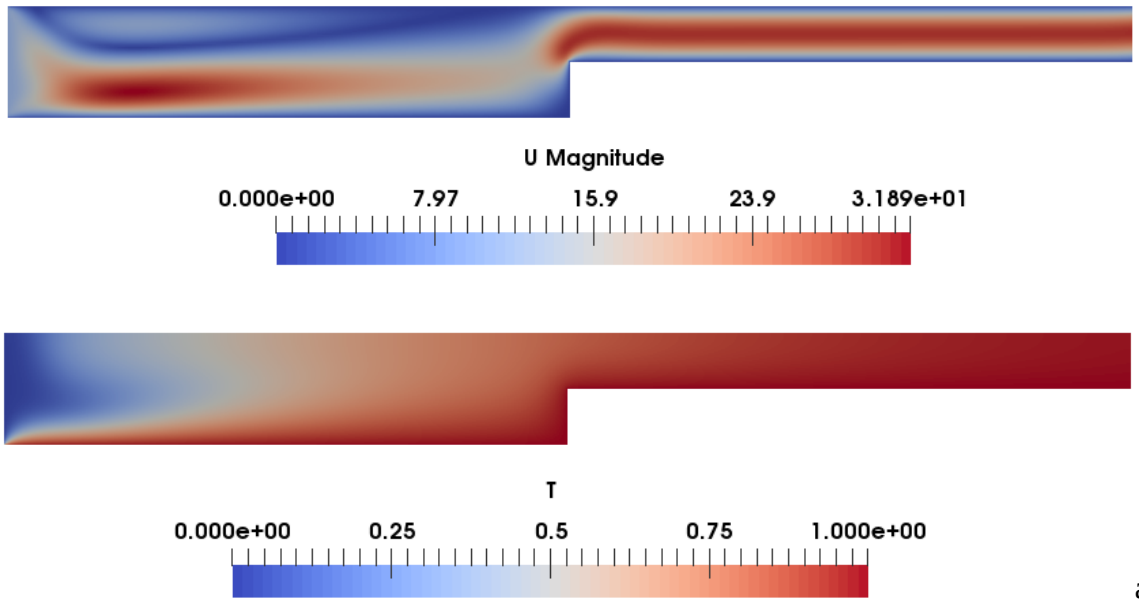

a)

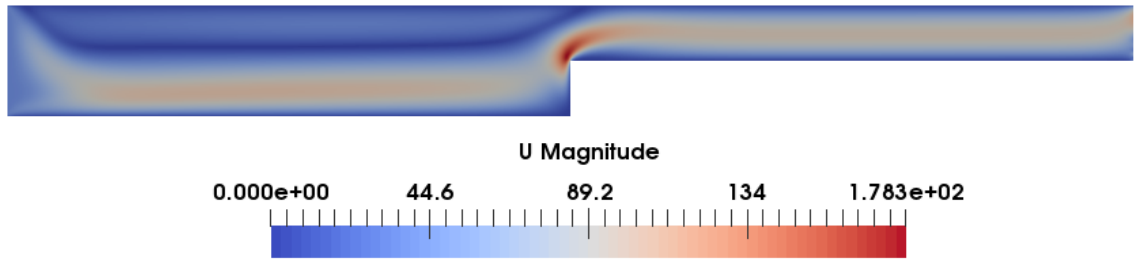
U Magnitude
0.000e+00
44.6
89.2
134
1.783e+02

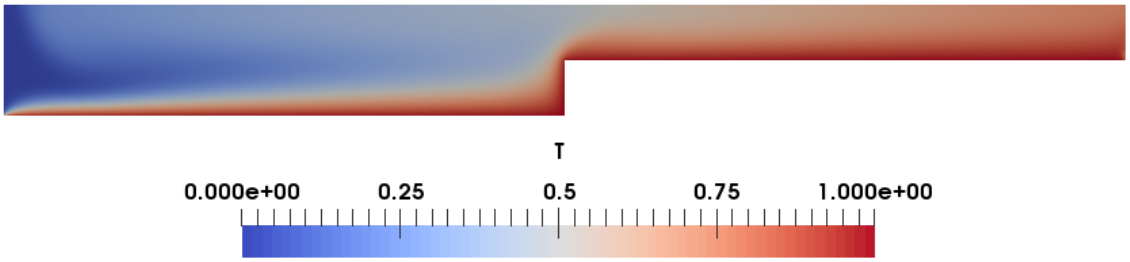
T
0.000e+00
0.25
0.5
0.75
1.000e+00

b)

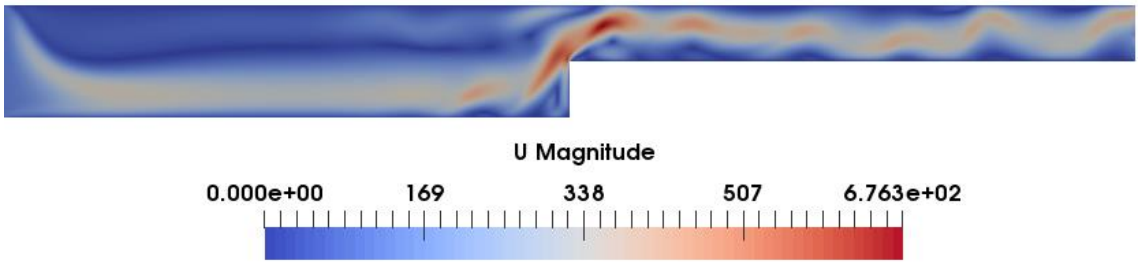
U Magnitude
0.000e+00
169
338
507
6.763e+02

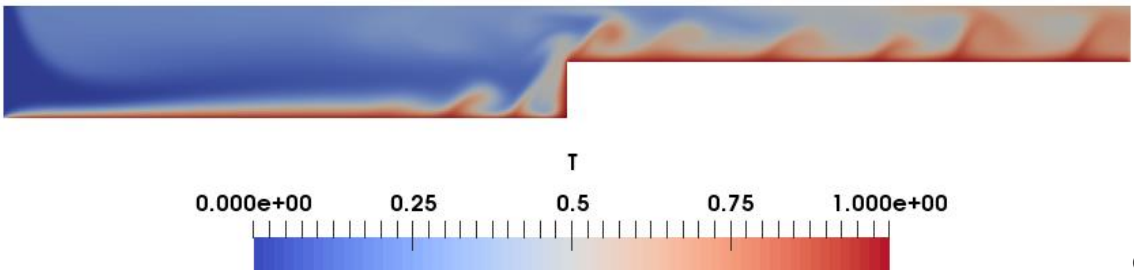
T
0.000e+00
0.25
0.5
0.75
1.000e+00

c)

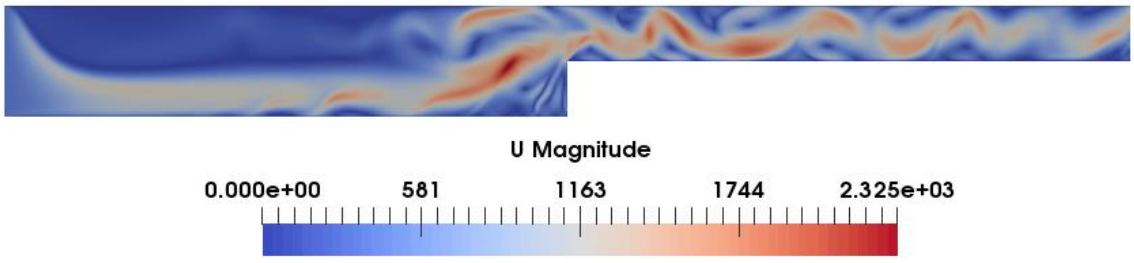
U Magnitude
0.000e+00
581
1163
1744
2.325e+03

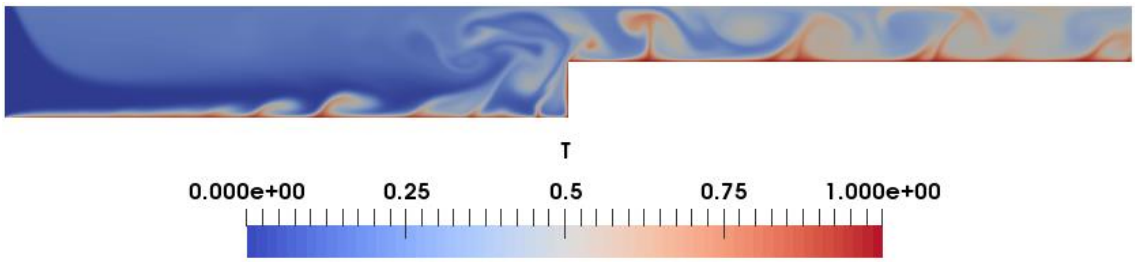

d)

Figure 6.6: Snapshots of velocity field and temperature distribution for the case of hybrid forced/buoyancy convection (*Ri*=100) and hot bottom wall: a) $Ra=10^4$, b) $Ra=10^5$, c) $Ra=10^6$, d) $Ra=10^7$.

Figure 6.6 shows the equivalent dynamics when the condition of adiabatic floor is replaced with that of wall at constant temperature.

In line with what one would expect on the basis of simple physical arguments (see Fig. 6.6a), "heat island" effects can be produced in the region located above the step (as a result of the increased amount of heat being transferred for x<A/2 from the solid boundary to the fluid). A significant change also becomes effective in the left portion of the cavity. A roll, adjacent the top wall and stretched in the horizontal direction, is created just after the inflow section. Owing to this convective effect, the fluid entering the system from the left is deflected towards the bottom and its velocity greatly increases (the maximum velocity being comparable to that obtained in the region of fluid located above the step). The cold fluid takes a downward route and travels very close to the floor for a while (x<A/2). As soon it reaches the hot step (x≅A/2) it is forced to rise, spreads itself in the right half portion of the domain and then continues to travel undisturbed in the downstream direction. For $Ra=1x10^5$ (Fig. 6.6(b)), no significant differences can be highlighted with regard to the flow topology and structure. In terms of temperature distribution, however, a mitigation of the above-mentioned heat island effect can be noticed (due to the increased amount of cold fluid being injected in the cavity per unit time).

The complexity of the velocity field starts to grow as soon as the Rayleigh is set to the value $Ra=1x10^6$ (Fig. 6.6c). The flow becomes time-dependent. As it is evident from the temperature distribution, thermal plumes now originate directly from the surface of the hot floor (x<A/2) and travel to the right. When a plume of such a series meets the hot vertical surface of the step, *it merges with the related (vertical) thermal boundary layer producing a disturbance* (a bulge in the thickness of the boundary layer) *directed upwards*. This disturbance is then transferred to the horizontal branch of boundary layer (developing from the leading edge of the step in the same direction of the prevailing flow, i.e., from left to right). Accordingly, a train of traveling plumes can be recognized above the entire horizontal surface of the step, which formally behaves as a wave propagating in the downstream direction.

The final increase in the Rayleigh number to $Ra=1x10^7$ (Fig. 6.6(d)), makes the velocity field more involved. Again, plumes originating from the extended surface of floor (x<A/2) and step (x>A/2) can be seen. The plumes have thin, sharp stem with well-defined cap and lobes that are

considerably deformed by vortex structures. As the reader will immediately realize by inspecting Fig. 6.7b, the velocity frequency spectrum is moderately turbulent and relatively similar to that obtained for the configuration with adiabatic bottom (Fig. 6.7a). Both align with the Kolmogorov law for ω in the range between $4x10^3$ and 10^5.

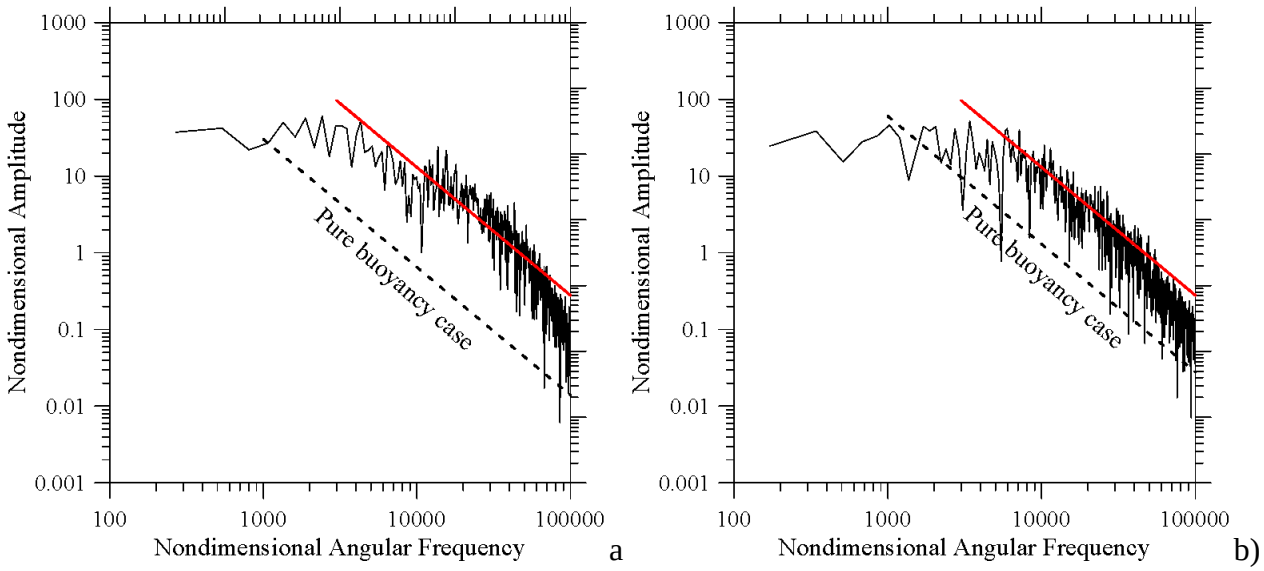

Figure 6.7: Frequency spectrum for *Ri*=100 and $Ra=10^7$: a) adiabatic bottom, b) Hot bottom. The dashed line indicates the corresponding trend for the pure buoyancy case ($Ri\rightarrow\infty$) and the red line refers to the Kolmogorov law.

Comparison with the corresponding trend obtained in the pure buoyancy case (see the dashed line), indicates that the overall spectrum is shifted to the right, i.e., that for *Ri*=100 the energy tends to reside on smaller temporal scales (which indirectly confirms that new instability mechanisms are enabled with respect to the situation with pure buoyancy convection considered in Sect. 6.1).
the snapshots of temperature and velocity fields are not shown for *Ri*=30 as they are qualitatively similar to those for *Ri*=100. However, precise information about the dependence of heat transfer on the problem parameters (as quantitatively substantiated through the Nusselt number vs *Ra* and *Ri*) is reported in the form of dedicated tables (the Reader being referred again to Tables 6.1 and 6.2).

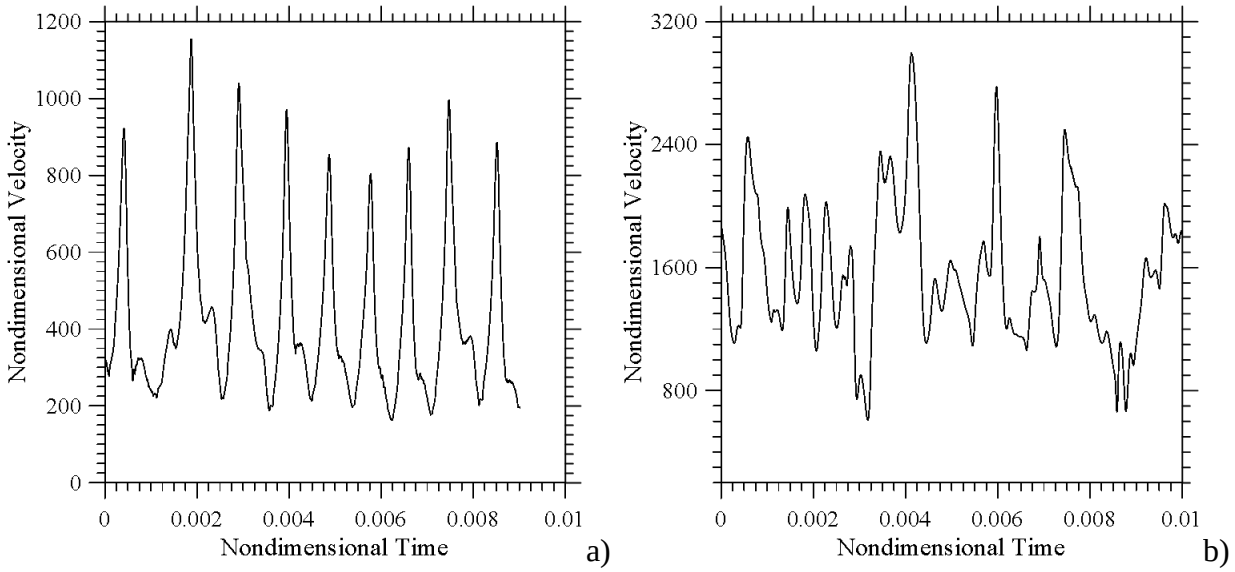

Figure 6.8: Velocity (horizontal component) signals for *Ri* =30 and $Ra=10^7$ provided by probes located in the region with reduced cross-sectional area (x>A/2): a) adiabatic floor case (probe point (9.5, 0.6)), b) hot floor case (probe point (5.5, 0.7)).

For this specific value of the Richardson number (*Ri*=30), here only the behaviour of the velocity signals for $Ra=10^7$ is considered. Insights into the role played by the thermal boundary conditions for this condition can immediately be gathered from Fig. 6.9. Indeed, as a fleeting glimpse into the right and left panels of this figure would immediately reveal, the signal for the adiabatic case displays a much more contained amplitude and a simpler frequency spectrum; this apparently innocuous observation should be regarded as an important clue for a notable difference in the related hierarchy of bifurcations (clarified further in Sect. 6.4.1).
Figures 6.8a and 6.8b are instructive also for another reason. They clearly illustrate that every time a thermal plume passes through a given observation point (the probe location indicated in the figure caption) a peak is produced in the corresponding horizontal component of the velocity. Such an increase can obviously be ascribed to the additional 'blocking' effect produced by the vertical eruptions of hot fluid (formally behaving as an additional obstruction in the flow forcing it to increase locally its horizontal velocity in order to conserve the volumetric flow rate).

6.3 Mixed convection for Ri=1

This section is devoted to the situation where forced and buoyancy convection have *comparable strength*, i.e., *Ri*=1. Since the numerical results for $Ra=10^4$ and 10^5 simply show regular and laminar (steady) flow, for the sake of conciseness, they are not described in detail here (the reader being referred once again to Tables 6.1 and 6.2 for some related quantitative details).
Interestingly, as revealed by Fig. 6.9a, though for $Ra=10^6$ and adiabatic floor no thermal plumes can be identified, some "corrugation" pops up in the shape of both the kinematic and thermal boundary layers developing along the top wall of the step (x>A/2). A further increase in the

Rayleigh number to Ra=1x10^7 (Fig. 6.9b) results in a slightly more complex velocity field. A horizontally stretched recirculation zone can be clearly observed on the surface of top wall of the step just after its leading edge.

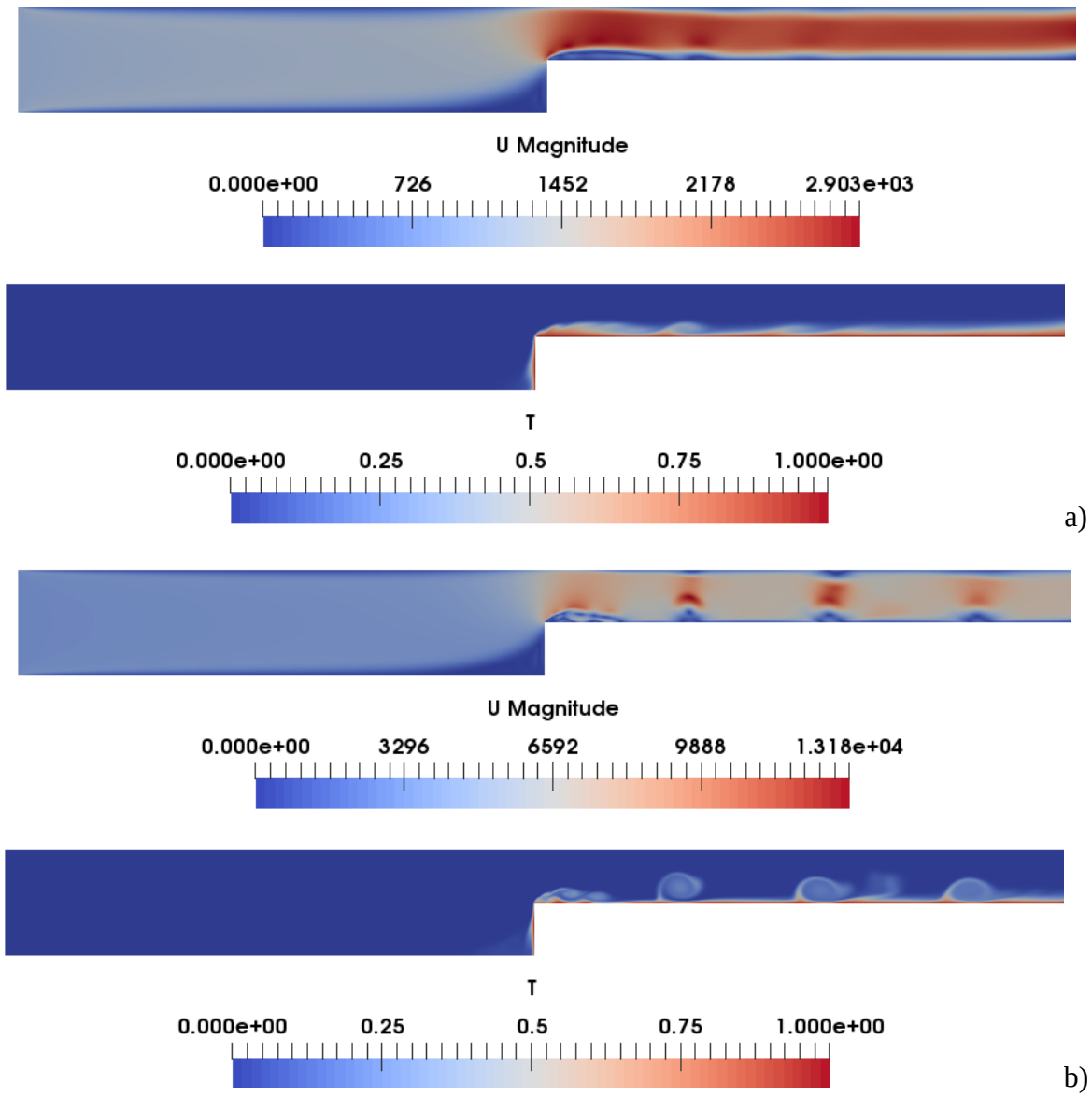

Figure 6.9: Snapshots of velocity field and temperature distribution for the case of hybrid forced/buoyancy convection (Ri=1) and cavity with adiabatic bottom wall a) Ra=10^6, b) Ra=10^7. A bubble of recirculating flow originating from the leading edge (the step corner) can be seen in all cases.

Though its horizontal extension changes slightly in time, this zone always originates from the corner. However, it is not the only recirculation region located on the top boundary of the step. Notably, for x>A/2 the kinematic boundary layer *separates and reattaches continuously* and, in light of the earlier results for larger values of the Richardson number, it can be argued that an explanation for this intermittent behaviour should be sought in the temperature field**.** Plumes are located at those specific points where the flow is seen to be rising. Plume formation forces the fluid to rise and as result to separate from the horizontal wall of the hot step. However, the flow *re-attaches quickly* (the small space that is left behind on the surface can be viewed as a *bump*). Put simply, the plumes formed in this case do not have enough time to extend in the vertical direction as the imposed horizontal flow continuously bends them. Interestingly, as evident in Fig. 6.9b, while plumes are transported by the dominant flow in the downstream direction, they can give rise to some fascinating spiral-like configurations.

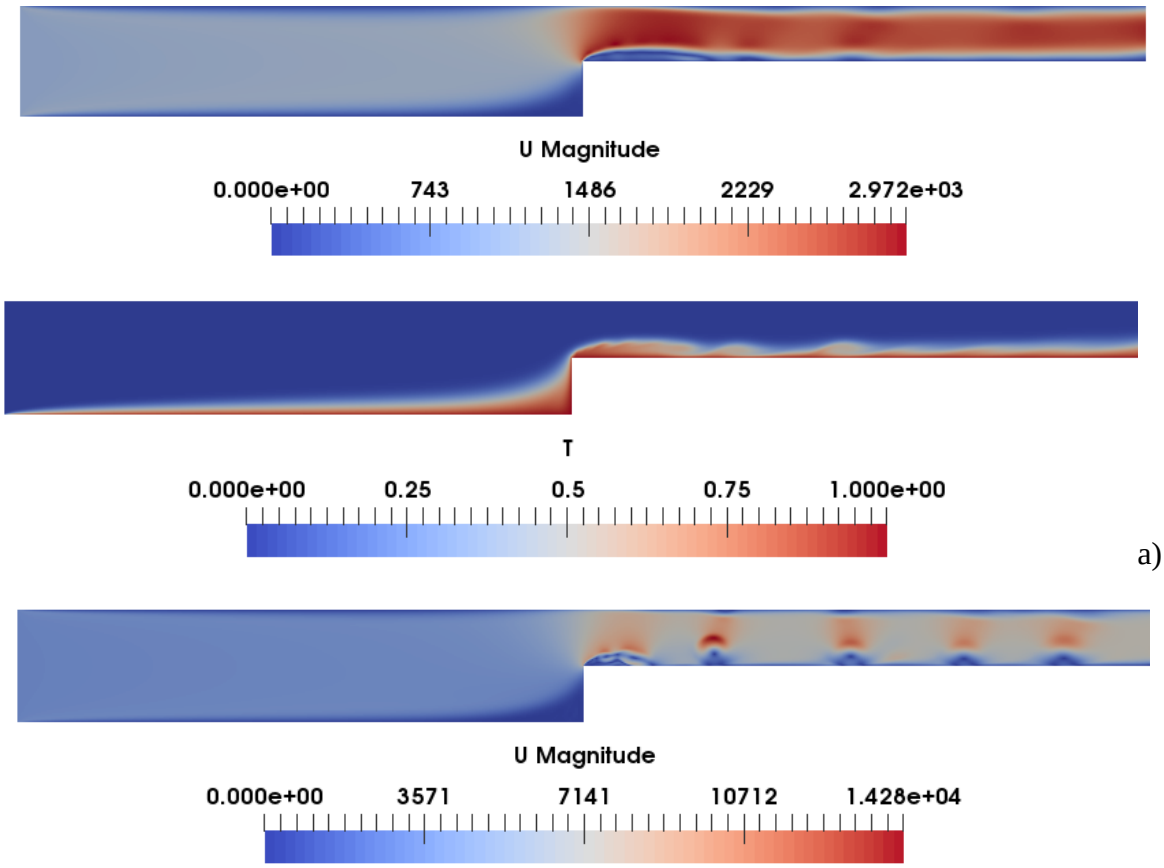

a)

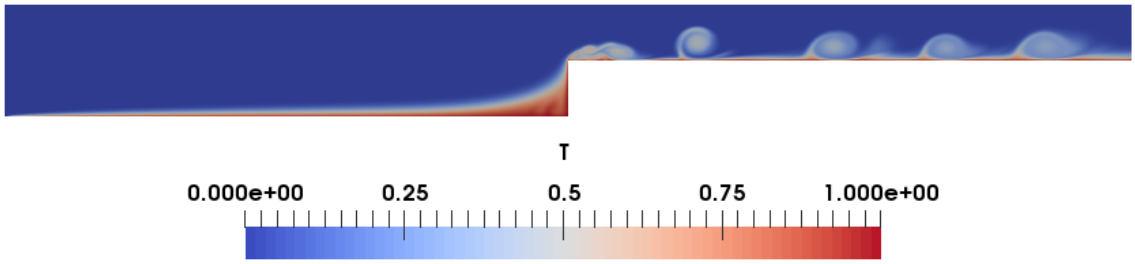

b)

Figure 6.10: Snapshots of velocity field and temperature distribution for the case of hybrid forced/buoyancy convection (*Ri*=1) and cavity with hot bottom wall: a) *Ra*=10^6, b) *Ra*=10^7. A bubble of recirculating flow originating from the leading edge (the step corner) can be seen in all cases.

Figure 6.10 refers to the other case in which the floor is kept at a constant temperature. The most striking change with respect to the situations with larger values of the Richardson number (see again Fig. 6.6) essentially concerns the pre-step area, i.e., x<A/2. Remarkably, for *Ri*=1 no bulges or *corrugation* of the thermal boundary layer can be detected in the left part of the domain even if the largest possible value of the Rayleigh number is considered (*Ra*=10^7 in Fig. 6.10b), which means that there the boundary layer is essentially stable from a fluid-dynamic point of view.

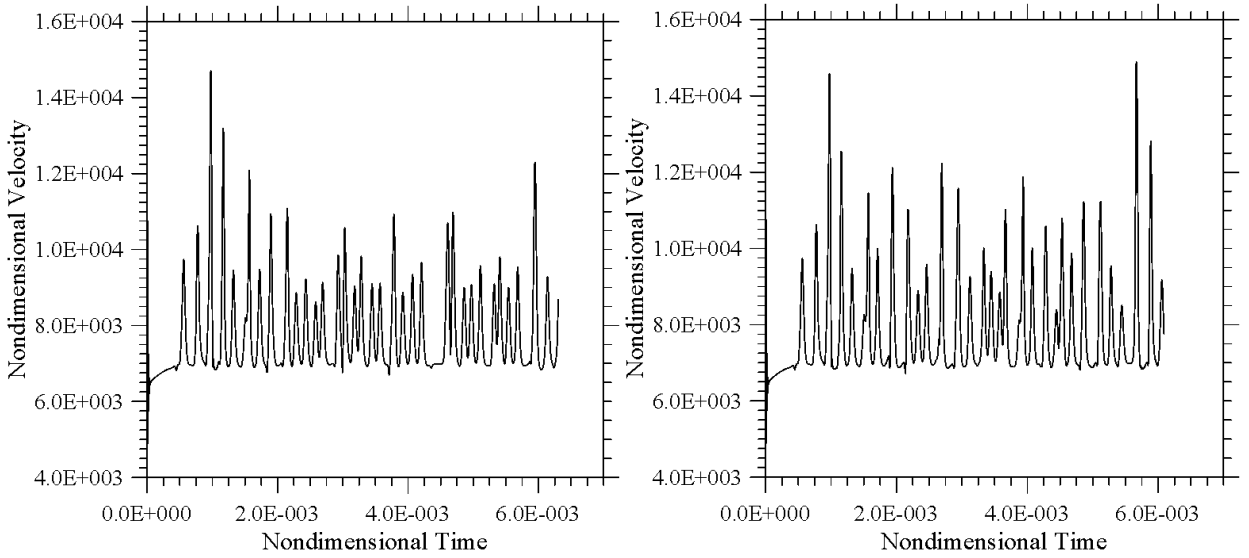

a) b)

Figure 6.11: Velocity signals for *Ri* =1 and *Ra*=10^7 provided by a probe located in the region with reduced cross-sectional area (7.5, 0.75): a) adiabatic floor case (ω≅3.58x10^4), b) hot floor case (ω≅3.38x10^4).

The velocity plot for *Ra*=10^7 (Fig. 6.11) however shows that the flow is highly unsteady in the region located above the step, where the complex interplay between thermal plumes responsible for *vertical* fluid motion and the *horizontal* forced flow results again in a series of "bubbles" (localized regions of vorticity) more or less uniformly spaced along the boundary (which travel

continuously in the downstream direction; the behaviour being similar to that observed for the adiabatic floor case).
Since a bubble of recirculating flow steadily attached to (originating from) the leading edge of the step can be seen in all cases, it can be concluded that hydrodynamic effects play a much important role for relatively small (unit) values of the Richardson number (more specifically, the primary source of disturbances, which for larger values of *Ri* is represented by the relatively strong thermal plume stemming from the step corner is gradually transferred to a strongly unsteady bubble of hydrodynamic nature located in the same area; this concept will be elaborated further in Sect. 6.4).
As already discussed to a certain extent before, however, bubbles are also present along the entire extension of the top surface of the step. On the basis of the present framework, relying on direct comparison of the statistics of the temporally evolving velocity field with the corresponding temperature field, it can be argued that these localized eddies should be simply seen as the limiting condition attained by thermal plumes *folding in on themselves due to the fluid coming from the left*. As shown by both Fig. 6.9b and 6.10b, regardless of the specific thermal condition used for the floor of the duct, their appearance in space is relatively ordered (flow eruptions being created at periodic intervals), this observation being also supported by the regularity of the corresponding velocity fluctuations measured in a fixed point (Fig. 6.11).

6.4. Discussion

In this section some general arguments are elaborated to interpret the trends displayed by the considered system. In particular, such a discussion is supported by the precise determination of *the conditions for the onset of the first Hopf bifurcation* (namely, the critical Rayleigh number to be exceeded to produce oscillatory flow for different values of *Ri*). These data are intentionally used alongside the structure of the related fluid-dynamic "disturbances" to get additional insights into the mechanisms that govern the onset of unsteadiness and the ensuing evolution towards chaos. It is important to remark that, given the nature of the numerical strategy used in the present study (relying on the direct solution of the balance equations for mass, momentum and energy in their complete, time-dependent and non-linear form, as illustrated in Chapter 2), the transition *Ra* has been determined by means of numerical experiments (by increasing it until the flow becomes oscillatory and then increasing/decreasing it in a certain neighbour of the previously found value). The final value has been determined through extrapolation to zero of the amplitude of oscillations. Moreover, the spatial structure of the fluid-dynamic disturbances responsible for the transition from steady to oscillatory flow has been determined 'a posteriori', i.e., by subtracting the time-averaged thermofluid-dynamic field to the instantaneous one for conditions located slightly above the transition point (i.e., *Ra* slightly larger than Ra_{cr}).
Towards the end to elaborate an exhaustive picture of the overall thermofluid-dynamic scenario, a discussion is elaborated for the quantitative data obtained for the heat exchange taking place between the fluid and the wall of the heated step (i.e., its vertical and horizontal boundaries) for

the different situations examined in Sect. 6.1,6.2 and 6.3. For the convenience of the Reader, all this information is organized in the form of synthetic tables and 'maps' where the critical conditions and the Nusselt number are reported as function of *Ra* and *Ri*.

6.4.1 Influence of the Richardson number on the bifurcation scenario

The bifurcation scenario for the system with adiabatic floor is presented in Fig. 6.12. Snapshots of the related disturbances have been collected in Fig. 6.13.

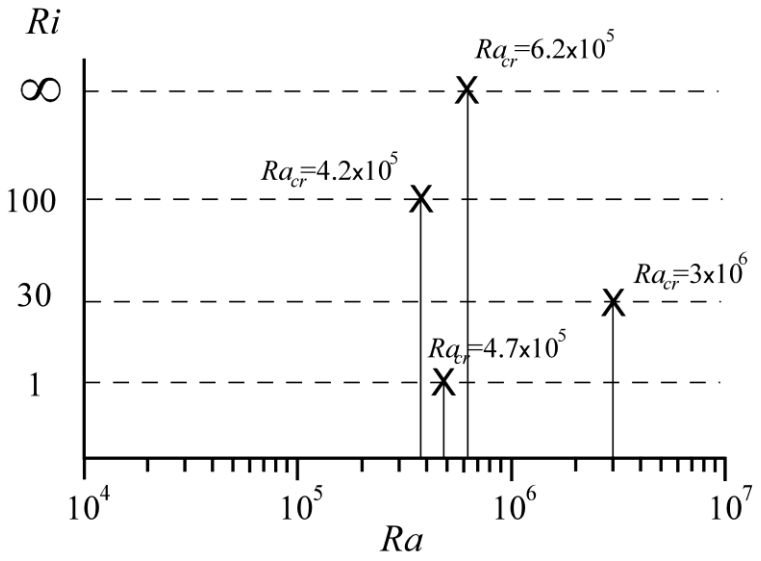

Figure 6.12: Bifurcation scenario for the adiabatic floor case.

On the basis of the numerical results shown in Figs. 6.1, it could have already been concluded that for pure buoyancy with the adiabatic floor the transition from stationary to oscillatory conditions occurs somewhere between $Ra = 10^5$ and $Ra = 10^6$. By means of an extensive parametric investigation conducted by refining iteratively the value of the Rayleigh number in this interval, the value of the *Ra* required for the Hopf bifurcation could be determined as $Ra_{cr} \cong 6.2 \times 10^5$ (see the line corresponding to $Ri \to \infty$ in Fig. 6.12).

A snapshot of the related disturbances (obtained by subtracting the time-averaged velocity field from the instantaneous one) is shown in Fig. 6.13a. This figure is instrumental in showing that the perturbations behave essentially as a wave traveling to the left region of the domain (using the upper branch of the Hadley circulation as a *substrate for propagation*, see Sect. 1.1.4.2). This wave apparently originates from the rolls of RB nature (Sect. 1.1.4.1) located above the step, in proximity to the corner ($A/2<x<3A/4$). Accordingly, it could be argued that the main source of the instability is located just above the step, in the area where the coalescence between the main Hadley circulation and the first roll of the RB series occurs. This observation, in turn, indicates that the transition process is essentially driven by a *competition of the RB and Hadley*

mechanisms in a very localized region. The existence of a wave travelling towards the left (visible in the left part of the cavity) should therefore be seen as a *secondary effect* induced by such a process. Put simply, the interplay of RB and Hadley flow in proximity to the corner is the main oscillatory mechanism that produces a local 'forcing' able to excite a shear-driven wave travelling in the left part of the cavity (where the Hadley flow is dominant). Dynamics of such a kind have been extensively observed in purely Hadley flow problems (buoyancy convection in rectangular containers heated from the side, Le Quéré and Behnia, 1998) where the forcing needed for the excitation the wave is generally provided by boundary layer instabilities or similar phenomena (Ferialdi et al. 2020, Gelfgat, 2020).

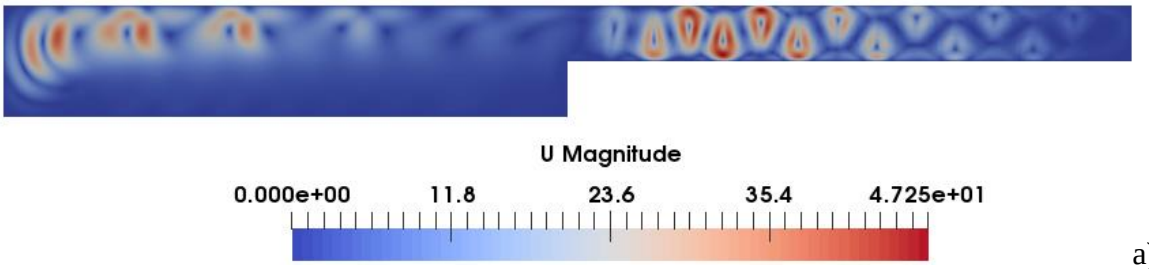

a)

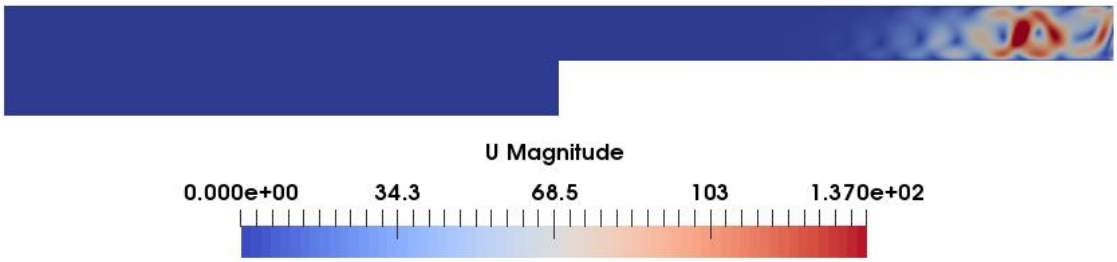

b)

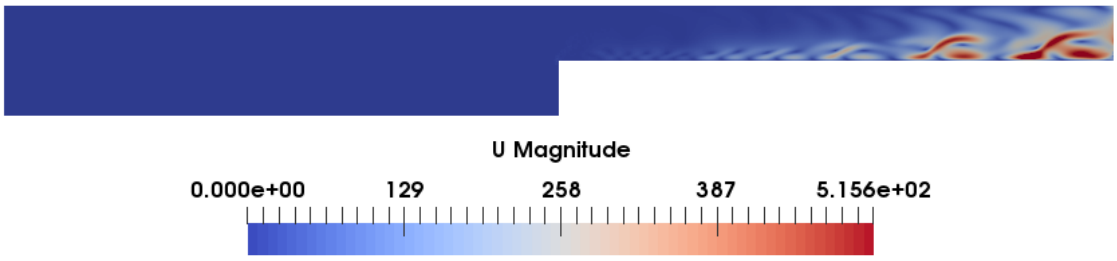

c)

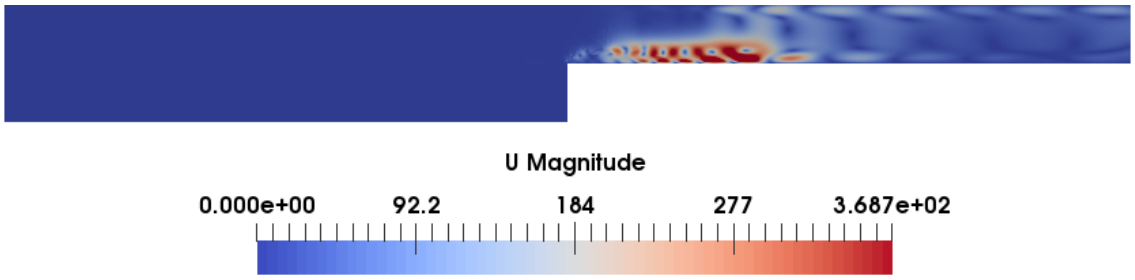

d)

Figure 6.13: Snapshot of the velocity disturbances for the cavity with the adiabatic floor (first Hopf bifurcation): a) $Ri \to \infty$, $Ra \cong 6.6 \times 10^5$, b) $Ri=100$, $Ra \cong 4.3 \times 10^5$, c) $Ri=30$, $Ra \cong 4 \times 10^6$, d) $Ri=1$, $Ra \cong 1 \times 10^6$.

For $Ri=100$, (Fig. 6.12, second line from the top) the value of the critical Rayleigh number decreases appreciably with respect to that obtained in the limit as $Ri \to \infty$. Remarkable changes can also be seen in the mechanism underpinning the instability (as revealed by Fig. 6.13b). The disturbances still manifest themselves in the form of a wave. The location and sense of propagation of this wave, however, are completely different. It is now located in the right part of the domain (the region x>A/2 with reduced cross-sectional extension). Moreover, the disturbances travel in the downstream direction with respect to the forced flow, i.e., from left to right (it was in the opposite sense for $Ri \to \infty$).

The key to understanding this behaviour lies in considering the competition between convection of the RB type and forced flow. While the former tends to create localized eruptions of hot fluid directed upwards (thermal plumes), the latter tends to displace fluid in the horizontal direction. The instability is essentially a result of the interplay of these two concurrent convective mechanisms along the entire top surface of the step.

A further decrease in the Richardson number ($Ri=30$), make obviously the contribution brought in by forced convection more important. This is indeed reflected by the morphology of disturbances. As a fleeting glimpse into Fig. 6.13c would confirm, λ-shaped disturbances essentially develop *inside the thermal and kinematic boundary layers* (which for Pr=1 have obviously comparable thickness). The required value of the Rayleigh number undergoes a significant increase, and a justification for this behaviour can be rooted directly in the nature of the disturbances per se (which, unlike those shown in Fig. 6.13b, are now forced to grow inside the boundary layer).

Figure 6.13d is extremely useful as it reveals that the main mechanism responsible for the development of unsteady flow is transferred from that associated with the propagation and growth of disturbances in the boundary layer for $Ri=30$, to a different process where disturbances are essentially produced inside the recirculating bubble of limited extension, which originates from the leading edge for $Ri=1$.

As a concluding remark for this analysis, it is important to highlight that the continuous switch from one instability mechanism to another as the Richardson number is varied should be regarded as a relevant justification for the scattered appearance of the critical points in Fig. 6.12.

The distribution of critical parameters for the companion configuration with the hot floor is illustrated in Fig. 6.14.

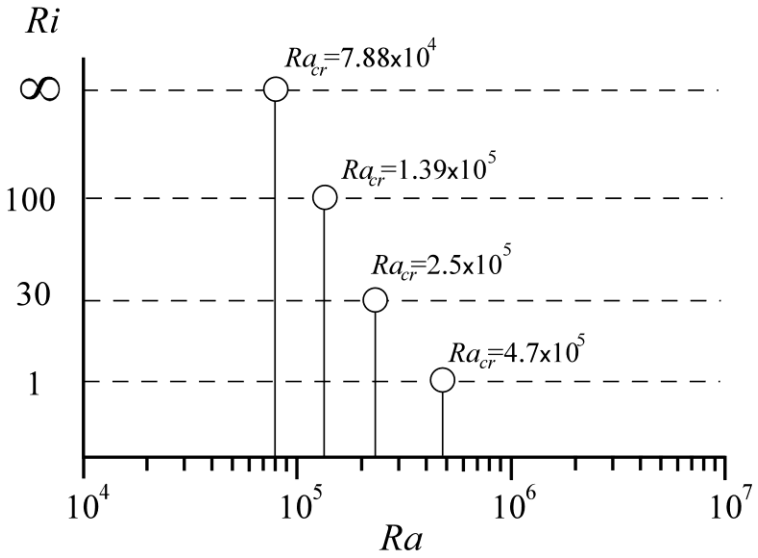

Figure 6.14: Bifurcation scenario for the hot floor case.

This figure and the companion sequence of fluid-dynamic disturbance snapshots collected in Fig. 6.15 indicate that interpreting the role played in such dynamics by the thermal conditions adopted for the floor (x<A/2) is not as straightforward as one would imagine.

As implicitly evident in Fig. 6.14, the instability scenario dramatically changes. As already indicated by the preliminary analysis (Sect. 6.1) conducted by progressively increasing the order of magnitude of the Rayleigh number, the transition to oscillatory flow for pure buoyancy flow ($Ri\rightarrow\infty$) takes place earlier for the hot floor in comparison to the adiabatic case (for a smaller *Ra*, i.e., $Ra_{cr}\cong 7.88\text{x}10^4$, determined using the same approach discussed before, see the line of Fig. 6.14 corresponding to $Ri\rightarrow\infty$). A striking difference can be spotted when the spatial structure of the related disturbances is considered (Fig. 6.15a). Fluid-dynamic perturbations keep on originating from the corner of the step as a result of the significant amount of vertical shear produced by the inclined thermal plume located there (as shown in Fig. 6.4 this plume is always inclined to the left). In this case, however, no wave traveling to the left is generated owing to the lack of a horizontal current of the Hadley type which can support it (Sect. 1.1.4.2).

An explanation for the decrease in the value of the critical Rayleigh number with respect to the equivalent configuration with the adiabatic floor can be elaborated in its simplest form on the basis of the argument that the system is entirely dominated (over its entire horizontal extension) by pure RB convection (Sect. 1.1.4.1). This leads to a significant *increase in the strength of the main thermal plume* originating from the corner of the step and in the ensuing associated shear stress responsible for the onset of the oscillatory instability (Pera and Gebhart, 1971; Desrayaud and Lauriat, 1993; Cortese and Balachandar, 1993; Vincent and Yuen, 1999).

As revealed by Fig. 6.15b (*Ri*=100), if a forced flow is superimposed on thermal convection, the disturbances generated by the corner plume (which changes its inclination in order to align with the forced flow) are transported in the downstream direction, thereby exciting a response that develops in the form of weak rolls superimposed on the horizontal current (it can be seen that the amplitude of this disturbance is amplified as it travels towards the outlet).
Interestingly, as quantitatively substantiated by the data reported in Fig. 6.14, a decrease in *Ri* has in general a beneficial effect in terms of critical Rayleigh number, i.e., Ra_{cr} becomes higher (the trend is monotonic). In other words, the presence of forced flow has a *stabilizing influence* on the overall dynamics, which requires a proper interpretation too.
The reader could be led to a heuristic realization of the related underlying cause-and-effect relationship by simply considering that, as already explained to a certain extent in the previous text, the instability of mixed forced-buoyancy convection is essentially driven by the competition of these two different mechanisms of convection. The tendency of hot fluid to rise vertically and the effect of the imposed horizontal flow that acts to bend it to the right (eventually causing the reattachment of the boundary layer) is the main mechanism leading to the unsteady production of vorticity in the form of "bubbles" which travel in the downstream direction. A decrease in *Ri*, i.e. an increase in the relative importance of forced flow with respect to thermal buoyancy, must necessarily correspond to higher values of the Rayleigh number needed to *excite the competition of buoyant and forced flow in the duct*.

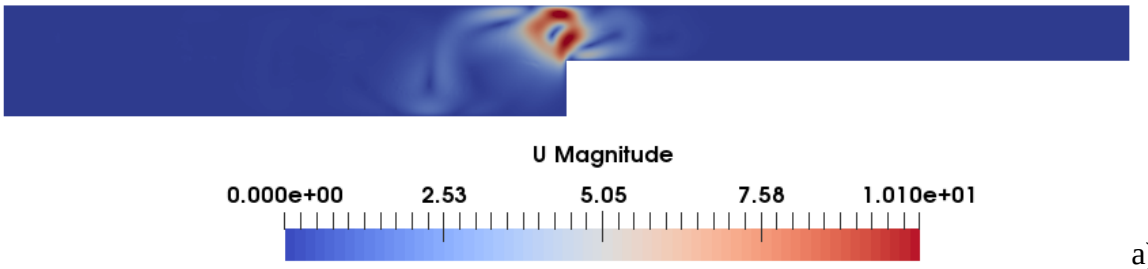

a)

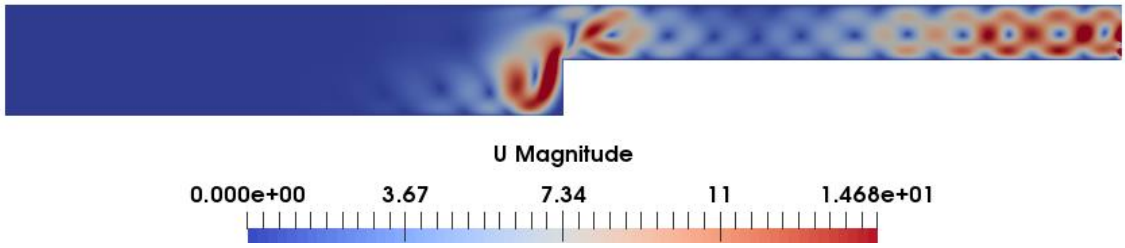

b)

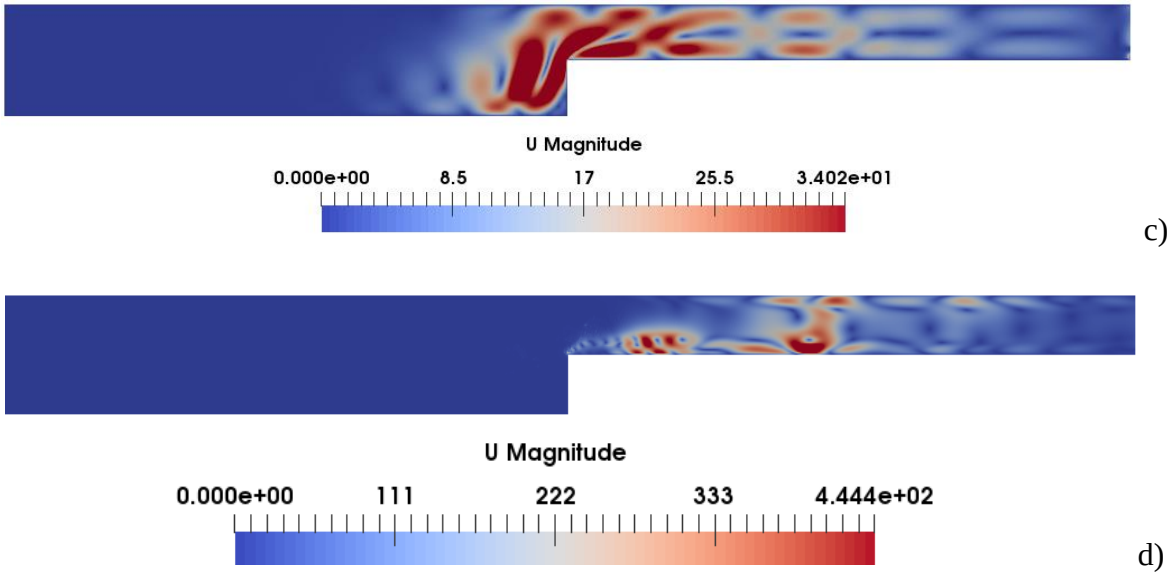

Figure 6.15: Snapshot of the velocity disturbances for the cavity with the hot floor, (first Hopf bifurcation): a) $Ri \to \infty$, $Ra \cong 7.89 \times 10^4$, b) $Ri=100$, $Ra \cong 1.5 \times 10^5$, c) $Ri=30$, $Ra \cong 3 \times 10^5$, d) $Ri=1$, $Ra \cong 1 \times 10^6$.

As witnessed by Fig. 6.15c, as *Ri* is decreased from 100 to 30, there is a small variation in the required value of the Rayleigh number and disturbances still take their energy from the main plume that originates from the leading edge. Comparison with the equivalent case with the adiabatic floor (Fig. 6.13c), indicates that the much higher value of Ra_{cr} in that case is due to the lack of the strong thermal plume located at $x \cong A/2$ (among other things, this observation also provides a justification for the different level of complexity displayed by the signals in the left and right panels of Fig. 6.8; the more complex spectrum for the hot floor case is obviously due to the two orders of magnitude of distance between $Ra=10^7$ and the Ra_{cr}).
For *Ri*=1, the corner plume finally collapses in a region of recirculating flow attached to the leading edge, thereby making the main instability mechanism for the hot floor case equivalent to that already discussed for the adiabatic floor configuration (as also indirectly confirmed by the fact that the critical Rayleigh number is essentially the same). Another way to think about this behaviour is to consider that for such circumstances the dynamics produced by buoyancy convection in the pre-step area ($x<A/2$) have an almost negligible influence on the mechanisms supporting the instability (which further confirms our interpretation about the more important role played by hydrodynamic disturbances in this case).

6.4.2 Heat Exchange

With the only exception of the purely diffusive state, in general, for the adiabatic floor configuration $Nu_{step}^{vert} > Nu_{step}^{horiz}$ (Table 6.1). This result is not unexpected. For the case of pure

buoyancy convection, a simple rationale for this behaviour can be elaborated taking into account the relative importance (or magnitude) of the buoyancy forces at work in the left (x<A/2) and right (x>A/2) regions of the physical domain. As the intensity of this force is known to scale with L^3 where L is the effective depth of the considered region, this fundamental dependence is the key ingredient needed to formulate a justification for the different magnitude of the Nusselt number related to the two sides of the step. Under a slightly different perspective, the same concept could be re-introduced basing it directly on the 'effective' Rayleigh number experienced by the fluid in the two sides of the cavity (that affecting the fluid located in the region x>A/2 being eight times smaller than that effective for x<A/2). Put simply, as the vertical side "feels" the strong convective cell of the Hadley type established in the left portion of the domain, the intensity of heat exchange along this wall is obviously higher (while the horizontal side is only subjected to the weak rolls of the RB type emerging there).

A similar argument holds when finite values of the Richardson number are considered (even though this case calls for a complementary explanation). For such a situation, for a given value of the Rayleigh number the velocity of fluid rising along the vertical side of the step is even higher than that produced for pure buoyancy convection. Such an increase in velocity obviously follows from the presence of two concurrent mechanisms driving the fluid along the vertical wall, namely, the buoyancy effect (which forces fluid to rise) and the additional upward velocity produced by the imposed flow (which forces fluid to turn around the step). Therefore, the reason for the even larger difference between Nu_{step}^{vert} and Nu_{step}^{horiz} when the values Ri = 30 and Ri =100 is considered resides in the presence of these two aiding (reciprocally reinforcing) effects.

Table 6.1: Nusselt number as a function *Ra* and *Ri* for the adiabatic floor case.

Ra	*Ri*	Nu_{step}^{horiz}	Nu_{step}^{vert}	Regime
0	N/A	2.0417	1.6731	Purely Diffusive
10^4	∞	2.0077	4.6240	Steady
10^5	-	5.6375	9.4742	Steady
10^6	-	9.8594 (average)	17.5227 (average)	Quasi-periodic
10^7	-	16.5836 (average)	30.9278 (average)	Moderately Turbulent
10^4	100	1.2987	5.6315	Steady
10^5	-	3.2347	10.6367	Steady
10^6	-	6.3597(average)	19.7056 (average)	Multi-frequency spectrum
10^7	-	16.5881(average)	35.8678(average)	Moderately Turbulent

10^4	30	2.2856	5.8999	Steady
10^5	-	4.1605	10.8647	Steady
10^6	-	6.1746 (average)	20.0669(average)	Steady
10^7	-	13.1961 (average)	36.3426 (average)	Time-periodic
10^4	1	5.1047	9.2652	Steady
10^5	-	7.6590	15.6639	Steady
10^6	-	12.7710 (average)	26.4171 (average)	Quasi-Periodic
10^7	-	39.07695 (average)	45.4150 (average)	Unsteady with dominant frequency

Table 6.2: Nusselt number as a function *Ra* and *Ri* for the hot floor case.

Ra	*Ri*	Nu_{step}^{horiz}	Nu_{step}^{vert}	Regime
0	N/A	2.0329	0.8782	Purely Diffusive
10^4	∞	2.0113	0.9457	Steady
10^5	-	5.6299	1.6408	Periodic
10^6	-	10.8293 (average)	3.0102 (average)	Periodic
10^7	-	18.6177 (average)	8.0191 (average)	Weakly Turbulent
10^4	100	0.2390	0.3284	Steady
10^5	-	1.4868	2.0256	Steady
10^6	-	5.5144 (average)	7.1233 (average)	Multifrequency
10^7	-	14.2736 (average)	19.5536 (average)	Moderately Turbulent
10^4	30	1.0157	0.9922	Steady
10^5	-	2.6784	2.7333	Steady
10^6	-	6.1050 (average)	8.2020 (average)	Multifrequency
10^7	-	16.1624 (average)	24.7982 (average)	Moderately Turbulent
10^4	1	3.6248	2.5971	Steady
10^5	-	5.4746	4.8390	Steady
10^6	-	10.2654 (average)	8.9180 (average)	Quasi-Periodic
10^7	-	38.1026 (average)	16.5762 (average)	Unsteady with dominant frequency

The data for the companion case with hot floor are quantitatively presented in Table 6.2. Careful comparison with Table 6.1 reveals a significant *lowering* of Nu_{step}^{vert}, which requires a proper justification.

In particular, a straightforward interpretation can be sought directly in the temperature distribution. In this regard, coming back to the results shown in Figs. 6.4, 6.6 and 6.10 is extremely useful; once again, these figures clearly show the presence of well-defined thermal (hot) boundary layers developing along the (hot) horizontal floor of the duct. To emphasize further the significance of this observation, one should keep in mind that, unlike the configuration with the adiabatic bottom (where all the fluid transported towards the step is cold), for these cases, fluid that has already acquired a significant amount of heat tends to be entrained into the boundary layer developing along the vertical step wall. The reduced temperature difference between the incoming fluid and the temperature of the step itself can obviously be regarded as the main factor contributing to the generalized observable shrinkage in the values of Nu_{step}^{vert}.

6.4.3 Critical comparison with compact cavity:

After clarifying the patterning behaviour and the related disturbances emerging for different values of *Ra* and *Ri*, in this section a comparison is made between the compact cavity case treated in Chapter 5 and the elongated channel considered in the present chapter. For the comparison, the value of *Ri*=1 is considered for which the forced convection and buoyancy convection have similar strength.

It is important to recall that for the compact cavity case with aligned inflow and outflow section, the value of the critical parameter for both adiabatic and hot floor was determined as $Ra_{critical} \cong 1.2 \times 10^6$ whereas for an elongated channel with FFS the value of the critical parameter is $Ra_{critical} \cong 4.7 \times 10^5$. The difference in the values of critical Rayleigh number can be attributed to the difference in the location of fluid dynamic disturbances and intensity. The disturbances in both cases have a significant hydrodynamic component due to the strong forced convection present inside the domain. For the case with elongated channel, disturbances of hydrodynamic oscillatory nature tend to develop inside the localised recirculating bubble originating from the step corner. By contrast, for the compact cavity case with aligned inlet and outlet, such a recirculation bubble is not formed near the corner of the step and a suitable justification for this can be found in the inability of the flow to directly strike the hot step. A recirculation bubble is typically observed when the flow comes in direct contact with an obstacle, however this behaviour is not observed due to the position of the inlet not being aligned with the step. Consequently, for both adiabatic and isothermal floor case, the disturbances instead of being localised near the step corner are seen to occupy the almost entire upper right portion of the compact cavity demonstrating a strong vertical shear driven nature. The hydrodynamic disturbances present inside elongated channel are stronger due to the much more abrupt variation

undergone by the flow in terms of curvature, which explains why the related critical value if smaller.

The understanding could be further increased by making a comparison between the elongated channel and compact cavity with misaligned inlet and outlet. The value of the Ra_{cr} for misaligned inflow and outflow case was determined as $Ra_{critical} \cong 3.8 \times 10^6$ and $Ra_{critical} \cong 3.2 \times 10^6$, for the cavity with adiabatic and hot floor, respectively. Again, it can be observed that these values are still higher as compared to Ra_{cr} values for elongated channel with FFS and it is worth examining the disturbances again. The disturbances for the misaligned inflow and outflow section (Fig. 5.17) are of shear driven nature essentially located above the step and left lower portion of the cavity. The role of buoyancy in inducing additional disturbances is very limited for the adiabatic and hot floor case which is a major difference in comparison to the elongated channel with FFS where the combined role of thermal and hydrodynamic effects was observed. This difference could be attributed to decrease horizontal extension in the compact cavity case which for the elongated channel serves as a breeding ground for the emergence of hot vertical convective structure (thermal plumes).

It is important to highlight that the quicker onset of oscillatory flow for the elongated channel also occurs due to the presence of relatively strong hydrodynamic perturbations which originates as a result of increased injection of cold fluid inside the domain. Such hydrodynamic effects are weaker inside the compact cavity where a small amount of fluid enters the domain through a small inlet (having a non-dimensional vertical extension d=0.1).

6.5. Conclusions

The main conclusions of the present chapter can be summarized as follows:

- When the floor of the region preceding the step is adiabatic a change from the condition $Ri=\infty$ to finite Ri causes a dramatic variation in the system oscillatory response and related patterning behaviour. While for pure buoyancy the Hopf bifurcation must be ascribed to an instability of the leftward directed current of the Hadley type originating from the step corner, for finite Ri=100, it manifests in the form of plumes that periodically nucleate at a certain distance (in the downstream direction) from the step corner and travel to the right.
- An increase in Ra at fixed Ri (yet for the thermally insulated floor) has a very interesting effect. Plumes are produced at a much smaller distance from the leading edge. Moreover, their extension in the vertical direction becomes progressively smaller, which can be interpreted taking into account the dual influence of a simultaneous increase of Ra and Re (the former contributing to make plume caps smaller, the latter reducing the available time for their stem to grow before they leave the domain through the outflow section).
- Regardless of the considered thermal condition for the floor preceding the step, when turbulent conditions are attained the overall frequency spectrum is shifted to the right

with respect to the case of pure buoyancy, i.e. for *Ri*=100 the energy tends to reside on smaller temporal scales (which indicates that new instability mechanisms are enabled with respect to the situation with pure buoyancy convection).

- A decrease in *Ri* (*Ri*=30), forces the disturbances to develop inside the thermal and kinematic boundary layers (which for Pr=1 have the same thickness).
- When the Richardson number is finally reduced to 1, the primary source of disturbances, which for larger values of *Ri* is represented by the relatively strong thermal plume originating from the step corner is gradually transferred to a strongly unsteady bubble located in the same area; hydrodynamic effects play a much important role in these cases; the kinematic boundary layer along the upper surface of the step separates and reattaches continuously (due to plumes being continuously formed and the imposed horizontal flow that quickly bends them).
- Another outcome of the focused comparison of the fundamental situations with adiabatic and bottom floors is that the dynamics of the boundary layer established along the vertical side of the step can play a crucial role in determining the heat exchange in this region.
- For the adiabatic floor case, the vigorous upward fluid motion is responsible for the higher values taken by the Nusselt number along the vertical wall (with respect to the corresponding value for the horizontal side of the step).
- When the bottom wall of the duct is kept at fixed hot temperature, the additional heat entrained into the vertical boundary layer is the main reason for which Nu_{step}^{vert} undergoes an appreciable decrease.

Chapter 7

Hybrid Forced-buoyancy convection in a channel with a backward-facing step

As evident from the title, in this chapter attention is paid to the BFS configuration. Prior to expanding on the results, for the convenience of the reader, the initial part of this chapter is used to provide some initial arguments which may help him/her to digest better some of the peculiar dynamics and related concepts presented in the following.

Along these lines, a start is made from the relatively simple remark that, given their intrinsic nature, thermally driven convective flows generally tend to emerge in the form of vertical currents potentially producing 'blockage' in the considered duct (in contrast to the diametrically opposite effect induced by the expansion in the available cross-sectional area). In addition to the hydrodynamic instabilities, known to affect the shear layer originating from the corner of the step and impinging on the bottom wall at $x=x_1$, the instabilities of the thermal boundary layer along heated surfaces can also become a relevant aspect of the problem.

By analysing situations where the forced transport of fluid in such a configuration closely interacts with natural convective phenomena of thermal origin, the aim is to reveal a variety of possible situations in which thermally driven effects support or counteract the emergence of flow instabilities. Towards this end, in particular, a deductive process is followed by which the Richardson number is progressively increased (the limiting situation $Ri \rightarrow 0$, being representative of the case with forced flow only). As a first relevant example along this analysis hierarchy, the cases $Ri<1$ and $Ri=7.5$ are considered (Sects. 7.1 and 7.2, respectively).

7.1. Dominant Forced convection Ri≤O(1)

Before starting to deal with the hybrid forced/buoyant flow, Fig. 7.1 provides an instructive short excursus on the case of forced flow (no buoyancy). This is intentionally used to bridge the gap with the earlier literature and recall the main properties of the simplified configuration with no thermal effects (a pre-requisite for the interpretation of more complex dynamics where buoyancy plays a significant role). The related sequence of figures (Figs. 7.1a-7.1d) merely shows that, as anticipated in the introduction, for a fixed expansion ratio, the location of the reattachment point is shifted in the downstream direction as the Reynolds number is increased. This figure also provides a glimpse of the more complex dynamics that are enabled when Re exceeds a given threshold (the first Hopf bifurcation occurring for $Re_{cr} \cong 2090$ according to the present simulations).

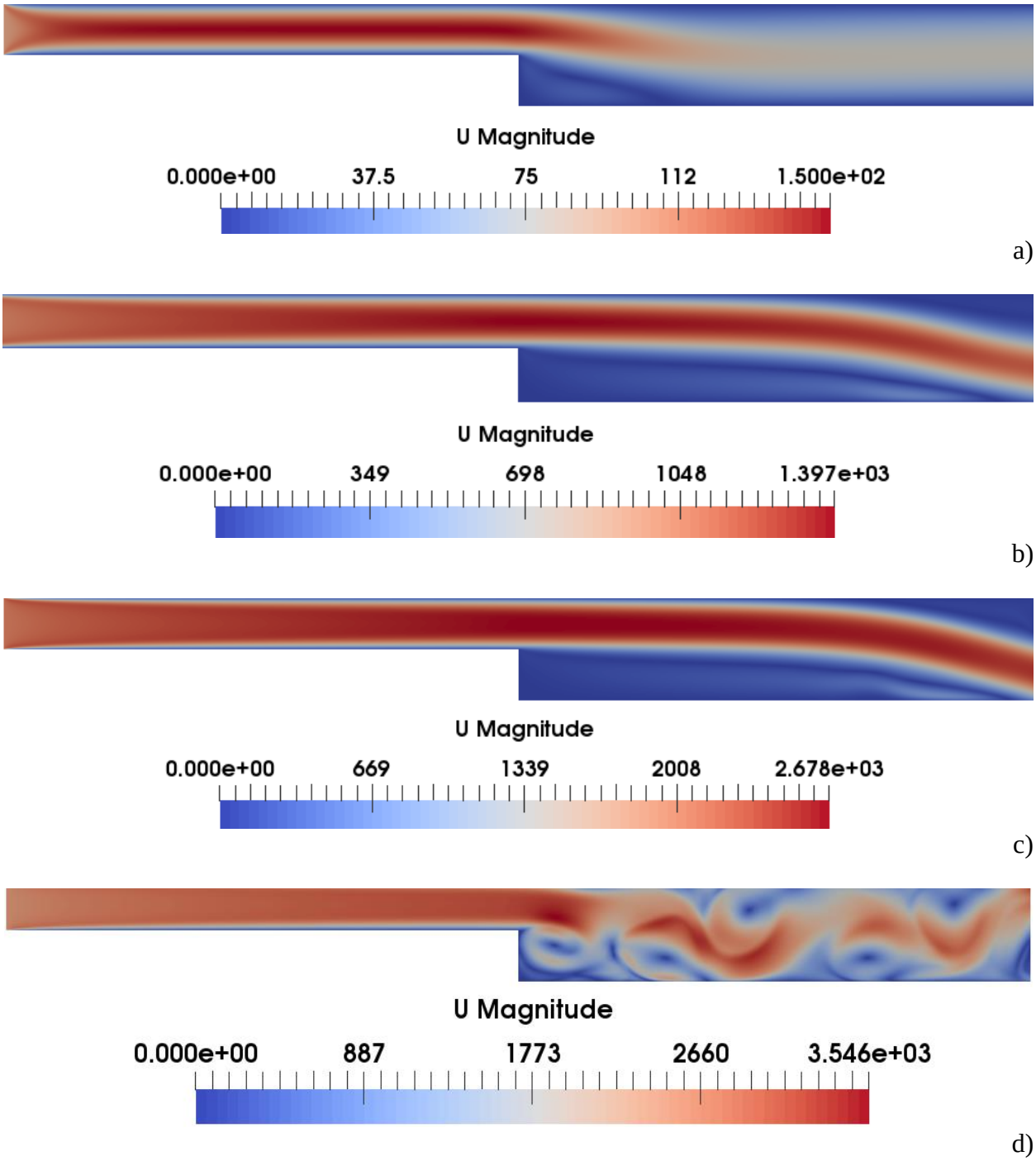

Figure 7.1: Forced convection for increasing values of Re (*Ra*=0): a) Re=100, b) Re=1000, c) Re=2090, d) Re=2500.

In the remainder of this section the focus is shifted to the scenario where, although, thermal effects are present (*Ri*≠0), forced flow is much stronger than buoyancy convection i.e. *Ri* =0.25. For simplicity, first the configuration with adiabatic floor is examined, i.e. the case where the

main flow is discharged into an ambient with larger cross-sectional area (x>A/2) where no thermal convection is being produced (see Fig. 7.2). Increasing values of the Rayleigh number are considered for fixed *Ri*.

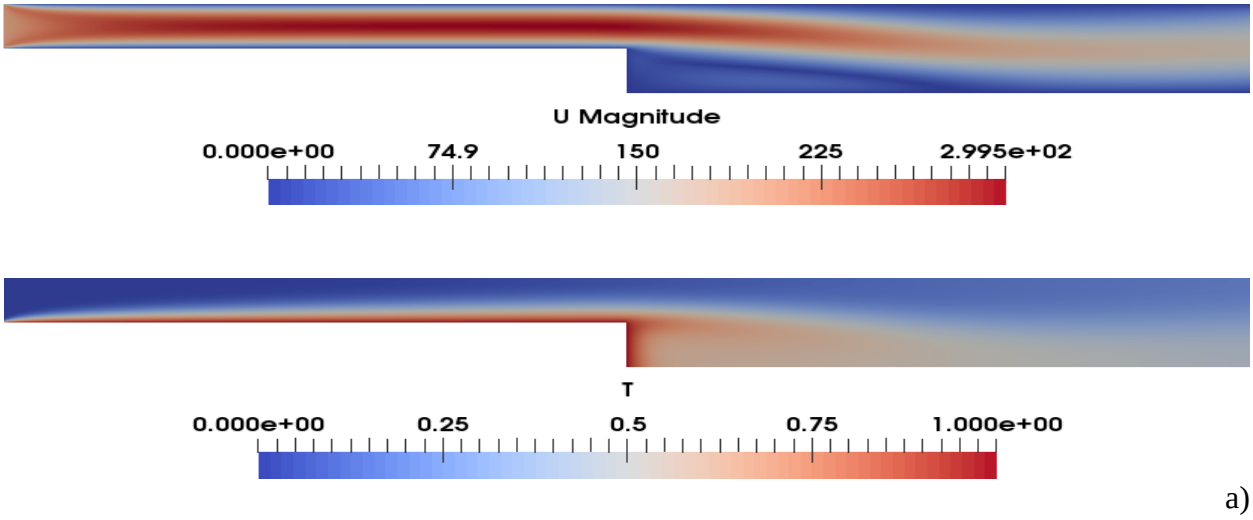

a)

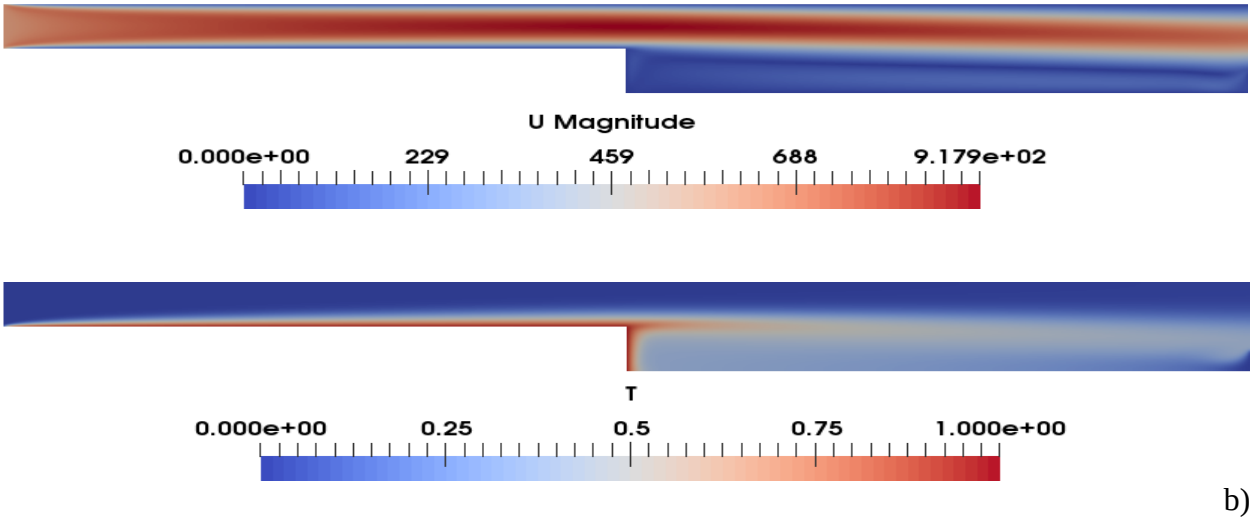

b)

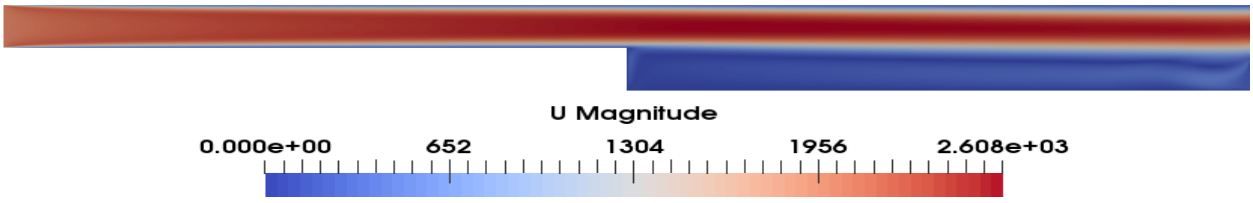

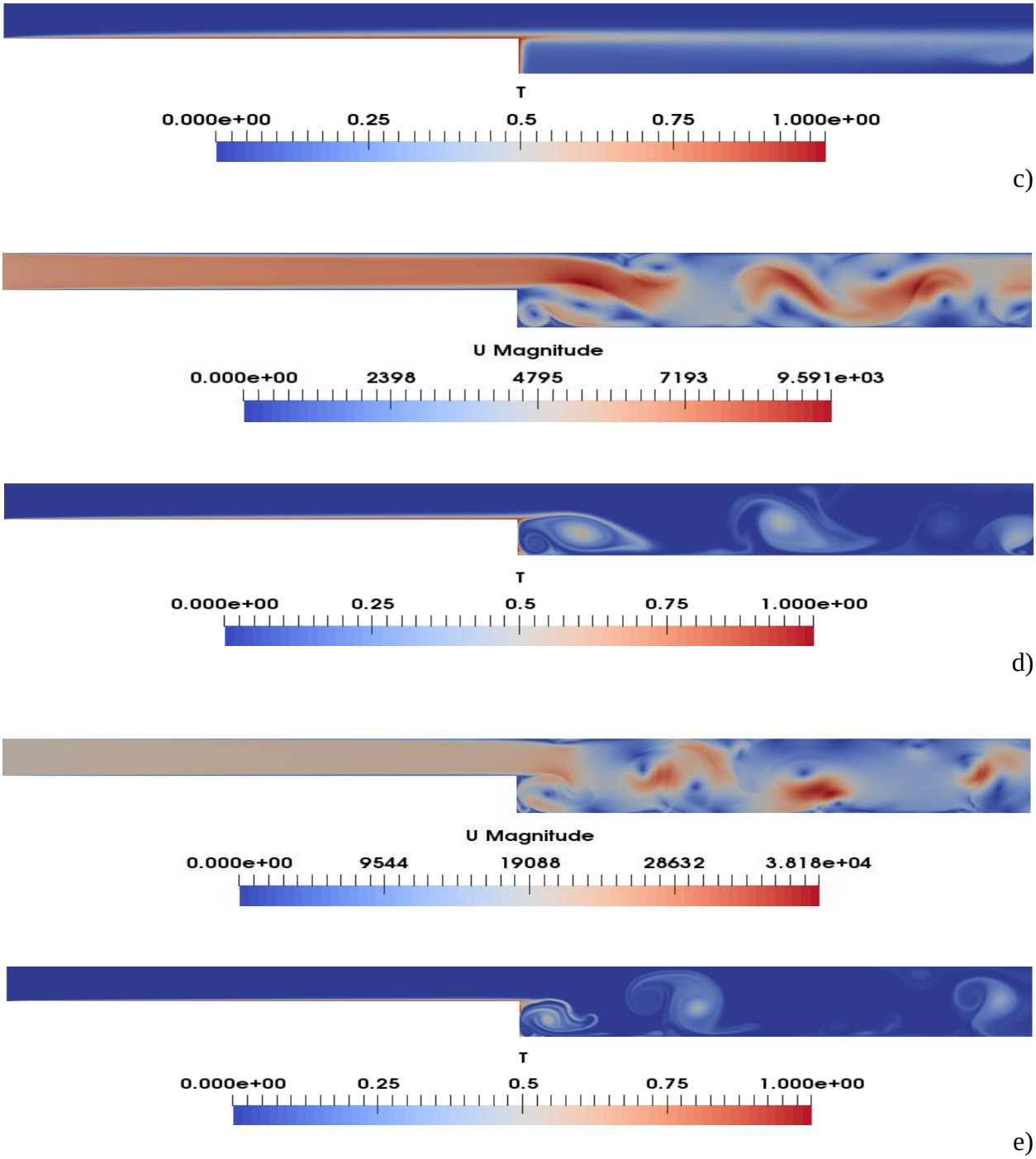

Figure 7.2: Snapshots of velocity field (top) and temperature distribution (bottom) for the case of dominant forced convection (*Ri*=0.25), and cavity with adiabatic floor: a) $Ra=10^4$; b) $Ra=10^5$; c) $Ra=10^6$; d) $Ra=10^7$; e) $Ra=10^8$.

The velocity distribution for $Ra=10^4$ and Re=200 ($Re \cong (Ra/RiPr)^{1/2}$) confirms the presence of a roll near the vertical step boundary (Fig. 7.2a). The horizontal size of this roll grows as *Ra* and Re are increased to 10^5 and 632, and 10^6 and 2000, respectively (Fig. 7.2b and Fig. 7.2c). Inspection of the associated temperature distributions does not reveal unexpected features. Thermal boundary layers develop along the heated surfaces (with thickness decreasing as the characteristic numbers grow while keeping *Ri* fixed to 0.25). An additional "free" layer of warm fluid originates from the step trailing edge (the corner) and marks the boundary between the primary roll and the overlying jet of cold fluid directed from left to right.

In agreement with the results for the purely forced convection, the flow undergoes a transition from a steady state to a time dependent for a value of the Reynolds number close to 2000 (a clearly time-dependent solution can be seen Fig. 7.2d for $Ra=10^7$, Re=6324, although some signs of such a transition can already be detected in Fig. 7.2c in proximity to the outlet). Several velocity rolls are formed in this case, one next to the vertical step (associated with flow separation) and others along the ceiling. Furthermore, the kinematic boundary layer separates and reattaches at two more points along the floor.

This behaviour is also indirectly revealed by the temperature field which shows the presence of thermal plumes at those particular points. The fluid rises and separates as a result of plume formation, anyhow the reattachment quickly occurs afterwards. A similar effect was already observed in previous studies described in Chapter 6 dealing with mixed convection in the FFS.

The flow becomes even more chaotic (moderately turbulent) for $Ra=10^8$ (Fig. 7.2e). Thermal plumes are still formed, but they are strongly bended by the cross flow which forces them to adopt a spiral like configuration.

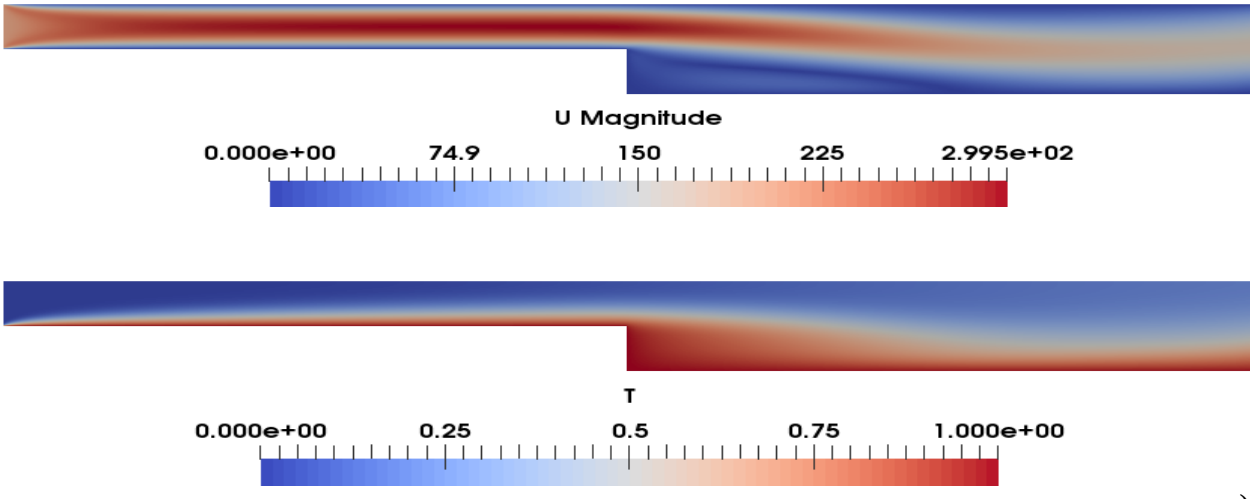

a)

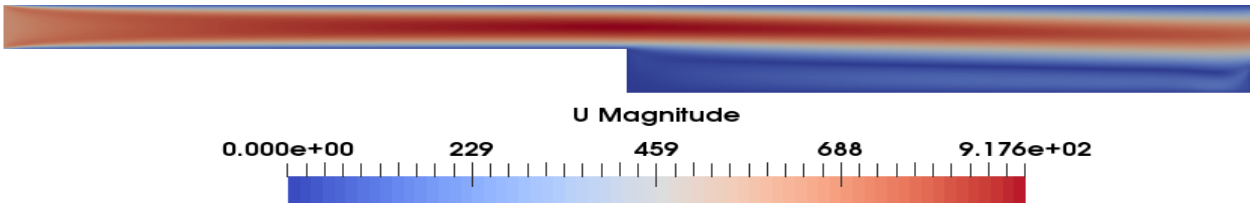
U Magnitude
0.000e+00
229
459
688
9.176e+02

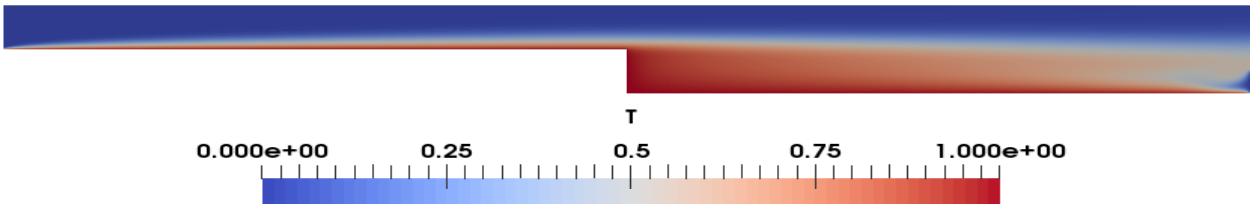
T
0.000e+00
0.25
0.5
0.75
1.000e+00

b)

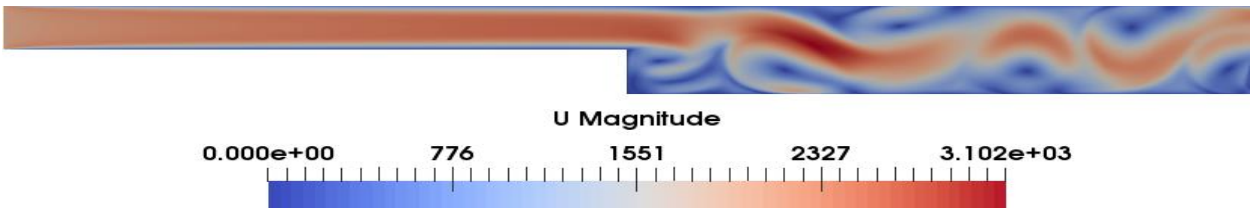
U Magnitude
0.000e+00
776
1551
2327
3.102e+03

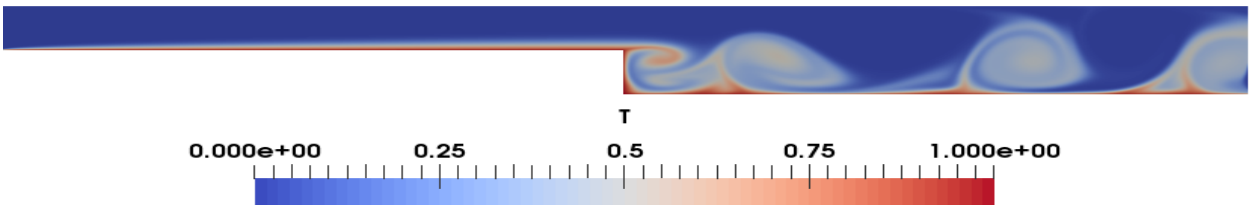
T
0.000e+00
0.25
0.5
0.75
1.000e+00

c)

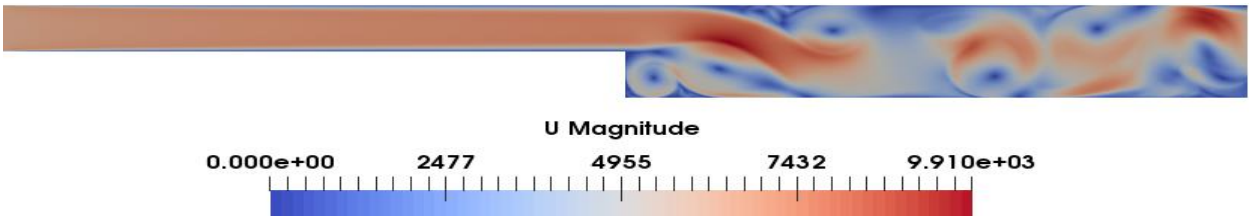
U Magnitude
0.000e+00
2477
4955
7432
9.910e+03

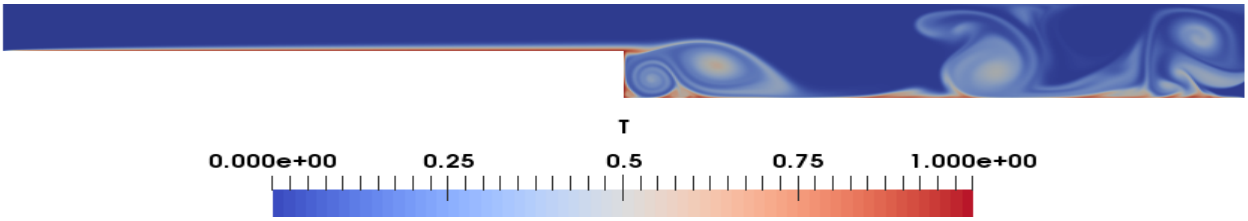
T
0.000e+00
0.25
0.5
0.75
1.000e+00

d)

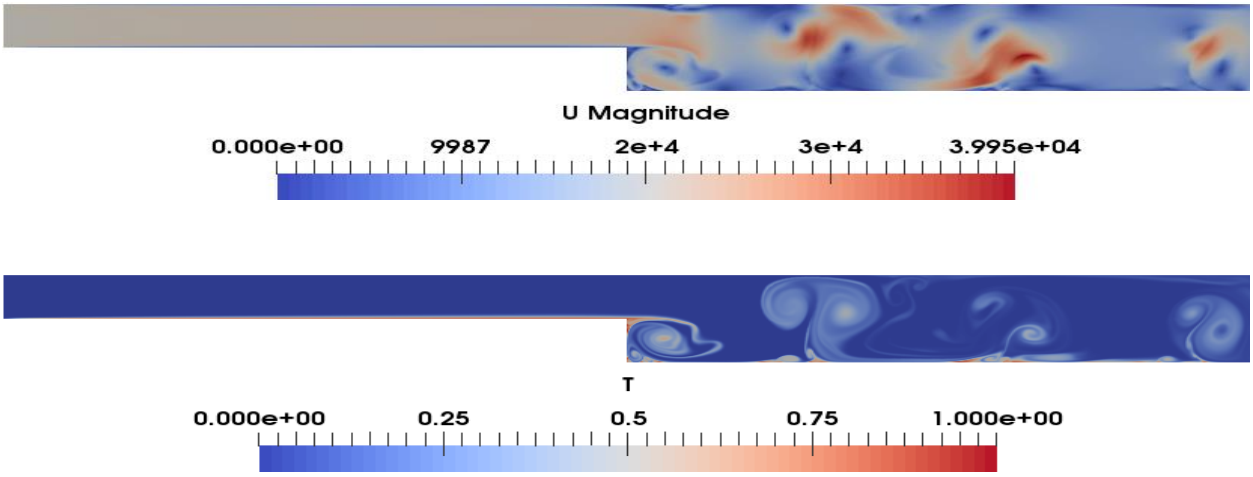

e)

Figure 7.3: Snapshots of velocity field (top) and temperature distribution (bottom) for the case of dominant forced convection (*Ri*=0.25), and cavity with hot floor: a) $Ra=10^4$; b) $Ra=10^5$; c) $Ra=10^6$; d) $Ra=10^7$; e) $Ra=10^8$.

Figure 7.3 represents the case with the floor (bottom boundary for x>A/2) heated at constant temperature. For $Ra=10^4$ and 10^5 the differences with respect to the dynamics already discussed for the adiabatic floor configuration are relatively limited, and they simply affect the temperature field (where an increase in the average temperature in the portion of the channel with larger cross-sectional area can be noticed). Nevertheless, it can be seen that when $Ra=10^6$, the flow undergoes a well-defined oscillatory behaviour (not present in the equivalent adiabatic case for Re=2000, compare Fig. 7.2c). As evident in Fig. 7.3c, thermal plumes are generated continuously along the hot boundary and assume a configuration where they are almost equally spaced along the horizontal direction (as a thermal plume leaves the system through the outflow, a new plume is generated just after the step so that on average the number of plumes present in the system is constant (N=3). This train of plumes traveling in the downstream direction causes a regular sinusoidal distortion of the main jet of cold fluid directed from left to right.
For $Ra=10^7$ and $Ra=10^8$ (see Figs. 7.3d and 7.3e, respectively), the behaviour becomes more complex, with the space separating the plumes and their average number not being constant. Moreover, a decrease in their vertical size and an increase in their number can be noticed.
Some additional insights into the role played by buoyancy in such relatively chaotic dynamics can be gathered from the frequency spectrum obtained using the signal of a virtual probe located at a fixed (representative) position (placed at a certain downstream distance from the step, i.e. x=9, y=0.25, see Fig. 7.4). This indicates that the spectrum aligns with the $k^{-5/3}$ law predicted by Kolmogorov for the so-called inertial frequency range (corresponding to the interval of wavenumbers where energy cascades at a constant rate, until it is dissipated due to viscous effects on the so-called Kolmogorov length scale). A similar correspondence has also been observed in other somehow related problems for instance, standard Rayleigh-Bénard convection (De et al. 2017), the FFS system in Chapter 6 or the case of a wind current interacting with a

distribution of hot blocks (Lappa, 2019). In the present case, comparison of the frequency spectra for the cases with adiabatic and hot floor reveals that the differences are almost negligible (note the peak-to-peak almost perfect correspondence) and quite an obvious interpretation for this behaviour can be directly rooted in the nature of the considered flow, which for $Ri<1$ may still be regarded as an essentially forced flow (the contribution of buoyancy being marginal).

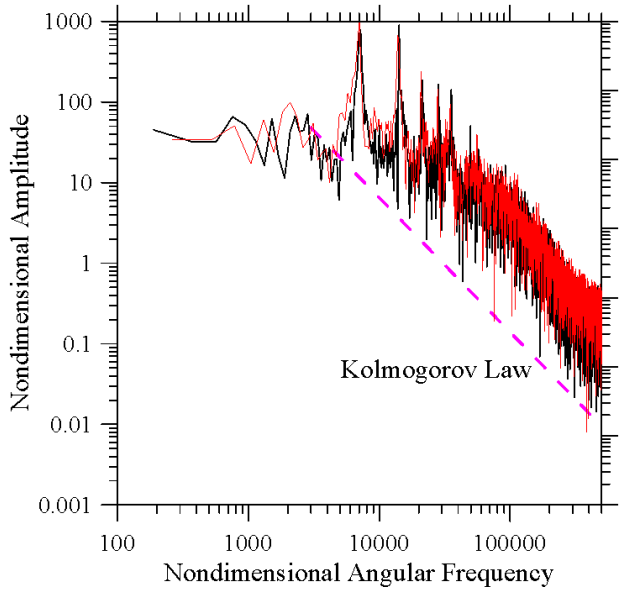

Figure 7.4: Frequency spectrum for Ri=0.25 and Ra=10^7 (Legend: black - adiabatic floor, red - hot floor, magenta – reference Kolmogorov law).

7.2 Mixed convection for Ri=7.5

If the Richardson number is increased to 7.5 (Fig. 7.5 for the adiabatic floor case), for the smallest value of the Rayleigh number considered, namely, Ra=10^4, the flow is still steady and follows a straight path after entering the channel through the inlet (Fig. 7.5a). In agreement with the general arguments provided in the introduction for $Ri<1$, a small roll is formed along the bottom wall just after the abscissa where the expansion occurs (i.e., in proximity to the hot vertical step wall). Moreover, as expected, the fluid leaves the outlet (x=A) with a lower velocity as compared to the velocity at the inlet (as a result of mass conservation, the velocity decreases as the cross-sectional area becomes larger). Interestingly, the temperature distribution shows the existence of a relatively warm area in the entire right portion of the domain. The heat is released from the surface of the horizontal wall for x<A/2 and spreads to the part of the channel with larger cross-sectional area. As for a fixed Ra, a larger value of Ri corresponds to a smaller value of the Reynolds number, the increase in the average temperature for x>A/2 with respect to that visible in the equivalent Fig. 7.2 for smaller Ri, must obviously be ascribed to the reduced flow rate of cold fluid.

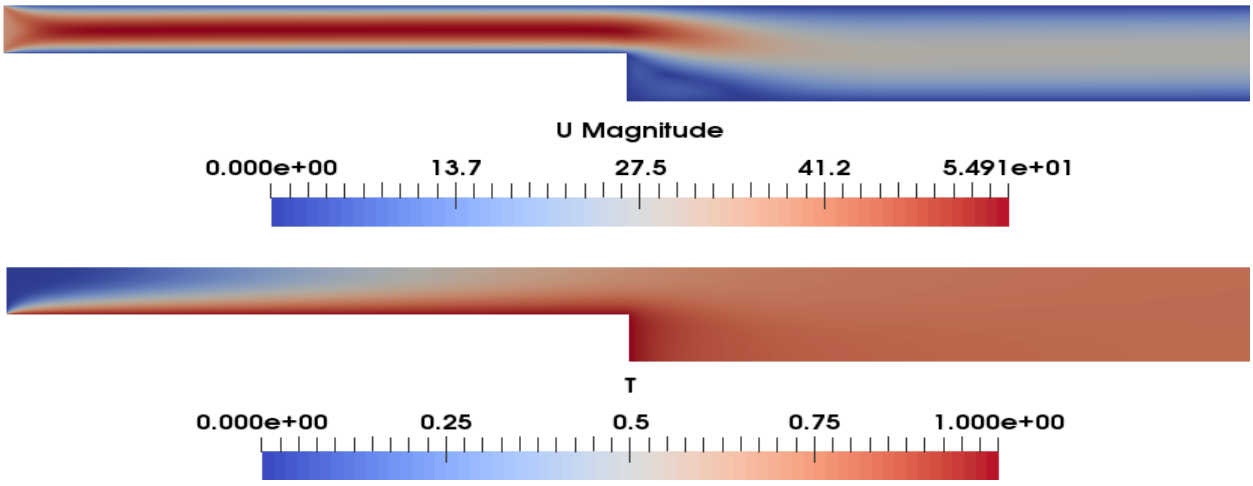
U Magnitude
0.000e+00
13.7
27.5
41.2
5.491e+01
T
0.000e+00
0.25
0.5
0.75
1.000e+00

a)

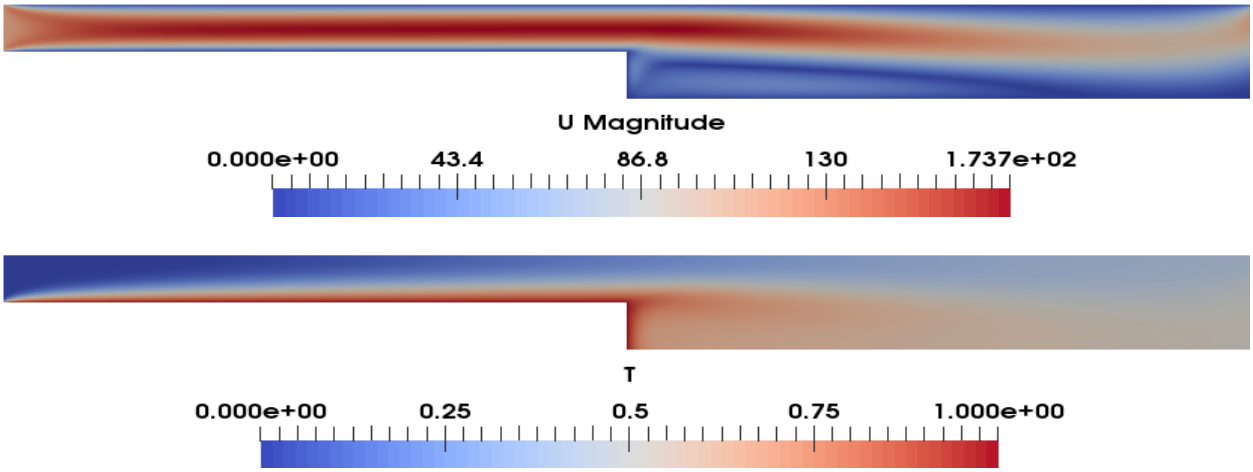
U Magnitude
0.000e+00
43.4
86.8
130
1.737e+02
T
0.000e+00
0.25
0.5
0.75
1.000e+00

b)

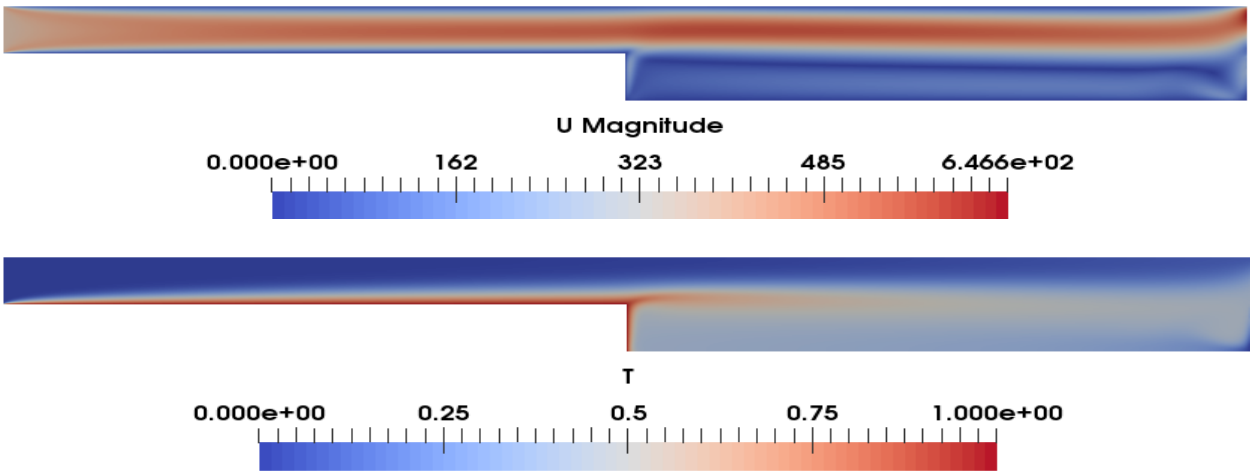
U Magnitude
0.000e+00
162
323
485
6.466e+02
T
0.000e+00
0.25
0.5
0.75
1.000e+00

c)

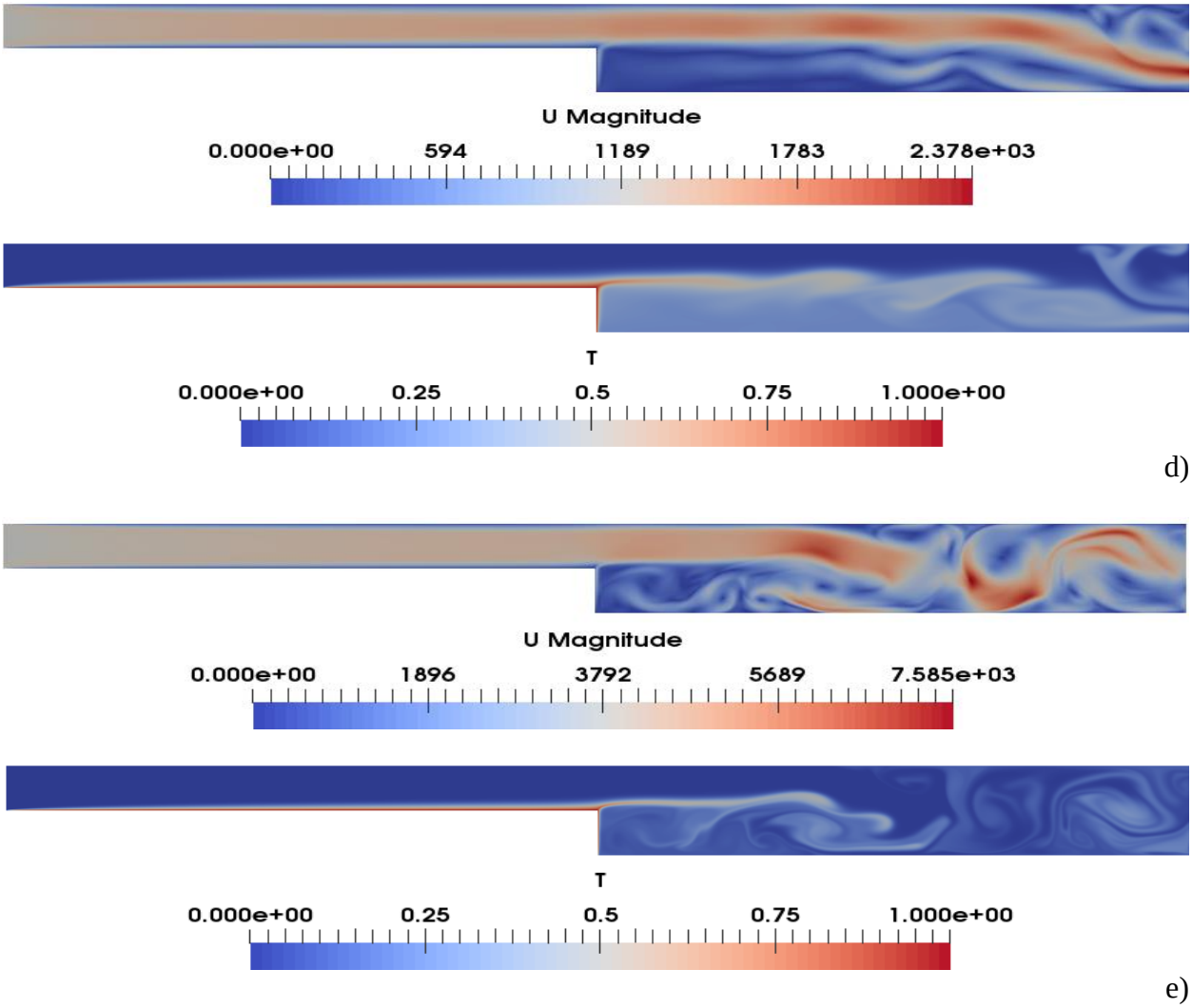

Figure 7.5: Snapshots of velocity field (top) and temperature distribution (bottom) for the case of hybrid forced/buoyancy convection (*Ri*=7.5) and cavity with adiabatic floor: a) $Ra=10^4$; b) $Ra=10^5$; c) $Ra=10^6$; d) $Ra=10^7$; e) $Ra=10^8$.

On increasing the Rayleigh number to $Ra=10^5$ (Re being ≅115 for *Ri*=7.5, see Fig. 7.5b), yet in qualitative agreement with known behaviours for the isothermal scenario and smaller values of *Ri*, the size of the localized vortex formed after the step becomes larger. In particular, for such a case the reattachment takes place just before the outlet. The 'heat island' effect spotted for $Ra=10^4$, becomes less dramatic due to the increased flow rate (higher Re) of cold fluid being injected in the system from the left.

As expected, if the Rayleigh number is increased by another order of magnitude (i.e., $Ra=10^6$, Fig. 7.5c) and, accordingly, the Reynolds number $\mathrm{Re}\cong(Ra/Ri\mathrm{Pr})^{1/2}$ becomes 365, the reattachment point is no longer located inside the domain. As a result, the cold fluid being injected in the channel from the left takes a straight route until it leaves the outlet with almost the same velocity at inlet. In terms of temperature distribution, well-defined (thin) thermal boundary layers become

visible along the hot solid surfaces. A thin layer of hot fluid is also released from the corner (trailing edge) of the step. This layer separates two regions of colder fluid, one located above it and the other underneath.

Most interestingly, an instability develops along this thin region of warm fluid if (yet keeping *Ri* fixed to 7.5), *Ra* is raised to 10^7 (and, accordingly, Re becomes 1154, Fig. 7.5d). The instability manifests itself in the form of undulations affecting the shape of the main jet of cold fluid leaving the step (entering the region with larger cross-sectional area). As a result of this oscillatory behaviour, the thin layer of hot fluid originating from the trailing edge of the step is broken into different packets of warm fluid. Nevertheless, no significant mixing occurs between the regions of fluid in the upper (y>1/2) and lower (y<1/2) portions of the domain.

For $Ra=10^8$, the level of vorticity present in the fluid increases significantly and the thin hot layer is finally mixed with the surrounding fluid at a certain distance from the step owing to the formation of vortices being pervasive throughout the vertical extension of the channel, Fig. 7.5e).

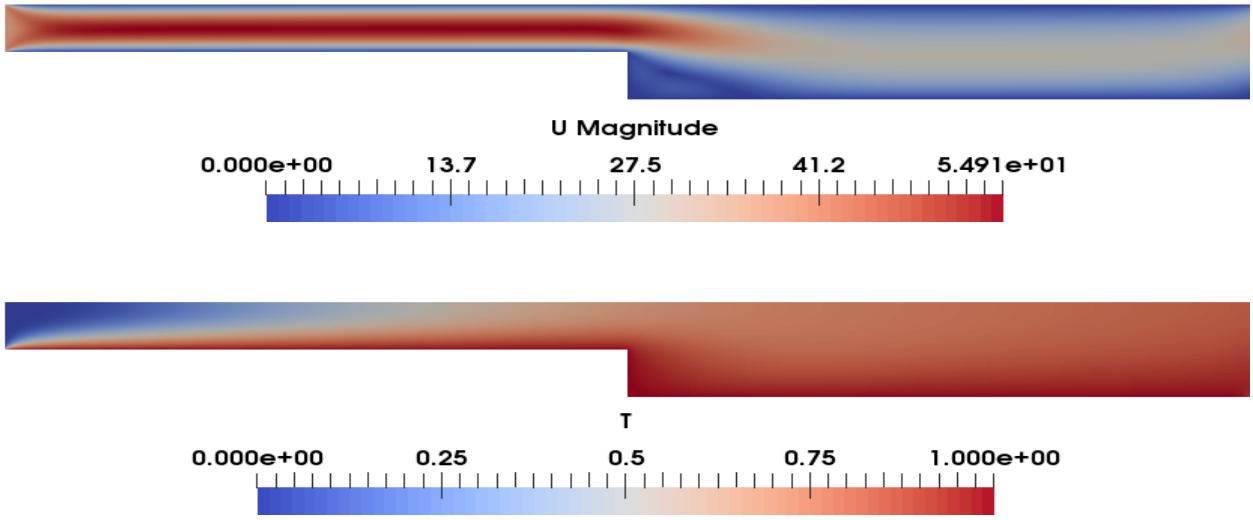

a)

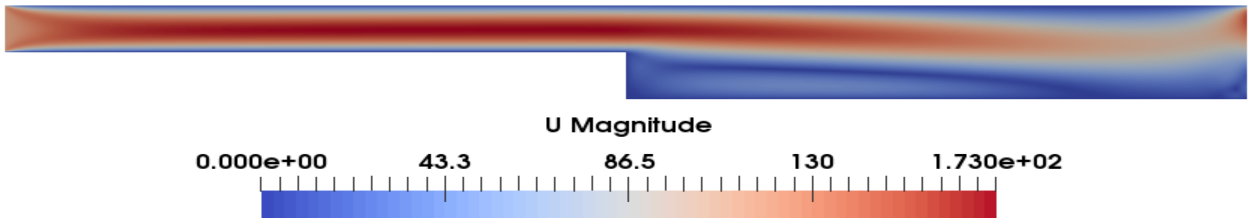
U Magnitude
0.000e+00
43.3
86.5
130
1.730e+02

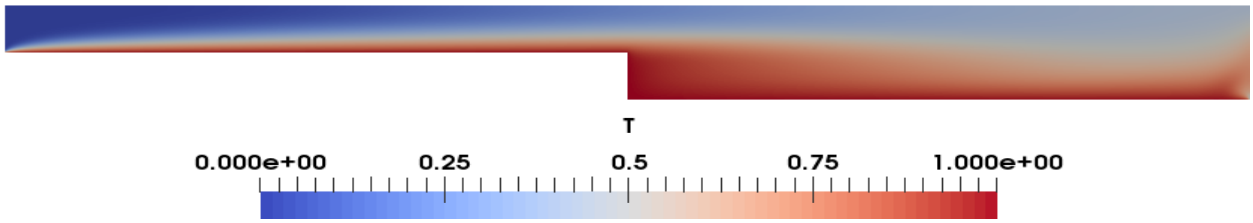
T
0.000e+00
0.25
0.5
0.75
1.000e+00

b)

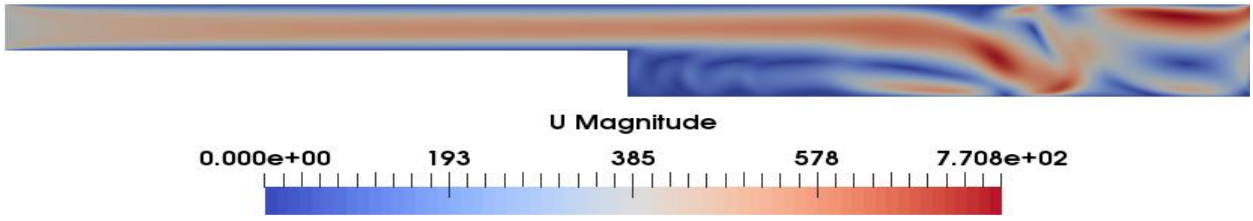
U Magnitude
0.000e+00
193
385
578
7.708e+02

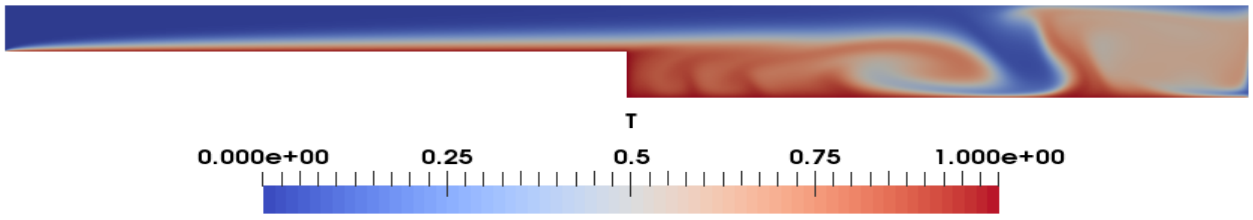
T
0.000e+00
0.25
0.5
0.75
1.000e+00

c)

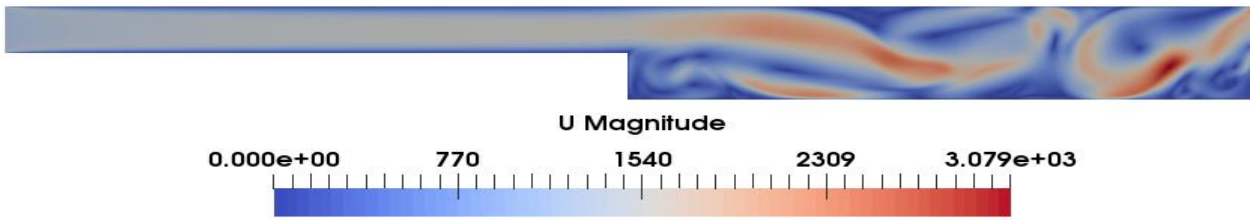
U Magnitude
0.000e+00
770
1540
2309
3.079e+03

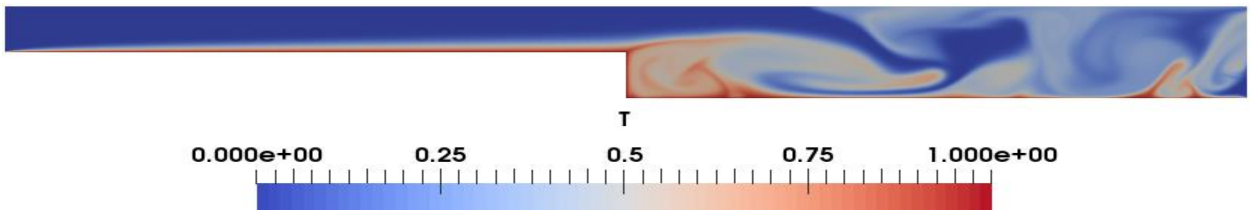
T
0.000e+00
0.25
0.5
0.75
1.000e+00

d)

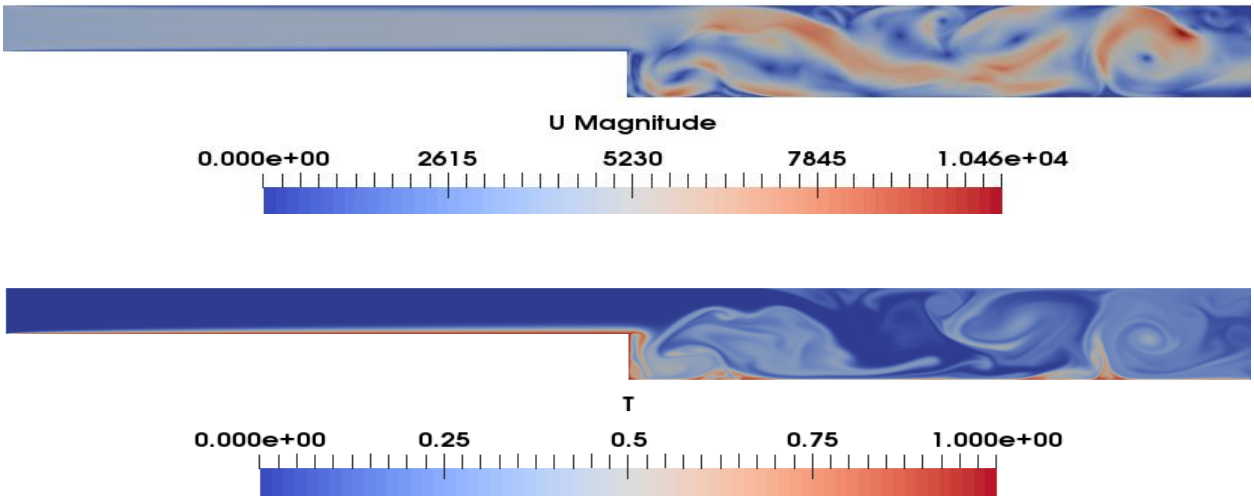

e)

Figure 7.6: Snapshots of velocity field (top) and temperature distribution (bottom) for the case of hybrid forced/buoyancy convection (*Ri*=7.5) and hot floor: a) *Ra*=10^4; b) *Ra*=10^5; c) *Ra*=10^6; d) *Ra*=10^7; e) *Ra*=10^8.

The companion situation in which the floor of the channel (y=0, x>A/2) is hot, and therefore it can contribute to the generation of convection, is illustrated in Fig. 7.6.

Direct comparison of Fig. 7.6a with the equivalent 7.5a, clearly indicates that, as expected, the heat island effect is enhanced if additional heat is injected into the system for x>A/2 (from below).

For *Ra*=10^5, again the dynamics are relatively similar. The heat island starts to reduce in terms of intensity; however, this effect is not as rapid as for the adiabatic floor case.

The departure from the configuration with adiabatic floor, however, becomes dramatic as soon as the next figure of the sequence is considered (Fig. 7.6c where *Ra*=10^6 and Re≅365). In these circumstances, the buoyancy effect in the right part of the channel (x>A/2) becomes so strong that it can cause the onset of (vertical) thermal plumes. For this value of the Rayleigh number, these convective features are so extended in the vertical direction that a kind of "blockage' is produced, with the jet of cold fluid directed from left to right being heavily bended and forced to create a strong vortex just before a visible large plume. By virtue of such a competition, the flow becomes strongly oscillatory.

The complexity generated in the velocity field further grows when the Rayleigh is again increased by an order of a magnitude i.e., *Ra*=10^7 (Fig. 7.6d). Quite surprisingly, however, in this case, the blockage effects discussed before is mitigated as the vertical currents of warm fluid originating from the hot floor *have a smaller size* (owing to the increase in the Rayleigh number, which leads to larger wavenumbers). Finally, for *Ra*=1x10^8 (Fig. 7.6e) the plumes become very small, and accordingly, the number of rolls produced by their interaction with the main horizontal stream of cold fluid increases. These rolls deeply influence the motion of fluid in the right side of the cavity as witnessed by the spiral like localized pattern visible in the distribution of temperature.

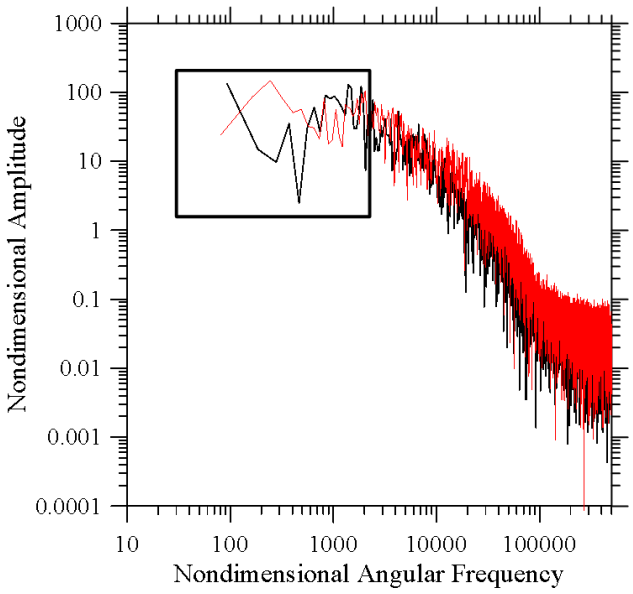

Figure 7.7: Frequency spectrum for Ri=7.5 and Ra=10^7 (Legend: black - adiabatic floor, red - hot floor).

Analysis of the frequency spectra for a fixed value of Ra (following the same approach undertaken in Sect. 7.1 for Ri=0.25, probe position x=9, y=0.25) is still instrumental in revealing the role of buoyancy forces, which in this case can be considered less marginal (see Fig. 7.7). This is clearly witnessed by the notable differences in the two spectra in the range of small frequencies (angular frequency $\leq O(10^3)$), which may be regarded as a clue for the different hierarchy of bifurcations characterizing the two systems with adiabatic or hot floor (this interesting concept will be discussed again in Sect. 7.4.1). The two spectra superpose almost perfectly in the range of high frequencies, which indirectly confirms that the behaviour of turbulence becomes universal on the small spatial scales as soon as 'memory' of the dynamics developing on larger scales is lost as theorized by Kolmogorov (1941ab).

7.3 Mixed convection for Ri≥O(10)

Following a logical approach where the effects of thermal buoyancy are progressively enhanced in comparison to forced convection, in this section, the value of the Richardson number is significantly increased ($Ri \geq O(10)$).

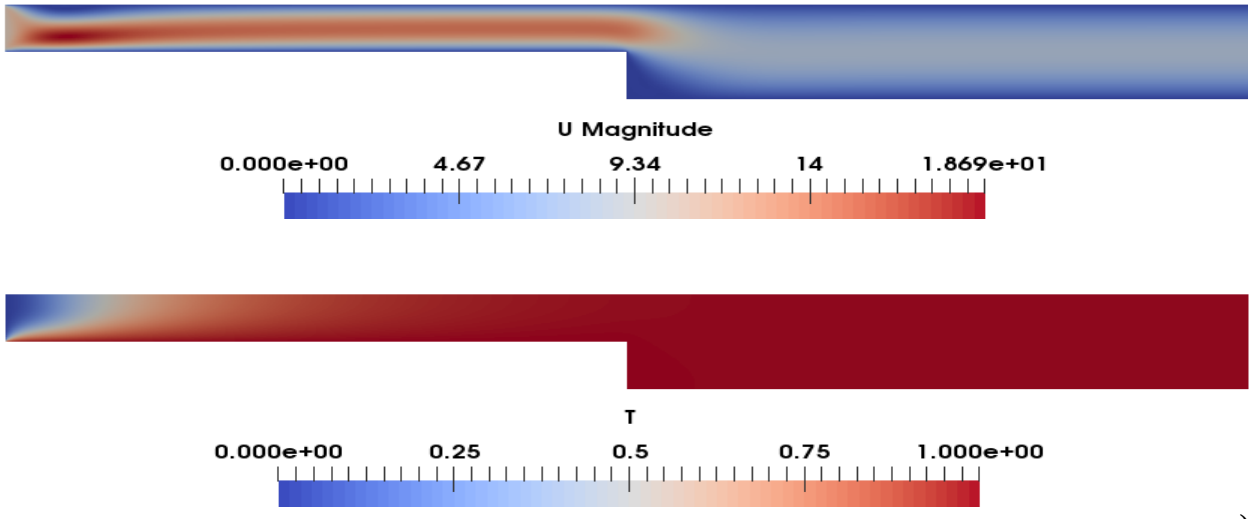
U Magnitude
0.000e+00
4.67
9.34
14
1.869e+01
T
0.000e+00
0.25
0.5
0.75
1.000e+00

a)

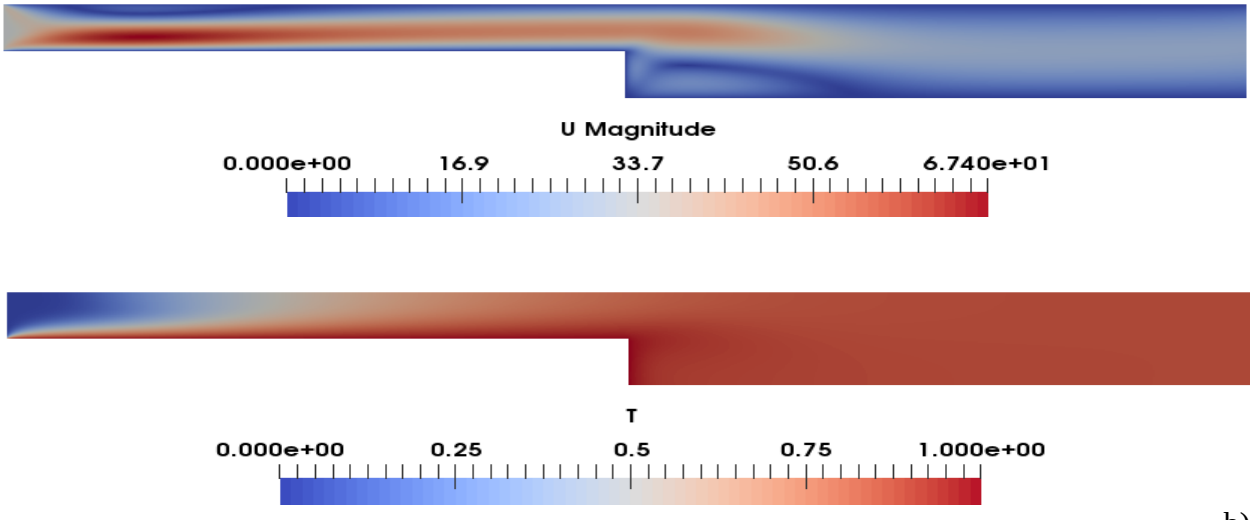
U Magnitude
0.000e+00
16.9
33.7
50.6
6.740e+01
T
0.000e+00
0.25
0.5
0.75
1.000e+00

b)

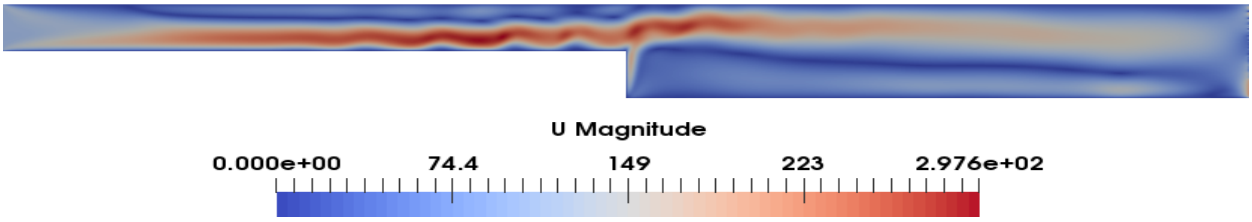
U Magnitude
0.000e+00
74.4
149
223
2.976e+02

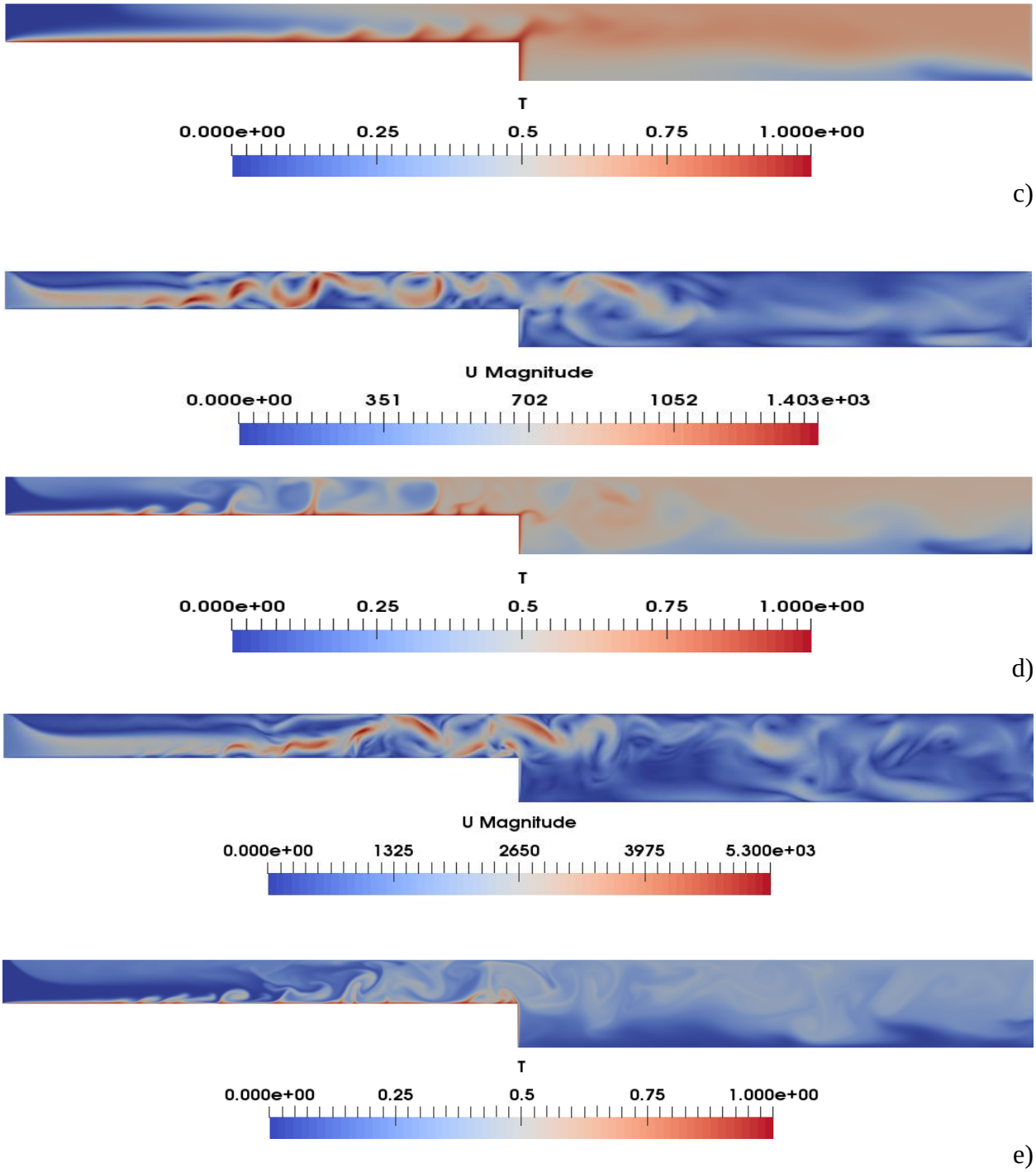

Figure 7.8: Snapshots of velocity field (top) and temperature distribution (bottom) for the case of hybrid forced/buoyancy convection (*Ri*=100), and cavity with adiabatic floor: a) $Ra=10^4$; b) $Ra=10^5$; c) $Ra=10^6$; d) $Ra=10^7$; e) $Ra=10^8$.

Once again, the two typical scenarios where the floor is either kept adiabatic or isothermal are considered in order to get relevant insights into the effects of thermal buoyancy.

The first situation is depicted in Fig. 7.8. In particular, as qualitatively substantiated by Fig. 7.8a, for $Ra=10^4$ and Re=10 (Fig. 7.8a), the velocity field shows that flow is highly laminar (the cold fluid enters the inlet and continues to travel straight without any disruption). Obviously, the heat island effect is greatly enhanced in these conditions. The examination of Fig. 7.8b confirms that this phenomenon can be mitigated by an increase in Re at fixed *Ri* ($Ra=10^5$, Re=31.6).

A very interesting change occurs for $Ra=10^6$ (Re=100, Fig. 7.8c). For the first time (with respect to all the dynamics discussed in the earlier sections), an instability develops along the thermal boundary layer *already in the left portion of the channel* (i.e., in the region of reduced cross-sectional area, x<A/2). This is made visible by the presence of a sequence of thermal plumes traveling in the downstream direction along the top boundary of the step and the ensuing distortions induced in the jet of cold fluid. The plumes (and related sinusoidal perturbations visible in the velocity field) are evenly spaced in the horizontal direction.

In these circumstances, the heat island effects inside the channel are weakened due to the increased injection (volumetric flow rate) of cold fluid from the left. The flow makes a shift from a steady regime to a time dependent one indicating that a Hopf bifurcation has taken place.

The next figure of the sequence (Fig. 7.8d) confirms that the complexity of the flow keeps increasing with *Ra* and Re. In particular, as the reader will realize by inspecting both Figs. 7.8d and 7.8e, phenomena of flow separation and reattachment can be identified directly in the left portion of the channel, i.e., before the fluid enters the region of larger cross-sectional area. As a result of the disturbances developing (and growing) inside the thermal boundary layer for x<A/2, a well-defined jet can no longer be recognized for x>A/2. In this region the flow is characterized by a chain of large vortices (having extension comparable to the vertical size of the channel) that spread from left to right continuously.

On increasing *Ra*, thermal boundary layers have become much thinner and a bending effect is observed in the shape of plumes for x<A/2. A rise in their number can also be observed. The increased volume of fluid injection per unit time results in entire channel being at moderate temperature.

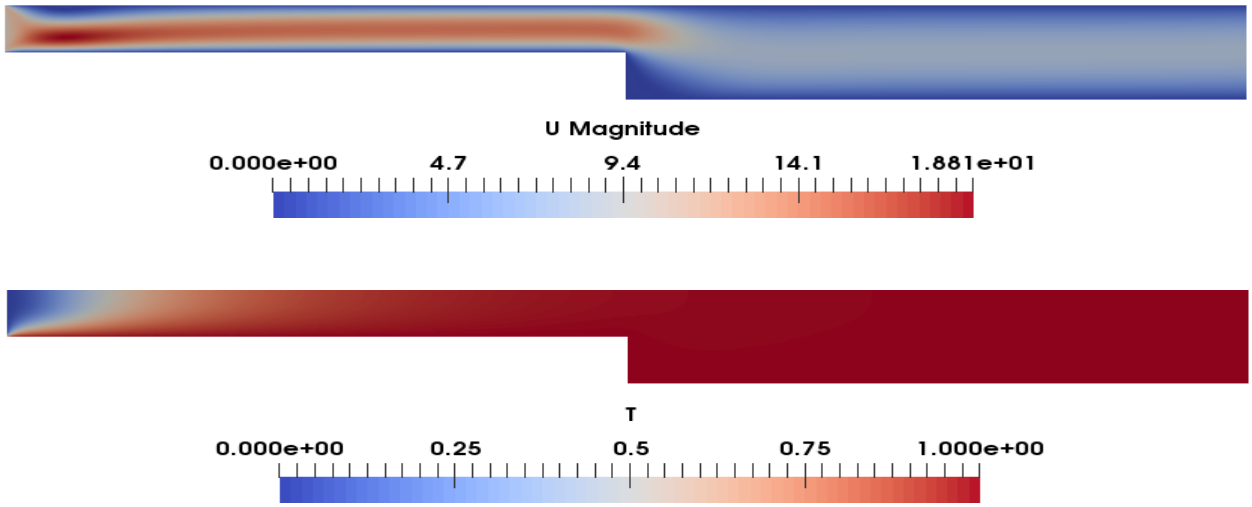

a)

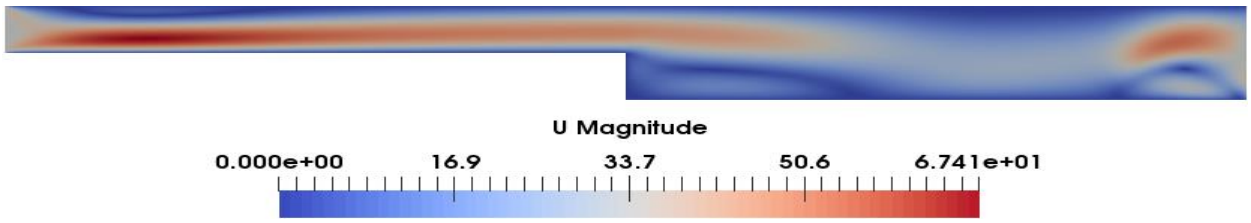
U Magnitude
0.000e+00
16.9
33.7
50.6
6.741e+01

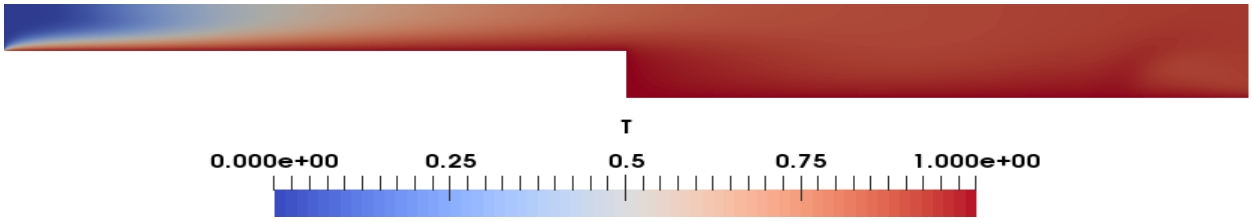
T
0.000e+00
0.25
0.5
0.75
1.000e+00

b)

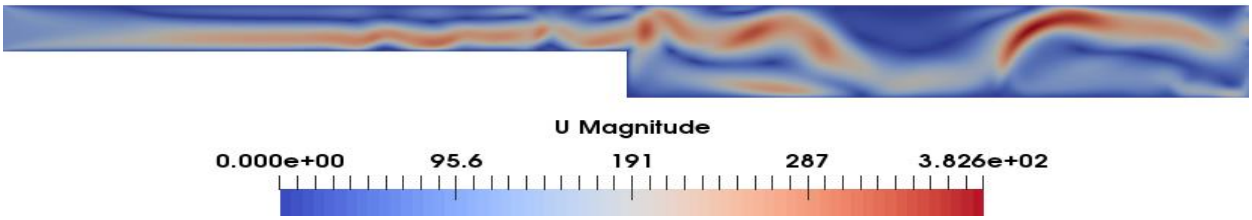
U Magnitude
0.000e+00
95.6
191
287
3.826e+02

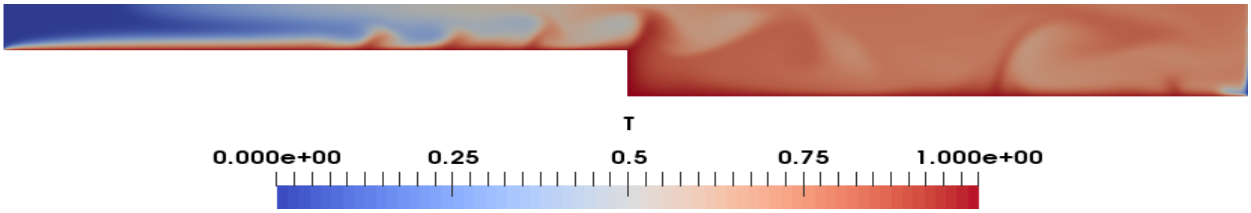
T
0.000e+00
0.25
0.5
0.75
1.000e+00

c)

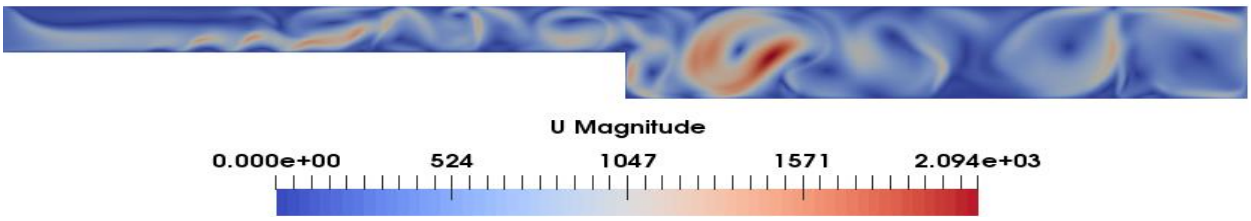
U Magnitude
0.000e+00
524
1047
1571
2.094e+03

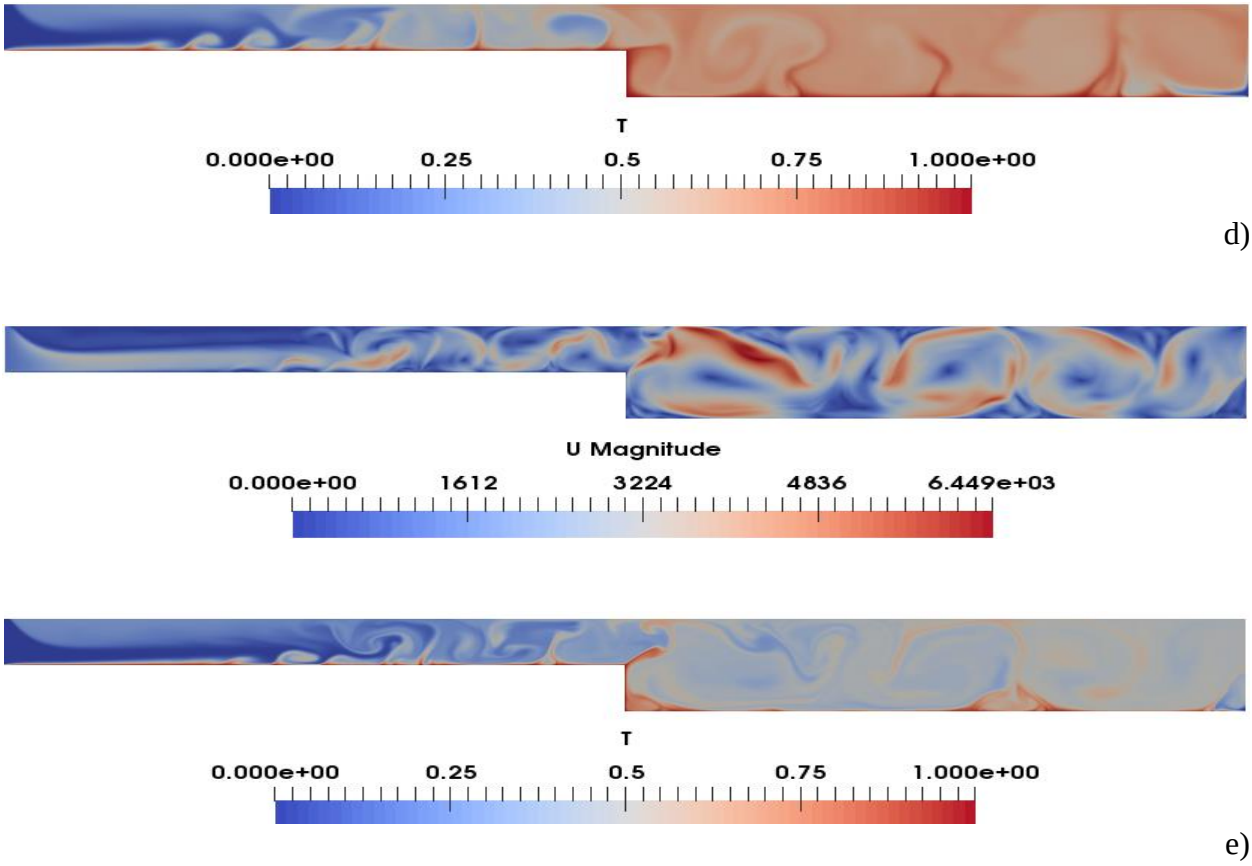

Figure 7.9: Snapshots of velocity field (top) and temperature distribution (bottom) for the case of hybrid forced/buoyancy convection (*Ri*=100 and cavity with hot floor: a) $Ra=10^4$; b) $Ra=10^5$; c) $Ra=10^6$; d) $Ra=10^7$; e) $Ra=10^8$.

Figure 7.9 illustrates the series of flow patterns which are produced when the condition of adiabatic floor is finally switched to that of isothermal (hot) floor.

For $Ra=10^4$ (Fig. 7.9a), no considerable modifications can be detected in the velocity and temperature distribution when a comparison is made with the equivalent adiabatic floor case. However, for $Ra=10^5$ (Re=31.6, Fig. 7.9b), the flow changes from a steady regime to a time dependent state, which must obviously be ascribed to the dynamics enabled in the region x>A/2 (given the absence of visible disturbances developing in the system for x<A/2). Two velocity rolls are formed in this circumstance in comparison to one formed in the adiabatic floor situation. As it is evident from the temperature distribution "heat island" effects are still very evident inside the domain.

As soon as the Rayleigh is increased to $Ra=10^6$ (Fig. 7.9c), the flow topology starts showing distinguishable signs of growing complexity, among them, a remarkable increase in the number of velocity rolls for x>A/2. The presence of these vortices near the vertical wall of step, ceiling and close to the floor near the outlet forces the fluid to adopt a "snake" like pattern until it leaves

the domain. The hot horizontal step wall and floor represent the breeding ground feeding the thermal plumes which travel from left to right behaving like a wave of hot air.
As expected, a subsequent rise in the value of Rayleigh number (Figs. 7.9d and 7.9e) generates a turbulent behaviour in the flow. The chaotic nature of the flow is witnessed by the number of rolls and the shape of thermal plumes in the region of larger cross-sectional area. The latter are no longer all inclined to the right. Moreover, the increased strength of buoyancy favours the development of plumes at a very fast rate. These have very distinct features and display thin sharp stems alongside sharp cap and lobes which are consistently deformed by vortex structures.
For the sake of brevity, the patterning behaviour for Ri=25 is not described in detail; the results indicate that the temperature and velocity fields for increasing values of Rayleigh number are relatively similar to those reported for Ri=100. However, taking a look at the related frequency spectra and comparing them with the equivalent ones for Ri=100 (Fig. 7.10) is instructive. Indeed, as the reader will realize by inspecting Figs. 7.10a and 7.10b, as Ri exceeds a value ≅ 10, the differences in the spectra for adiabatic and hot floor are no longer limited to the region of small frequencies. A clear departure can also be seen in the range where the spectrum roughly aligns with the theoretical predictions by Kolmogorov. In general, a more energetic distribution of amplitudes can be seen when the hot floor case is considered, and the key to understanding this trend lies in considering that the presence of the hot floor obviously causes a surge in the rate of plume generation (increased number of thermal plumes passing through a probe point per unit time obviously implies a shift of the related fixed amplitude signal to a higher frequency).

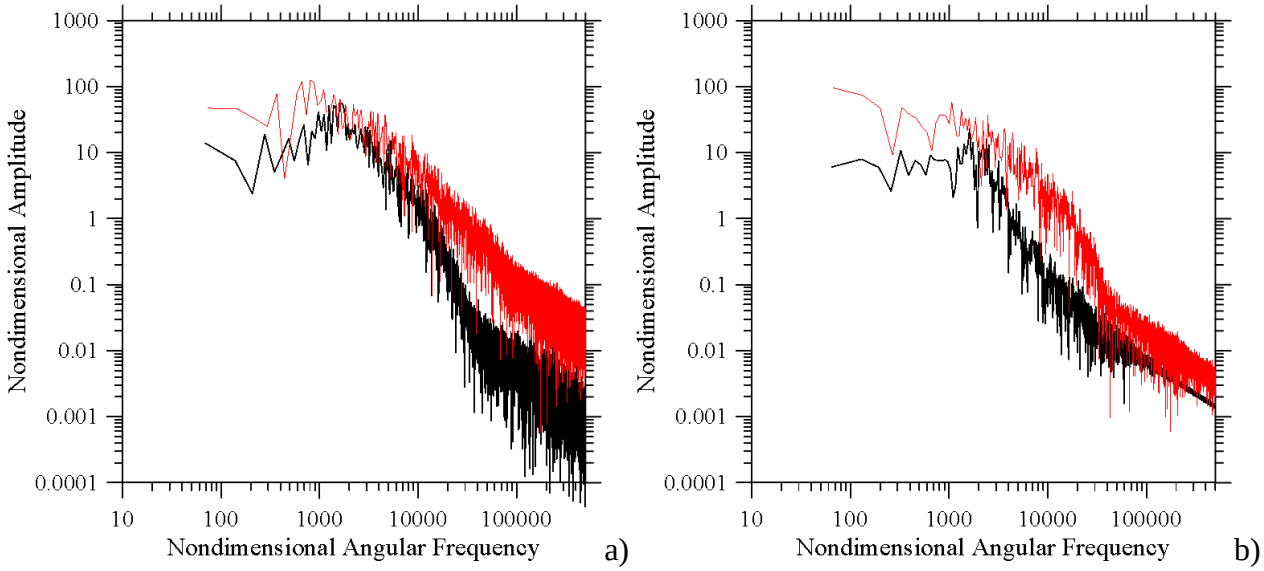

Fig. 7.10: Frequency spectrum for Ra=10^7 (Legend: black - adiabatic floor, red - hot floor, probe position x=9, y=0.25): a) Ri=25; b) Ri=100.

7.4 Discussion

This section is dedicated to a critical discussion of the results on the basis of arguments related to the transition to time-dependence and ensuing evolution towards chaos. In this regard, the analysis is directly based on the examination of the structure of the disturbances that are produced as a consequence of the first bifurcation of the flow from steady state to oscillatory behaviour, i.e., the first Hopf bifurcation. The related "critical" conditions have been determined in the present work through an iterative procedure where, while keeping the Richardson number fixed, *Ra* and Re are increased/decreased in order to determine the corresponding values (*Ra*, Re) for which the flow becomes oscillatory as precisely as possible (the critical value being finally determined through quadratic extrapolation of the amplitude of the maximum oscillatory velocity to zero, see Table 7.1).
The associated disturbances (being ideally equal to zero in the critical conditions) are also provided in the present section (for values of *Ra* and Re, slightly larger than the critical ones). Following the same approach already implemented in Chapter 6 for FFS, in practice such perturbations have been obtained by subtracting a time-averaged velocity field (computed over one period of the oscillations) to the instantaneous field provided by the solution of the non-linear governing equations described in Chapter 2.

7.4.1 Critical conditions and Disturbances

Table 7.1. Values of Critical parameters (Ra_{cr}, Re_{cr}) for the BFS with adiabatic and hot floor.

	Adiabatic floor (Ra_{cr}, Re_{cr})	Hot Floor (Ra_{cr}, Re_{cr})
Ri=0.25	$1.22\text{x}10^6$, 2209	$5.15\text{x}10^5$, 1435
Ri=7.5	$2.56\text{x}10^6$, 584	$1\text{x}10^5$, 115
Ri=25	$6.35\text{x}10^5$, 159	$6.5\text{x}10^4$, 51
Ri=100	$3.03\text{x}10^5$, 55	$6.1\text{x}10^4$, 25

For consistency with Sect. 7.1,7.2 and 7.3, the discussion is implemented starting from the with adiabatic floor, the associated disturbances being collected in Fig. 7.11. The simplest case is obviously represented by the condition Ri=0.25 for which the critical conditions ($Re_{cr}\cong 2210$) are almost identical to those determined for purely forced flow (let us recall that for Ri=0, $Re_{cr}\cong 2090$). The proximity of the critical values clearly indicates that the role of buoyancy can be considered almost negligible in this case. As shown in Fig. 7.11a, the disturbances develop just after the abscissa where the sudden change in the cross-sectional area occurs. These perturbations can be considered of hydrodynamic nature, i.e., they are induced by the vertical shear present in the separated shear layer (originating from the corner of the step and reattaching at a certain distance from it).
As the Richardson number becomes larger than 1, however, a notable change in the disturbance patterning behaviour can be noticed (Fig. 7.11b for Ri=7.5). The perturbations are now

essentially located in the portion of fluid located under the layer of relatively warm fluid originating from the step trailing edge. Fluid-dynamic disturbances are generated close to the vertical wall of the step in the form of weak rolls and their amplitude grows as the rolls are spread in the downstream direction. As this layer is still characterized by significant vertical shear, the instability still has a hydrodynamic component. The decrease in the value of the critical Reynolds number, however, witnesses the role played by thermal buoyancy in this process. The shear layer, indeed, is affected by a destabilizing vertical temperature gradient with respect to the fluid located in the upper part of the channel.

The aiding role of hydrodynamic and thermal (buoyant) effects is reflected in the significant lowering of both the critical *Ra* and Re for *Ri*=25 (Fig. 7.11c). These are reduced from (2.56×10^6, 584) to (6.35×10^5, 159), respectively. In this case, buoyancy is able to produce modes of convection, which also significantly affect the upper part of the channel. These develop in the form of a wave (very evident for x>A/2, as qualitatively substantiated by Fig. 7.11c). Most notably, the wave originates in the left part of the channel, i.e., just above the hot surface of the step (x<A/2), before the separated shear layer is generated, which indicates that the instability has a significant buoyant component. When *Ri* is increased to 100, the most dangerous disturbances (i.e., those responsible for the primary bifurcation to time-dependent flow) are produced in the region with larger cross-sectional area. However, the location where they attain their maximum amplitude is progressively shifted to the left (in the upstream direction) as *Ra* is increased beyond Ra_{cr} (Fig. 7.11d), which may be regarded once again as a clear signature of the buoyant effect.

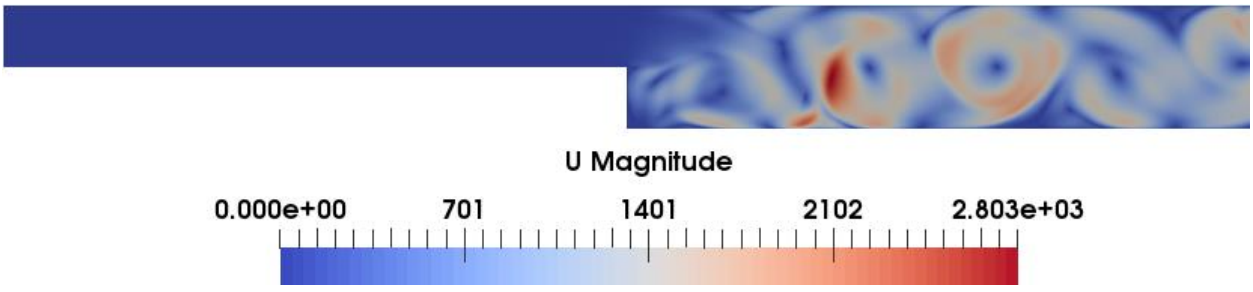

a)

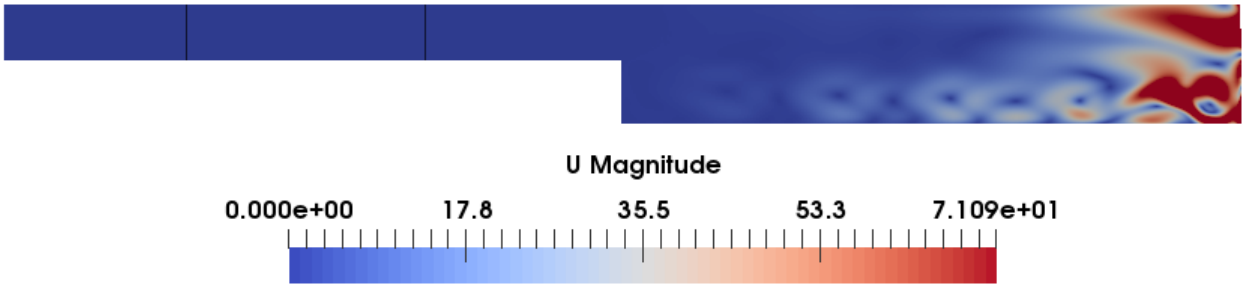

b)

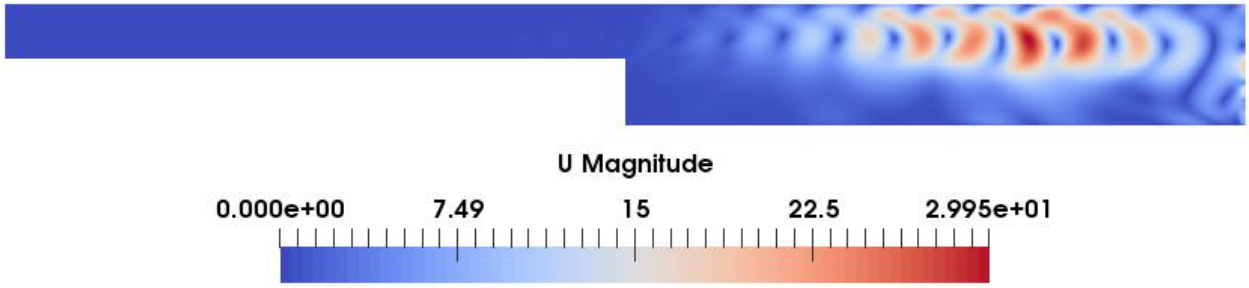

c)

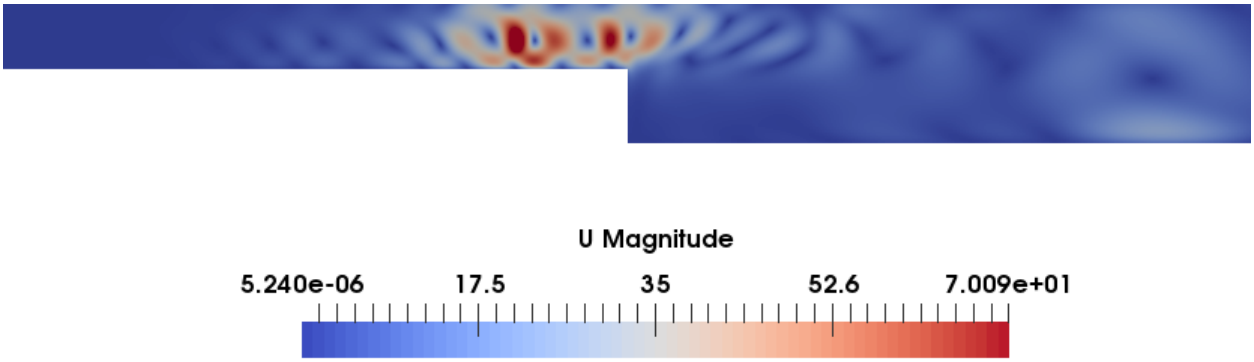

d)

Figure 7.11: Snapshots of the velocity disturbances for the cavity with the adiabatic floor (first Hopf bifurcation), a) Ri=0.25, Ra≅1.3x10^6, b) Ri=7.5, Ra≅3x10^6, c) Ri=25, Ra≅7x10^5, d) Ri=100, Ra≅5x10^5.

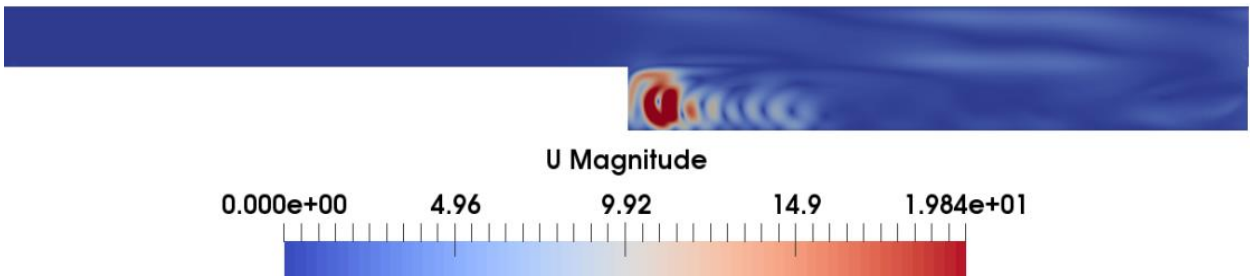

a)

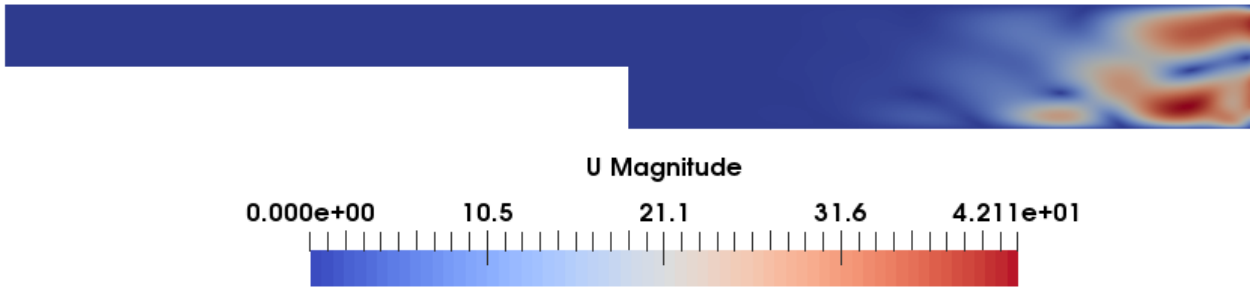

b)

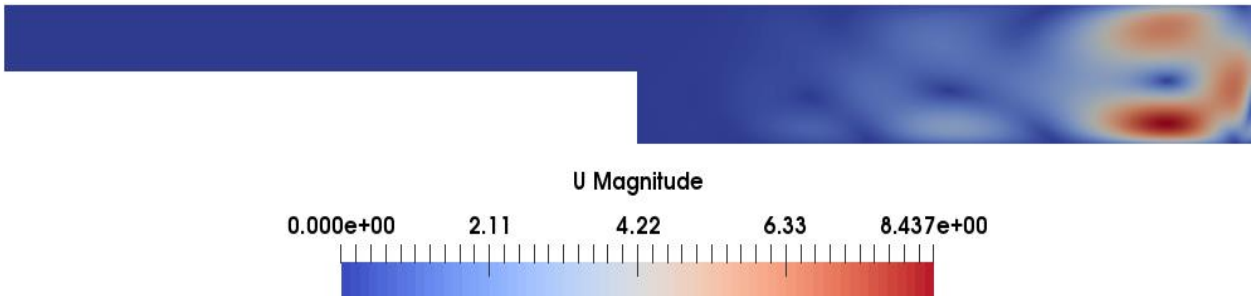

c)

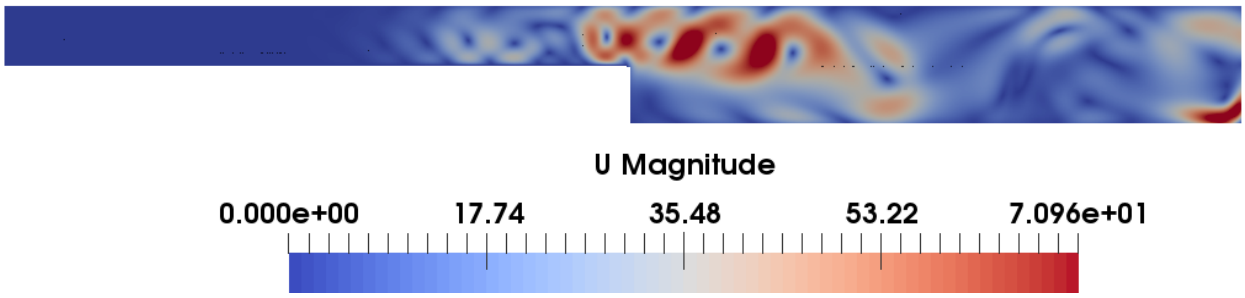

d)

Figure 7.12: Snapshots of the velocity disturbances for the cavity with the hot floor (first Hopf bifurcation), a) Ri=0.25, Ra≅5.7x10^5, b) Ri=7.5, Ra≅1.1x10^5, c) Ri=25, Ra≅7x10^4, d) Ri=100, Ra≅7x10^5.

The role of gravitational effects may be obviously expected to become increasingly more important when the configuration with hot floor is considered (Fig. 7.12, Table 7.1). Comparison of the second and third columns of Table 7.1, indeed, leads to the realization that replacement of the adiabatic condition with a (destabilizing) hot wall systematically induces a decrease in the critical values for the onset of oscillatory flow (in some cases by one order of magnitude for the needed value of Ra). Such changes are reflected by significant modifications in the structure of the disturbances.

For Ri=0.25, these are initially localized in the small roll formed in proximity to the vertical side of the hot step. The significant role of buoyancy is witnessed by the aforementioned notable

lowering of the required value of the critical Reynolds number, which shifts from the value almost identical to that needed for isothermal flow found in the adiabatic floor case (2210) to 1435 (a significant shrinkage can also be spotted in the corresponding value of the Rayleigh number).

For Ri>1, the shear layer of warm fluid originating from the trailing edge of the step (its corner) and protruding into the right part of the channel (acting as a kind of watershed between the regions y<1/2 and y>1/2) is no longer a feature of the flow. In these cases (see Figs. 7.12b and 7.12c for Ri=7.5 and 25, respectively), the disturbances are essentially connected to the thermal plumes which stem directly from the thermal boundary layer developing along the hot floor of the channel. Such disturbances are transported in the downstream direction as a result of forced flow and become much more pronounced close to the outlet region. The same property also applies to the case Ri=100 (not shown).

Simulations conducted for larger values of Ra have led to the conclusion that, in general, for Ri>O(1), an increase in Ra at fixed Ri causes a displacement of the region where disturbances are produced and amplified in the upstream direction (in an area located in proximity to the step corner, Fig. 7.12d).

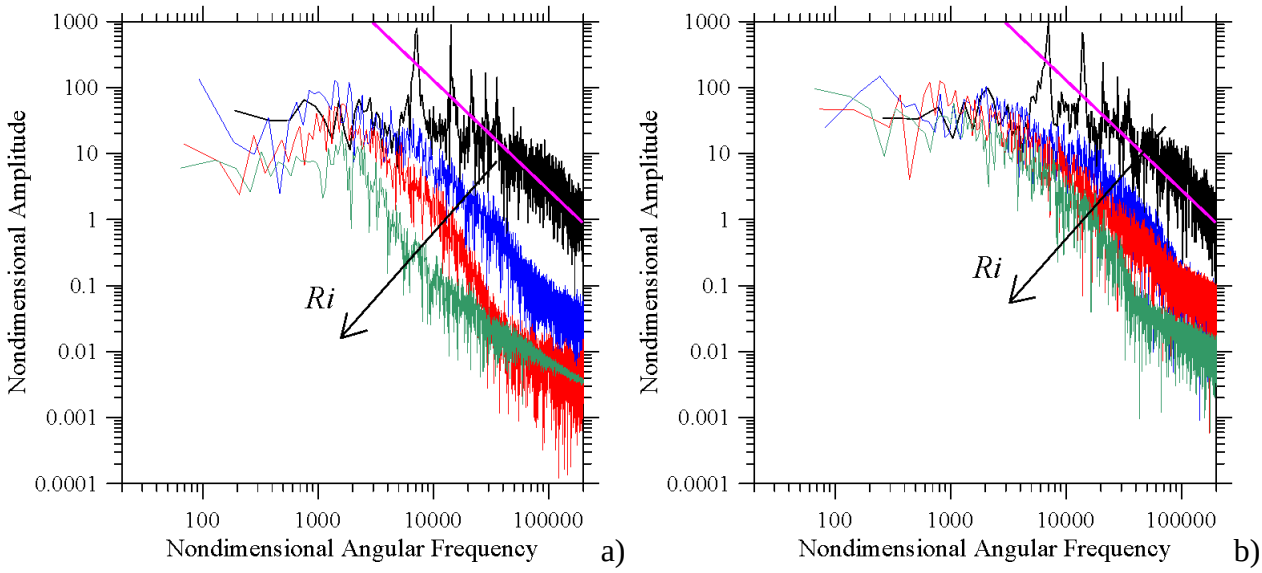

Figure 7.13: Frequency spectra for Ra=10^7 (Legend: black - Ri=0.25, blue - Ri=7.5, red - Ri=25, green - Ri=100, magenta – reference Kolmogorov law): a) adiabatic floor, b) hot floor.

Along these lines, additional insights can be directly gathered from Fig, 7.13, where the frequency spectra obtained for a fixed value of the Rayleigh number (Ra=10^7) have been collected for increasing values of Ri. The dichotomy considered for the thermal boundary condition at the bottom wall is once again reflected by the two separate plots shown in Figs. 7.13a and 7.13b, respectively. Transcending the differences induced by the different nature of the

floor, some general and meaningful conclusions can be drawn. Both plots indeed witness the hybrid (thermal-hydrodynamic) nature of the instabilities affecting the flow for finite values of the Richardson number. On decreasing *Ri* (increasing Re at fixed *Ra*), the spectra become more energetic due to the hydrodynamic contribution brought in by the forced flow (the branches are shifted upwards in the vertical direction). Under a slightly different perspective, the role of buoyancy forces might be recognized observing that the differences between the spectra for adiabatic and hot floor tend to be enhanced as *Ri* is increased at fixed *Ra* (as *Ri* becomes higher, Re is decreased accordingly and the role of most dangerous disturbances is progressively transferred from the hydrodynamic ones to those of a purely thermal nature).

7.4.2 Comparison with the Forward-Facing Step

Having completed a sketch of the disturbances patterning behaviour and an assessment of the trends of the critical parameters in relation to the role played by thermal buoyancy, the remainder of this section is finally devoted to a meaningful comparison with the companion case represented by the channel with a Forward-Facing Step (FFS, for which the interplay of hydrodynamic and buoyant effects has been investigated in Chapter 6.

For the purely hydrodynamic case (no thermal or buoyancy effects), consensus exists in the literature that the typical outcomes of the flow-step interaction are more complex when the decrease of the cross-sectional area occurs in the downstream direction (i.e., for the FFS case). Indeed, whilst for the BFS, only one region of separated flow is induced downstream of the geometrical expansion (the reader being referred again to the introduction and to the examples in Fig. 7.1), with the forward-facing step, vorticity can be produced at several stations (both upstream and downstream from the step, see, e.g., Kiya and Sasaki (1983); Cherry et al. (1984); Largeau and Moriniere (2007). These localized regions of recirculating fluid can induce unsteadiness and other complex phenomena.

The problem where buoyancy enters the FFS dynamics causing a departure from the classical hydrodynamic scenario has been tackled in the aforementioned numerical study in Chapter 6 where configurations mirror symmetric with respect to those assumed in the present work were examined (bottom wall of the region with larger cross-sectional area being either adiabatic or kept at the same temperature of the vertical and horizontal boundaries of the step). Equivalent conditions were also considered there in terms of values of the Rayleigh number (Rayleigh number based on the vertical extension of the region of larger cross-sectional area spanning the range from 10^4 to 10^8). It is also worth noticing that the values of the Richardson number based on the velocity at the inflow were 4 times the corresponding values assumed in Sect. 7.1, 7.2 and 7.3 (i.e., $Ri_{FFS}=4Ri_{BFS}$), which implies the volumetric flow rates of cold fluid injected in the channel were identical to those considered in the present work for any given value of the Rayleigh number.

For the convenience of the reader, the main outcomes of that study are reported in Table 7.2.

Table 7.2. Values of Critical parameters (Ra_{cr}, Re_{cr}) for the FFS with adiabatic and hot floor.

Ri_{FFS}	Adiabatic floor (Ra_{cr}, Re_{cr})	Hot Floor (Ra_{cr}, Re_{cr})
Ri=4x0.25=1.0	$4.7x10^5$, 685.6	$4.7x10^5$, 685.6
Ri=4x7.5=30	$3x10^6$, 316.2	$2.5x10^5$, 91.3
Ri=4x25=100	$4.2x10^5$, 64.8	$1.39x10^5$, 37.3

It can be seen immediately that for the FFS configuration with adiabatic floor the critical parameter (for the first Hopf bifurcation) displays a non-monotonic dependence on the Richardson number. According to investigations performed in Chapter 6, this trend could be ascribed to a change in the nature of the fluid-dynamic disturbances, which evolve from a purely hydrodynamic oscillatory mode of convection (developing in the localized bubble originating from the step corner) for Ri_{FFS} =1 to perturbations of hybrid buoyant-hydrodynamic nature in the region of reduced cross-sectional area for Ri_{FFS} >O(1) (in the form of disturbances growing continuously inside the thermal and kinematic boundary layer for Ri_{FFS} =30, or manifesting directly as thermal plumes extended over the entire vertical and horizontal extension of that region for Ri_{FFS} =100).

As the reader will easily realize through cross comparison of Tables 7.1 and 7.2 (adiabatic floor cases), the behaviour for the BFS is much more regular, and the key to understanding such results lies in considering that in the present case, rather than a 'switch' from an instability mechanism to another, thermal effects play the role of 'aiding factors' in enabling instability mechanisms. More precisely, buoyancy contributes to make the shear layer of hot fluid that originates from the trailing edge of the step more unstable with respect to the situation where the only source of disturbances is represented by vertical shear (among other things, this is clearly witnessed by the decreasing value of the critical Reynolds number of increasing Ra). On the basis of these argument, one may therefore conclude that the statement about the increased complexity of the FFS problem with respect to the BFS one might be extended to the situation where thermal buoyancy is present.

A further understanding of these concepts may be gained through examination of the cases with hot floor. As qualitatively illustrated in the third column of Tables 7.1 and 7.2, the differences between the BFS and the FFS become less striking in this case (an increase in Ri leading to a monotonic decrease in the value of the critical parameter regardless of the orientation of the step); once again, an explanation/justification for this trend can be elaborated in its simplest form on the basis of the realization that in both cases the instability of the hybrid forced-buoyancy convection is supported by both types of convection. The competition between the forced flow tending to displace parcels of cold fluid to the right and natural convection forcing parcels of hot (cold) fluid to move vertically upwards (downwards) is the main process responsible for the onset of oscillations.

Obviously, the details of the effective instability mechanisms enabled in the framework of such interplay of concurrent effects also depend sensitively on the forward or backward facing arrangement of the step. Indeed, the orientation of the step causes a rupture of the symmetry of

the considered system with respect to vertical planes (Lappa, 2017). Under a slightly different perspective, the reader may be led to a more heuristic realization of this argument by considering that, being a shear flow with variable shear along the horizontal direction, the forced convection in a channel with a step obviously breaks the in-plane isotropy which would be typical of a layer of fluid uniformly heated from below.
As reported in Chapter 6 for the FFS with hot floor, disturbances responsible for the onset of oscillatory flow are essentially generated by the plume originating from the corner of the step (that is reinforced by the hot fluid rising along the vertical side of the step thereby leading to an increase in the shear). These (shear driven) disturbances are transported in the downstream direction in the region of reduced cross-sectional area (x>A/2 for the FFS), thereby exciting a response that develops in the form of weak buoyant rolls (superimposed on the horizontal current in this region). For the BFS, as illustrated in Sect 7.1, 7.2 and 7.3 the scenario is quite different. Disturbances emerge directly in the form of thermal plumes in the region of larger cross-sectional area (yet x>A/2 for the BFS). As a result of the vertically extended configuration of these plumes, however, mechanisms based on the hydrodynamic (or mixed buoyant/hydrodynamic) instability of the warm layer of fluid released from the trailing edge of the step are essentially no longer relevant (most of the destabilizing effects being introduced by buoyancy).

7.5 Conclusions

In order to fill a gap in the literature about the role played by thermal buoyancy in problems of (incompressible) flow expansion in channels with a backward facing step (BFS), a suite of numerical simulations have been performed varying the parameters that account for strength of forced flow and thermal (natural) convection. To compare the simulations on an equal footing for different hydrodynamic conditions, fixed values of the Rayleigh number have been considered (allowed to span five orders of magnitude for any selected value of the Richardson number). In order to discern specific mechanisms depending on thermal effects, the Richardson number has been progressively increased from 0 (purely forced flow) to 10^2 (dominant buoyancy convection) and the ensuing numerical problem has been solved for two companion boundary conditions, namely, adiabatic or isothermal wall at the bottom of the portion of the domain with larger cross-sectional area (the ‘floor’).
This specific modus operandi has been complemented with a focused investigation aimed to determine the critical conditions for which the considered system undergoes a transition from a steady state to a time-dependent one. It has been found that, in general, buoyancy convection of thermal nature reinforces the hydrodynamic mechanisms responsible for the onset of oscillatory flow in the purely forced (isothermal) flow case. This is witnessed by the lowering of the related value of the (critical) Reynolds number for fixed values of the Richardson number. As expected, this process is mediated by the specific thermal boundary conditions assumed for the floor.

When it is adiabatic, both the vertical shear in the separated layer originating from the corner of the step and the destabilizing temperature difference established between this layer and the surrounding fluid support the onset of fluid-dynamic disturbances. If the floor is kept at the same temperature of the step, the role of buoyancy becomes much more important; the instability of the aforementioned layer is taken over by a process where thermal plumes nucleate directly at the bottom of the channel and become pervasive throughout its vertical extension.

Analysis of the chaotic frequency spectra for different values of the Richardson number has confirmed the hybrid nature of disturbances affecting the flow even at larger values of the Rayleigh number. In fact, the progressive displacement of the spectrum towards higher amplitudes as the Richardson number is decreased (while keeping fixed the Rayleigh number) provides indirect evidence for the role played by hydrodynamic perturbations. Vice versa, correlation of the spectra obtained for fixed *Ra* for growing values of *Ri* and different thermal boundary condition at the bottom wall reveals the increasingly more important influence that buoyancy effects can exert on the flow in these circumstances.

Purely geometrical effects do also play a role in all these dynamics. Meaningful comparison with the equivalent phenomena known to affect the companion configuration (FFS) has led to the conclusion that the differences between these two systems essentially stem from the facing orientation of the step, which causes a rupture of the symmetry of the channel with respect to the direction of the flow. In the isothermal case (no buoyancy), the reduced complexity of the BFS depends on its inability to induce vorticity and related shear effects both upstream and downstream of the step leading edge. In the non-isothermal case with adiabatic floor, the scenario for the BFS is yet less complex, as the role of buoyancy is limited to inducing additional disturbances in the separated shear layer with respect to those potentially produced by a purely hydrodynamic shear-driven mechanism (for the FFS, more complex dynamics are enabled due the disjoint influence of hydrodynamic and thermal effects). For the hot floor case, the flow instability in both BFS and FFS systems are essentially driven by buoyancy, which explains why the trend of the critical parameter is monotonic for both paradigms (some existing differences are due to the facing orientation of the step and the related forced flow, which break the in-plane isotropy which would be typical of a layer of fluid uniformly heated from below).

Chapter 8

Large eddy simulation of three-dimensional hybrid forced-buoyancy convection in channels with an abrupt section variation

In this chapter three-dimensional FFS and BFS configurations are finally considered. As already explained in Chapter 4, the problem is tackled in the frame of a LES approach to reduce the otherwise prohibitive number of required gird points.

Given the still heavy computational weight of these simulations, attention is restricted to a single value of the Rayleigh number, i.e. $Ra=10^7$, in line with the arguments provided in Sect. 4.6.1. Moreover, in order to have the same mass flow rate for the FFS and the BFS, the Richardson number is set to 100 and 25, respectively (the Richardson number, defined through eq. (2.15) being based on U_{forced}, i.e. the constant velocity of the fluid at the inflow section) .

At this stage, it is important to recall that the LES approach has been successfully applied to pure thermal convection (Eidson, 1985; Wong and Lilly, 1994; Kimmel and Domaradzki, 2000; Yan, 2007), circumstances involving various kinds of jets in cross flow (Li and Ma, 2003) flows (without buoyancy) in ducts with "turbulators" (Ciofalo and Collins, 1992; Murataa and Mochizuki, 2000; Labbé, 2002; Cui et al., 2003; Lohász et al., 2006) and forced flows in ducts with buoyancy effects (Cabot, 1993; Durrani et al., 2015; Duan and He, 2017; DeLeon and Senocak, 2017).

Although the ranges of values of Pr_T and Cs commonly used are $0.4\leq Pr_T\leq 1$ (Edison, 1985; Kimmel and Domaradzki, 2000) and $0.065\leq Cs\leq 0.2$ (Li and Ma, 2003), or $0.0265\leq C_k\leq 0.119$ (assuming $C_\epsilon=1.048$), general consensus exist that universally valid values for these parameters do not exist and that a proper choice of them should be based on careful comparison with experiments or with the outcomes of dedicated DNS. It is essential to remark that this specific aspect becomes even more critical for the present work, where conditions for which the flow *has just entered the turbulent regime* are considered and for which, therefore, the values traditionally used in the literature may not work properly.

Towards the end to determine reliable values for such parameters, a preliminary set of simulations has been conducted comparing the outcomes of the LES model with DNS simulations.

Given the aforementioned prohibitive cost of 3D DNS simulations and taking advantage of the isotropic (universal) nature of turbulence on small scales (described in Sect. 4.6), in particular, this initial study has been conducted in the framework of two-dimensional (2D) simulations, as illustrated in detail in Sect. 8.1.

Table 8.1: Non-dimensional values of main frequency for DNS and LES cases (Two-dimensional numerical simulation, $Ra=10^7$). The location of the probes for the FFS case are x=7.9, y=0.65 (adiabatic floor) and x=4.8, y=0.5 (hot floor).The location of the probes for the BFS case with both adiabatic and hot floor are x=9, y=0.25.

Configuration	DNS	LES
Adiabatic floor, *Ri*=100 (FFS)	20817.6	17478
Hot floor, *Ri*=100 (FFS)	12900	10370
Adiabatic floor, *Ri*=25 (BFS)	8760.4	7759
Hot floor, *Ri*=25 (BFS)	10960	8798.8

8.1 Comparison of LES with DNS

In the light of the criteria shown in Sect. 4.6.1, a mesh size of 740x120 has been used for all the 2D LES simulations with $Ra=10^7$ (such a choice corresponding to $\Delta x=1.35x10^{-2}$, $\Delta y=8.3x10^{-3}$), whereas for the corresponding DNS the mesh size has been based on the Kolmogorov length scale, i.e. eq. (4.5) (which implies $\Delta x=\Delta y=7.5x10^{-3}$). The values of C_k and turbulent Prandtl number have been changed continuously to understand which ideal set of values can reproduce the DNS results with an acceptable agreement.

Initially, such an iterative procedure has been implemented for the FFS with adiabatic floor. By virtue of extensive parametric analysis, the best set of values for both constants C_k and Pr_T have been found to be $Pr_T=0.9$ and $C_k=10^{-3}$. As the reader will realize by inspecting Fig. 8.1, the velocity and temperature fields, display almost the same dynamics observed for the DNS case (see Fig. 6.5d in Chapter 6, where a mesh with the size of the Kolmogorov length scale was used). The results are indeed consistent in terms of *number of plumes* present in the domain at a given instant and related *velocity of propagation* in the downstream direction. This has also been confirmed through analysis of the main frequency of the signal measured by a probe located at a fixed position in the flow. These values are reported in the first row of Table 8.1.

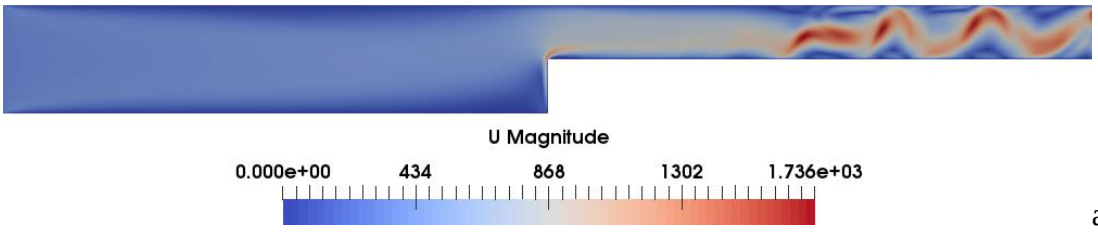

a)

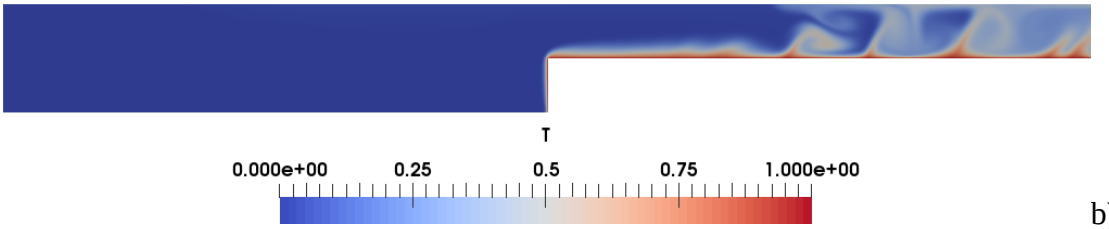

b)

Figure 8.1: Snapshots of velocity field (a) and temperature distribution (b) for the FFS (*Ri*=100) with adiabatic floor (LES, C_k=1x10^{-3} and Pr_T=0.9).

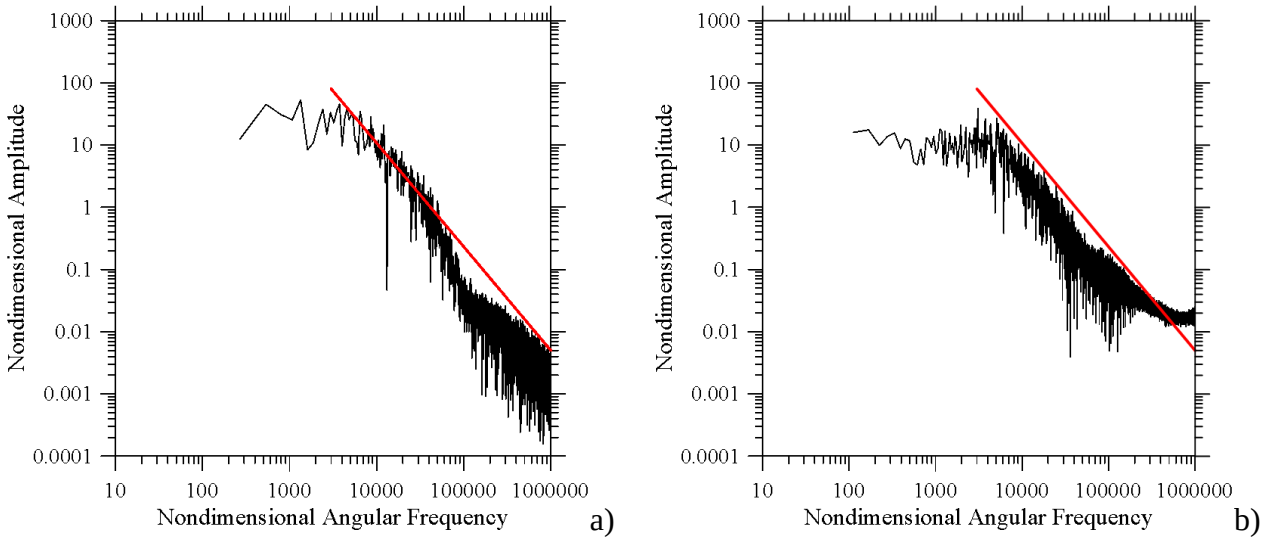

Figure 8.2: Frequency spectrum for the FFS (*Ri*=100) with adiabatic floor (probe position x=7.9, y=0.65): a) DNS, b) LES.

As an additional check, the entire frequency spectrum has been plotted for both cases. As qualitatively and quantitatively substantiated by Fig. 8.2, both the spectra for LES and DNS follow the Kolmogorov law in a wide interval of frequencies. As expected, some differences can only be spotted for $\omega \geq O(10^5)$, which is consistent with the principles of the LES strategy (the spatiotemporal behaviour on very small scales or high frequencies being implicitly taken into account via the subgrid viscosity rather than being captured directly by the numerical simulation).

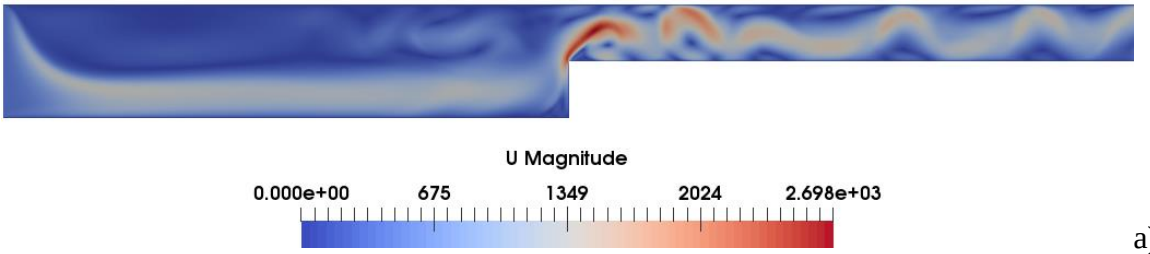

a)

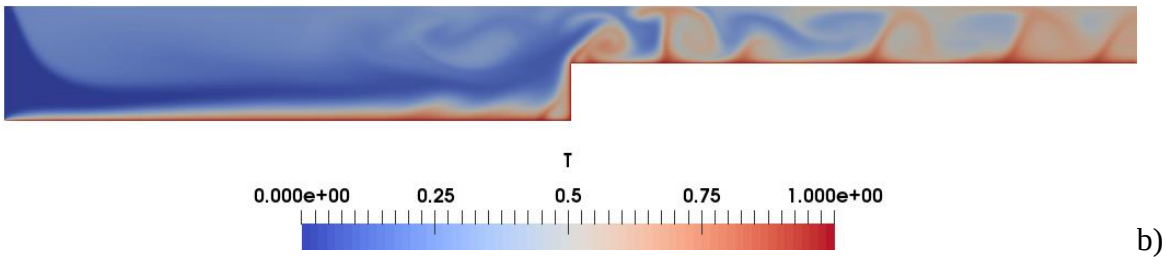

b)

Figure 8.3: Snapshots of velocity field (a) and temperature distribution (b) for the FFS (*Ri*=100) with hot floor (LES, $C_k=2x10^{-3}$ and $Pr_T=0.9$).

In order to determine the sensitivity of the constant C_k to the extent of buoyancy effects present in the domain, the same parametric analysis has been repeated considering the equivalent configuration in which the entire bottom wall of the channel is hot. This additional set of simulations has revealed that the agreement between LES (Fig. 8.3) and DNS still holds provided the value of C_k is slightly increased ($C_k=2x10^{-3}$ and $Pr_T=0.9$), as witnessed by Table 8.1 (second row) and Fig. 8.4.

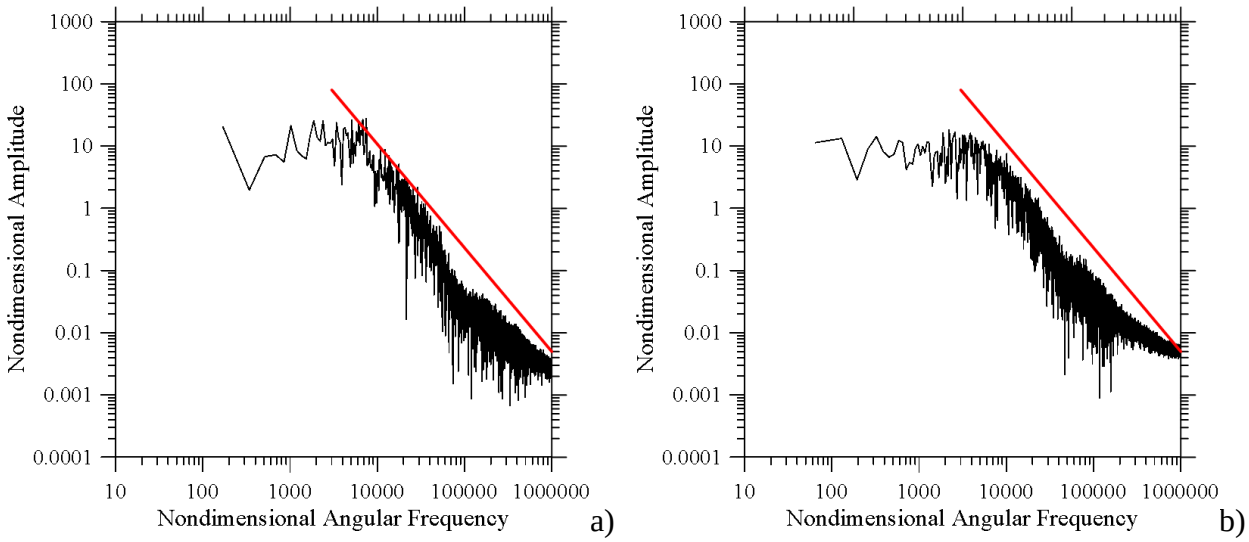

Figure 8.4: Frequency spectrum for the FFS (*Ri*=100) with hot floor (probe position x=4.8, y=0.5): a) DNS, b) LES.

For the sake of completeness, Fig. 8.5 provides some additional instructive information, namely, the ratio of the main frequencies determined by means of DNS and LES, as a function of the constant C_k. It can be seen that as the optimal aforementioned value is exceeded, a further increase in this parameter causes a mitigation of the dominant flow frequency until a completely steady state is attained for $C_k=0.1$.

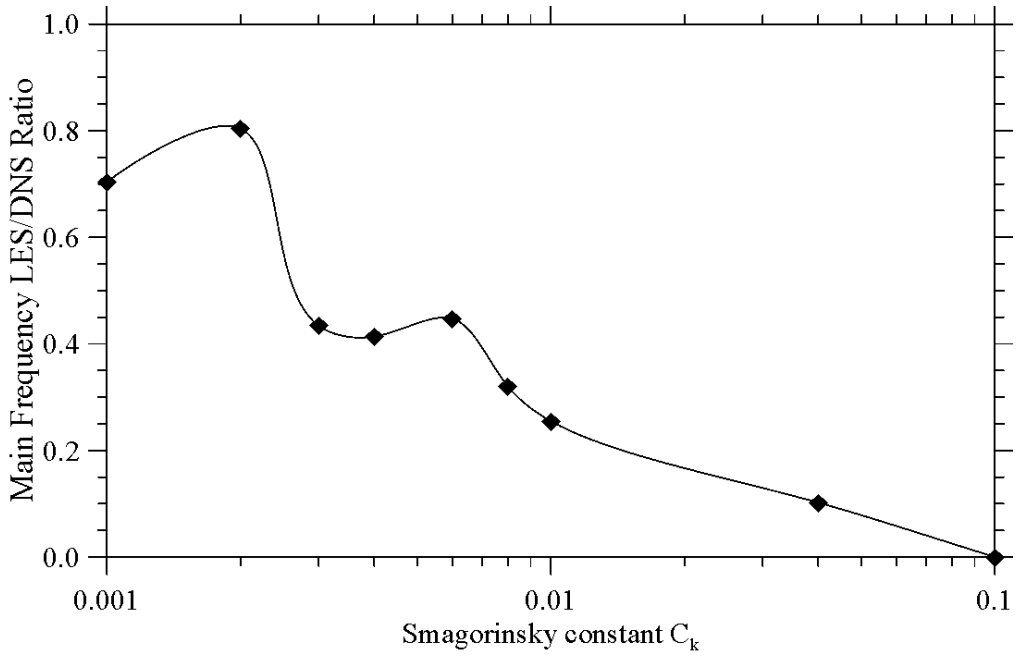

Figure 8.5: LES/DNS ratio of main flow frequency (FFS with hot floor, the spline is used to guide the eye).

This may be regarded as a clear example of a well-known shortcoming of the LES approach, i.e. its tendency to induce flow re-laminarization due to excessive dissipation occurring on the small scales if the value of the constant appearing in the expression of the subgrid viscosity is not properly tuned. The Smagorinsky model is known to often over-predict subgrid-scale dissipation and modify the true energy cascade. Just to cite a few examples, Montazerin et al. (2015) found the Smagorinsky coefficient for squirrel-cage fans to be considerably less than its classical value Cs=0.166 (corresponding to C_k=0.094); similarly, Bartosiewicz and Duponcheel (2019) observed that even a value as small as Cs=0.027 (equivalent to $C_k \cong 8 \times 10^{-3}$) can cause flow re-laminarization in some regions of the fluid domain. This problem becomes even more critical if conditions for which the flow has just entered the turbulent regime are considered. Relevant information about this specific point can be found in the earlier studies mentioned in Chapter 6 and Chapter 7 where the evolution of hybrid convection for both FFS and BFS systems was tracked as a function of the Rayleigh number from steady states up to fully developed turbulence. For the values of *Ri* considered in the present work, chaos was observed for $Ra \cong 10^7$ as a realization of the complex unsteady behavior of thermal plumes sparked by earlier flow Hopf bifurcations. In turn, these were found to be the outcome of the complex interplay of inertial and buoyancy effects (see Chapter 6 and Chapter 7).

As indicated by the present study, the choice of the Smagorinsky constant becomes a particularly delicate aspect in problems where initial transition to time-periodic flow and later to turbulence (on further increasing the governing parameters) is supported by the aiding influence of fluid-dynamic disturbances of shear-driven and buoyant nature. Too high values of this constant may

cause an unphysical alteration of the velocity of propagation of waves in the fluid domain (slowing down the trains of thermal plumes traveling in horizontal direction) and even prevent completely the flow from developing the required hierarchy of bifurcations that leads to chaotic behavior.

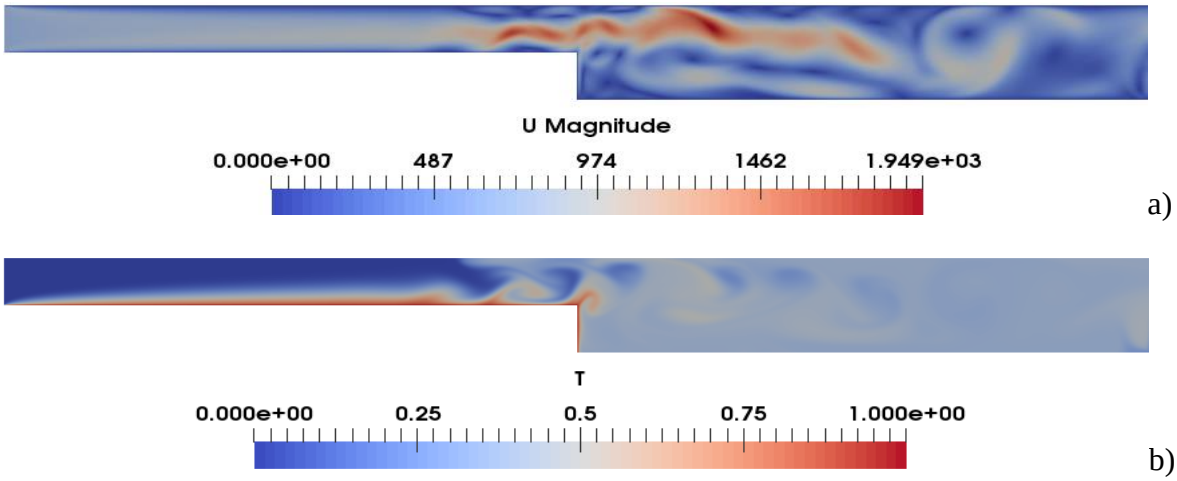

Figure 8.6: Snapshots of velocity field (a) and temperature distribution (b) for the BFS (*Ri*=25) with adiabatic floor (LES, C_k=2x10^{-3} and Pr_T=0.9).

To demonstrate the validity of this conceptual architecture (and the related modus operandi), the procedure implemented for the FFS has been duplicated to determine the equivalent optimal parameters of C_k and Pr_T for the BFS configuration. The outcomes of the related simulations (summarized in Figs. 8.6-8.7 and 8.8, and in Table 8.1 for the cases with adiabatic and hot floor, respectively) essentially confirm that C_k=2x10^{-3} and Pr_T=0.9 would still be relevant choices.

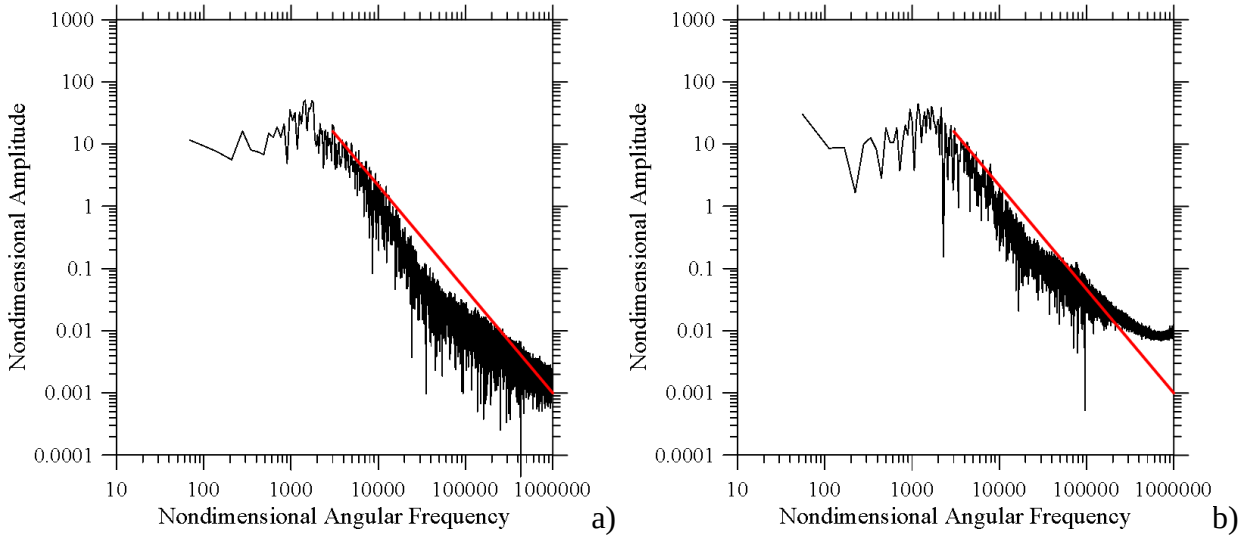

Figure 8.7: Frequency spectrum for the BFS (*Ri*=25) with adiabatic floor (probe position x=9, y=0.25): a) DNS, b) LES.

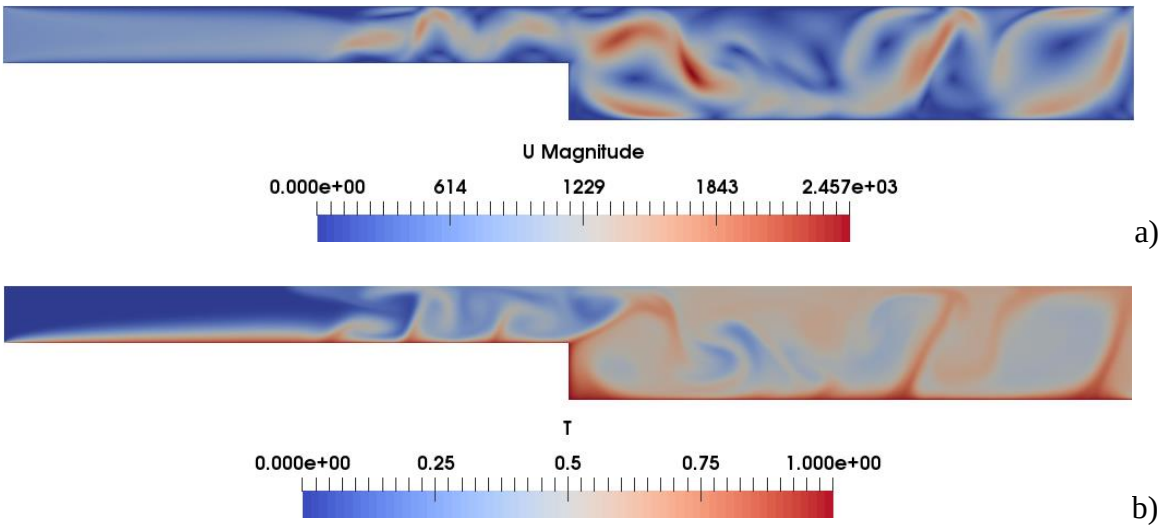

Figure 8.8: Snapshots of velocity field (a) and temperature distribution (b) for the BFS (*Ri*=25) with hot floor (LES, $C_k=2x10^{-3}$ and $Pr_T=0.9$).

8.2 Three-dimensional Mixed Convection for Ri=100 (FFS)

After determining the optimal values of the LES parameters by which good agreement is obtained between DNS and LES (the latter having been conducted, as explained before, with a coarser mesh such that its size is in located within the inertial range), dedicated 3D simulations have been performed. In the light of the earlier results provided by the 2D simulations (Sect 8.1), a mesh with 740x120x60 points has been used (corresponding to a total of more than 5 million computational nodes, with $\Delta x=1.35x10^{-2}$, $\Delta y=8.3x10^{-3}$ and $\Delta z=1.66x10^{-2}$). Obviously, these simulations have been executed with the specific intent to clarify the role potentially played in the considered problem by the third spatial direction. A detailed description of the corresponding dynamics in 2D can be found in Chapter 6 and, for the sake of brevity, it is not duplicated here. Rather, it should be recalled that the flow is characterized by the onset of thermal plumes in the region above the step and their propagation in the downstream direction. In particular, while for $Ra=10^6$, their spacing is regular and plumes appear at a distance l from the leading edge (i.e. the corner of the step) that is approximately 5 times the height of the step i.e. $l \cong 5/2$, for $Ra=10^7$, plumes are produced *at a much smaller distance from the leading edge* ($l \cong 2$). Moreover, plumes are no longer evenly distributed in space and display relatively chaotic dynamics (see Chapter 6). As a fleeting glimpse into Fig. 8.9 would confirm, most of these characteristics are retained in the 3D case, i.e. a region free of plume can still be identified above the step (with extension $l \cong 2$) and plumes display quite an irregular behavior in the remaining space. The most striking difference is represented by the morphology of the plumes, which now nucleate in the form of rising 'columns' of fluid distributed along the spanwise direction, actually marking a transition from an initially 2D behaviour to a fully 3D scenario as a distance $l \cong 2$ from the step leading

edge is exceeded. In particular 3 distinct plumes can be seen along z in proximity to the corner (Fig. 8.9); as time passes and plumes are transported by the imposed forced flow, however, coalescence phenomena are enabled. As a result of plume merging, the number of plumes in the spanwise direction (i.e. the flow wavenumber along z) is reduced, while their transversal size and vertical extension grow continuously until these convective structures leave the system through the outlet.

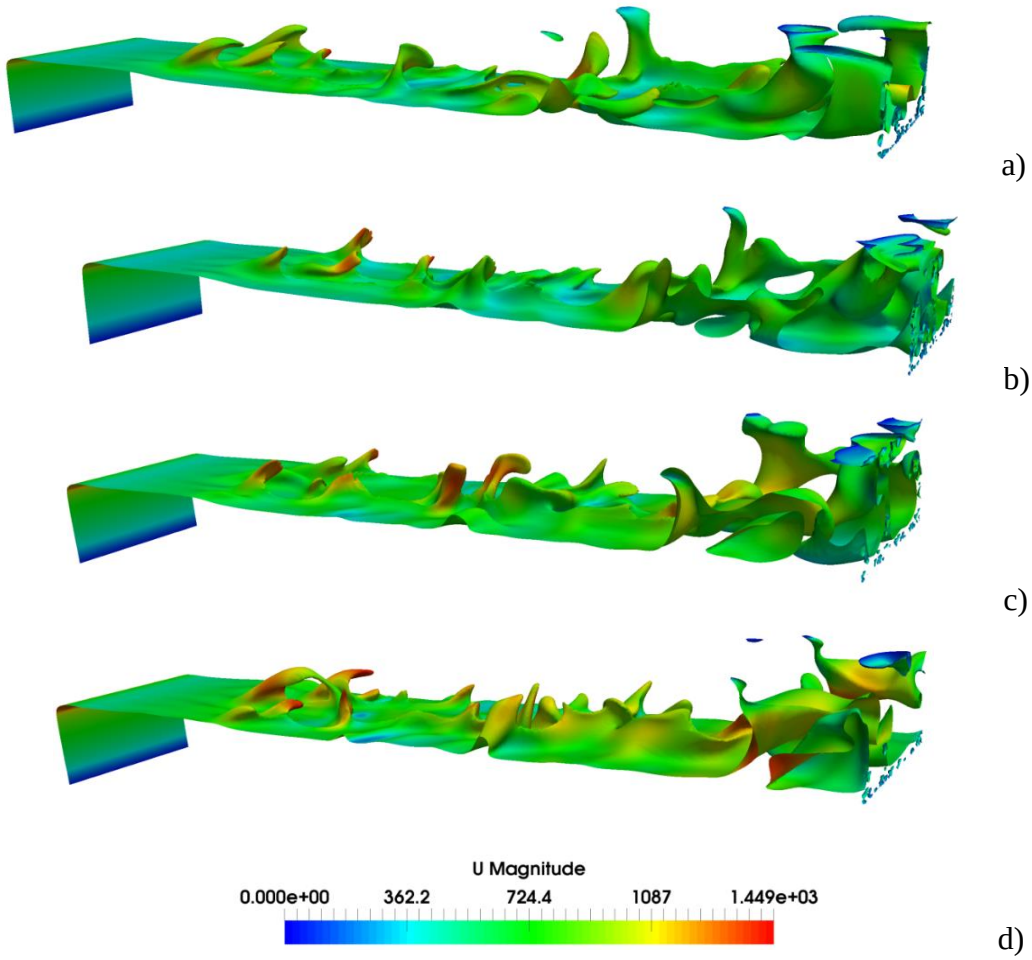

Figure 8.9: Snapshots of the three-dimensional iso surfaces of temperature coloured according to the velocity magnitude for the FFS (*Ri*=100) with adiabatic floor. The snapshots are at a) t=0.04843, b) t=0.04885, c) t=0.04926, d) t=0.04972.
.

If the adiabatic floor is replaced with a hot boundary (at the same temperature of the step), the scenario becomes even more complex (Fig. 8.10). The plume nucleation region is transferred from the top surface of the step to the heated floor. When plumes initially traveling along the floor meet the hot vertical surface of the step, they interact with the related (vertical) thermal boundary layer producing well-defined convective features. Most surprisingly, plumes are able

to retain their identity (in the sense that, despite the interaction with the vertical thermal boundary layer, 3 distinct plumes originating from the floor of the channel can still be identified in proximity to the vertical side of the step). The caps of these plumes (being reinforced by the fluid rising due to continuity as a result of the reduction in the available cross-sectional area) extend well-beyond the vertical extension of the step and, as such, are able to interfere directly with the flow developing after the step. Every time that the cap of one of these plumes impinges on the top surface of the step, a new plume is created along this boundary. Accordingly, no buffer (plume-free) region exists in this case.

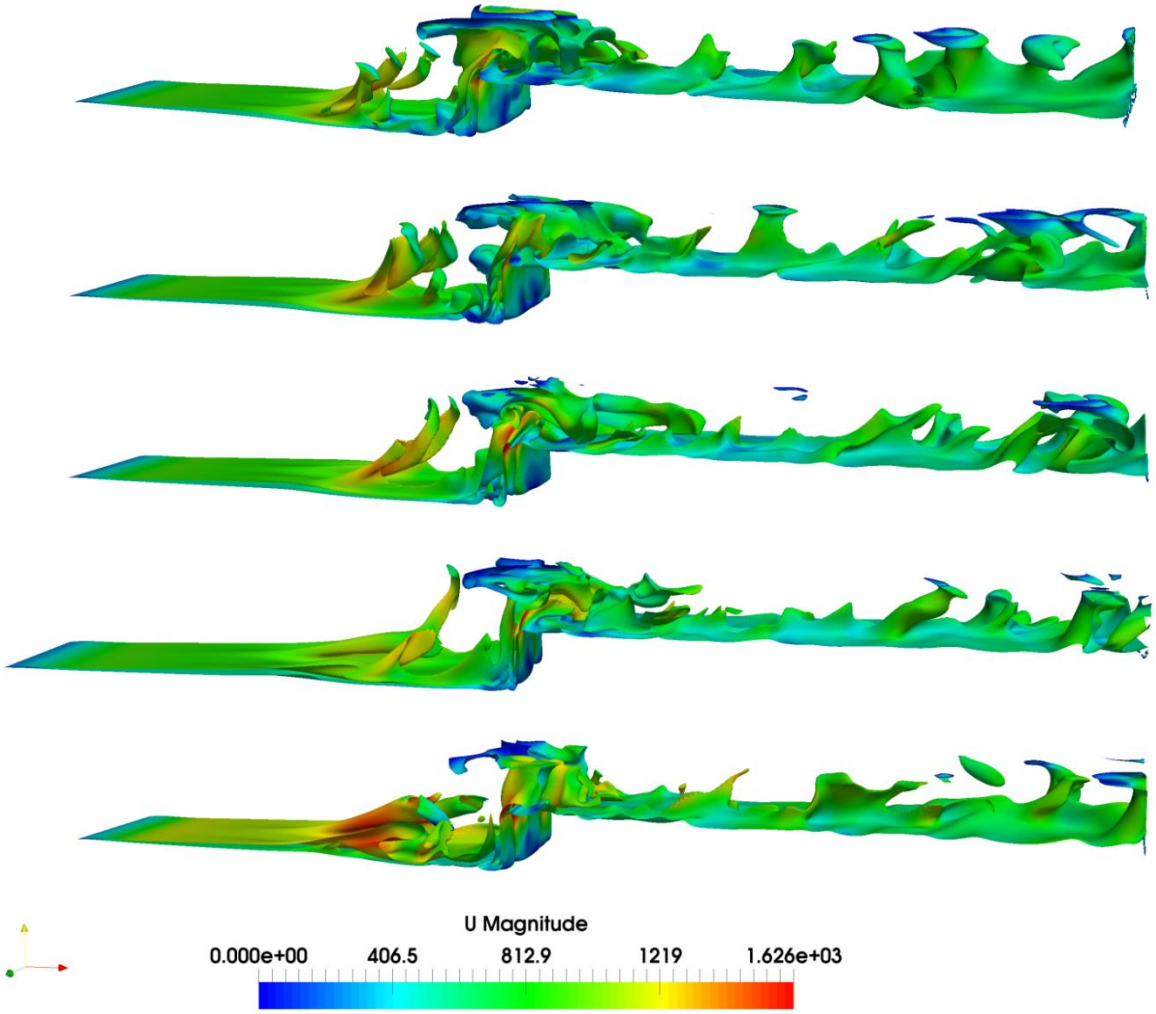

Figure 8.10: Snapshots of the three-dimensional iso surfaces of temperature coloured according to the velocity magnitude for the FFS (*Ri*=100) with hot floor. The snapshots are at a) t=0.04219, b) t=0.04286, c) t=0.04350, d) t=0.04416, e) t=0.04483.

Additional insights into this scenario can be gathered from the signals provided by thermocouples (numerical probes) located just before and after the step (at a non-dimensional distance 0.25 from the step position and from the bottom boundary, in the horizontal and vertical

directions, respectively, and evenly space along the spanwise direction yet at a relative distance 0.25 from one another).

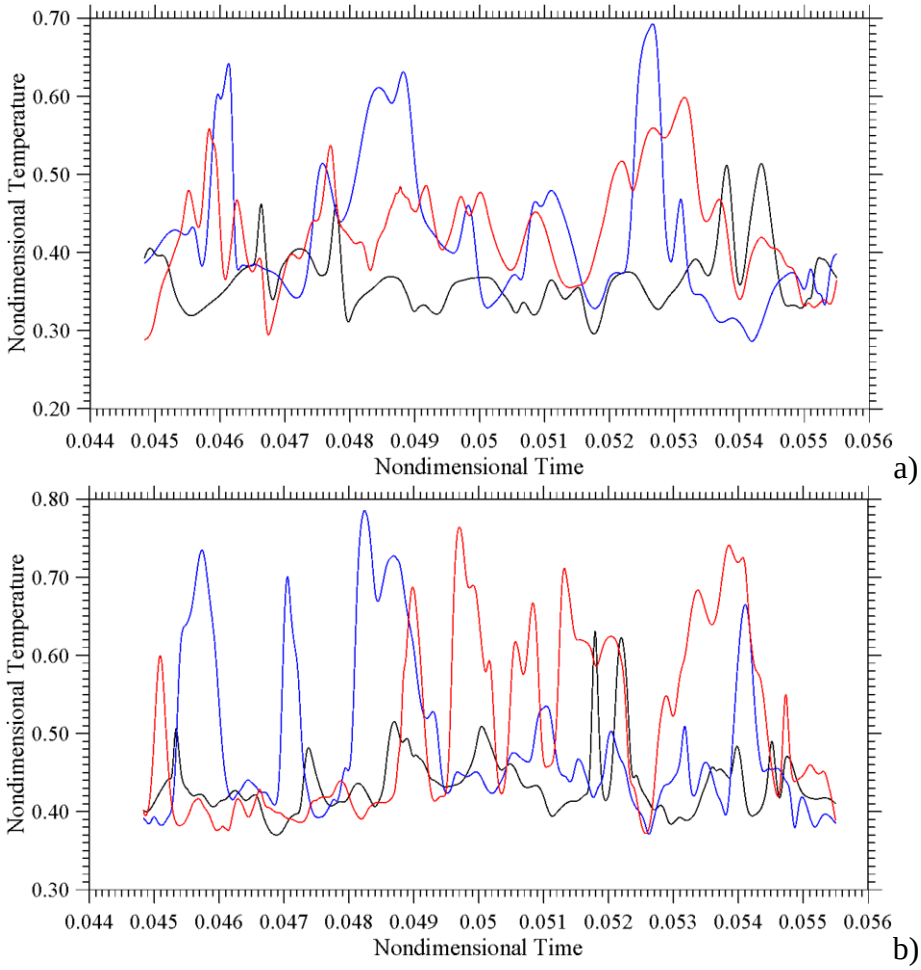

Figure 8.11: Temperature signals measured by three probes evenly spaced along the spanwise direction (z=0.25, 0.5 and 0.75) located before and after the step for the FFS case (*Ri*=100) with hot floor: a) x= 4.75, y=0.25 (before the step), b) x=5.25, y=0.75 (after the step, the presence of peaks in one signal seems to exclude the possibility to have peaks with comparable amplitude in the other signals).

Interestingly, (see Fig. 8.11) while before the step, peaks of similar magnitude are present in all the signals (with peak overlap at certain times, which indicates plume coexistence along the spanwise direction), after the step, significant peaks can be seen in one signal at a time. As an example, while for t< 0.049, significant peaks can only be detected in the blue signal, for t>0.049 this role is transferred to the red signal. This apparently innocuous observation has important implications in terms of flow structure and plume evolution. Indeed, it indicates that the wavenumber undergoes a strong decrease across the step. Before the step, "more" plumes (up to "three" along the spanwise extension A_z of the domain) can be present at the same time along the streamwise direction (at a fixed station x), whereas beyond the step, only a plume with relatively

extended horizontal cross-diameter is allowed. This can be alternately located in proximity to the $z=A_z$ boundary (blue signal), or at $z \cong A_z/2$ (red signal).
As a concluding remark for this section, it is worth mentioning that comparison of the 2D and 3D frequency spectra for both the FFS with adiabatic and hot floor (not shown for the sake of brevity) has led to the conclusion that, despite some differences in the low-frequency range (the spectrum in this interval being more energetic in the 3D case due to the smaller size and larger number of plumes in this case), the amplitude distributions are almost identical in the inertial range (where they align with the Kolmogorov law). This indicates that the mechanisms driving the cascading behavior of energy for the FFS do not depend significantly on the dimensionality of the problem.

8.3 Three-dimensional Mixed Convection for Ri=25 (BFS)

Having completed a sketch of the 3D dynamics for the FFS case, attention is now turned to interpreting the equivalent results for the BFS configuration. Following the same approach undertaken in the earlier sections, an incremental understanding of the considered phenomena is achieved through the stepwise consideration, first, of the simpler configuration with adiabatic floor, and, then of the more complex scenario where the floor is kept at the same temperature of the step.

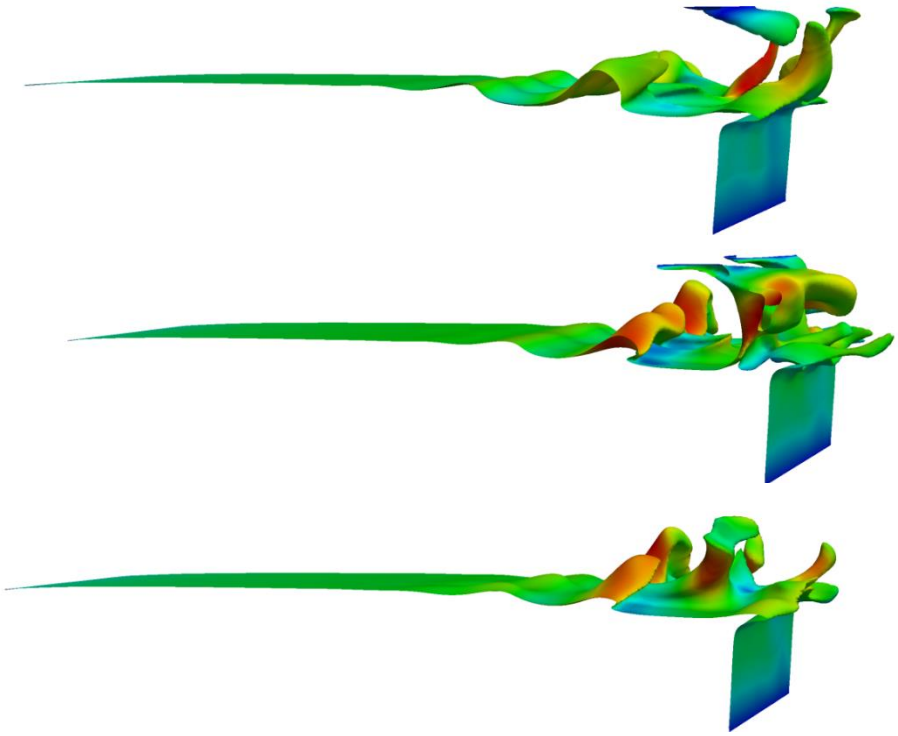

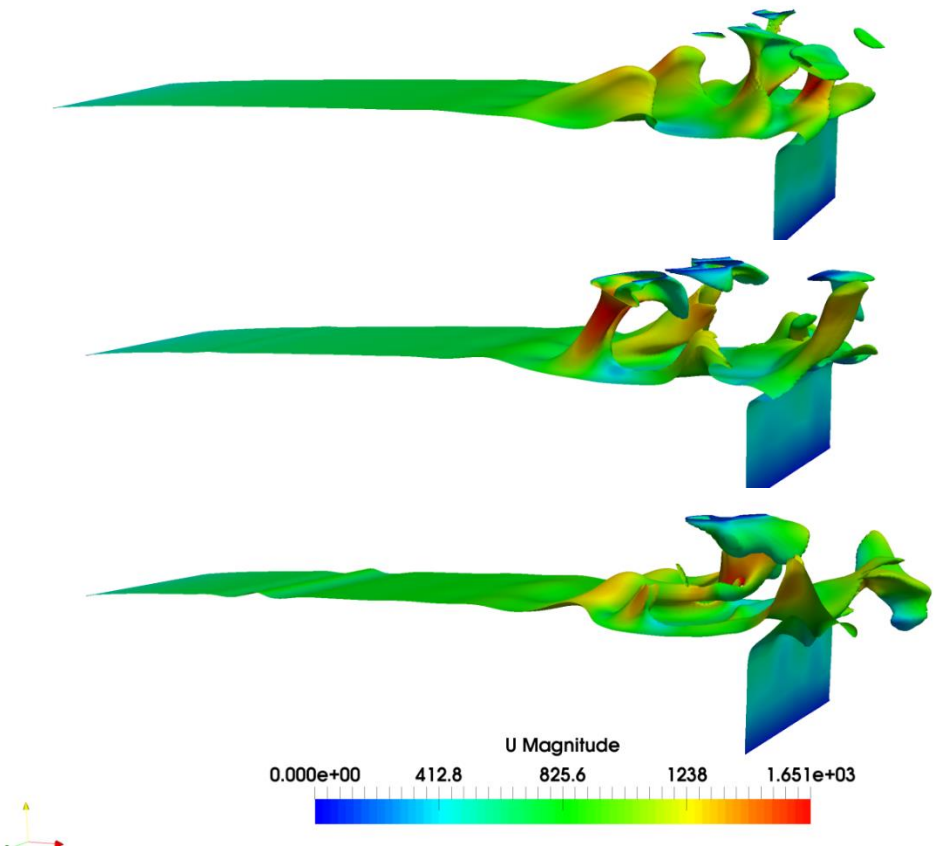

Figure 8.12: Snapshots of the three-dimensional iso surfaces of temperature coloured according to the velocity magnitude for the BFS (*Ri*=25) with adiabatic floor. The snapshots are at a) t=0.03242, b) t=0.03313, c) t=0.03401, d) t=0.03459, e) t=0.03514, f) 0.03574.

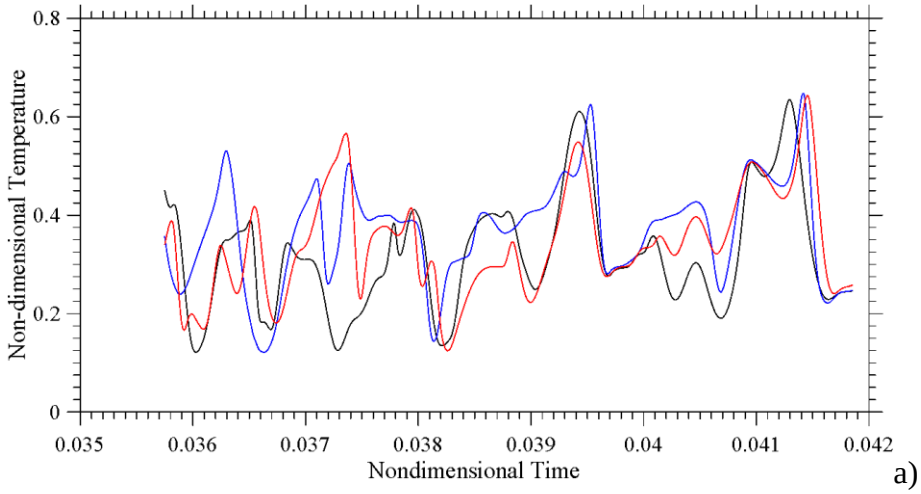

a)

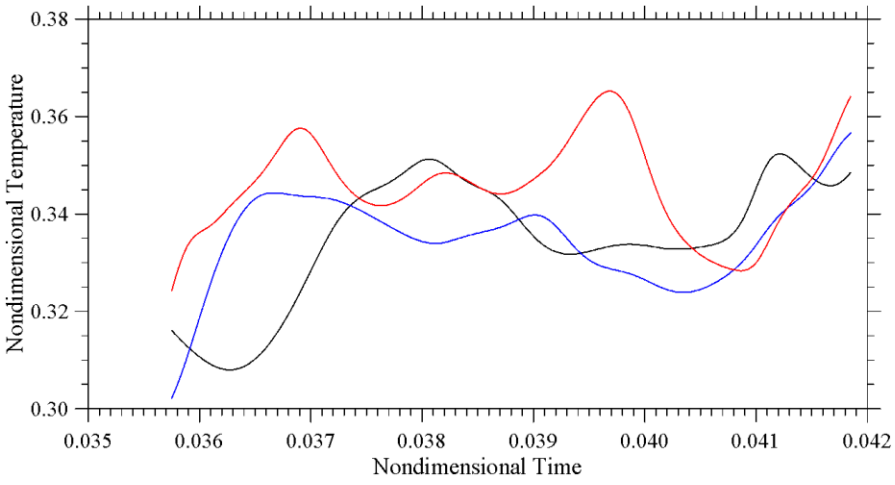

b)

Figure 8.13: Temperature signals measured by three probes evenly spaced along the spanwise direction (z=0.25, 0.5 and 0.75) located before and after the step for the BFS case (*Ri*=25) with adiabatic floor: a) x= 4.75, y=0.75 (before the step), b) x= 5.25, y=0.25 (after the step).

As evident in Fig. 8.12, for the BFS with adiabatic floor, a 3D instability develops along the thermal boundary layer in the left portion of the channel (i.e. in the region of reduced cross-sectional area, $x < A_x/2$). This is revealed by the presence of bulges or sinusoidal distortions in the isosurfaces of velocity, which finally evolve in thermal plumes apparently originating from the step trailing edge (the corner). While initially the flow separates and reattaches several times producing bulges that display a weak modulation along the spanwise direction (3 peaks along z), it is only in correspondence of the corners that well-defined (distinct) rising currents with horizontally extended caps are produced.

These observations are complemented by Fig. 8.13 where the probe signals have been reported considering again stations located before and after the step. It shows that in the present case the peaks are not mutually exclusive. Unlike the behavior seen in Fig. 8.11b, peaks occur approximately at the same times in Fig. 8.13a, which indicates plumes can exist in parallel along the spanwise direction (as also evident in Fig. 8.12).

However, while a synchronous plume behavior can be seen just before the step, a well-defined correlation can no longer be identified after it. Moreover, both the signal amplitude and frequency undergo a significant decrease, which indicates that just after the section $x=A_x/2$ the degree of unsteadiness is largely reduced in the lower half of the domain (the probes being located at x= 5.25, y=0.25).

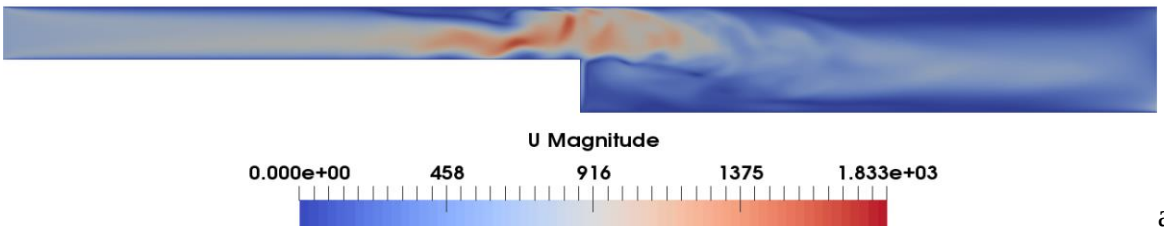

a)

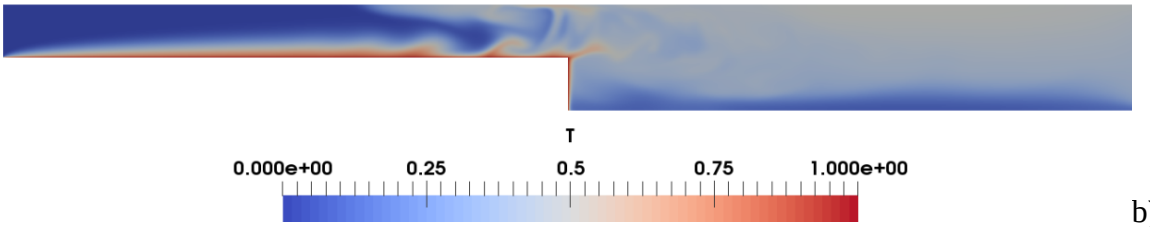

b)

Figure 8.14: Snapshots of velocity field (a) and temperature distribution (b) for the BFS (*Ri*=25) with adiabatic floor (plane z=0).

As a final look at Fig. 8.14 would indicate, a weak recirculation region is created in that area (with the fluid moving from right to left along the floor of the channel). Vice versa a relatively strong horizontal jet can still be seen in the upper half of the channel. However, owing to the vigorous plumes originating from the step (the corner) and the vortices which are periodically released from their caps, such a jet undergoes a significant modulation in time, especially for $A_x/2<x<3A_x/4$. Strong mixing occurs in that interval as a result of the presence of the aforementioned vortices, which travel continuously in the downstream direction (Fig. 8.14). Along these lines, the next figure of the sequence (Fig. 8.15) illustrates that mixing is effective not only in xy planes. The flow has a significant velocity component along the spanwise direction too, as witnessed by the presence of several visible vortices in planes perpendicular to x. Only for $x\geq3A_x/4$ the almost perfect parabolic profile of horizontal velocity that is typical of the planar Poiseuille flow is re-established (Fig. 8.14a) and mixing effects become relatively weak (Fig. 8.16a). Figs. 8.14b and 8.16b shed some additional light on this behavior, by showing that the temperature distribution becomes essentially uniform over 90% of the entire vertical extension of the channel, with the 10% residual cold fluid being located under the warm fluid (stable thermal stratification).

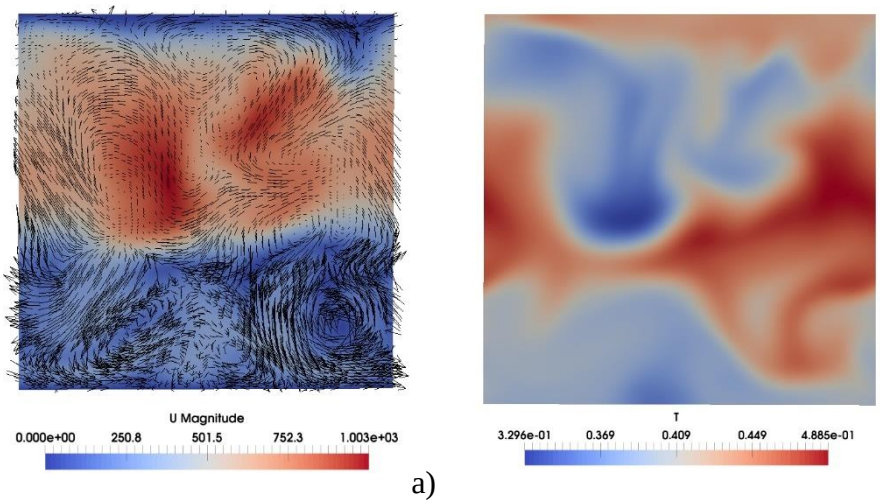

a) b)

Figure 8.15: Snapshots of velocity and temperature fields in the yz plane for $x=5A_x/8=6.25$.

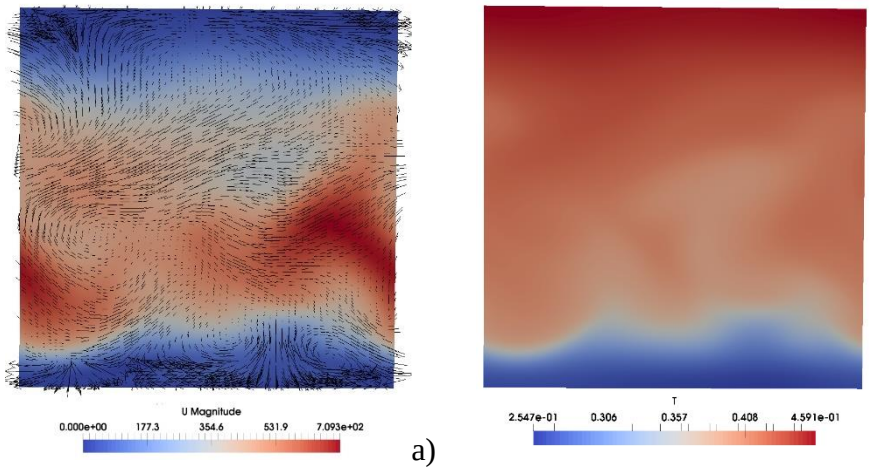

Figure 8.16: Snapshots of streamlines and temperature in the yz plane for $x=3A_x/4=7.5$. Comparison with Fig. 8.15 indicates that the magnitude of velocity is significantly (one order of magnitude) smaller and the distribution of temperature becomes much more uniform.

Comparison with the equivalent 2D flow (Fig. 8.6) is instrumental in showing that when the flow is prevented from developing a velocity component in the spanwise direction, the horizontal current entering the region with increased cross-section area (the aforementioned jet) can survive for a longer time before losing its identity. The key to understanding this behavior lies in considering that in 2D no vorticity like that shown in Fig. 8.15a and 8.16a can be produced, thereby allowing the fluid leaving the step to use the available kinetic energy to spread along the x direction.

If the adiabatic floor is replaced with a thermally heated boundary (yet at the same temperature of the step), as anticipated, the complexity of the problem increases (Fig. 8.17). A "sea" of thermal plumes develops on the floor of the channel for $x>A_x/2$. However, plumes still manifest along the top boundary of the step as a result of the aforementioned disturbance propagating along (growing inside) the thermal boundary layer located there.

Unlike the situation examined for the BFS with adiabatic floor, in this case, the behavior in proximity to the corner does not depend only on what happens in the region with reduced cross-sectional area (i.e. for $x<A_x/2$). Just after the step a localized clockwise oriented vortex is created in the lower half of the domain as a consequence of the tendency of the separated main flow to reattach to the bottom. Comparison of Figs 8.14a and 8.18a, indicates that in this case the vortex is relatively strong. Accordingly, a current is established along the floor, by which thermal plumes are transported in the upstream direction (i.e. towards the step). Owing to this current, heat is funneled into the vertical boundary layer developing along the vertical wall of the step and this contributes to strengthen the plumes there (the effect being similar to that already described for the FFS case with hot floor).

Due to this mechanism two different regions of plume growth can be identified for $x> A_x/2$, one in which the vertical extension of the plumes decreases along x (from the step position towards

the reattachment line), and a second region where plume size grows in the downstream direction (from the reattachment line towards the outflow section). Put differently, two counter-propagating waves or trains of plumes affect the region with increased cross-sectional area at the same time. These originate from the line where the flow leaving the step hits the floor, and for each of them, plume growth is caused by the additional heat being injected inside plumes from below as time passes and the concurrent plume merging phenomena (the latter cause the coalescence of plumes initially located at different positions along the spanwise direction).

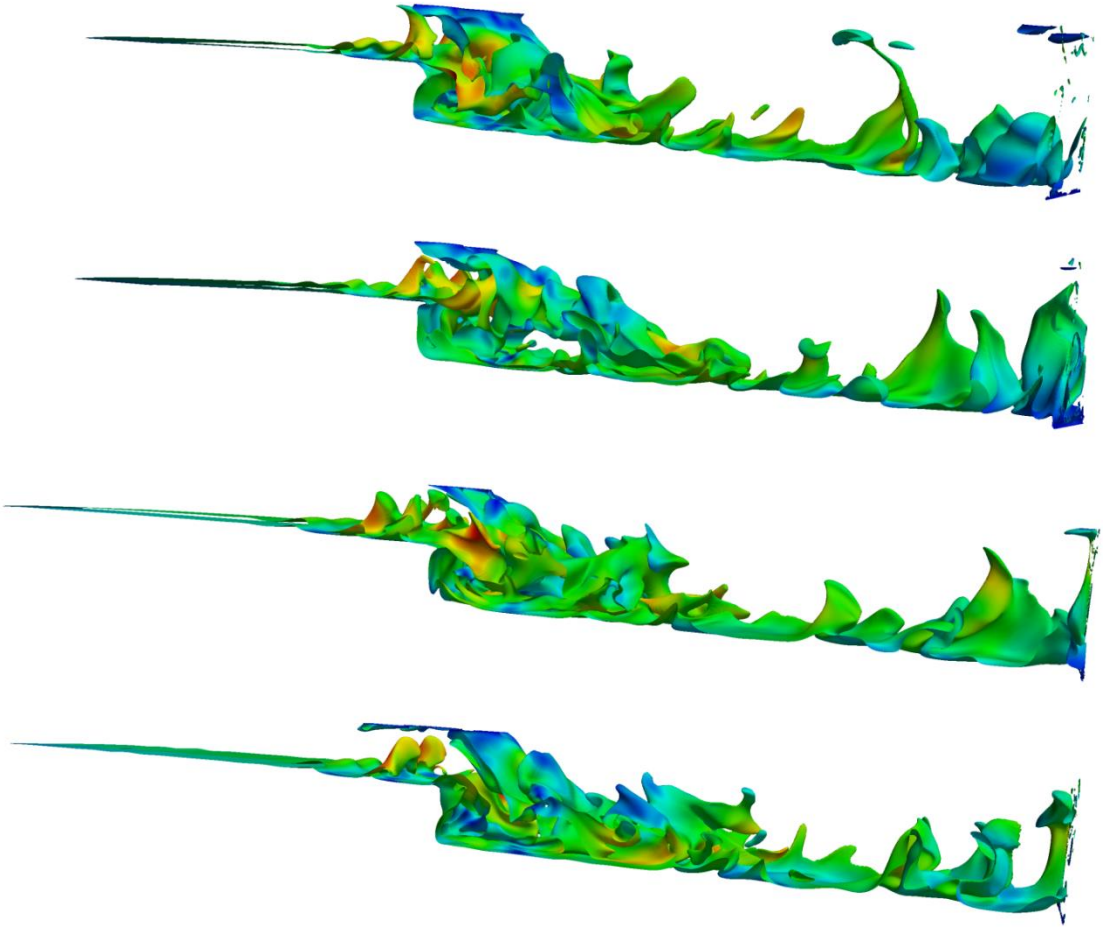

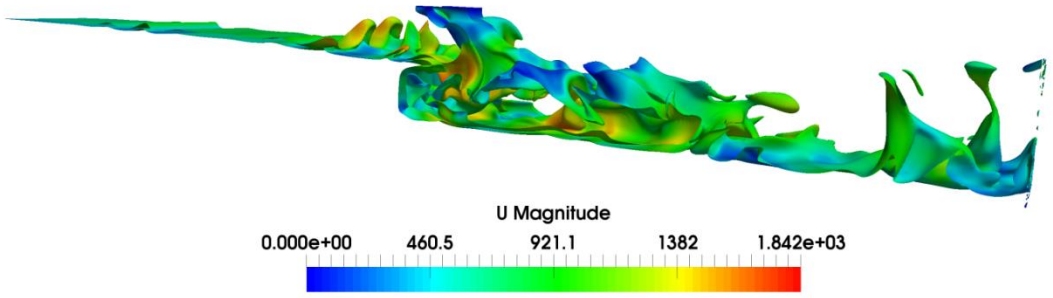

Figure 8.17: Snapshots of the three-dimensional iso surfaces of temperature coloured according to the velocity magnitude for the BFS (*Ri*=25) with hot floor. The snapshots are at a) t=0.02999, b) t=0.03072, c) t=0.03145, d) t=0.03235, e) t=0.03290.

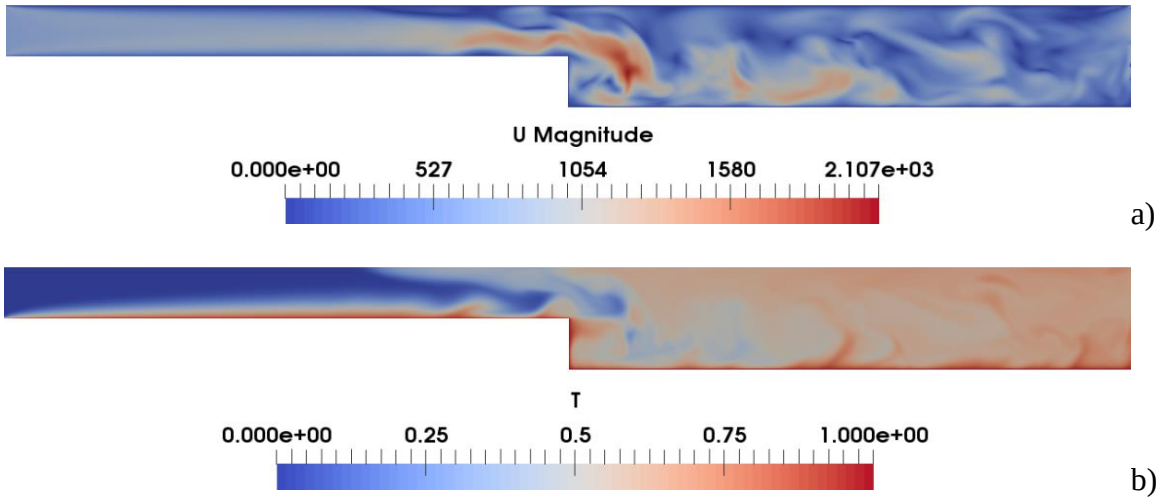

Figure 8.18: Snapshots of velocity field (a) and temperature distribution (b) for the BFS (*Ri*=25) with hot bottom wall (plane z=0).

Correlation of Fig. 8.18 with the equivalent 2D results (Fig. 8.8) is also instructive. It qualitatively substantiates the realization that the 3D flow is more chaotic, as also confirmed by the more uniform (due to mixing) distribution of temperature established in the domain for $x>A_x/2$ and $y>1/2$. Unlike the BFS with adiabatic floor, the highest values of velocity for $x>A_x/2$ can be found in the lower half of the channel as a consequence of the train of thermal plumes developing there, whereas extended regions can be seen in the upper half of the domain where the *fluid moves in opposite direction* (which explains the different inclination taken by the plumes for $y>1/2$). This may be regarded as an important distinguishing mark with respect to the

equivalent 2D simulations (Fig. 8.8) where this effect is not present (plumes displaying a constant inclination to the right over the entire channel vertical extension).
Again, the distribution of velocity and temperature in the plane yz can be used to demonstrate the increased level of complexity taken by the 3D flow in terms of flow structure and temperature distribution (Figs. 8.19 and 8.20).

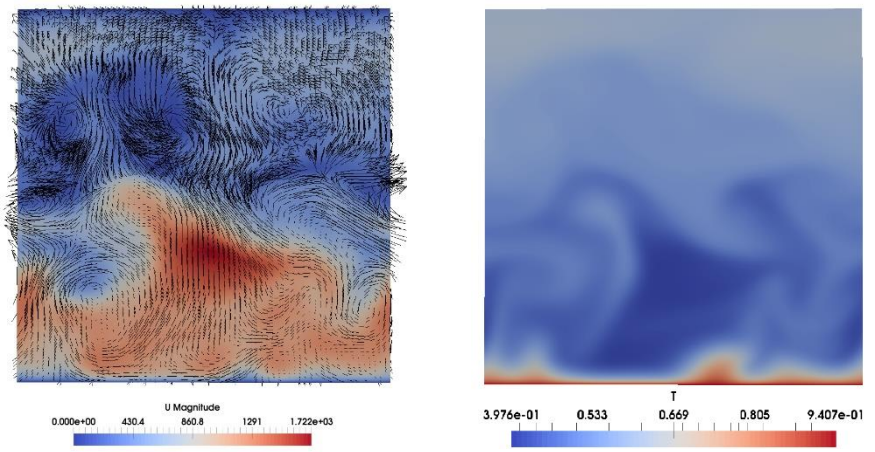

a) b)

Figure 8.19: Snapshots of velocity and temperature fields in the yz plane for $x=5A_x/8=6.25$.

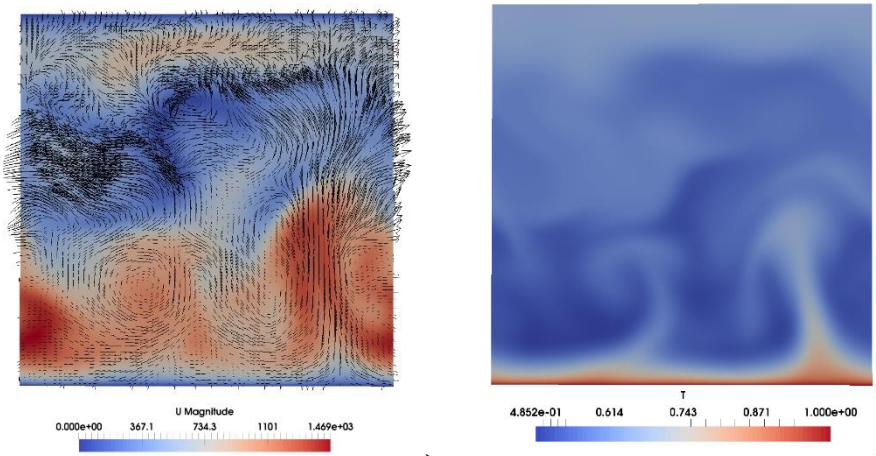

a) b)

Figure 8.20: Snapshots of streamlines and temperature in the yz plane for $x=3A_x/4=7.5$. Comparison with Fig. 8.19 indicates that the magnitude of velocity does not change significantly.

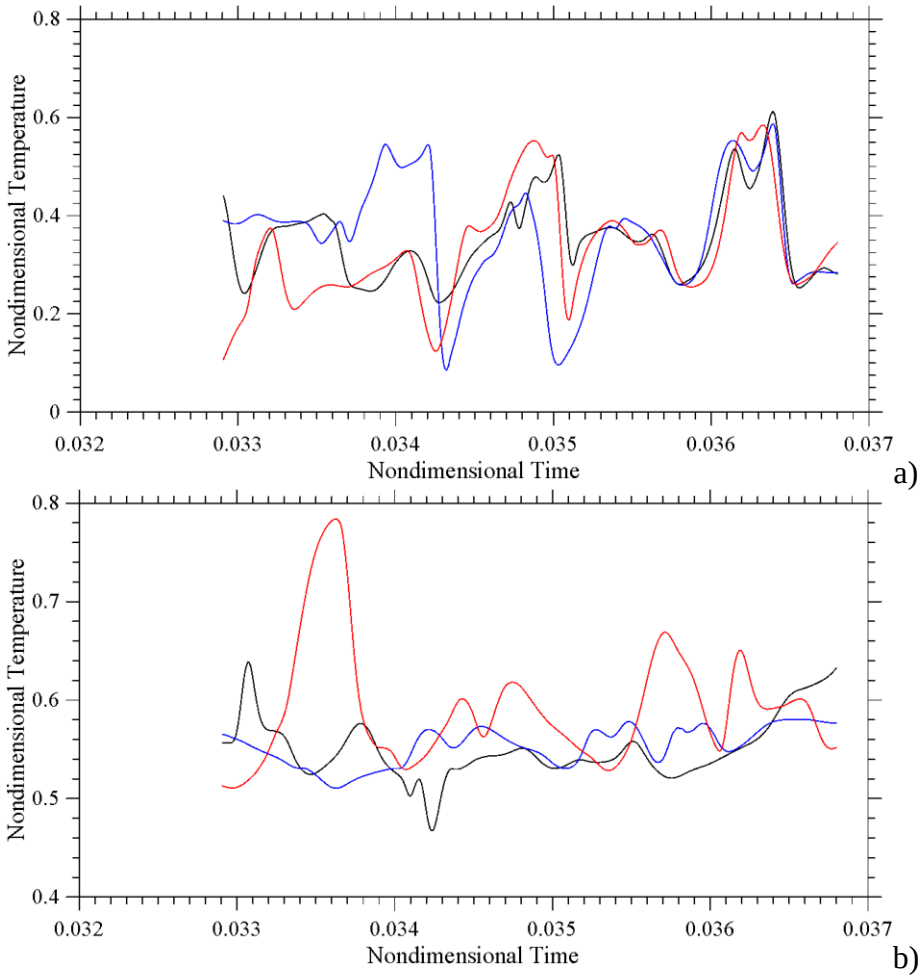

Figure 8.21: Temperature signals measured by three probes evenly spaced along the spanwise direction (z=0.25, 0.5 and 0.75) located before and after the step for the BFS case (*Ri*=25) with hot floor: a) x= 4.75, y=0.75 (before the step), b) x= 5.25, y=0.25 (after the step).

A final characterization of the observed dynamics in proximity to the step can be gained by considering once again the probe signals (Fig. 8.21). While the temperature signals display a synchronous behavior just before the step (denoting a quasi-2D scenario, Fig. 8.21a), a well-defined correlation can no longer be identified after the step (Fig. 8.21b), which (in agreement with the information reported in Fig. 8.19) indicates that the flow gains 3D behaviour as soon as the fluid enters the region of increased cross-sectional area.

For the sake of completeness, Fig. 8.22 illustrates the frequency spectra for the cases with adiabatic and hot floor, respectively. It is evident that both align with the $\omega^{-5/3}$ law put forward by Kolmogorov. However, a difference can be spotted in terms of energy content. The frequency spectrum for the hot floor case (Fig. 8.22b) displays a richer content in the high-frequency range, and this is due to the presence of an increased number of thermal plumes (put simply, the higher number of plumes passing through the location of probe results in a continuous addition of high frequency components to the spectrum).

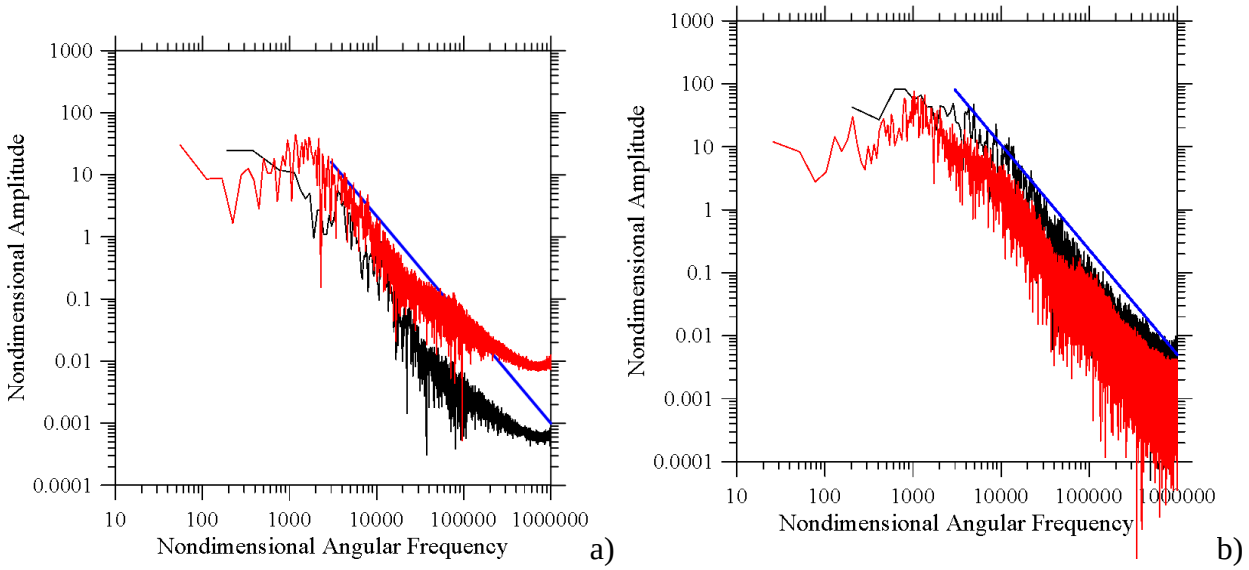

Figure 8.22: Frequency spectrum for the BFS (*Ri*=25) (color legend: black-3D results, red-2D results, blue-Kolmogorov scaling, probe position x=9, y=0.25): a) adiabatic floor, b) hot floor.

Vice versa, for the adiabatic floor case, this trend is reversed, with the 2D flow being more energetic for $\omega \geq 10^3$ (Fig. 8.22a). A proper justification for this counter-intuitive behavior can be elaborated in its simplest form on the basis of the argument that in the 3D case the almost perfect parabolic profile of horizontal velocity that is typical of the planar Poiseuille flow is re-established at a certain horizontal distance from the step, whereas this does not happen in 2D (compare again Figs. 8.6 and 8.14); to elucidate further the significance of this observation, one should keep in mind that the flow partial re-laminarization for $x>3A_x/4$ is essentially a result of the uniform temperature distribution produced beyond this station by the strong mixing effects experienced by the fluid in the preceding portion of the channel, i.e. for $x<3A_x/4$ (the less energetic nature of the spectrum at high frequencies for $x >3A_x/4$ in the 3D case can be directly rooted into this specific behavior, i.e. the absence of buoyancy effects).

8.4 Discussion

Following up on the last argument provided in the earlier section, this section is finally used as an opportunity to discuss critically the main outcomes of the present 3D investigation in relation to what is already known for the companion problem with no buoyancy (i.e. the cases with purely *forced flow*). As already discussed to a certain extent in the introduction, only a few studies have appeared where the problem was tackled in the framework of a 3D numerical approach. Taking into account the main findings of these investigations, here emphasis is put on analogies and differences with respect to the hybrid flow configurations treated in Sects. 8.2 and 8.3.

In line with those sections, the discussion progresses through the examination of both the FFS and the BFS. As a fleeting glimpse into the existing literature for the forced flow case would

immediately reveal, indeed, these two paradigms do not have a linear historical trajectory, in the sense that they have always simultaneously been used over the years to get insights into the behavior of flows with sudden contractions or expansions. The most evident realization of this modus operandi is the discovery that, regardless of the orientation of the step, these forced flows are always characterized by some degree of separation and ensuing generation of vorticity and eventually flow instabilities.

In particular, for the isothermal FFS, regardless of the dimensionality of the problem (be it 2D or 3D), the flow separates and reattaches in two different regions. More precisely, one recirculation zone is created upstream of the step adjacent to the bottom wall, while the second recirculation (typically in the form of a small bubble stretched in the horizontal direction) nucleates adjacent to the stepped wall downstream of the step edge. It is known that the related dynamics are governed by the Reynolds number. On increasing this parameter, the size of these recirculation zones generally grows. Moreover, the point of where flow separation occurs ahead of the step tends to migrate in the upstream direction.

Available 3D numerical studies for this problem are due to Wilhelm et al. (2003), Barbosa-Saldaña and Anand (2007) and Scheit et al. (2013) (a similar information about the BFS will be provided later in this section). Towards the end to gain better insight into the three-dimensionality that is typically observed in the aforementioned separation regions before the step, Wilhelm et al. (2003) conducted high-resolution simulations in the framework of a mixed spectral/spectral-element method. Moreover, a linear stability study of the flow at the step was also performed. Assuming a value of the Reynolds number 330 and periodic boundary conditions along the spanwise direction, it was found that the difference between the two-dimensional field and the averaged three-dimensional field is marginal, making clear that the 3D break-up of the separation region at the step is only a weak perturbation to the two-dimensional base flow (the amplitude of the spanwise velocity component being small in comparison to the maxima of the streamwise and normal velocities at the step). Nevertheless, for a larger value of the Reynolds number ($Re=8x10^3$), Scheit et al. (2013) found the departure from 2D flow to become more evident. By plotting the isosurfaces of the fluctuating pressure, they could reveal spanwise-elongated structures close to the edge of the step. These were observed to grow in streamwise extent downstream of the step and finally pair with each other.

Our work adds another piece to the puzzle by showing that buoyancy can significantly contribute to determine the dominant dynamics both before and after the step. As already shown in Sect. 8.2, although the Reynolds number is relatively high ($Re\cong3160$), if the Richardson number is of $O(10^2)$ (i.e. buoyancy effects are sufficiently strong, $Ra=10^7$ in our case), the tendency of fluid to rise along the vertical (hot) side of the step *can suppress the recirculation* which would otherwise be established there (Figs. 8.1 and 8.3).

This effect, however, should not be misread as implying a tendency of the flow to retain a two-dimensional behaviour. As already discussed in Sect. 8.2, although, it can annihilate the recirculation ahead of the step, buoyancy can cause significant 3D effects. A good impression of

these can be achieved by presenting the flow streamlines for both cases with adiabatic and hot floor (Figs. 8.23).

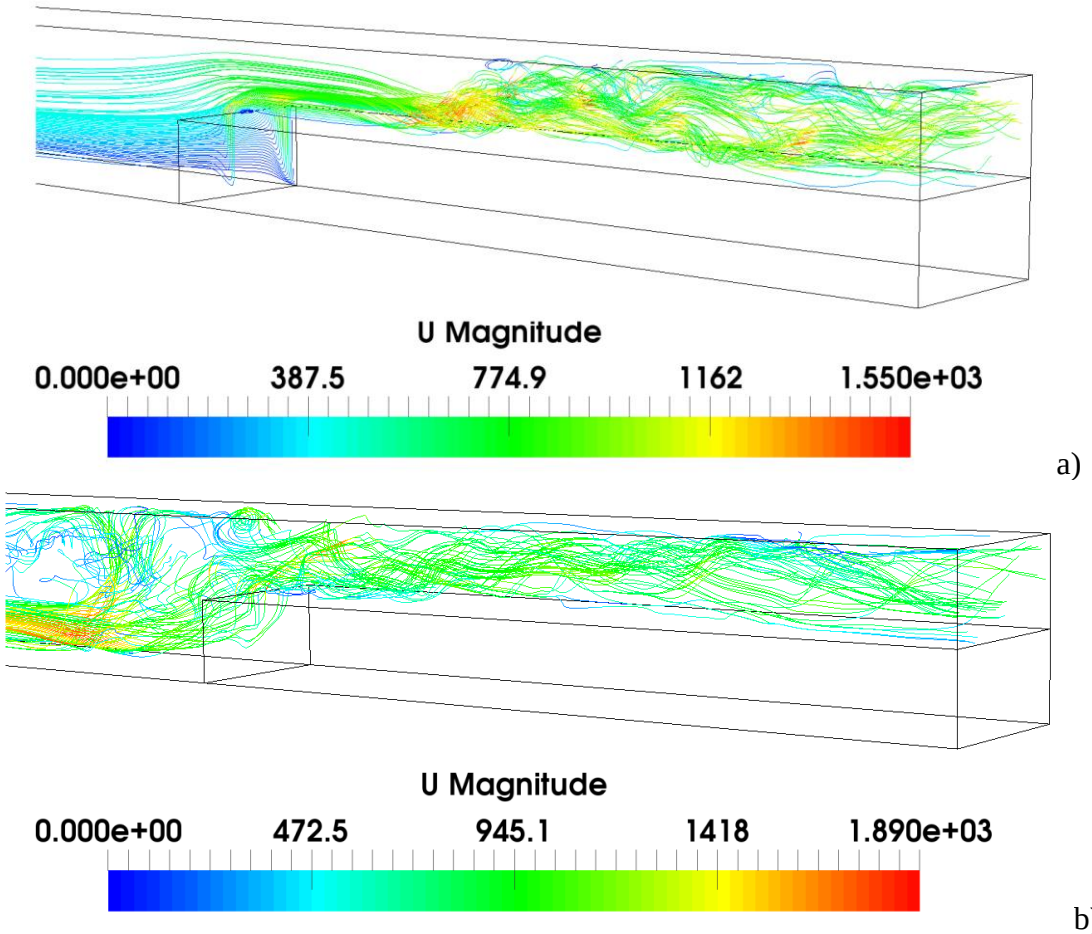

Figure 8.23: 3D streamlines (snapshots) for the FFS (*Ri*=100, *Ra*=10^7): a) adiabatic floor, b) hot floor.

The significance of these additional figures resides in their ability to make evident that the flow separates and reattaches several times along the top horizontal surface of the step. Although a phenomenological similarity might be established with the findings reported for a larger value of the Reynolds number by Scheit et al (2013), it is worth pointing out that these phenomena should not be regarded as an outcome of purely hydrodynamic effects. In the present case, thermal plumes (Figs. 8.9 and 8.10) do play a significant role in causing the flow evolution. Separation essentially occurs as a result of the interaction of the horizontal flow with the vertical currents established in the stem of the plumes. Owing to the peculiar distribution of plumes along the z axis, separation and attachment occur *at different positions in the spanwise direction for different streamlines*. This is also qualitatively and quantitatively substantiated by the figures showing the distribution of the derivative of the horizontal component of velocity with respect to the vertical

coordinate evaluated along the solid wall delimiting the fluid domain from below. The regions where this derivative takes a value ≅0 obviously represent the loci of points where the flow has just undergone separation.

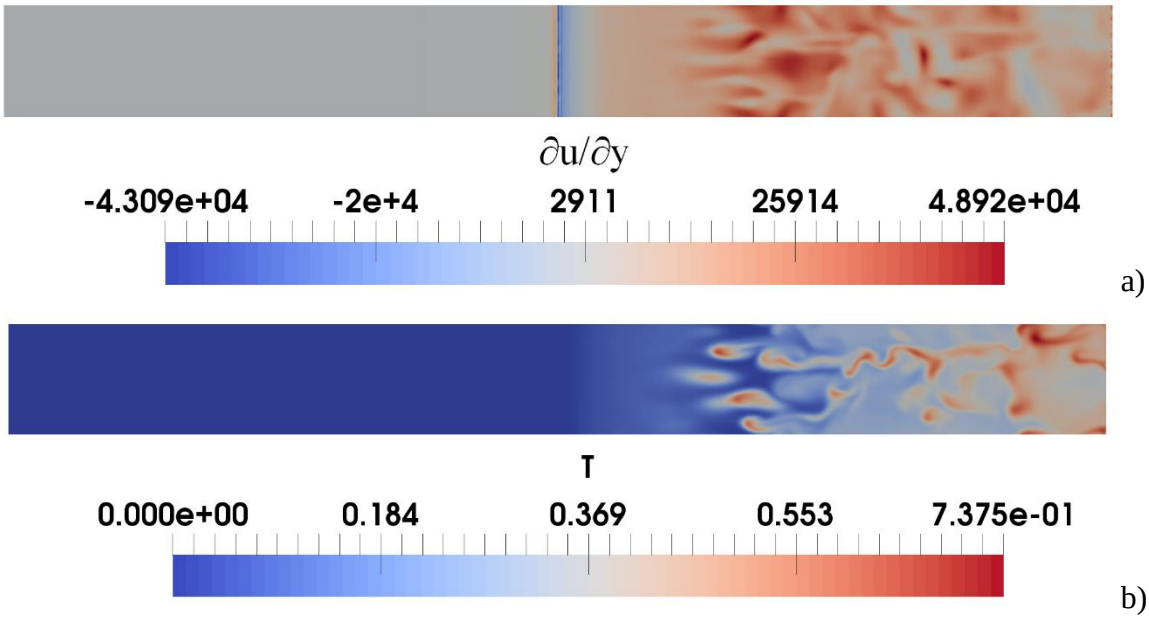

Figure 8.24: FFS (*Ri*=100, *Ra*=10^7, adiabatic floor): a) distribution of $\partial u/\partial y$ at y=0.5, b) *T* at y=0.65.

For the FFS with adiabatic floor (Fig. 8.24), comparison of the distribution of $\partial u/\partial y$ along the solid top boundary of the step and the temperature taken at a station y just outside the thermal boundary layer is instrumental in showing that a close correspondence exists between the loci of points where thermal plumes are located and flow separation occurs. Such a figure is useful as it also clearly reveals the quiet zone located between the edge of the step and the station where plumes start to nucleate.

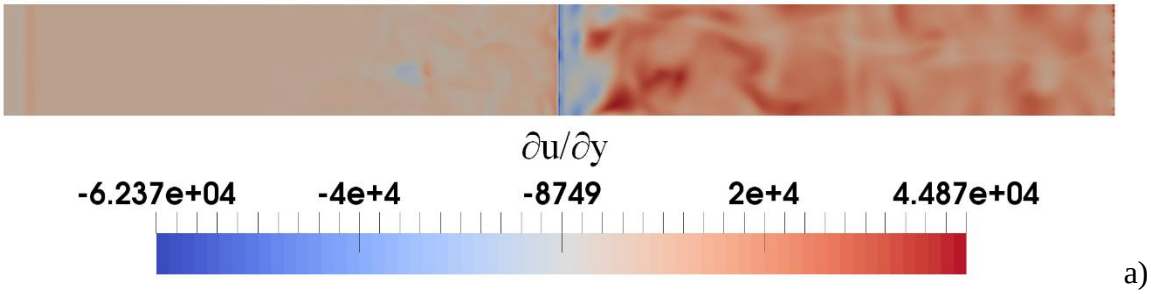

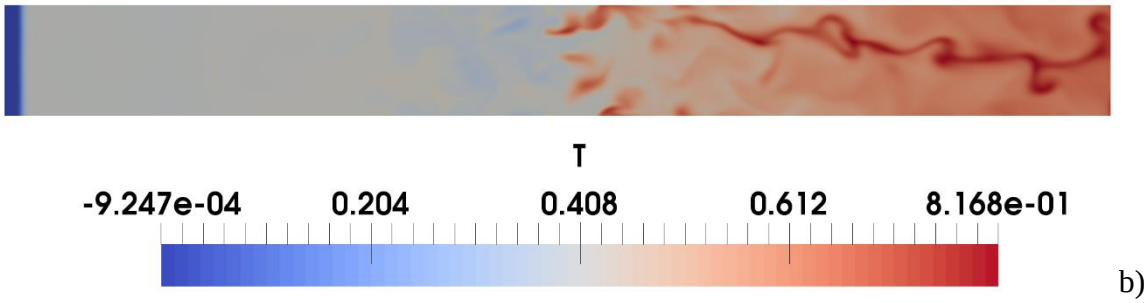

b)

Figure 8.25: FFS (*Ri*=100, *Ra*=10^7, hot floor): a) distribution of $\partial u/\partial y$ at y=0.5, b) *T* at y=0.65.

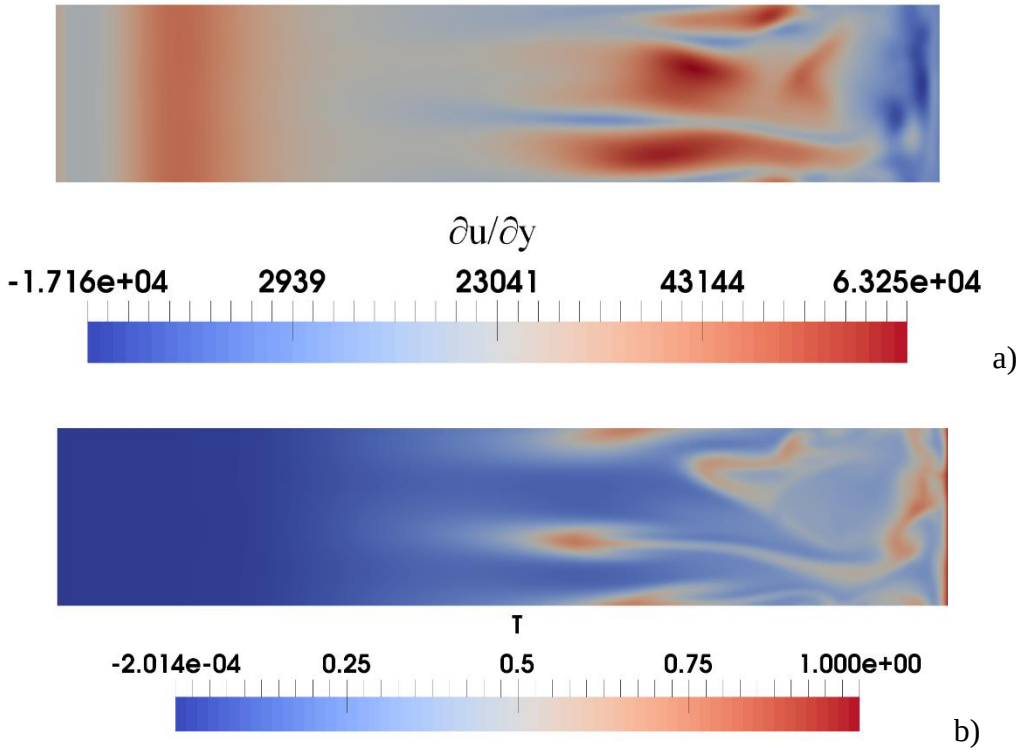

a)

b)

Figure 8.26: FFS (*Ri*=100, *Ra*=10^7, hot floor): a) distribution of $\partial u/\partial y$ at y=0 for x<5, b) *T* at y=0.15 for x<5.

Moving on to the case with hot floor (Figs. 8.25 and 8.26), spanwise-elongated structures close to the edge of the step similar to those originally observed in the purely forced flow case by Scheit et al. (2013) can be recognized (Fig. 8.25a). As the fluid moves there in the upstream direction (as indicated by the negative sign of the shear rate in Fig. 8.25a), this indicates that a small bubble adjacent to the stepped wall downstream of the step edge can be created in this case. However, the strict connection between plumes and flow separation still holds. In particular, Fig.

8.26 demonstrates that the flow separation occurring before the step must be ascribed essentially to the nucleation and growth of thermals in that area.

All these arguments logically pave the way to the remainder of this section, where attention is paid to the companion BFS configuration (for which the dynamics are appreciable more complex). As the reader might expect at this stage, following the same approach already undertaken for the FFS, the discussion begins again from a survey of the general dynamics known for the purely forced flow (and a short description of the related available 3D results).

In analogy with the FFS, forced BFS flow is known to separate as a result of the abrupt variation in the cross-sectional area and other related hydrodynamic effects. A single recirculation (between the step trailing edge and the reattachment point along the channel floor) is produced for relatively small values of the Reynolds number. However, if the Reynolds number is increased, recirculations of higher order can appear along the ceiling (secondary and tertiary rolls, etc.). Consensus exists in the literature that the reattachment length associated with the primary roll can be reduced with an increase in ER (for small or moderate values of Re), while making the Reynolds number higher can have a two-fold effect, i.e. a displacement of this point in the downstream direction and the onset of time-dependence. As an example, the formation and detachment from the step of large-scale vortices was found to be the primary cause of the periodic movement of the reattachment location in the two-dimensional study by Friedrich and Arnal (1990); these authors observed that the free-shear layer emanating from the step had a vertical motion causing the reattachment location to oscillate.

Three-dimensional studies of relevance to the subject include those by Le et al. (1997) and Xu et al. (2017). In particular, the analysis by Le et al. (1997) for ER=1.20 and Re=2500 is extremely instructive as a comprehensive characterization of the dynamics of separation and reattachment was provided there for the case with no buoyancy. Most interestingly, it was observed that the large-scale roll-up of the shear layer extending to the reattachment region is produced by many small, high-intensity counter-rotating vortices originating from the step (trailing) edge. As a result of existing spanwise phase shifts in the nucleation time of these vortices, the temporal trace of the reattachment locations on the floor of the channel can display a saw-tooth shape (see Fig. 3 in their work). A simple rationale for this behavior was elaborated as follows: "*the shear layer rolls up forming a large-scale structure behind the step, as the large-scale structure grows, the reattachment locations travel downstream; the reattachment length then suddenly decreases indicating a detachment of the turbulent large-scale structure from the step*" (this evolution was also tracked in terms of pressure fluctuations given the known correspondence of low pressure regions with the centers of coherent vortices).

Later, Xu et al. (2017) have shed some additional light on these behaviours by showing that the vortexes shed constantly and periodically in the downstream direction as a result of the Kelvin–Helmholtz instability occurring in the shear layer of the primary recirculation zone can give rise to repeated separation phenomena along the remaining extension of the channel (see Fig. 14 in their work for ER=2 and Re=1000).

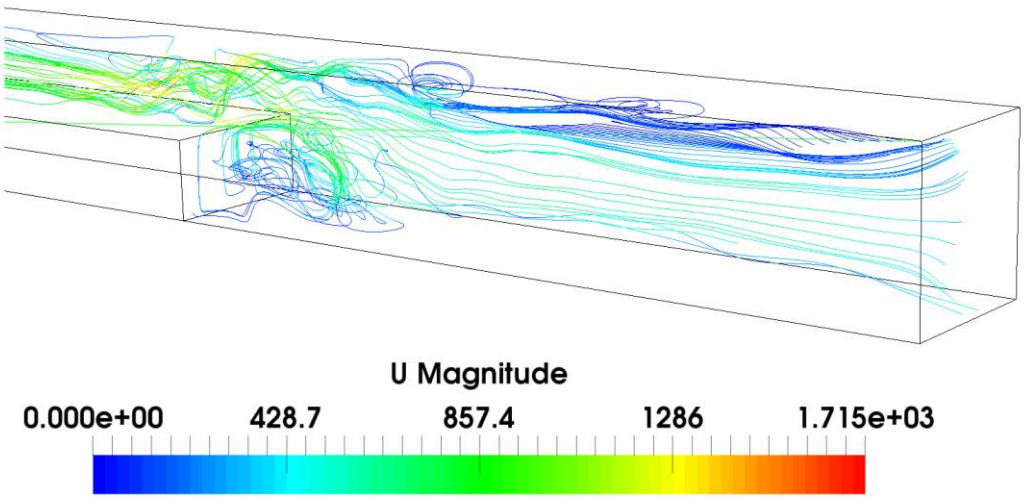

a)

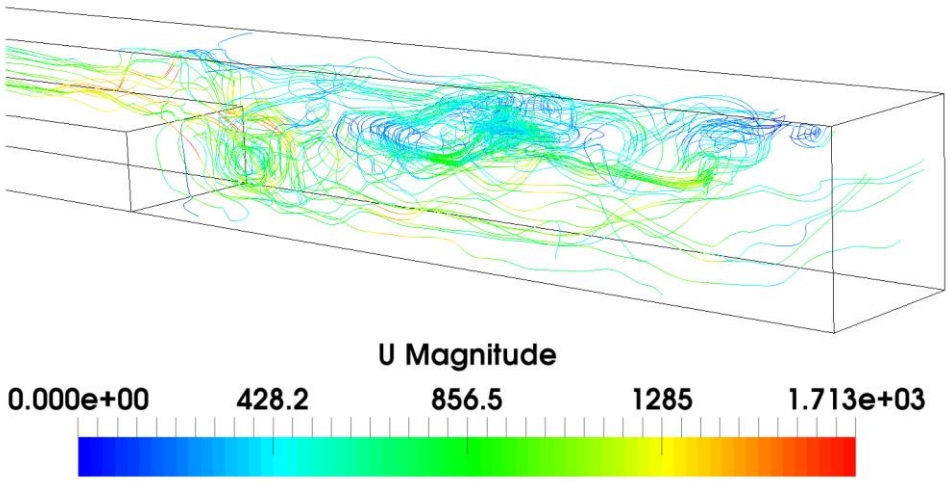

b)

Figure 8.27: 3D streamlines (snapshots) for the FFS (Ri=25, Ra=10^7): a) adiabatic floor, b) hot floor.

When buoyancy enters the dynamics (Fig. 8.27), however, a significant departure from the known scenario for purely forced flow takes place. For the BFS with either adiabatic or hot floor (Figs. 8.28 and 8.29, respectively), alternating separation and reattachment phenomena start to affect the flow directly in the region of reduced cross-sectional area, i.e. above the step. This is evident in the distribution of $\partial u/\partial y$, where bands of alternating colors can clearly be recognized. The almost straight nature of these bands is consistent with what has been reported in Sect. 8.3, where some emphasis has been put on the initially two-dimensional nature of this phenomenon.

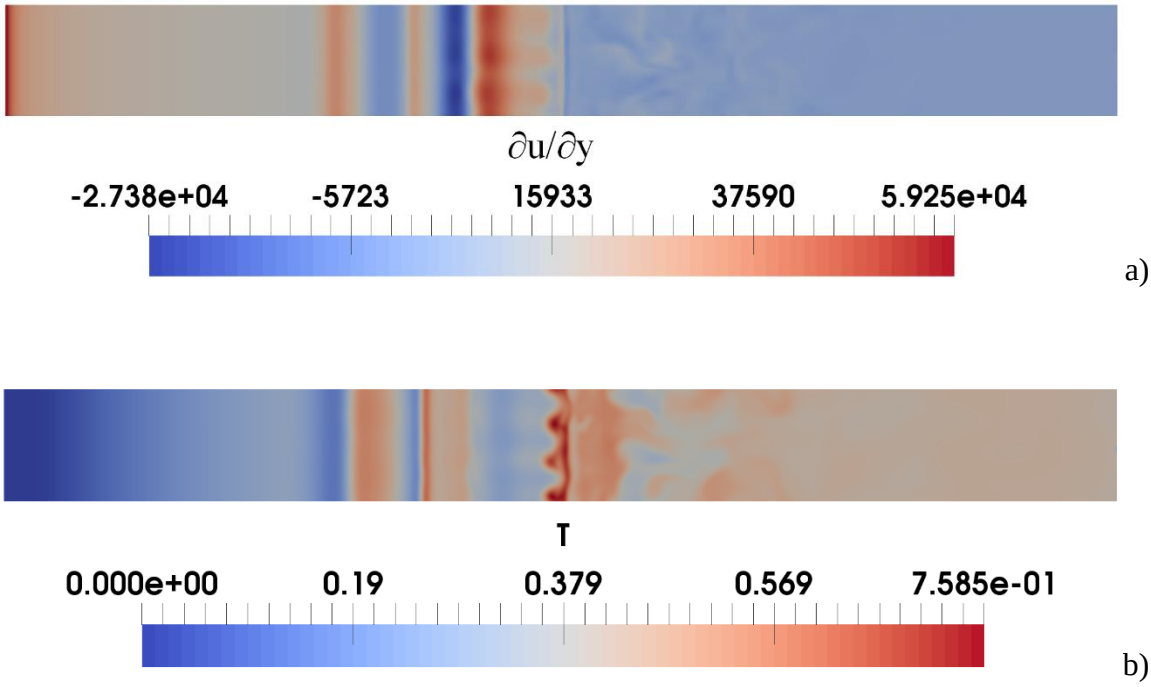

Figure 8.28: BFS (*Ri*=25, *Ra*=10^7, adiabatic floor): a) distribution of ∂u/∂y at y=0.5, b) *T* at y=0.65.

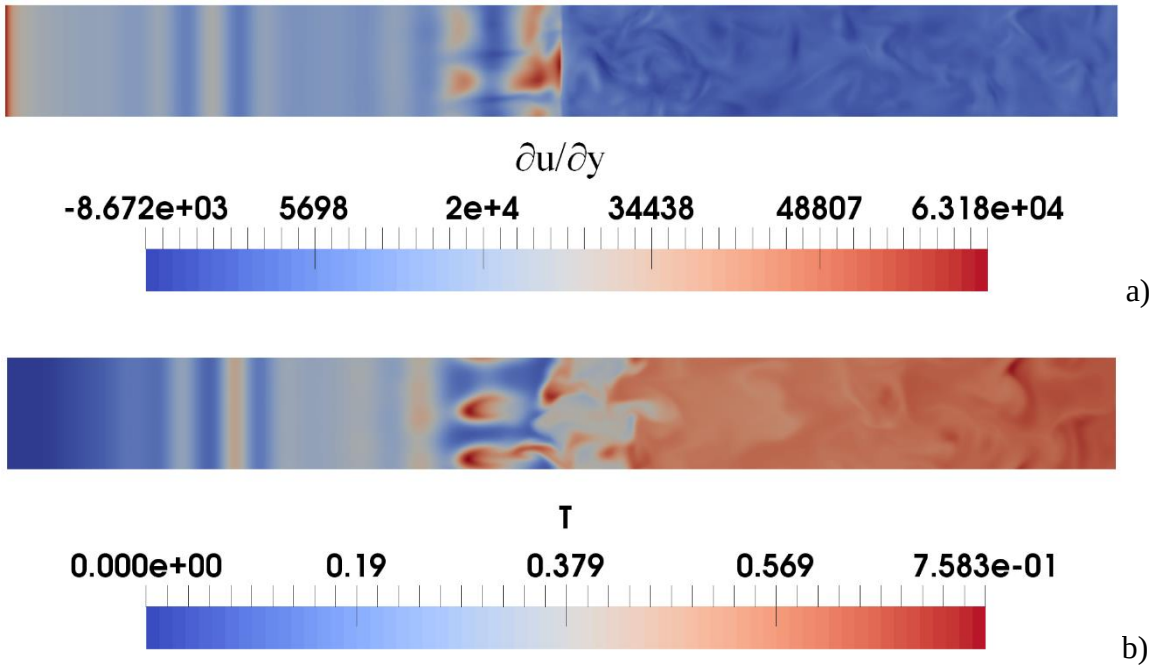

Figure 8.29: BFS (*Ri*=25, *Ra*=10^7, hot floor): a) distribution of ∂u/∂y at y=0.5, b) *T* at y=0.65.

Cross comparison of Figs. 8.28 and 8.29, however, indicates that, a notable difference exists, i.e. the 3D nature of the flow in proximity to the step is much more marked in the case with hot floor. The root cause for this dissimilarity (yet ascribable to the presence of plumes) has already been clarified in Sect. 8.3. Here the discussion is limited to emphasise that along the hot floor (Fig. 8.30) a well-defined correlation can still be defined between the regions where separation occurs ($\partial u/\partial y \cong 0$) and those where thermals are located. In proximity to the step, the existence of a recirculation along the bottom floor is witnessed by the opposite sign of $\partial u/\partial y$ in Fig. 8.30a; downstream of this region, separation essentially occurs in regions which are stretched along the x direction. As qualitatively substantiated by Fig. 8.30b, these yet correspond to thermal plumes. These are also visible in the spanwise cut through the flow at $x=3A_x/4=7.5$ provided in Fig. 8.20b and in the 3D view of Fig. 8.17 and assume this specific flattened (sail-like) shape owing to their interaction with the horizontal 'wind'.

On the basis of these arguments, one may therefore conclude that the convoluted structure of the flow (visible in Fig. 8.27b) is primarily a consequence of the eruptive phenomena originating from the thermal boundary layer at the bottom as a result of buoyancy effects, rather than a manifestation of a Kelvin–Helmholtz instability like that reported by Xu et al. (2017).

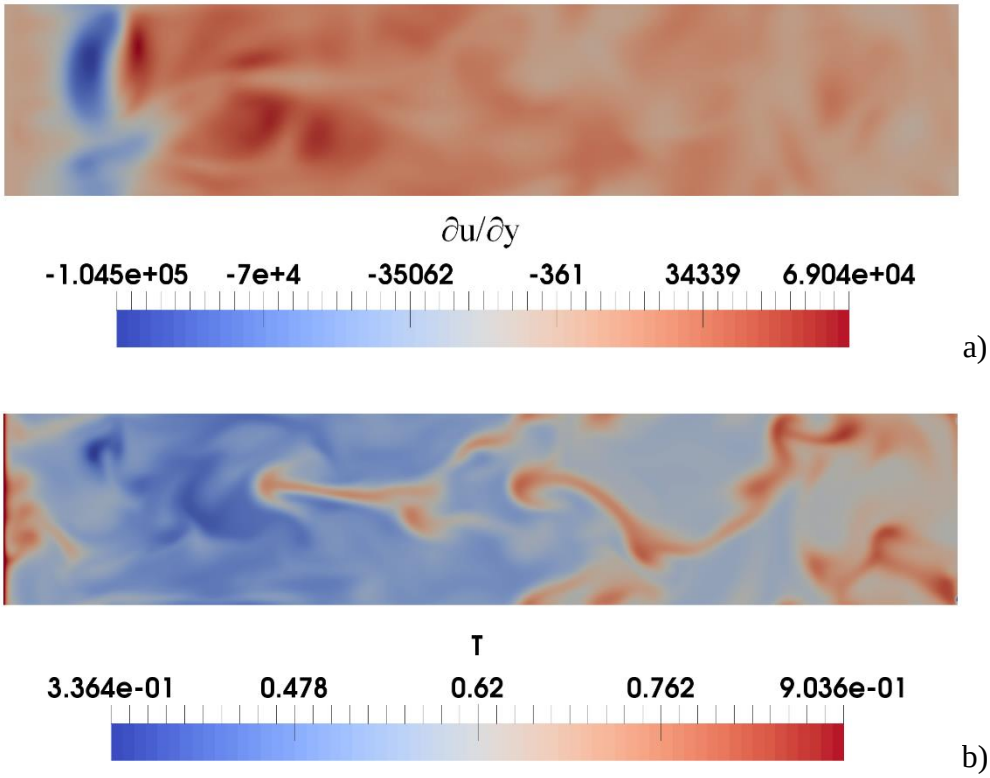

Figure 8.30: BFS (*Ri*=25, *Ra*=10^7, hot floor): a) distribution of $\partial u/\partial y$ at y=0 for x>5, b) *T* at y=0.15 for x>5.

8.5 Conclusions

The present study builds on two earlier chapters of this thesis where these problems have been tackled in the framework of DNS and under the limiting assumption of 2D flow (required to make the otherwise intractable scale of these problems compatible with available computational resources).
Here the constraint of two-dimensionality has been removed in order to reduce the gap between physical reality (where disturbances in the spanwise direction may represent a relevant aspect of the problem) and the virtual environment represented by CFD.
In order to reduce once again the scale of the problem to a level where it is affordable, the analysis has been developed using a LES strategy by which notable computational savings can be obtained. This approach has been used to model the behavior of the flow in 3D situations for which no data are available in the literature (values of the Richardson number of $O(10^2)$ and a value of the Rayleigh number for which the flow has just entered the turbulent regime). Two-dimensional simulations have been used to tune some of (otherwise undetermined) constants appearing in the LES model through comparison of high-resolution DNS and LES simulations (this modus operandi reflecting well-defined theory whose foundations were laid by Kolmogorov approximately 80 years ago that turbulence becomes isotropic on small scales, i.e. independent from the considered space direction).
Critical comparison of 2D and 3D results has been instrumental in showing that when the flow is allowed to develop along the third direction, appreciable differences emerge. These are not limited to the flow macroscopic scale (where energy is injected into the system), but in some circumstances can also have an impact on the cascading energy phenomena developing inside the inertial range of scales. While for the FFS the differences essentially affect the structure of plumes, for the BFS they are more substantial as they imply the generation of a significant macroscopic component of vorticity along the main flow direction and the displacement of the portion of the spectrum corresponding to the inertial regime towards higher or smaller amplitudes (depending on the thermal boundary condition considered for the channel floor).
From a macrophysical (coarse-grained) point of view, interestingly, the sudden variation in the channel cross-sectional area can be associated with an abrupt change in the flow characteristic wavenumber in the spanwise direction (FFS case) and/or the step corner can behave as a locus of accumulation of thermal plumes and generation of both transverse and longitudinal vorticity (BFS case). From a fine-grained (micromechanical) standpoint, for the BFS with adiabatic floor, the strong mixing induced in the fluid after the step can cause temperature homogenization and/or stable stratification at a certain distance from it with ensuing suppression of buoyancy convective effects and flow re-laminarization. Vice versa for the BFS with hot floor, the intrinsically small-scale nature of 3D plumes can cause an enhancement of the high-frequency components present in the inertial range.
Meaningful comparison with the earlier literature, synergistically exploiting some definitions and concepts elaborated for the cases where only hydrodynamic effects play a role, has led to the

conclusion that, for the considered set of parameters, separation of horizontal flow essentially occurs as a result of its interaction with the vertical currents associated with thermal plumes. Depending on the mutual interference between flow with significant vertical shear (the forced flow) and currents featuring intense horizontal shear (the plumes), many complexities and a rich variety of flow phenomena can take place, which are otherwise prevented if the presence of buoyancy is neglected.

Another of the main conclusion of the present study is that the widespread practice of using values of the Smagorinsky constant located in theoretically determined intervals (which have proven to work in some circumstances) should be deeply re-thought. Mixed forced-buoyant flows can display a peculiar hierarchy of bifurcations before entering the turbulent state where both disturbance of hydrodynamic (shear-driven) and thermal (buoyant) nature can play a substantial role. Over-predictions or over-estimation of the Smagorinsky constant may result in suppression of some of these mechanisms therefore leading to resolved states that do not reproduce properly reality (or DNS results) as they lack some of the related physical behaviours.

Chapter 9

Conclusion

To fill a gap in the existing literature and provide useful information for the interpretation/optimisation of several technological processes, hybrid (mixed) forced-buoyancy convection in different geometrical domains displaying an abrupt variation in the cross-sectional area has been investigated. Relatively compact or horizontally extended systems where the flow undergoes a sudden expansion or contraction have been examined. These archetypal systems were heated from below to facilitate the production of fluid motion of buoyancy nature driven by the interaction of the cold fluid (injected into the channel) with the heated solid boundaries.

Initially, as explained in Chapter 5 a compact cavity with a square obstruction located in its bottom-right corner was considered and the relative importance of the above-mentioned mechanisms was examined by considering different values of the Rayleigh number (spanning several order of magnitude). Also, a further degree of freedom was added by using a specific analysis hierarchy where selected effects were included or not depending on the targeted regime. First attention was paid to the situation where pure thermo-gravitational convection emerges due to the presence of vertical and horizontal heated surfaces (the hot sides of the obstruction). Afterwards, the focus shifted towards the hybrid regime where buoyancy convection was modulated by currents of forced flow (cold fluid) injected into the cavity at different heights for values of the Richardson number $\cong 1$.

It was found that, on increasing the value of Rayleigh number, the multicellular nature of the problem is enhanced (the number of rolls grows) as a result of the thermal plumes originating from the corner of the step. These hot vertical structures take a different inclination depending on the considered condition, for instance horizontal or inclined structure for adiabatic bottom and almost a 90° vertical structure for isothermal bottom. Most importantly, the formation of *heat islands* can occur in certain cases (mostly located in the lower portion of the domain for pure buoyancy case and hybrid convection case with aligned inflow and outflow sections). However, these can be suppressed if the position of inflow section is properly changed.

In Chapter 6, the treatment was extended to an elongated duct with a forward-facing step subjected to a horizontal pressure gradient and a vertical temperature difference. Investigations were performed yet for the pure buoyancy case (closed domain) and mixed convection case (channel) in order to gain additional insights from cross-comparison of these situations.

It has been shown that on increasing the Rayleigh number (while keeping fixed the Richardson number), the distance between the point where thermal plumes starts to be produced and the step corner becomes smaller. Moreover, their vertical extension tends to be reduced, which can be ascribed to the dual influence of a simultaneous increase of Ra and Re (the former contributing to make plume caps smaller, the latter reducing the available time for their stem to grow before they leave the domain through the outflow section). Most interestingly, when the flow becomes

turbulent, for Ri=100 the energy tends to reside on relatively small temporal scales (which demonstrates that new instability mechanisms are enabled with respect to the situation where only buoyancy convection is present). A decrease in *Ri* (*Ri*=30), forces these disturbances to grow inside the thermal and kinematic boundary layers. When the Richardson number is finally reduced to 1, the primary source of disturbances, which for larger values of Ri is represented by the relatively strong thermal plume originating from the step corner is gradually transferred to a mechanisms of hydrodynamic nature, i.e., a strongly unsteady bubble located in proximity to the step corner. The continuous switch from one instability mechanism to another as the Richardson number is varied for the configuration with adiabatic floor should be regarded as a relevant justification for the scattered appearance of the critical points. When the floor is isothermal (hot) a decrease in *Ri* has in general a beneficial effect in terms of critical Rayleigh number, i.e., Ra_{cr} becomes higher (the trend is monotonic). In other words, the presence of forced flow has a *stabilizing influence* on the overall dynamics and this happens because an increase in the relative importance of forced flow with respect to thermal buoyancy, must necessarily correspond to higher values of the Rayleigh number needed to *excite the competition of buoyant and forced flow in the duct*.

Chapter 7 integrated and expanded the information provided in Chapter 6 i.e., unsteady hybrid forced buoyancy convection in a duct with forward-facing step by addressing the mirror configuration where the fluid flowing in a channel undergoes a sudden expansion (i.e., a channel with a backward facing step). The interplay of forced and buoyancy convection was investigated numerically to understand any similarities and differences with the equivalent forward-facing step configuration.

It has been found for the BFS, in general, buoyancy convection reinforces the hydrodynamic mechanisms responsible for the onset of oscillatory flow in the purely forced (isothermal) flow case. This results in a shrinkage of the critical Reynolds number similar to that observed for the FFS with the hot floor. For the BFS, however, this process is influenced by the specific thermal boundary conditions assumed for the floor. When it is adiabatic, both the vertical shear in the separated layer originating from the corner of the step and the destabilizing temperature difference established between this layer and the surrounding fluid support the onset of fluid-dynamic disturbances. If the floor is kept at the same temperature of the step, the role of buoyancy becomes much more important; the instability of the aforementioned layer is taken over by a process where thermal plumes nucleate directly at the bottom of the channel and become pervasive throughout its vertical extension. This interpretation still holds for the turbulent regime. The progressive displacement of the spectrum towards higher amplitudes as the Richardson number is decreased (while keeping fixed the Rayleigh number) provides indirect evidence for the role played by hydrodynamic perturbations. Vice versa, correlation of the spectra obtained for fixed *Ra* for growing values of *Ri* and different thermal boundary condition at the bottom wall reveals the increasingly more important influence that buoyancy effects can exert on the flow in these circumstances.

Meaningful comparison with the equivalent phenomena known to affect the companion configuration (FFS) has led to the conclusion that the differences between these two systems essentially stem from the facing orientation of the step, which causes a rupture of the symmetry of the channel with respect to the direction of the flow. In the isothermal case (no buoyancy), the reduced complexity of the BFS depends on its inability to induce vorticity and related shear effects both upstream and downstream of the step leading edge. In the non-isothermal case with adiabatic floor, the scenario for the BFS is yet less complex, as the role of buoyancy is limited to inducing additional disturbances in the separated shear layer with respect to those potentially produced by a purely hydrodynamic shear-driven mechanism (for the FFS, more complex dynamics are enabled due the disjoint influence of hydrodynamic and thermal effects). For the hot floor case, the flow instability in both BFS and FFS systems are essentially driven by buoyancy, which explains why the trend of the critical parameter is monotonic for both paradigms (some existing differences are due to the facing orientation of the step and the related forced flow, which break the in-plane isotropy which would be typical of a layer of fluid uniformly heated from below).

Building on the results presented in the two earlier chapters, Chapter 8 has been dedicated to extending the analysis by taking into account the effect of the third dimension, i.e., by allowing the convective disturbances to develop also along the spanwise direction Yet, FFS and BFS systems have been considered allowing the floor to be either adiabatic or isothermal (hot). However, given the computational weight of 3D simulations (5 million computational nodes), the study was performed for the turbulent regime only [Ri=O(10^2) and Ra=O(10^7)] in the framework of the large eddy simulation (LES) approach.

Interestingly, it has been shown that the theoretically determined intervals of the Smagorinsky constant available in the literature do not hold when hybrid convection is considered in channels with a step. Mixed forced-buoyant flows can display a peculiar hierarchy of bifurcations before entering the turbulent state where both disturbance of hydrodynamic (shear-driven) and thermal (buoyant) nature can play a substantial role. Over-predictions or over-estimation of the Smagorinsky constant may result in suppression of some of these mechanisms therefore leading to resolved states that do not reproduce properly reality (or DNS results) as they lack some of the related physical behaviors.

Comparison between 2D and 3D results helped to highlight the differences that emerge as a result of the additional spatial degree of freedom represented by the third direction. For the FFS case, the difference was spotted in terms of the number and structure of thermal plumes whereas for BFS an enhanced role of step corner was observed, this acting as a source of transverse and longitudinal vorticity as well as a breeding ground for the accumulation of thermal plumes. Some additional insightful differences were also discovered for the BFS case where the flow for the 2D adiabatic floor case was found to be more energetic in comparison with the 3D case (temperature homogenization in 3D leading to the suppression of buoyancy effects causing flow relaminarization). However, an opposite effect was detected for the BFS case where the large

number of small 3D convective structures (thermal plumes) can lead to more energetic flow due to the addition of high frequency components to the spectrum.

In the light of all these observations and related arguments, it can be concluded that the evolution of these systems from initially steady states towards chaos (i.e. the related hierarchy of bifurcations) depends on delicate interplay of purely hydrodynamic and buoyant-in-nature disturbances. In turn, this interplay sensitively depends on the orientation of the step with respect to the forced flow (obviously, the problem is not invariant with respect to a reflection with respect to the section where the step is located) and on the ability of the floor to contribute (or not) to the production of thermal buoyancy. Although, allowing the disturbances to develop in the spanwise direction can produce a localized departure from the corresponding 2D simulations in some circumstances, according to the present results, 2D simulations can capture most of the physics of these systems.

These results have been produced under the optimistic hope that in the future they will help fluid physicists, engineers and professionals working in all the fields highlighted in the introduction to interpret the steady, unsteady and chaotic flow behaviors in channels with variable cross section in the presence of temperature gradients or thermal inhomogeneities.

Finally, any researcher wishing to perform analysis on mixed forced-buoyant flows in framework of large eddy simulation (LES) approach is advised to consider the values determined in this thesis keeping in mind that the over-prediction and over-estimation of the Smagorinsky constants may lead to a departure from the equivalent results which would be produced by DNS.

Appendices

Appendix A

File structure of cases in OpenFOAM

The present Appendix will highlight different directories present inside an OpenFOAM case and the files present inside those directories which are needed to run different simulation cases. The three important directories or folders which are required to run an OpenFOAM case are zero directory, constant directory and system directory. These directories contain essential files which have to be filled with important information related to flow and geometry for developing the simulation. The following sections will provide information on such directories and the various files that are present inside them.

A.1 Zero directory

The zero folder contains files which are used to set up boundary conditions for different cases. In the present thesis, the two key properties which have influenced the results are velocity and temperature. The zero directory contain both of these files which have been used to apply appropriate boundary conditions.

A.1.1 Velocity

The velocity could be considered as one of the key properties in simulations that have been run in the framework of this thesis. In OpenFOAM, the velocity is present in the form of a text file which contains value of the velocity at inlet and the boundary condition applied on different surfaces of the domain. As already mentioned in Chapter 3, for the cases with pure buoyancy convection no inlet and outlet were present on the surfaces. Hence a no slip ($\underline{V}$=0) boundary condition was applied on the solid walls. For the cases with hybrid convection, an inlet and outlet were introduced and the value of the injection velocity (U_{forced}) was continuously changed depending on the value of Richardson number. A velocity file for an elongated channel with FFS for a value of Ri=100 and Ra=1x10^7 is shown in Fig. A1. It highlights three main parts, dimensions, internal field and boundary conditions. The dimension part underlines the physical dimensions based on international system of units which are [kg m s K mol Amp Candela]. However, it can be seen in Fig. A1, the velocity file only requires the units of velocity which is m/s. The internal field parameter is used to set up values in cell volumes of the mesh. It is set up as uniform which means the value is constant throughout the entire domain. Finally, for the boundary condition part, different boundary conditions were set up for different parts of the channel. The following three BCs were used.

noSlip In this BC, the velocity is fixed to zero at the walls. It can be seen in Fig. A1, that a no slip boundary condition is applied at the floor, ceiling, building (horizontal and vertical step wall) and fixed walls.

fixedValue In this BC, a fixed value is supplied at the inlet which is selected by the user. This BC is applied at the inlet as the value of inlet velocity will vary depending on the case being simulated. According to Fig. A1, a value of 0.03162 is fixed at the inlet in x direction whereas velocity is zero along y and z.

inletOutlet This boundary condition is meant for providing a general outflow condition where a value of inflow is specified in the case of return flow. It can be seen in Fig. A1; velocity is set to zero in all direction for the case of return flow.

empty An empty BC is used for cases with reduced dimensions such as 1-D and 2-D domains. It is applied to those surfaces with a normal aligning with geometric directions that fails to account for solution directions.

```
/*--------------------------------*- C++ -*----------------------------------*\
| =========                 |                                                 |
| \\      /  F ield         | OpenFOAM: The Open Source CFD Toolbox           |
|  \\    /   O peration     | Version:  4.1                                   |
|   \\  /    A nd           | Web:      www.OpenFOAM.org                      |
|    \\/     M anipulation  |                                                 |
\*---------------------------------------------------------------------------*/
FoamFile
{
    version     2.0;
    format      ascii;
    class       volVectorField;
    object      U;
}
// * * * * * * * * * * * * * * * * * * * * * * * * * * * * * * * * * * * * //

dimensions      [0 1 -1 0 0 0 0];

internalField   uniform (0 0 0);

boundaryField
{
    floor
    {
        type            noSlip;
    }
    building
    {
        type            noSlip;
    }


    ceiling
    {
        type            noSlip;
    }

    fixedWalls
    {
        type            noSlip;
    }
    inlet
    {
        type            fixedValue;
        value           uniform (0.03162 0 0);
    }
         outlet
    {
         type            inletOutlet;
        value           $internalField;
        inletValue      uniform (0 0 0);
      /*  value           $internalField;
        inletValue      uniform (0 0 0);*/
    }
    empty
    {
        type            empty;
    }
```

Figure A1: Snapshot of velocity text file which shows how the BCs are set up for the case of hybrid forced/buoyancy convection (Ri=100 and Ra=10^7) and hot bottom wall.

A.1.2 Temperature

The temperature file again highlights the three main parts which are dimensions, internal field and boundary conditions (Fig. A2). It is illustrated in Fig. A2, the temperature file only requires the units of temperature which is K. The parameter internal field is selected as uniform with a 300 value in all the directions. Finally, following boundary conditions were used:

fixedValue: floor and building were assigned the role of hot surfaces by fixing the temperature to 310 and fluid entering from inlet was rendered cold by fixing the temperature to 300. This was done in order to create a temperature gradient inside the domain promoting buoyancy convection.

zeroGradient A zero gradient boundary condition was applied on the ceiling and fixedWalls which mean $\partial T/\partial y=0$ or zero heat flux. It is worth recalling that ceiling was considered cold (by assigning a value of T=300) for pure buoyancy cases.

```
/*--------------------------------*- C++ -*----------------------------------*\
| =========                 |                                                 |
| \\      /  F ield         | OpenFOAM: The Open Source CFD Toolbox           |
|  \\    /   O peration     | Version:  4.1                                   |
|   \\  /    A nd           | Web:      www.OpenFOAM.org                      |
|    \\/     M anipulation  |                                                 |
\*---------------------------------------------------------------------------*/
FoamFile
{
    version     2.0;
    format      ascii;
    class       volScalarField;
    object      T;
}
// * * * * * * * * * * * * * * * * * * * * * * * * * * * * * * * * * * * * * //

dimensions      [0 0 0 1 0 0 0];

internalField   uniform 300;

boundaryField
{
    floor
    {
        type            fixedValue;
        value           uniform 310;
    }
    building
    {
        type            fixedValue;
        value           uniform 310;
    }
    inlet
    {
        type            fixedValue;
        value           uniform  300;
    }
    outlet
    {
        type            inletOutlet;
        value           $internalField;
        inletValue    uniform  300;
    }

    ceiling
    {
        type            zeroGradient;
    }

    fixedWalls
    {
        type            zeroGradient;
    }
    empty
    {
        type            empty;
    }
}
```

Figure A2: Snapshot of temperature text file which shows how the BCs are set up for the case of hybrid forced/buoyancy convection (Ri=100 and Ra=10^7) and hot bottom wall.

A.2 Constant directory

This directory contains various folders with essential information regarding the simulation such as material properties in addition to physics and chemistry of the simulation. For the cases considered in this thesis, the constant folder contains only two text files which are transport properties and turbulence properties.

A.2.1 Transport properties

This file contains information regarding the properties of the fluid. As already mentioned in Chapter 3, the fluid considered in this case is air which is a Newtonian fluid. Fig. A3 demonstrates that data entries must contain the name of the property as a keyword followed by dimensions and then value of that particular property. The first property is kinematic viscosity (ν) with a value of $1x10^{-5}$ m^2/s. After that comes the thermal expansion coefficient (β) whose value is varied to account for the changes in the value of Rayleigh number. For Ra=$1x10^7$, thermal expansion coefficient has a value of $1x10^{-2}$ followed by reference temperature with a value T=300 and Prandtl number which is 1 for the fluid considered in this thesis. The dimension part indicates that Prandtl number is a non-dimensional number.

```
/*--------------------------------*- C++ -*----------------------------------*\
| =========                 |                                                 |
| \\      /  F ield         | OpenFOAM: The Open Source CFD Toolbox           |
|  \\    /   O peration     | Version:  4.1                                   |
|   \\  /    A nd           | Web:      www.OpenFOAM.org                      |
|    \\/     M anipulation  |                                                 |
\*---------------------------------------------------------------------------*/
FoamFile
{
    version     2.0;
    format      ascii;
    class       dictionary;
    object      transportProperties;
}

// * * * * * * * * * * * * * * * * * * * * * * * * * * * * * * * * * * * * //

transportModel Newtonian;

// Laminar viscosity
nu              [0 2 -1 0 0 0 0] 1e-05;

// Thermal expansion coefficient
beta            [0 0 0 -1 0 0 0] 1e-02;

// Reference temperature
TRef            [0 0 0 1 0 0 0] 300;

// Laminar Prandtl number
Pr              [0 0 0 0 0 0 0] 1;

// Turbulent Prandtl number
Prt             [0 0 0 0 0 0 0] 0.7;

// ************************************************************************* //
```

Figure A3: Snapshot of transport properties file which highlights the values of different quantities for the case of hybrid forced/buoyancy convection (Ri=100 and Ra=10^7) with hot bottom wall.

A.2.2 Turbulence properties:

This files contains information regarding the turbulence model which have been used for a particular case. This file contains a keyword simulationType that specifies the type of turbulence model that could be used. It could be either:

Laminar It indicates no turbulence model is used.
RAS Indicates the use of Reynolds-averaged stress (RAS) modelling.
LES Indicates the use of large-eddy simulation (LES) or detached-eddy simulation (DES).

No turbulence model has been used for the 2D cases run using DNS. For the 3D cases, simulations were run in the framework of LES approach to save the computational time. The entries that are needed in the LES subdictionary are listed as follows:

LESModel Name of LES model
Delta Name of delta δ model
<LESModel>Coeffs Dictionary of coefficients for the respective LESModel
<delta>Coeffs Dictionary of coefficients for each delta model

Fig. A4 indicates how to set up a LES dictionary. The LESModel selected for incompressible flow was SmaorinskyLilly. Turbulence and printCoeffs were turned on. Delta was selected as VanDriest to apply the Van Driest damping function near the wall region. Afterwards the coefficients for Smagorinsky Lilly model were defined using the keyword entry SmagorinskyLillyCoeffs. The values of constants specified for the elongated channel case with FFS (Ri=100 and Ra=1x10^{7}) were C_k=1x10^{-3}, C_e=1.048 (default value), beta=1x10^{-2} and g=9.81(negative sign indicates the downward direction of gravity along y-axis). In the end values were specified for the Van Driest coefficients. Constants such as kappa, Aplus and Cdelta are optional entries with default values.

```
/*--------------------------------*- C++ -*----------------------------------*\
| =========                 |                                                 |
| \\      /  F ield         | OpenFOAM: The Open Source CFD Toolbox           |
|  \\    /   O peration     | Version:  4.0                                   |
|   \\  /    A nd           | Web:      www.OpenFOAM.org                      |
|    \\/     M anipulation  |                                                 |
\*---------------------------------------------------------------------------*/
FoamFile
{
    version     2.0;
    format      ascii;
    class       dictionary;
    location    "constant";
    object      turbulenceProperties;
}
// * * * * * * * * * * * * * * * * * * * * * * * * * * * * * * * * * * * * * * * * //

simulationType  LES;
LES
{
        LESModel        SmagorinskyLilly;
        turbulence      on;
        printCoeffs     on;
        delta           vanDriest;
        cubeRootVolCoeffs{deltaCoeff      1;}
        SmagorinskyLillyCoeffs
        {
            Ck                  0.001;
            Ce                  1.048;
            beta                1e-02;
            g                   (0 -9.81 0);
        }
        vanDriestCoeffs
    {
        delta           cubeRootVol;
        cubeRootVolCoeffs
        {
            deltaCoeff      1;
        }
        kappa           0.41;
        Aplus           26;
        Cdelta          0.158;
    }

}


// ************************************************************************* //
```

Figure A4: Snapshot of turbulence properties file which highlights different keyword, respective data entries and values of constants for the case of hybrid forced/buoyancy convection (*Ri*=100 and $Ra=10^7$) with hot bottom wall.

A.3 System directory

The system directory contains important files which are needed for setting up the parameters which specifies the procedure of the solution. The four important text files are blockMeshDict, controlDict, fvSchemes and fvSolution. These files play a key role in the running and development of the simulation.

A.3.1 BlockMeshDict

OpenFOAM contains a mesh generation utility known as blockMesh which generates parametric meshes with grading and curved edges. The desired mesh is produced from a dictionary file with the name blockMeshDict present inside the system folder. The blockMesh utility creates the mesh by reading this dictionary and writes down the mesh data to points, cells, faces and boundary files present inside the same system folder. In principle, blockMesh decomposes the geometrical configuration into a different set of 3D hexahedral blocks which could be one or

more. Edges of the blocks are either composed of straight lines, arc or splines. Fig. A5 shows different keywords in blockMeshDict file which can be described as follows:

Keywords	Description
convertToMeters	It indicates a scaling factor for the coordinates of the vertices
Vertices	List specifying the vertex coordinates
Block	A list which contains the vertex labels and mesh size in ordered manner
Patches	Specifies the list of patches
mergePatchPairs	Indicates the list of patches needed to be merged

It can be seen in Fig. A5, the vertices are specified for the elongated channel with FFS. After that, the keyword of block is present containing three different entries which can be defined as follows:

Vertex numbering	This is the first entry which specifies the shape of the block. It can be seen in Fig. A5 that the shape is hex as the blocks always show a hexahedral geometry. After the shape identifier entry the vertex number for that particular block are written in an orderly manner.
Number of cells	The second entry defines the mesh size i.e. the number of cells present in x, y and z direction for a particular block
Cell expansion ratios	The final entry indicates the cell expansion ratio in each direction of the block. It enables the user to refine the mesh in particular direction. Fig. A5 indicates a keyword of simpleGrading which highlights a uniform expansion in x, y and z direction with 3 expansion ratios for instance simpleGrading (1 2 3).

Finally, the boundary of the mesh is specified through the use of a keyword boundary. The boundary is further broken into different regions or patches which are given a name by the user. The names specified here for the patches acts as an identifier which helps to set up boundary conditions in the velocity and temperature files present inside zero directory. Further information on the patch is provided by a sub-dictionary with

- type: As shown in Fig. A5 the patch type for an elongated channel case with FFS is wall for the regions building (vertical and horizontal step wall), floor and ceiling whereas for the inlet and outlet the patch type is a generic patch.
- faces: As shown in Fig. A5, afterwards the keyword faces is used to specify block faces that makes up different patches/regions.

```
/*--------------------------------*- C++ -*----------------------------------*\
| =========                 |                                                 |
| \\      /  F ield         | OpenFOAM: The Open Source CFD Toolbox           |
|  \\    /   O peration     | Version:  4.1                                   |
|   \\  /    A nd           | Web:      www.OpenFOAM.org                      |
|    \\/     M anipulation  |                                                 |
\*---------------------------------------------------------------------------*/
FoamFile
{
    version     2.0;
    format      ascii;
    class       dictionary;
    object      blockMeshDict;
}
// * * * * * * * * * * * * * * * * * * * * * * * * * * * * * * * * * * * * * //

convertToMeters 1;

vertices
(
        (0 0 0) //0
        (0.5 0 0)
        (0 0.05 0)
        (0.5 0.05 0)
        (1 0.05 0) //4
        (0 0.1 0)
        (0.5 0.1 0)
        (1 0.1 0)
        (0 0 0.01) //0
        (0.5 0 0.01)
        (0 0.05 0.01)
        (0.5 0.05 0.01)
        (1 0.05 0.01) //4
        (0 0.1 0.01)
        (0.5 0.1 0.01)
        (1 0.1 0.01)

);

blocks
(
       hex (0 1 3 2 8 9 11 10)  (1000 100 1) simpleGrading (1 1 1)
       hex (2 3 6 5 10 11 14 13)  (1000 100 1) simpleGrading (1 1 1)
       hex (3 4 7 6 11 12 15 14)  (1000 100 1) simpleGrading (1 1 1)
);

edges
(
);

boundary
(
  floor
    {
        type wall;
        faces
        (
                (0 1 8 9)
        );
    }
building
    {
        type wall;
        faces
        (
                (1 9 11 3)
                (3 4 12 11)
        );
    }
    ceiling
    {
        type wall;
        faces
        (
           (5 13 14 6)
          (6 14 15 7)
        );
    }
     inlet
    {
        type patch;
        faces
        (
                (8 10 2 0)    //inlet
                (10 13 5 2)
        );
        }
        outlet
    {
        type patch;
        faces
        (
                (12 15 7 4) //outlet
        );
        }
```

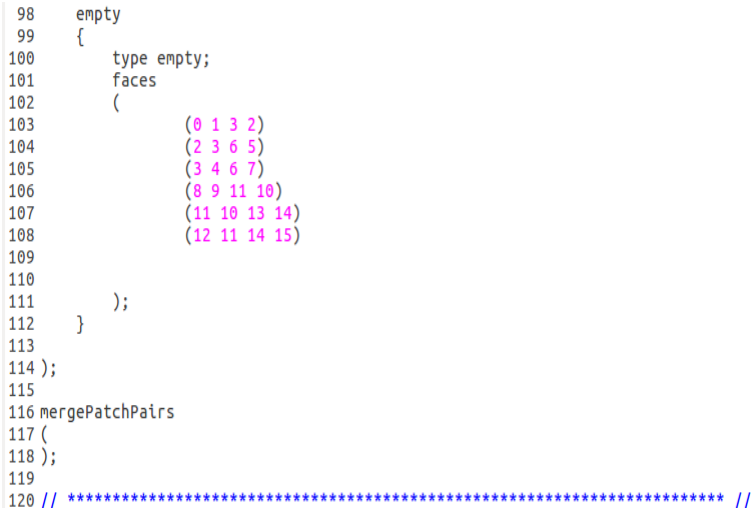

Figure A5: Snapshot of blockMeshDict file which provides information about the mesh created to run the simulation for the case of hybrid forced/buoyancy convection in elongated channel (Ri=100 and Ra=10^7) and hot bottom wall.

A.3.2 ControlDict

The OpenFOAM solver starts the simulation by creating a database. The controlDict dictionary plays an important role in this regard as contains input parameters which are considered essential for the creation of a database. The keyword entries mentioned inside a controlDict file are illustrated in Fig. A6. The entries inside a controlDict file forms the part of time control and data writing process.

A.3.2.1 Time control

As shown in Fig. A6 the first keyword is application for which the name of solver is specified i.e. buoyantBoussinesqPimpleFoam. Afterwards, the following keyword entries are used:

startFrom	It is meant to control the start time of the simulation. • latestTime: It is used to initiate the simulation from the latest time step.
startTime	It indicates the start time for the simulation.
stopAt	It is meant for controlling the end time of simulation. • endTime: This keyword entry indicates the stoppage time.
endTime	Simulation's end time which in this case is 195 (Fig. A6).
deltaT	Specifies the time step of the simulation. Set to 0.2 in Fig. A6

A.3.2.2 Data writing

After deltaT data writing keyword entries which are explained as follows:

writeControl It controls the timing at which output is written to the file.
- timestep: It used to write data after every writeInterval time steps.
- runTime: It is used to write data after every writeInterval seconds of simulated time.

writeInterval Indicates a scalar value after which the data is written. As shown in Fig. A6 it is set up as 3000.

purgeWrite Indicates an integer which is used to specify a limit on the amount of time directories that are generated by overwriting time directories in a cyclic manner. In Fig. A6 the purgeWrite is set to 0 (default) which means purging is disabled.

writeFormat Indicates the format of data files
- ascii: In Fig. A6, it can be seen that the default ascii format is selected which is written to writePrecision significant figures.
- binary: Indicates the binary format.

writePrecision Specifies an integer value which is used in relation to keyword writeFormat mentioned above. In Fig. A6 a default value of 6 is set up.

writeCompression Specifies whether the generated files are compressed when written. It can be set as on/off. Fig. A6 indicates it is set up as off.

timeFormat Specifies the format in which the time directories are names. There are three format which are as follows:
- fixed: ±m.dddddd where the keyword timePrecision indicates the numbers of ds.
- Scientific: ±m.dddddde± xx where the keyword timePrecision specifies the numbers of ds.
- general (default): Makes use of scientific format if the exponent is less than -4 or greater than or equal to the integer indicated by the keyword entry timePrecision.

timePrecision Indicates the value of the integer that is used in relation with timeFormat mentioned above. It is set up as 6 (default value) as shown in Fig. A6.

runTimeModifiable This keyword indicates whether the user wants the controlDict dictionary to be re-read during a simulation just when the time step begins. It is set up as true as shown in Fig. A6 which enables the user to alter the parameters during a simulation.

adjustTimeStep This keyword entry enables the user to adjust the time step during the simulation according to the value of maxCo.

maxCo Indicates the maximum value of Courant number. It is set up as 1.

```
/*--------------------------------*- C++ -*----------------------------------*\
| =========                 |                                                 |
| \\      /  F ield         | OpenFOAM: The Open Source CFD Toolbox           |
|  \\    /   O peration     | Version:  4.1                                   |
|   \\  /    A nd           | Web:      www.OpenFOAM.org                      |
|    \\/     M anipulation  |                                                 |
\*---------------------------------------------------------------------------*/
FoamFile
{
    version     2.0;
    format      ascii;
    class       dictionary;
    location    "system";
    object      controlDict;
}
// * * * * * * * * * * * * * * * * * * * * * * * * * * * * * * * * * * * * * //

application     buoyantBoussinesqPimpleFoam;

startFrom       latestTime;

startTime       0;

stopAt          endTime;

endTime         195;

deltaT          0.2;

writeControl    timeStep;

writeInterval  3000;

purgeWrite      0;

writeFormat     ascii;

writePrecision  6;

writeCompression off;

timeFormat      general;

timePrecision   6;

runTimeModifiable true;

adjustTimeStep  yes;

maxCo           1;

// ************************************************************************* //
functions
{
    probes
    {
        type            probes;
        libs ("libsampling.so");
        outputControl    timeStep;
        writeinterval    1;
        probeLocations
        (
           (0.48 0.05 0.005)   //bottom left
            (0.86 0.075 0.005)   //top left
            (0.96 0.075 0.005) //top right
        );
        fixedLocations  false;
        fields
        (
            T
            U
        );
    }

}
```

Figure A6: Snapshot of controlDict file which provides information about the main simulation properties for the case of hybrid forced/buoyancy convection in elongated channel (Ri=100 and Ra=10^7) and hot bottom wall.

A.3.4 fvSchemes

The systems directory contains the *fvSchemes* file which is used to set up numerical schemes for different terms which appears in equations mentioned in Chapter 2 such as derivatives which are computed during a simulation. This section provides information on how to set up numerical schemes in the *fvSchemes* dictionary. The terms appearing in the equations that should be designated a numerical scheme range from derivatives such as gradient ∇ to interpolations of values from one set of points to another. OpenFOAM provides user the freedom of choice which starts from the freedom to choose a discretisation practice which is usually a standard Gaussian finite volume integration. This method sums the values on control volume i.e., cell faces which are interpolated from cell centres. The different terms which require a numerical scheme are subdivided inside the *fvSchemes* dictionary into the following categories:

- **gradSchemes**: used for gradient ∇
- **divSchemes**: used for divergence $\nabla \bullet$
- **timeScheme**: used for first and second time derivatives such as $\partial/\partial t$, $\partial^2/\partial^2 t$
- **laplacianScheme**: used for Laplacian ∇^2
- **interpolationSchemes**: used for the purpose of interpolating values from cell to face
- **snGradSchemes**: used for component of gradient normal to a cell face.

It can be seen in Fig. A7 different keywords are used which highlights the name of a *Schemes* sub-dictionary containing terms of particular type such as *gradSchemes* includes all the gradient derivative terms present inside equations mentioned in Chapter 3 such as grad (p) denotes ∇p. A default entry is used inside the *gradSchemes* sub-dictionary (Fig. A7) which essentially means that a same scheme will be used for each gradient term appearing in equations such as ∇p and ∇U.

A.3.4.1 Gradient schemes

In OpenFOAM the default discretisation scheme that is most commonly used for gradient terms is:

```
default         Gauss linear;
```

The purpose of the Gauss entry is to indicate a finite volume discretisation of Gaussian integration needing a scheme that interpolates the values from cell centres to face centres. Hence, for that reason, a linear interpolation or central differencing scheme is used which is specified using the linear entry (Fig. A7).

A.3.4.2 Divergence schemes

The sub-dictionary which includes all the divergence terms is specified by the keyword entry *divSchemes* which are usually written as ∇ • . . . and excludes Laplacian terms. It includes terms which are advective in nature for instance ∇ • (U*k*), where the advective flux is provided by velocity U. Moreover, it also includes diffusive terms such as ∇ • *v*(∇U) T. The non-advective terms are usually written as div(U) however, the advective terms are specified using the keyword identifier of the form div (phi,…). The term phi indicates volumetric flux of velocity on the cell faces for incompressible flow such as div (phi, U) indicates the advection of velocity, div (phi, T) indicates advection of temperature. All the schemes make use of Gauss integration through the flux phi and interpolation of the advective field to the cell faces is achieved by means of a numerical scheme. Here the schemes used for advection of velocity and temperature will be highlighted as they are the most important terms. As shown in Fig. A7 a **Q**uadratic **U**pstream **I**nterpolation for **C**onvective **K**inematics (QUICK) scheme which is a second order central difference scheme was used for these terms.

A.3.4.3 Laplacian schemes

The sub-dictionary that contains the Laplacian terms is written as *LaplacianSchemes* (Fig. A7). An example of Laplacian term is ∇ • (*v*∇U) which is the diffusion term in momentum equation. The Gauss scheme is used for discretisation which requires a combination of interpolation scheme for the diffusion coefficient i.e., kinematic viscosity (*v*) and a surface normal gradient scheme i.e., ∇U. Hence the following scheme was used

```
default         Gauss linear corrected;
```

Where corrected is a central-difference snGrad scheme with non-orthogonal correction.

```
/*--------------------------------*- C++ -*----------------------------------*\
| =========                 |                                                 |
| \\      /  F ield         | OpenFOAM: The Open Source CFD Toolbox           |
|  \\    /   O peration     | Version:  4.1                                   |
|   \\  /    A nd           | Web:      www.OpenFOAM.org                      |
|    \\/     M anipulation  |                                                 |
\*---------------------------------------------------------------------------*/
FoamFile
{
    version     2.0;
    format      ascii;
    class       dictionary;
    location    "system";
    object      fvSchemes;
}
// * * * * * * * * * * * * * * * * * * * * * * * * * * * * * * * * * * * * * //

ddtSchemes
{
    default         Euler;
}

gradSchemes
{
    default         Gauss linear;
}

divSchemes
{
   //default         Gauss linear;

    div(phi,U)      Gauss QUICK;
    div(phi,T)      Gauss QUICK;
    div(phi,k)      Gauss upwind;
    div(phi,epsilon) Gauss upwind;
    div(phi,R)      Gauss upwind;
    div(R)          Gauss linear;
    div((nuEff*dev2(T(grad(U))))) Gauss linear;
}

laplacianSchemes
{
    default         Gauss linear uncorrected;
}

interpolationSchemes
{
    default         linear;
}

snGradSchemes
{
    default         uncorrected;
}


// ************************************************************************* //
```

Figure A7: Snapshot of *fvSchemes* file which provides information about different numerical schemes set up for the case of hybrid forced/buoyancy convection in elongated channel (*Ri*=100 and *Ra*=10^7) and hot bottom wall.

A.3.5 fvSolution

This *fvSolution* dictionary contains information about the solvers, the tolerances and algorithms of the simulation. It further contains sub-dictionaries at the end that includes *solvers* and *relaxationFactors*. As shown in Fig. A8, the first sub-dictionary is solvers which indicates each linear solver that is used for each discretised equation. The term *linear*-solver is different to an *application* solver which is buoyantBoussinesqPimpleFoam in the present thesis. It can be defined as a technique of number crunching to solve a matrix equation. All the entries inside the solvers begins with a keyword that is set up as the variable solved in a particular equation. The variable keyword further relates to a sub-dictionary which specifies the solver type and various parameters used by solver such as tolerance, relTol and preconditioner. The Fig. A8 shows for

the pressure, GAMG is used a solver which is used to obtain the solution of Poisson equation (4.3). The solver tolerance represents the residual level which should be small enough for the solution to be considered accurate, hence for that reason it is set up as $1x10^{-6}$. The term relative tolerance which is specified by a keyword relTol limits the relative improvement from initial to final solution and set up as 0.1 as illustrated in Fig. A8. A smoother needs to be specified for the solvers that use a smoother so a GaussSeidel smoother was used for every case. After specifying the smoother, the user has the option to specify the number of sweeps and the following optional entries have been used as represented in Fig. A8.

- **nPreSweeps**: Indicates the number of sweeps as the algorithm coarsens. Set to a default value of 0.
- **nPostSweeps**: Indicates the highest number of sweeps as the algorithm coarsens. Set to a default value of 2.

The agglomeration process of the cell is achieved through the use of a keyword agglomerator. The default faceAreaPair method is used (Fig. A8). Additional optional entries are also used to control the agglomeration which are as follows:

- **cacheAgglomeration**: It is a switch which indicates the caching of agglomeration process. Set to default true.
- **mergeLevels**: It is used to control the speed of coarsening or refinement process. Set to 2 as the mesh is quite simple.

For the variables U (velocity) and T (temperature) a Preconditioned Bi-Conjugate Gradient (PBiCG) was used as a linear solver where an incomplete Lower Upper (DILU) preconditioner was used in the predictor step (Fig. A8). The *fvSolution* file contains a second sub-dictionary known as relaxationFactors meant to control under-relaxation, a method employed for improving the stability of computation. An under-relaxation factor $\alpha = 1$ was specified which guarantees matrix diagonal equality.

```
/*--------------------------------*- C++ -*----------------------------------*\
| =========                 |                                                 |
| \\      /  F ield         | OpenFOAM: The Open Source CFD Toolbox           |
|  \\    /   O peration     | Version:  4.1                                   |
|   \\  /    A nd           | Web:      www.OpenFOAM.org                      |
|    \\/     M anipulation  |                                                 |
\*---------------------------------------------------------------------------*/
FoamFile
{
    version     2.0;
    format      ascii;
    class       dictionary;
    location    "system";
    object      fvSolution;
}
// * * * * * * * * * * * * * * * * * * * * * * * * * * * * * * * * * * * * * //

solvers
{
    p_rgh
    {
        solver           GAMG;
        tolerance        1e-6;
        relTol           0.1;
        smoother         GaussSeidel;
        nPreSweeps       0;
        nPostSweeps      2;
        cacheAgglomeration on;
        agglomerator     faceAreaPair;
        nCellsInCoarsestLevel 200;
        mergeLevels      2;
       /* solver          PCG;
        preconditioner  DIC;
        tolerance       1e-6;
        relTol          0.1;*/
    }

    p_rghFinal
    {
        $p_rgh;
        relTol          0;
    }

    "(U|T|k|epsilon|R)"
    {
        solver          PBiCG;
        preconditioner  DILU;
        tolerance       1e-6;
        relTol          0.1;
    }

    "(U|T|k|epsilon|R)Final"
    {
        $U;
        relTol          0;
    }
}

PIMPLE
{
    momentumPredictor no;
    nOuterCorrectors 1;
    nCorrectors      2;
    nNonOrthogonalCorrectors 0;
    pRefCell         0;
    pRefValue        0;
}

relaxationFactors
{
    equations
    {
        "(U|T|k|epsilon|R)" 1;
        "(U|T|k|epsilon|R)Final" 1;
    }
}

// ************************************************
```

Figure A8: Snapshot of *fvSolution* file which provides information about linear solvers, tolerance and algorithms set up for the case of hybrid forced/buoyancy convection in elongated channel (Ri=100 and Ra=10^7) and hot bottom wall.

References

Abdalla, I.E., Yang, Z. and Cook, M., (2009), Computational analysis and flow structure of a transitional separated-reattached flow over a surface mounted obstacle and a forward-facing step. *International Journal of Computational Fluid Dynamics*, *23*(1), pp.25-57.

Abu-Mulaweh, H.I., (2003), A review of research on laminar mixed convection flow over backward-and forward-facing steps. *International Journal of Thermal Sciences*, *42*(9), pp.897-909.

Abu-Mulaweh, H.I., Armaly, B.F. and Chen, T.S., (1993), Measurements of laminar mixed convection flow over a horizontal forward-facing step. *Journal of thermophysics and heat transfer*, *7*(4), pp.569-573.

Ali, S.Z. and Dey, S., (2017), Hydrodynamic instability of meandering channels. *Physics of Fluids*, *29*(12), p.125107.

Antonia, R.A. and Luxton, R.E., (1971), The response of a turbulent boundary layer to a step change in surface roughness Part 1. Smooth to rough. *Journal of Fluid Mechanics*, *48*(4), pp.721-761.

Armaly, B.F., Durst, F., Pereira, J.C.F. and Schönung, B., (1983), Experimental and theoretical investigation of backward-facing step flow. *Journal of fluid Mechanics*, *127*, pp.473-496.

Armfield, S. and Street, R., (1999), The fractional-step method for the Navier–Stokes equations on staggered grids: the accuracy of three variations. *Journal of Computational Physics*, *153*(2), pp.660-665.

Armfield, S. and Street, R., (2002), An analysis and comparison of the time accuracy of fractional-step methods for the Navier–Stokes equations on staggered grids. *International Journal for Numerical Methods in Fluids*, *38*(3), pp.255-282.

Arrif, T., Chehhat, A., Abo-Serie, E. and Benchabane, A., (2018), Numerical Study of Natural Convection in Square Tilted Solar Cavity Considering Extended Domain. *FDMP-Fluid Dynamics & Materials Processing*, pp.223-242.

Auteri, F. and Parolini, N. (2002) Numerical investigation of the first instabilities in the differentially heated 8:1 cavity, *Int. J. Num. Methods Fluids*, 40 (8), 1121–1132.

Avancha, R.V. and Pletcher, R.H., (2002), Large eddy simulation of the turbulent flow past a backward-facing step with heat transfer and property variations. *International Journal of Heat and Fluid Flow*, *23*(5), pp.601-614.

Barbosa-Saldaña J., Anand N., Sarin V., (2005), Numerical simulation of mixed convective flow over a three-dimensional horizontal backward facing step, *J. Heat Transf.* 127(9), pp. 1027-1036.

Barbosa-Saldaña J.G. and Anand N. K., (2007), "Flow Over a Three-Dimensional Horizontal Forward-Facing Step", *Numerical Heat Transfer, Part A: Applications*, 53(1), pp.1-17.

Barkley, D., Gomes, M.G.M. and Henderson, R.D., (2002), Three-dimensional instability in flow over a backward-facing step. *Journal of fluid mechanics*, *473*, pp.167-190.

Bartosiewicz Y. and Duponcheel M., (2019), 6.1.2 - Large-eddy simulation: Application to liquid metal fluid flow and heat transfer, in Thermal Hydraulics Aspects of Liquid Metal Cooled Nuclear Reactors, 2019 Pages 245-271, https://doi.org/10.1016/B978-0-08-101980-1.00017-X

Bhattacharjee J.K., (2015), Kolmogorov argument for the scaling of the energy spectrum in a stratified fluid, *Physics Letters* A, 379(7), pp. 696–699.

Biswas, G., Breuer, M. and Durst, F., (2004), Backward-facing step flows for various expansion ratios at low and moderate Reynolds numbers. *J. Fluids Eng.*, *126*(3), pp.362-374.

Bolgiano R., (1959), Turbulent spectra in a stably stratified atmosphere, *J. Geophys. Res*. 64(12), pp. 2226-2229

Bouabdallah, S., Ghernaout, B., Teggar, M., Benchatti, A. and Benarab, F.Z., (2016), Onset of natural convection and transition laminar-oscillatory convection flow in rayleigh-bénard configuration. *International journal of heat and technology*, *34*, pp.151-157.

Brottier L. and Bennacer R., (2020), "Thermal performance analysis of 28 PVT solar domestic hot water installations in Western Europe", *Renewable Energy*, 160, pp. 196-210

Bucchignani, E. (2009), An implicit unsteady finite volume formulation for natural convection in a square cavity, *Fluid Dyn. Mater. Process*., 5 (1), pp.37–60.
Busse, F.H. and Clever, R.M., (1979), Instabilities of convection rolls in a fluid of moderate Prandtl number. *Journal of Fluid Mechanics*, *91*(2), pp.319-335.

Busse, F.H., (1978), Non-linear properties of thermal convection. *Reports on Progress in Physics*, *41*(12), p.1929.

Cabot W.H., (1993), Large eddy simulations of time-dependent and buoyancy-driven channel flows, Annual Research Briefs, 1992, pp.45-60, Document ID 19940007815, https://ntrs.nasa.gov/citations/19940007815

Carruthers, J.R., (1977), Crystal growth in a low gravity environment. *Journal of Crystal Growth*, *42*, pp.379-385.

Celik I., Klein M., Freitag M., Janicka J. (2006), Assessment measures for URANS/DES/LES: an overview with applications. *J. Turbul.*, 7, p.N48.

Çengel, Y.A., Turner, R.H., Cimbala, J.M. and Kanoglu, M., 2008. *Fundamentals of thermal-fluid sciences* (Vol. 703). New York: McGraw-Hill.

Chandra, P.R., Alexander, C.R. and Han, J.C., (2003), Heat transfer and friction behaviors in rectangular channels with varying number of ribbed walls. *International Journal of Heat and Mass Transfer*, *46*(3), pp.481-495.

Chen, L., Asai, K., Nonomura, T., Xi, G. and Liu, T., (2018), A review of Backward-Facing Step (BFS) flow mechanisms, heat transfer and control. *Thermal Science and Engineering Progress*, *6*, pp.194-216.

Cherry, N.J., Hillier, R. and Latour, M.E.M.P., (1984), Unsteady measurements in a separated and reattaching flow. *Journal of Fluid Mechanics*, *144*, pp.13-46.

Choi H. and Moin P., (2012), Grid-point requirements for large eddy simulation: Chapman's estimates revisited, *Phys. Fluids*, 24, p.011702.

Chorin, A.J., (1968), Numerical solution of the Navier-Stokes equations. *Mathematics of computation*, *22*(104), pp.745-762.

Ciofalo M. and Collins M.W., (1992), Large-eddy simulation of turbulent flow and heat transfer in plane and rib-roughened channels, *Int. J. Numer. Methods Fluids* 15 (4), 453–489.

Clever, R.M. and Busse, F.H., (1974), Transition to time-dependent convection. *Journal of Fluid Mechanics*, *65*(4), pp.625-645.

Clever, R.M. and Busse, F.H., (1978), Large wavelength convection rolls in low Prandtl number fluids. *Zeitschrift für angewandte Mathematik und Physik ZAMP*, *29*(4), pp.711-714.

Coceal, O., Thomas, T.G., Castro, I.P. and Belcher, S.E., (2006), Mean flow and turbulence statistics over groups of urban-like cubical obstacles. *Boundary-Layer Meteorology*, *121*(3), pp.491-519.

Cortese, T. and Balachandar, S., (1993), Vortical nature of thermal plumes in turbulent convection. *Physics of Fluids A: Fluid Dynamics*, *5*(12), pp.3226-3232.

Corvaro, F. and Paroncini, M., (2007), Experimental analysis of natural convection in square cavities heated from below with 2D-PIV and holographic interferometry techniques. *Experimental thermal and fluid science*, *31*(7), pp.721-739.

Counihan, J.J.C.R., Hunt, J.C.R. and Jackson, P.S., (1974), Wakes behind two-dimensional surface obstacles in turbulent boundary layers. *Journal of Fluid Mechanics*, *64*(3), pp.529-564.

Cross, M.C., Daniels, P.G., Hohenberg, P.C. and Siggia, E.D., (1980), Effect of distant sidewalls on wave-number selection in Rayleigh-Bénard convection. *Physical Review Letters*, *45*(11), p.898.

Cui J., Patel V.C., Lin C.L., (2003), Large-eddy simulation of turbulent flow in a channel with rib roughness, *Int. J. Heat Fluid Flow* 24(3), pp. 372–388.
Dai, Z.Y., Li, T., Zhang, W.H. and Zhang, J., (2020), Numerical study on aerodynamic performance of high-speed pantograph with double strips. *Fluid Dynamics & Materials Processing*, *16*(1), pp.31-40.

Daniels, P. G. and Patterson, J. C. (1997), On the long-wave instability of natural-convection boundary layers, *J. Fluid Mech*., 335, pp.57–73

Daniels, P. G. and Patterson, J. C. (2001), On the short-wave instability of natural convection boundary layers, *Proc. Math. Phys. Eng. Sci* ., 457, pp.519–538.
Davis, S.H., 1967. Convection in a box: linear theory. *Journal of Fluid Mechanics*, *30*(3), pp.465-478.

De Leon R. and Senocak I., (2017), Turbulent Inflow Generation for Large-eddy Simulation of Incompressible Flows Through Buoyancy Perturbations, AIAA 2017-3294, Session: Numerical Methodologies for DNS and LES, https://doi.org/10.2514/6.2017-3294 https://arc.aiaa.org/doi/10.2514/6.2017-3294.

De Vahl Davis, G. and Jones, I., (1983), Natural convection in a square cavity: a comparison exercise. *International Journal for numerical methods in fluids*, *3*(3), pp.227-248.

De, A.K., Eswaran, V. and Mishra, P.K., (2017), Scalings of heat transport and energy spectra of turbulent Rayleigh-Bénard convection in a large-aspect-ratio box. *International Journal of Heat and Fluid Flow*, *67*, pp.111-124.

Delgado-Buscalioni R. (2001a), Convection patterns in end-heated inclined enclosures *Phys. Rev. E*, 64, 016303-1–016303–17.
Delgado-Buscalioni R. and Crespo del Arco E., (2001), Flow and heat transfer regimes in inclined differentially heated cavities, *Int. J. Heat Mass Transfer*, 44(10), pp. 1947-1962.

Desrayaud, G. and Lauriat, G., (1993). Unsteady confined buoyant plumes. *Journal of Fluid Mechanics*, *252*, pp.617-646.

Dong, S., Karniadakis, G.E. and Chryssostomidis, C., (2014), A robust and accurate outflow boundary condition for incompressible flow simulations on severely truncated unbounded domains. *Journal of Computational Physics*, *261*, pp.83-105.

Drazin, P.G. and Reid, W.H., (1981), Hydrodynamic stability. *NASA STI/Recon Technical Report A*, *82*, p.17950.

Duan Y. and He S., (2017), Large eddy simulation of a buoyancy-aided flow in a non-uniform channel – Buoyancy effects on large flow structures, *Nuclear Engineering and Design*, 312, pp. 191-204. https://www.sciencedirect.com/science/article/pii/S0029549316301030

Dunn, W.E., Policastro, A.J. and Paddock, R.A., (1975), *Surface thermal plumes: Evaluation of mathematical models for the near and complete field* (Vol. 1). Argonne National Laboratory.

Durrani F., Cook M.J., McGuirk J.J., (2015), Evaluation of LES and RANS CFD modelling of multiple steady states in natural ventilation, *Building and Environment*, 92, pp. 167-181.

Eidson, T.M., (1985), Numerical simulation of the turbulent Rayleigh–Bénard problem using subgrid modelling. *Journal of Fluid Mechanics*, *158*, pp.245-268.

Erturk, E., (2008), Numerical solutions of 2-D steady incompressible flow over a backward-facing step, Part I: High Reynolds number solutions. *Computers & Fluids*, *37*(6), pp.633-655.

Farhangnia, M., Biringen, S. and Peltier, L.J., (1996), Numerical Simulation of Two–Dimensional Buoyancy–Driven Turbulence in a Tall Rectangular Cavity. *International journal for numerical methods in fluids*, *23*(12), pp.1311-1326.

Ferialdi, H., Lappa, M. and Haughey, C., (2020), On the role of thermal boundary conditions in typical problems of buoyancy convection: A combined experimental-numerical analysis. *International Journal of Heat and Mass Transfer*, *159*, p.120012.

Fortin, A., Jardak, M., Gervais, J.J. and Pierre, R., (1997), Localization of Hopf bifurcations in fluid flow problems. *International Journal for Numerical Methods in Fluids*, *24*(11), pp.1185-1210.

Friedrich, R. and Arnal, M. (1990), Analysing turbulent backward-facing step flow with the lowpass-filtered Navier-Stokes equations. *J. Wind Engineering and Industrial Aerodynamics.*, 35, pp. 101-128.

Gelfgat, A.Y., (2020), Instability of natural convection in a laterally heated cube with perfectly conducting horizontal boundaries. *Theoretical and Computational Fluid Dynamics*, *34*(5), pp.693-711.

Gelfgat, A.Y., (2020), Instability of natural convection of air in a laterally heated cube with perfectly insulated horizontal boundaries and perfectly conducting spanwise boundaries. *Physical Review Fluids*, *5*(9), p.093901.

Georgiadis N.J., Rizzetta D.P. and Fureby C., (2010), Large-Eddy Simulation: Current Capabilities, Recommended Practices, and Future Research, *AIAA Journal*, 48(8), pp. 1772-1784.

Gershuni, G.Z., Laure, P., Myznikov, V.M., Roux, B. and Zhukhovitsky, E.M., (1992), On the stability of plane-parallel advective flows in long horizontal layers. *Microgravity Q*, *2*(3), pp.141-151.

Getling, A.V., (1998), *Rayleigh-Bénard convection: structures and dynamics* (Vol. 11). World Scientific.

Gill, A. E. and Davey, A. (1969), Instabilities of a buoyancy-driven system, *J. Fluid Mech*., 35 (4), pp.775–798

Gill, A.E., (1974), A theory of thermal oscillations in liquid metals. *Journal of Fluid Mechanics*, *64*(3), pp.577-588.

Goldhirsch, I., Pelz, R.B. and Orszag, S.A., (1989), Numerical simulation of thermal convection in a two-dimensional finite box. *Journal of Fluid Mechanics*, *199*, pp.1-28.

Gollub, J. and Benson, S.V., (1980), Many routes to turbulent convection. *Journal of Fluid Mechanics*, *100*(3), pp.449-470.

Gray, D.D. and Giorgini, A., (1976), The validity of the Boussinesq approximation for liquids and gases. *International Journal of Heat and Mass Transfer*, *19*(5), pp.545-551.

Graziani, A., Lippert, M., Uystepruyst, D. and Keirsbulck, L., (2017), Scaling and flow dependencies over forward-facing steps. *International Journal of Heat and Fluid Flow*, *67*, pp.220-229.

Guo, Z.Y., Li, D.Y. and Liang, X.G., (1996), Thermal effect on the recirculation zone in sudden-expansion gas flows. *International journal of heat and mass transfer*, *39*(13), pp.2619-2624.

Hadley, G., (1735), VI. Concerning the cause of the general trade-winds. *Philosophical Transactions of the Royal Society of London*, *39*(437), pp.58-62.

Han, H., Lu, J. and Weizhu, B.A.O., (1994), A discrete artificial boundary condition for steady incompressible viscous flows in a no-slip channel using a fast iterative method. *Journal of Computational Physics*, *114*(2), pp.201-208.

Harlow F.H. and Welch J.E. (1965), "Numerical calculation of time-dependent viscous incompressible flow with free surface", *Phys. Fluids*, 8: 2182-2189

Hart, J.E., (1972), Stability of thin non-rotating Hadley circulations. *Journal of Atmospheric Sciences*, *29*(4), pp.687-697.

Hart, J.E., (1983), Low Prandtl number convection between differentially heated end walls. *International Journal of Heat and Mass Transfer*, *26*(7), pp.1069-1074.

Hattori, H. and Nagano, Y., (2010), Investigation of turbulent boundary layer over forward-facing step via direct numerical simulation. *International Journal of Heat and Fluid Flow*, *31*(3), pp.284-294.

Hattori, T., Norris, S.E., Kirkpatrick, M.P. and Armfield, S.W., (2013), Comparison of non-reflective boundary conditions for a free-rising turbulent axisymmetric plume. *International Journal for Numerical Methods in Fluids*, *72*(12), pp.1307-1320.

Hemchandra, S., Shanbhogue, S., Hong, S. and Ghoniem, A.F., (2018), Role of hydrodynamic shear layer stability in driving combustion instability in a premixed propane-air backward-facing step combustor. *Physical Review Fluids*, *3*(6), p.063201.

Henkes, R. A. W. M. and Hoogendoorn, C. J. (1990), On the stability of the natural convection flow in a square cavity heated from the side, *Appl. Sci. Res*., 47 (3), pp.195–220.

Hier Majumder, C.A., Yuen, D.A. and Vincent, A.P., (2004), Four dynamical regimes for a starting plume model. *Physics of Fluids*, *16*(5), pp.1516-1531.

Hillier, R. and Cherry, N.J., (1981), The effects of stream turbulence on separation bubbles. *Journal of wind engineering and industrial aerodynamics*, *8*(1-2), pp.49-58.

Hurle, D.T.J., (1972), Hydrodynamics, convection and crystal growth. *Journal of Crystal Growth*, *13*, pp.39-43.

Hutchinson, B.R. and Raithby, G.D., (1986), A multigrid method based on the additive correction strategy. *Numerical Heat Transfer, Part A: Applications*, *9*(5), pp.511-537.

Issa, R.I., (1986), Solution of the implicitly discretised fluid flow equations by operator-splitting. *Journal of computational physics*, *62*(1), pp.40-65.

Iwai, H., Nakabe, K. and Suzuki, K., (2000), Flow and heat transfer characteristics of backward-facing step laminar flow in a rectangular duct. *International Journal of Heat and Mass Transfer*, *43*(3), pp.457-471.

Janssen, R. J. A. and Henkes, R. A. W. M. (1995), Influence of Prandtl number on instability mechanisms and transition in a differentially heated square cavity, *J. Fluid Mech*., 290, pp.319–344.

Jeffreys, H., (1926), The stability of a fluid layer heated from below. *Philosophical Magazine*, *2*, pp.833-844.

Jeffreys, H., (1928), Some cases of instability in fluid motion. *Proceedings of the Royal Society of London. Series A, Containing Papers of a Mathematical and Physical Character*, *118*(779), pp.195-208.

Kachi, S., Bensouici, F.Z., Ferroudj, N. and Boudebous, S., (2019), Effect of richardsonnumber on unsteady mixed convection in a square cavity partially heated from below. *Fluid Dynamics & Materials Processing*, *15*(2), pp.89-105.

Kanna, P.R. and Das, M.K., (2006), Conjugate heat transfer study of backward-facing step flow–a benchmark problem. *International journal of heat and mass transfer*, *49*(21-22), pp.3929-3941.

Keating, A., Piomelli, U., Bremhorst, K. and Nešić, S., (2004), Large-eddy simulation of heat transfer downstream of a backward-facing step. *Journal of Turbulence*, *5*(1), pp. 20.

Kerr, R.M., (1996), Rayleigh number scaling in numerical convection. *Journal of Fluid Mechanics*, *310*, pp.139-179.

Khanafer, K., Al-Azmi, B., Al-Shammari, A. and Pop, I., (2008), Mixed convection analysis of laminar pulsating flow and heat transfer over a backward-facing step. *International journal of heat and mass transfer*, *51*(25-26), pp.5785-5793.

Khatra, L., El Qarnia, H. and El Ganaoui, M., (2019), The Effect of the Fin Length on the Solidification Process in a Rectangular Enclosure with Internal Fins. *Fluid Dynamics & Materials Processing*, *15*(2), pp.125-137.

Kherbeet, A.S., Safaei, M.R., Mohammed, H.A., Salman, B.H., Ahmed, H.E., Alawi, O.A. and Al-Asadi, M.T., (2016), Heat transfer and fluid flow over microscale backward and forward-facing step: a review. *International Communications in Heat and Mass Transfer*, *76*, pp.237-244.

Kim, J. and Moin, P., (1985), Application of a fractional-step method to incompressible Navier-Stokes equations. *Journal of computational physics*, *59*(2), pp.308-323.

Kimmel, S.J. and Domaradzki, J.A., (2000), Large eddy simulations of Rayleigh–Bénard convection using subgrid scale estimation model. *Physics of Fluids*, *12*(1), pp.169-184.

Kiya, M. and Sasaki, K., (1983). Structure of a turbulent separation bubble. *Journal of Fluid Mechanics*, *137*, pp.83-113.

Kolmogorov, A.N. (1941a) "The local structure of turbulence in incompressible viscous fluids at very large Reynolds numbers", *Dokl. Akad. Nauk. SSSR* 30, 299-303. Reprinted in *Proc. R. Soc. London* A 434, 9-13 (1991)

Kolmogorov, A.N. (1941b) "Dissipation of energy in isotropic turbulence", In *Dokl. Akad. Nauk SSSR* (Vol. 32, pp. 325-327).

Kolmogorov, A.N., (1941c) On degeneration (decay) of isotropic turbulence in an incompressible viscous liquid. In *Dokl. Akad. Nauk SSSR* (Vol. 31, pp. 538-540).

Kraichnan, R.H., (1974), On Kolmogorov's inertial-range theories. *Journal of Fluid Mechanics*, *62*(2), pp.305-330.

Kumar A., Chatterjee A.G., and Verma M.K., (2014), Energy spectrum of buoyancy-driven turbulence, *Phys. Rev.* E 90(2), p. 023016

Kumar, B.R. and Naidu, K.B., (1993), A streamline upwinding streamfunction-vorticity finite element analysis of Navier-Stokes equations. *Applied numerical mathematics*, *13*(4), pp.335-344.

Kuo, H.P. and Korpela, S.A., (1988), Stability and finite amplitude natural convection in a shallow cavity with insulated top and bottom and heated from a side. *The Physics of fluids*, *31*(1), pp.33-42.

Labbe O., Sagaut P. and Montreuil E., (2002), Large-eddy simulation of heat transfer over a backward-facing step, *Numerical Heat Transfer: Part A: Applications*, *42*(1-2), pp.73-90.

Ladyzhenskaya, O.A., (1969), *The mathematical theory of viscous incompressible flow* (Vol. 2, pp. xviii+-224). New York: Gordon and Breach.

Lappa M., (1997), "Strategies for parallelizing the three-dimensional Navier-Stokes equations on the Cray T3E"; Science and Supercomputing at CINECA, 11, 326-340. ISBN-10: 88-86037-03-1, M. Voli, Editor (Bologna, Italy)

Lappa, M. and Gradinscak, T., (2018), On the oscillatory modes of compressible thermal convection in inclined differentially heated cavities. *International Journal of Heat and Mass Transfer*, *121*, pp.412-436.

Lappa, M., (2009), *Thermal convection: patterns, evolution and stability*. John Wiley & Sons.

Lappa, M., (2011), Some considerations about the symmetry and evolution of chaotic Rayleigh–Bénard convection: The flywheel mechanism and the "wind" of turbulence. *Comptes Rendus Mécanique*, *339*(9), pp.563-572.

Lappa, M., (2017), On the oscillatory hydrodynamic modes in liquid metal layers with an obstruction located on the bottom. *International Journal of Thermal Sciences*, *118*, pp.303-319.

Lappa, M., (2019), On the gravitational suppression of hydrothermal modes in liquid layers with a blockage on the bottom wall. *International Journal of Thermal Sciences*, *145*, p.105987.

Lappa, M., (2019), On the highly unsteady dynamics of multiple thermal buoyant jets in cross flows. *Physics of Fluids*, *31*(11), p.115105.

Lappa, M., 2007. Secondary and oscillatory gravitational instabilities in canonical three-dimensional models of crystal growth from the melt. Part 2: Lateral heating and the Hadley circulation. *Comptes Rendus Mécanique*, *335*(5-6), pp.261-268.

Largeau, J.F. and Moriniere, V., (2007), Wall pressure fluctuations and topology in separated flows over a forward-facing step. *Experiments in Fluids*, *42*(1), pp.21-40.

Le H., Moin P. and Kim J., (1997), Direct numerical simulation of turbulent flow over a backward-facing step, *J. Fluid Mech*., 330, pp. 349-374.

Le Quere, P. (1990), Transition to unsteady convection in a tall water-filled cavity,´ *Phys. Fluids A*, 2 (4), pp.503–515.

Le Quéré, P. and Behnia, M., (1998). From onset of unsteadiness to chaos in a differentially heated square cavity. *Journal of fluid mechanics*, *359*, pp.81-107.

Le Quere, P. and Penot, F. (1987), Numerical and experimental investigation of the transition to unsteady natural convection of air in a vertically differentially heated cavity, *ASME HTD*, 94, pp.75–82.

Lee, J.H.W. and Chu, V., (2003), *Turbulent jets and plumes: A Lagrangian approach* (Vol. 1). Springer Science & Business Media.

Lee, M.J., Do Oh, B. and Kim, Y.B., (2001), Canonical fractional-step methods and consistent boundary conditions for the incompressible Navier–Stokes equations. *Journal of computational physics*, *168*(1), pp.73-100.

Li C.W.and Ma F.X., (2003), Large eddy simulation of diffusion of a buoyancy source in ambient water, *Applied Mathematical Modelling* 27, 649-663.

Liou, T.M., Hwang, J.J. and Chen, S.H., (1993), Simulation and measurement of enhanced turbulent heat transfer in a channel with periodic ribs on one principal wall. *International Journal of Heat and Mass Transfer*, *36*(2), pp.507-517.

Lohász MM, Rambaud P, Benocci C., (2006), Flow features in a fully developed ribbed duct flow as a result of MILES, *Flow Turbulence and Combust*, 77(1), pp.59–76.

Mayne, D. A., Usmani, A. S. and Crapper, M. (2000), h-Adaptive finite element solutions of high Rayleigh number thermally driven cavity problem, *Int. J. Num. Methods Heat Fluid Flow*, 10, pp.598–615.

Miyake, Y., Tsujimoto, K. and Nakaji, M., (2001), Direct numerical simulation of rough-wall heat transfer in a turbulent channel flow. *International Journal of Heat and Fluid Flow*, *22*(3), pp.237-244.

Mizushima, J. and Adachi, T., (1997), Sequential transitions of the thermal convection in a square cavity. *Journal of the Physical Society of Japan*, *66*(1), pp.79-90.

Moghadam Z.S., Guibault F. and Garon A., (2021) On the Evaluation of Mesh Resolution for Large-Eddy Simulation of Internal Flows Using Openfoam, *Fluids* 2021, 6(1), p.24. https://doi.org/10.3390/fluids6010024

Molochnikov, V.M., Mazo, A.B., Kalinin, E.I., Malyukov, A.V., Okhotnikov, D.I. and Dushina, O.A., (2019), Formation and turbulent breakdown of large-scale vortical structures behind an obstacle in a channel at moderate Reynolds numbers. *Physics of Fluids*, *31*(10), p.104104.

Montazerin N., Akbari G., Mahmoodi M.,(2015), 1 - General introduction of forward-curved squirrel-cage fan, Developments in Turbomachinery Flow ,Forward Curved Centrifugal Fans, 2015, Pages 1-23, https://doi.org/10.1016/B978-1-78242-192-4.00001-4

Moosavi, R. and Gandjalikhan Nassab, S.A., (2008), Turbulent Forced Convection Over A Single Inclined Forward Step In A Duct: Part I–Flow Field. *Engineering Applications of Computational Fluid Mechanics*, *2*(3), pp.366-374.

Morsli, S., Boussoufi, M., Sabeur, A., El Ganaoui, M. and Bennacer, R., (2018), Small to large scale mixed turbulent convection: buildings application. *International Journal of Numerical Methods for Heat & Fluid Flow*.

Moss, W.D. and Baker, S., (1980), Re-circulating flows associated with two-dimensional steps. *Aeronautical Quarterly*, *31*(3), pp.151-172.

Murataa A., Mochizuki S., (2000), Large eddy simulation with a dynamic subgrid-scale model of turbulent heat transfer in an orthogonally rotating rectangular duct with transverse rib turbulators, *Int. J. Heat Mass Transfer* 43 (7), pp.1243– 1259.

Nadjib, H., Adel, S., Djamel, S. and Abderrahmane, D., (2018), Numerical Investigation of Combined Surface Radiation and Free Convection in a Square Enclosure with an Inside Finned Heater. *FDMP-FLUID DYNAMICS & MATERIALS PROCESSING*, *14*(3), pp.155-175.

Napolitano, L.G., (1982), Surface and buoyancy driven free convection. *Acta Astronautica*, *9*(4), pp.199-215.

Nassab, S.G., Moosavi, R. and Sarvari, S.H., (2009), Turbulent forced convection flow adjacent to inclined forward step in a duct. *International Journal of Thermal Sciences*, *48*(7), pp.1319-1326.

Obukhov A.M., (1959), On the influence of Archimedean forces on the structure of the Temperature field in a turbulent flow, *Dokl. Akad. Nauk SSSR*, 125, pp. 1246-1248

Ouertatani, N., Cheikh, N.B., Beya, B.B. and Lili, T., (2008), Numerical simulation of two-dimensional Rayleigh–Bénard convection in an enclosure. *Comptes Rendus Mécanique*, *336*(5), pp.464-470.

Öztop, H.F., (2006), Turbulence forced convection heat transfer over double forward facing step flow. *International communications in heat and mass transfer*, *33*(4), pp.508-517.

Oztop, H.F., Dagtekin, I. and Bahloul, A., (2004), Comparison of position of a heated thin plate located in a cavity for natural convection. *International communications in heat and mass transfer*, *31*(1), pp.121-132.

Oztop, H.F., Mushatet, K.S. and Yılmaz, İ., (2012), Analysis of turbulent flow and heat transfer over a double forward-facing step with obstacles. *International Communications in Heat and Mass Transfer*, *39*(9), pp.1395-1403.

Paolucci, S. and Chenoweth, D.R., (1989), Transition to chaos in a differentially heated vertical cavity. *Journal of Fluid Mechanics*, *201*, pp.379-410.

Paolucci, S., (1990), Direct numerical simulation of two-dimensional turbulent natural convection in an enclosed cavity. *Journal of Fluid Mechanics*, *215*, pp.229-262.

Papazian, K., Al Hajaj, Z. and Saghir, M.Z., (2020), Thermal performance of a heated pipe in the presence of a metal foam and twisted tape inserts. *Fluids*, *5*(4), p.195.

Pellew, A. and Southwell, R.V., (1940), On maintained convective motion in a fluid heated from below. *Proceedings of the Royal Society of London. Series A. Mathematical and Physical Sciences*, *176*(966), pp.312-343.

Peng, W., Jiang, P.X., Wang, Y.P. and Wei, B.Y., (2011), Experimental and numerical investigation of convection heat transfer in channels with different types of ribs. *Applied Thermal Engineering*, *31*(14-15), pp.2702-2708.

Pera, L. and Gebhart, B., (1971), On the stability of laminar plumes: some numerical solutions and experiments. *International Journal of Heat and Mass Transfer*, *14*(7), pp.975-984.

Plant R.D. and Saghir S., (2021), "Numerical and experimental investigation of high concentration aqueous alumina nanofluids in a two and three channel heat exchanger", *International Journal of Thermofluids*, 9, 100055.

Pope, S.B. and Pope, S.B., (2000), *Turbulent flows*. Cambridge university press.

Rao J. and Lynch S.P. (2021),Large Eddy Simulation of Flow and Heat Transfer over Forward-Facing Steps with Upstream Injection, AIAA 2021-0161, Session: Wall-Bounded Turbulent Flows II, Published Online:4 Jan 2021https://doi.org/10.2514/6.2021-0161.

Ravi, M.R., Henkens, R.A.W.M. and Hoogendoorn, C.J. (1994), On the high Rayleigh-number structure of steady natural convection flow in a square enclosure, *J. Fluid Mech*., 262, pp.325–351.

Rayleigh, L., (1916), LIX. On convection currents in a horizontal layer of fluid, when the higher temperature is on the under side. *The London, Edinburgh, and Dublin Philosophical Magazine and Journal of Science*, *32*(192), pp.529-546.

Redchyts, D.O., Shkvar, E.A. and Moiseienko, S.V., (2020), Computational simulation of turbulent flow around tractor-trailers. *Fluid Dynamics & Materials Processing*, *16 (1)*, pp.91-103.

Rouizi, Y., Girault, M., Favennec, Y. and Petit, D., (2010), Model reduction by the Modal Identification Method in forced convection: Application to a heated flow over a backward-facing step. *International journal of thermal sciences*, *49*(8), pp.1354-1368.

Roux, B., Ben Hadid, H. and Laure, P., (1989), Hydrodynamical regimes in metallic melts subject to a horizontal temperature gradient. *European journal of mechanics. B, Fluids*, *8*(5), pp.375-396.

Saravanan, S. and Sivaraj, C., (2015), Combined natural convection and thermal radiation in a square cavity with a nonuniformly heated plate. *Computers & Fluids*, *117*, pp.125-138.

Saravanan, S., Hakeem, A.A., Kandaswamy, P. and Lee, J., (2008), Buoyancy convection in a cavity with mutually orthogonal heated plates. *Computers & Mathematics with Applications*, *55*(12), pp.2903-2912.

Scheit C., Esmaeili A. and Becker S., (2013), Direct numerical simulation of flow over a forward-facing step – Flow structure and aeroacoustic source regions, *Int. J. Heat Fluid Flow*, 43, pp. 184–193

Schlüter, A., Lortz, D. and Busse, F., (1965), On the stability of steady finite amplitude convection. *Journal of Fluid Mechanics*, *23*(1), pp.129-144.

Seban, R.A., (1966), The effect of suction and injection on the heat transfer and flow in a turbulent separated airflow.

Sherry, M., Jacono, D.L. and Sheridan, J., (2010), An experimental investigation of the recirculation zone formed downstream of a forward-facing step. *Journal of Wind Engineering and Industrial Aerodynamics*, *98*(12), pp.888-894.

Skinner S.N. and Behtash H. Z., (2017), "Semi-span wind tunnel testing without conventional peniche", *Experiments in Fluids*, 58(12), pp.1-18.

Smagorinsky J., (1963), General circulation experiments with the primitive equations. Part I: the basic experiment, *Monthly Weather Rev*. 91(3), pp. 99–164.

Smith, F.T. and Walton, A.G., (1998), Flow past a two–or three–dimensional steep–edged roughness. *Proceedings of the Royal Society of London. Series A: Mathematical, Physical and Engineering Sciences*, *454*(1968), pp.31-69.

Souissi, F., Guellouz, M.S., Ben Salah, N. and Kaddeche, S., (2020), The flow structure in the narrow gaps of compound channels: a linear stability analysis. *International Journal of Computational Fluid Dynamics*, *34*(1), pp.14-24.

Stevens, R.J., Verzicco, R. and Lohse, D., (2010), Radial boundary layer structure and Nusselt number in Rayleigh–Bénard convection. *Journal of fluid mechanics*, *643*, pp.495-507.

Stüer, H., Gyr, A. and Kinzelbach, W., (1999), Laminar separation on a forward-facing step. *European Journal of Mechanics-B/Fluids*, *18*(4), pp.675-692.

Sun Z. and Jaluria Y., (2011), "Conjugate thermal transport in gas flow in long rectangular microchannel", *J. Electron. Packag.* 133(2), 021008 (11 pages).

Taher, A.M. and Adam, I.G., (2010), February. Numerical investigations of a turbulent flow over triple forward facing step. In *2010 The 2nd International Conference on Computer and Automation Engineering (ICCAE)* (Vol. 5, pp. 303-307). IEEE.

Temam, R., (1969), Sur l'approximation de la solution des équations de Navier-Stokes par la méthode des pas fractionnaires (I). *Archive for Rational Mechanics and Analysis*, *32*(2), pp.135-153.

Thevenard, D., Rouzand, A., Comera, J. and Favier, J.J., (1991), Influence of convective thermal oscillations on a solidification interface in Bridgman growth. *Journal of crystal growth*, *108*(3-4), pp.572-582.

Tian, Y.S. and Karayiannis, T.G. (2000), Low turbulence natural convection in an air filled square cavity. Part I: the thermal and fluid flow fields, *Int. J. Heat Mass Transfer*, 1 (43), pp.849–866.

Van Driest E.R., (1956), On Turbulent Flow Near a wall, AIAA Journal, 23 (11), pp. 1007-1011

Venkatasubbaiah, K. and Jaluria, Y., (2012), Numerical simulation of enclosure fires with horizontal vents. *Numerical Heat Transfer, Part A: Applications*, *62*(3), pp.179-196.

Vincent, A.P. and Yuen, D.A., (1999), Plumes and waves in two-dimensional turbulent thermal convection. *Physical Review E*, *60*(3), p.2957.

Vogel J.C. and Eaton J.K., (1985), Combined heat transfer and fluid dynamic measurements downstream of a backward-facing step, *J. Heat Transfer* 107 (4), pp.922–929.

Wilhelm, D., Härtel, C. and Kleiser, L., (2003), Computational analysis of the two-dimensional–three-dimensional transition in forward-facing step flow. *Journal of Fluid Mechanics*, *489*, pp.1-27.

Wong, V.C. and Lilly, D.K., (1994), A comparison of two dynamic subgrid closure methods for turbulent thermal convection. *Physics of Fluids*, *6*(2), pp.1016-1023.

Xie, W.A. and Xi, G.N., (2017), Fluid flow and heat transfer characteristics of separation and reattachment flow over a backward-facing step. *International Journal of Refrigeration*, *74*, pp.177-189.

Xie, W.A. and Xi, G.N., (2017), Geometry effect on flow fluctuation and heat transfer in unsteady forced convection over backward and forward-facing steps. *Energy*, *132*, pp.49-56.

Xin, S. and Le Quer´ e, P. (1995), Direct numerical simulations of tw´ o-dimensional chaotic natural convection in a differentially heated cavity of aspect ratio 4, *J. Fluid Mech*., 304, pp.87–118.

Xu, J.H., Zou, S., Inaoka, K. and Xi, G.N., (2017), Effect of Reynolds number on flow and heat transfer in incompressible forced convection over a 3D backward-facing step. *International Journal of Refrigeration*, *79*, pp.164-175.

Yahata, H. (1997), Thermal convection in a vertical slot with lateral heating, *J. Phys. Soc. Jpn*., 66 (11), pp.3434–3443.

Yahata, H. (1999), Stability analysis of natural convection in vertical cavities with lateral heating, *J. Phys. Soc. Jpn*., 68 (2), pp.446–460.

Yan Z. H., (2007), Large-eddy simulations of a turbulent thermal plume, *Heat Mass Transfer* 43, 503–514.

Yarin, L.P., Mosyak, A. and Hetsroni, G., (2009), Cooling Systems of Electronic Devices. *Fluid Flow, Heat Transfer and Boiling in Micro-Channels*, pp.7-101.

Yoshizawa A. and Horiuti K., (1985), A Statistically-Derived Subgrid-Scale Kinetic Energy Model for the Large-Eddy Simulation of Turbulent Flows. *Journal of the Physical Society of Japan*, 54(8), pp. 2834-2839.

Yu, H., Li, N. and Ecke, R.E., (2007), Scaling in laminar natural convection in laterally heated cavities: is turbulence essential in the classical scaling of heat transfer?. *Physical Review E*, *76*(2), p.026303.

Zh, H. and Fu, S., (2017), Forward-facing steps induced transition in a subsonic boundary layer. *SCIENCE CHINA Physics, Mechanics & Astronomy*, *60*(10), pp.1-11.

Zhang, Y., Zhang, J., Li, T. and Zhang, L., (2017), Investigation of the aeroacoustics behaviour and aerodynamic noise of a high-speed train pantograph. *Science China Technological Sciences*, *60*(4), pp.561-575.

Zierep, J., (1963), Zur Theorie der Zellularkonvektion: Zellular-Konvektionsströmungen in Gefäßen endlicher horizontaler Ausdehnung. *Beitr. Phys. Atmos.*, *36*, pp.70-76.